



TECHNISCHE
UNIVERSITÄT
DARMSTADT

*Neutron matter, neutron pairing, and neutron drops
based on chiral effective field theory interactions*

*Neutronenmaterie, Neutronenpairing und Neutronentropfen
basierend auf Wechselwirkungen aus chiraler effektiver Feldtheorie*

VOM FACHBEREICH PHYSIK
DER TECHNISCHEN UNIVERSITÄT DARMSTADT

ZUR ERLANGUNG DES AKADEMISCHEN GRADES
DOCTOR RERUM NATURALIUM
(DR. RER. NAT.)

GENEHMIGTE DISSERTATION VON
THOMAS KRÜGER, M.Sc.
GEBOREN IN GROSS-GERAU

REFERENT: PROFESSOR ACHIM SCHWENK, PH.D.
KORREFERENT: PROFESSOR DR. RER. NAT. JENS BRAUN

TAG DER EINREICHUNG: 19. SEPTEMBER 2016
TAG DER PRÜFUNG: 19. OKTOBER 2016

DARMSTADT 2016
D17

Neutron matter, neutron pairing, and neutron drops
based on chiral effective field theory interactions

Neutronenmaterie, Neutronenpairing und Neutronentropfen
basierend auf Wechselwirkungen aus chiraler effektiver Feldtheorie

Genehmigte Dissertation von Thomas Krüger, geboren in Groß-Gerau.

Referent: Professor Achim Schwenk, Ph.D.

Korreferent: Professor Dr. rer. nat. Jens Braun

Tag der Einreichung: 19. September 2016

Tag der Prüfung: 19. Oktober 2016

2016 – Darmstadt – D17

Bitte zitieren Sie dieses Dokument als:

URN: urn:nbn:de:tuda-tuprints-56495

URL: <http://tuprints.ulb.tu-darmstadt.de/5649>

Dieses Dokument wird bereitgestellt von tuprints,
E-Publishing-Service der TU Darmstadt

<http://tuprints.ulb.tu-darmstadt.de/>

tuprints@ulb.tu-darmstadt.de



Die Veröffentlichung steht unter folgender Creative Commons Lizenz:

CC BY-NC-SA 4.0 International – Attribution, NonCommercial, ShareAlike

<https://creativecommons.org/licenses/by-nc-sa/4.0/>

Neutron matter, neutron pairing, and neutron drops based on chiral effective field theory interactions

ABSTRACT

The physics of neutron-rich systems is of great interest in nuclear and astrophysics. Precise knowledge of the properties of neutron-rich nuclei is crucial for understanding the synthesis of heavy elements. Infinite neutron matter determines properties of neutron stars, a final stage of heavy stars after a core-collapse supernova. It also provides a unique theoretical laboratory for nuclear forces. Strong interactions are determined by quantum chromodynamics (QCD). However, QCD is non-perturbative at low energies and one presently cannot directly calculate nuclear forces from it. Chiral effective field theory circumvents these problems and connects the symmetries of QCD to nuclear interactions. It naturally and systematically includes many-nucleon forces and gives access to uncertainty estimates. We use chiral interactions throughout all calculation in this thesis.

Neutron stars are very extreme objects. The densities in their interior greatly exceed those in nuclei. The exact composition and properties of neutron stars is still unclear but they consist mainly of neutrons. One can explore neutron stars theoretically with calculations of neutron matter. In the inner core of neutron stars exist very high densities and thus maybe exotic phases of matter. To investigate whether there exists a phase transition to such phases even at moderate densities we study the chiral condensate in neutron matter, the order parameter of chiral symmetry breaking, and find no evidence for a phase transition at nuclear densities. We also calculate the more extreme system of spin-polarised neutron matter. With this we address the question whether there exists such a polarised phase in neutron stars and also provide a benchmark system for lattice QCD. We find spin-polarised neutron matter to be an almost non-interacting Fermi gas. To understand the cooling of neutron stars neutron pairing is of great importance. Due to the high densities especially triplet pairing is of interest. We calculate the pairing gaps in neutron matter and provide uncertainty estimates.

The formation of heavy elements in the early universe proceeds through the rapid neutron-capture process. This process requires precise knowledge of the properties of very neutron-rich nuclei, which are unstable and at present not accessible in experiments. Thus, one can explore their properties only with theoretical calculations. Currently the only approach to the properties of all nuclei are energy-density functionals (EDFs). All EDFs used today are based on phenomenological models and fits to stable nuclei, which makes their predictive power for unknown (neutron-rich) nuclei unclear. Deriving an *ab initio* EDF directly from the nuclear forces is an important goal of nuclear theory. A promising approach is the optimised effective potential (OEP) method. We take a step into that direction and calculate neutron drops within the OEP formalism. In addition to the exact-exchange approximation we study for the first time the effect of second-order contributions and compare to quantum Monte Carlo and other results.

Neutronenmaterie, Neutronenpairing und Neutronentropfen basierend auf Wechselwirkungen aus chiraler effektiver Feldtheorie

ZUSAMMENFASSUNG

Der Physik neutronenreicher Systeme begegnet man in der Kern- und Astrophysik mit großem Interesse. Präzise Kenntnisse der Eigenschaften neutronenreicher Kerne sind für das Verständnis von der Synthese schwerer Kerne unerlässlich. Unendlich ausgedehnte Neutronenmaterie bestimmt die Eigenschaften von Neutronensternen, einem letzten Entwicklungszustand schwerer Sterne nach einer Kernkollaps-Supernova. Sie bildet außerdem ein einzigartiges Theorielabor für Kernkräfte.

Die starke Wechselwirkung wird durch die Quantenchromodynamik (QCD) beschrieben. Allerdings ist QCD im Niederenergiebereich nicht perturbativ und derzeit lassen sich Kernkräfte nicht direkt aus ihr herleiten. Chirale effektive Feldtheorie umgeht diese Probleme und verbindet die Symmetrien der QCD mit der Kernkraft. Sie beinhaltet auf natürliche Weise und systematisch Vielteilchenkräfte und bietet Möglichkeiten zu einer Unsicherheitsabschätzung. In dieser Dissertation verwenden wir in allen Rechnungen chirale Wechselwirkungen.

Neutronensterne sind sehr extreme Objekte. Die Dichten in ihrem Inneren übersteigen die in Atomkernen bei Weitem. Die genaue Zusammensetzung und Eigenschaften von Neutronensternen sind immer noch unklar, allerdings bestehen sie zum größten Teil aus Neutronen. Man kann Neutronensterne durch Berechnungen von Neutronenmaterie theoretisch erforschen. Im innersten Kern von Neutronensternen existieren sehr hohe Dichten und daher möglicherweise exotische Phasen von Materie. Um zu erforschen, ob es schon bei moderaten Dichten einen Phasenübergang zu solchen Phasen gibt, untersuchen wir das chirale Kondensat in Neutronenmaterie, den Ordnungsparameter chiraler Symmetriebrechung, und finden keinen Anhaltspunkt für einen Phasenübergang im nuklearen Dichtebereich. Außerdem berechnen wir das sehr extreme System Spin-polarisierter Neutronenmaterie. Dadurch können wir der Frage nachgehen, ob es in Neutronensternen eine solche polarisierte Phase gibt und bieten ein Benchmark-System für Gitter-QCD. Wir zeigen, dass Spin-polarisierte Neutronenmaterie ein nahezu nicht wechselwirkendes Fermigas darstellt. Um die Abkühlung von Neutronensternen zu verstehen ist Pairing sehr wichtig. Durch die hohen Dichten ist vor allem Triplet-Pairing von großem Interesse. Wir berechnen die Energielücken in Neutronenmaterie und geben dazu Unsicherheiten an.

Die Entstehung schwerer Elemente im jungen Universum erklärt sich durch den schnellen Neutroneneinfangsprozess. Dieser Prozess setzt präzise Kenntnisse der Eigenschaften sehr neutronenreicher Kerne voraus, welche instabil und experimentell nicht zugänglich sind. Daher kann man ihre Eigenschaften nur durch theoretische Berechnungen erforschen. Derzeit besteht der einzige Zugang zu den Eigenschaften aller Kerne aus Energiedichtefunktionalen (EDF). Alle zurzeit ver-

wendeten EDF basieren auf phänomenologischen Modellen und Fits an stabile Kerne, wodurch ihre Vorhersagekraft für unbekannte (neutronenreiche) Kerne unklar ist. Die Herleitung eines *ab initio* EDF direkt aus den Kernkräften ist ein wichtiges Ziel der theoretischen Kernphysik. Ein vielversprechender Ansatz besteht in der Methode des optimierten effektiven Potentials (OEP). Wir schreiten in diese Richtung und berechnen Neutronentropfen im OEP-Formalismus. Ergänzend zur Näherung des exakten Austauschs untersuchen wir zum ersten Mal auch den Einfluss von Beiträgen zweiter Ordnung und vergleichen unsere Berechnungen mit Quanten-Monte-Carlo-Simulationen und anderen Ergebnissen.

Contents

1	INTRODUCTION	1
1.1	Motivation	2
1.2	Neutron-rich systems: From nuclei to neutron stars	5
1.3	Energy-density functionals	17
1.4	Chiral effective field theory	24
2	INFINITE NEUTRON-RICH SYSTEMS	35
2.1	The chiral condensate in neutron matter	37
2.2	Spin-polarised neutron matter	45
2.3	The pairing gap in neutron matter	54
3	TOWARDS <i>AB INITIO</i> ENERGY-DENSITY FUNCTIONALS	77
3.1	Hartree-Fock and many-body perturbation theory	78
3.2	The optimised effective potential method	87
3.3	Including correlations at second order	101
4	FINITE NEUTRON-RICH SYSTEMS	107
4.1	Calculational details, approximations, and benchmarks	108
4.2	Neutron drops based on local chiral interactions	114
5	CONCLUSIONS	121
	APPENDICES	125
A	NUMERICAL DETAILS	127
B	DETAILS ON THE POLARISED-NEUTRON-MATTER CALCULATION	129
C	PW DECOMPOSITION OF THE MINNESOTA INTERACTION	133

MEINER OMA.

*O glücklich, wer noch hoffen kann,
Aus diesem Meer des Irrtums aufzutauchen!
Was man nicht weiß, das eben brauchte man,
Und was man weiß, kann man nicht brauchen.*

J. W. von Goethe, Faust, 1064ff.

1

Introduction

THE DISCOVERY OF THE NEUTRON in 1932 by James Chadwick [1] set the foundations of our current understanding of atomic nuclei. Since then the description of nuclei as compound objects consisting of neutrons and protons has steadily been further developed. Early semi-empirical descriptions within the liquid drop model such as the Bethe-Weizsäcker mass formula in 1935 [2] have been followed by microscopic models in the 1950s, which assumed nucleons to strongly interact via short-range meson exchanges, following the theory by Hideki Yukawa [3]. With the development of quantum chromodynamics (QCD) the understanding of the strong interaction was brought to the next level: Nucleons are composed of colour-charged quarks, which interact via gluon exchanges and are confined to colour-neutral objects.

Even though the main aspects of QCD had been settled in the early 1970s, calculations with phenomenological meson-exchange potentials were still widely used in the 90s in nuclear-physics and are still used even today. The main reason for that is that QCD is non-perturbative at low momenta which makes it at present impossible to directly derive nuclear forces from first principles. However, in the beginning of the 90s Steven Weinberg laid the foundations of chiral effective field theory connecting the symmetries of QCD to nuclear forces [4]. This modern approach allows a systematic description of nuclear interactions including many-nucleon forces and uncertainty estimates.

More than eight decades after the discovery of the neutron the physics of neutron-rich systems is still of great interest and we study some of its aspects in this thesis.

1.1 MOTIVATION

MORE THAN 7000 ATOMIC NUCLEI are expected to be bound. However, up to proton number $Z = 120$ only around 3000 nuclei have been studied experimentally, by a majority close to the valley of stability [5, 6]. In particular neutron-rich nuclei in the medium- to high-mass region far from stability are of interest in nuclear astrophysics. They are crucial for the description of heavy-element nucleosynthesis and shed light on the theoretical description of neutron stars.

NEUTRON STARS are the final stage of core-collapse supernovae and consist mainly of neutrons with a small fraction of protons and electrons [7]. They have one to two times the mass of our sun but typical radii of only around 10 km. Thus, in their interior exist densities even higher than in nuclei and a neutron star can be seen as a gigantic nucleus which is bound by gravitation. Neutron stars can be observed throughout a wide range of the electromagnetic spectrum. There exist precise measurements of neutron-star masses and in particular the relatively recent observations of two-solar-mass neutron stars [8–10] gained great attention. These measurements rule out many models of nuclear interactions that did not support such heavy neutron stars. While neutron-star masses can be measured with a relative error on the sub-per cent level, the determination of their radii is more difficult [11, 12].

The properties of neutron stars can be constrained by calculations of infinite neutron matter. The equation of state, *i.e.*, the energy per particle as a function of density, of neutron matter can be used to predict the mass-radius relation of neutron stars [13, 14]. Another open question of neutron-star physics is the composition of the neutron star's inner core. There are speculations about phase transitions to quark matter at nuclear densities [15]. To investigate this in detail we study the chiral condensate, the order parameter of chiral symmetry breaking, in neutron matter.

Neutron matter is also a unique system to test nuclear forces. Among neutrons, tensor forces are weaker and chiral many-nucleon forces are fully predicted [16]. With perturbative calculations of neutron matter it is possible to constrain empirical nuclear models like energy-density functionals fitted to experimental data. In this thesis we calculate the more extreme system of spin-polarised neutron matter, which can in addition to these constraints also be used as a benchmark system for lattice QCD. The aim of lattice QCD is to calculate nuclear systems from first principles using quarks and gluons as degrees of freedom [17]. It is currently limited to small or simple systems with reduced degrees of freedom. Such a system is spin-polarised neutron matter, because there are fewer non-trivial contractions. It can also give rise to the question whether there exists a phase of polarised matter in neutron stars.

We also address the phenomenon of pairing in neutron stars. From the rotational properties of neutron stars one expects a superfluid phase inside the star at nuclear densities, which also affects neutron-star cooling. We thus study the pairing gaps in neutron matter. Neutron pairing does not only play an important role in neutron stars but also affects the properties of neutron-rich nuclei.

THE FORMATION OF ELEMENTS heavier than iron cannot be explained by fusion reactions in stars, since the binding energy per nucleon is lower for heavier nuclei. There are, nevertheless, models to describe heavy-element nucleosynthesis. One of these is the rapid neutron-capture process (r-process) [18]. It occurs in extremely dense neutron-rich environments like core-collapse supernovae or neutron-star mergers. An initial seed nucleus from the iron region rapidly captures neutrons from its surroundings and then β decays into nuclei with higher atomic number. This process of rapid neutron capture and β decay repeats many times until the nucleus either undergoes fission or decays to heavy stable nuclides. For a theoretical description of the r-process and accurate calculations of nucleosynthesis yields precise knowledge about neutron-rich nuclei along the r-process path is key. In particular, accurate half-lives and ground-state energies are needed for r-process simulations.

The experimental access to these neutron-rich nuclei is very challenging. Neutron-rich nuclei have extremely short lifetimes and their production is difficult. At present, experimental facilities are limited in neutron excess, see, *e.g.*, the recent measurements along the calcium isotopic chain [19, 20]. However, there exist many facilities under construction worldwide (*e.g.*, FAIR at the GSI Helmholtz Centre in Darmstadt, or FRIB at the Michigan State University in East Lansing, USA) which will access a great extent of the neutron-rich regime of the nuclear chart but will not reach the neutron drip line of heavy elements.

Also the theoretical calculation of the properties of heavy neutron-rich nuclei is currently limited. There exist many *ab initio*, so-called quasi-exact methods which are limited to light nuclei up to mass numbers $A \lesssim 20$. Widely used examples are the no-core shell model (NCSM) [21, 22], Green's function Monte Carlo (GFMC) [23], or lattice effective field theory (EFT) [24, 25]. All these approaches are limited by computer power and memory. In the intermediate-mass region further approximations are necessary. Near shell closures coupled-cluster (CC) calculations [26, 27] are possible. Intermediate-mass nuclei can also be calculated with the microscopic shell model (SM) [28, 29] or within the in-medium similarity renormalisation group (IM-SRG) [30, 31]. Heavy elements, especially far from closed shells, can only be calculated with energy-density functionals (EDF). However, models like Skyrme [32] and Gogny [33] are not directly based on microscopic nuclear interactions and have to be fitted to experimentally known nuclei. While describing, *e.g.*, the ground-state energies of known nuclei with a root-mean-square precision $\sim 1 \text{ MeV}^1$, they make unreliable predictions for unknown isotopes, especially on the neutron-rich side [6]. The derivation of energy-density functionals directly from nuclear interactions is an important goal of nuclear theory [34].

In this thesis we want to take a step in that direction. Within the optimised effective potential method (OEP) we calculate neutron drops using chiral interactions. The OEP method is similar to the Hartree-Fock approximation and many-body perturbation theory and is widely used in quantum

¹Note that we use natural units $\hbar = c = 1$ throughout the whole thesis.

chemistry. It provides a path from a general energy functional to a local Kohn-Sham potential [35]. In Ref. [36], Joaquín E. Drut and Lucas Platter introduced the OEP to nuclear physics and calculated neutron drops with a benchmark interaction. We will go a step further by studying also second-order contributions and using chiral interactions. Our results can be compared to quasi-exact quantum Monte Carlo methods and used as benchmark systems to constrain empirical energy-density functionals.

THIS THESIS is organised as follows: In the subsequent Sections we give a more detailed introduction to the physics of neutron-rich systems, density functionals, and chiral effective field theory interactions. In Chapter 2 we present calculations for infinite systems: The chiral condensate in neutron matter, spin-polarised neutron matter, and the pairing gap in neutron matter. Chapter 3 starts with a summary of Hartree-Fock calculations for neutron drops and provides the details about the optimised effective potential method. Results and details about the numerical calculations of neutron drops are discussed in Chapter 4. We conclude in Chapter 5 and give an outlook.

1.2 NEUTRON-RICH SYSTEMS: FROM NUCLEI TO NEUTRON STARS

OVER A WIDE RANGE OF DENSITIES neutron-rich systems gained interest in many areas of nuclear physics. At very low densities neutron matter exhibits universal properties due to the large neutron-neutron scattering length. It can thus be probed in experiments with cold atoms [37]. In the region of intermediate densities ($\sim 0.5n_0$, where $n_0 = 0.16 \text{ fm}^{-3} \approx 2.7 \times 10^{14} \text{ g cm}^{-3}$ denotes nuclear saturation density) medium-mass to heavy nuclei close to the neutron dripline are of interest. As mentioned above, the knowledge of key observables of these neutron-rich nuclei is crucial for nuclear astrophysics, *e.g.*, r-process simulations [18]. Experimental efforts into that direction are at present and will be made at facilities worldwide, *e.g.*, at The Radioactive Isotope Beam Factory (RIBF) at RIKEN in Tokyo, Japan [38], as well as the Facility for Antiproton and Ion Research (FAIR) at the GSI Helmholtz-Centre for Heavy-Ion Research in Darmstadt [39] and the Facility for Rare Isotope Beams (FRIB) at the Michigan State University in East Lansing, USA [40], which are currently under construction. In the regime of intermediate to high densities of several times nuclear saturation density the equation of state of neutron matter governs the main properties of neutron stars [14]. Besides the energy also the understanding of pairing in neutron matter is key to explain observations of neutron stars like the neutrino cooling after their formation or their rotational dynamics.

1.2.1 NEUTRON-RICH NUCLEI

An overview of all experimentally known nuclei is shown in Fig. 1.1. Stable nuclei are depicted in black. On the neutron-rich side, *i.e.*, below the stable nuclei, most nuclides are unstable with respect to β^- decay, while the neutron-deficient nuclei usually undergo β^+ decays.

The lower edge of the nuclear chart marks the neutron drip line. It is reached at a nuclide with proton and neutron number (Z, N) where the one-neutron separation energy

$$S_{1n} = E_B(Z, N - 1) - E_B(Z, N), \quad (1.1)$$

becomes negative. Here E_B denotes the positively defined binding energy of the nucleus. At $S_{1n} = 0$ the nucleus is unstable with respect to neutron emission. Analogously one defines the proton drip line, the upper limit of the nuclear chart.

On the neutron-deficient or proton-rich end the drip line is almost settled experimentally while the neutron-rich side is still a *terra incognita*.

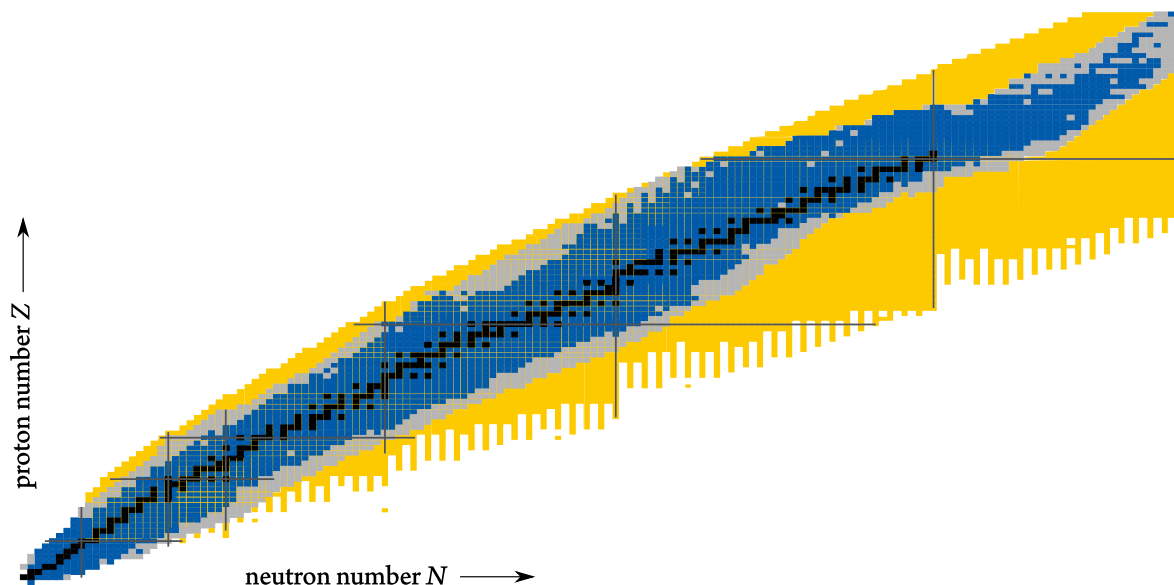


Figure 1.1: Overview of the nuclear chart: Stable nuclei are indicated as black boxes. In blue we show all nuclides where the masses are known according to the AME₂₀₁₂ atomic mass evaluation [41]. For nuclei depicted in grey only other properties, *e.g.*, half-lives are known. The yellow region is based on theoretical predictions and these nuclei have not been observed in experiments.

IMPORTANCE OF NEUTRON-RICH NUCLEI IN NUCLEOSYNTHESIS

The properties of neutron-rich nuclei have great importance for nuclear astrophysics [18]. The formation of elements heavier than iron cannot be explained with fusion reactions during stellar burning since it is energetically not favoured. However, it can be explained with three types of reaction mechanisms: The p-, s-, and r-process. The p- or proton-capture process takes place on the proton-rich side of the nuclear chart, creating proton-rich nuclei. It only plays a minor role in nucleosynthesis. Both the s- and r-processes involve neutron-rich nuclei but differ in their reaction time and physical sites of occurrence. While the slow neutron-capture or s-process takes place in low- to medium-mass stars at moderate neutron densities, the rapid neutron-capture (r-)process only occurs at very extreme densities and temperatures. It involves nuclei close to the neutron drip line and produces half of the heavy elements.

One of possible r-process sites are core-collapse supernovae. When a massive star reaches the end of its lifetime and runs out of fuel it cannot stand against its own gravity and collapses. Directly after the collapse exist extreme conditions with very high temperatures and neutron densities. Extreme neutron-rich conditions can also be found in neutron-star mergers, which are also possible candidates for r-process sites. In such environments (neutron-rich) iron nuclei (the final state of solar burning) can rapidly capture neutrons. In this way the nucleus will accumulate more and more neutrons until its β decay rate overcomes the capture rate. After a β decay it may capture new neutrons and this process runs along neutron-rich nuclei close to the drip line up to heavy elements like uranium until the nucleus decays to a stable state or undergoes spontaneous fission.

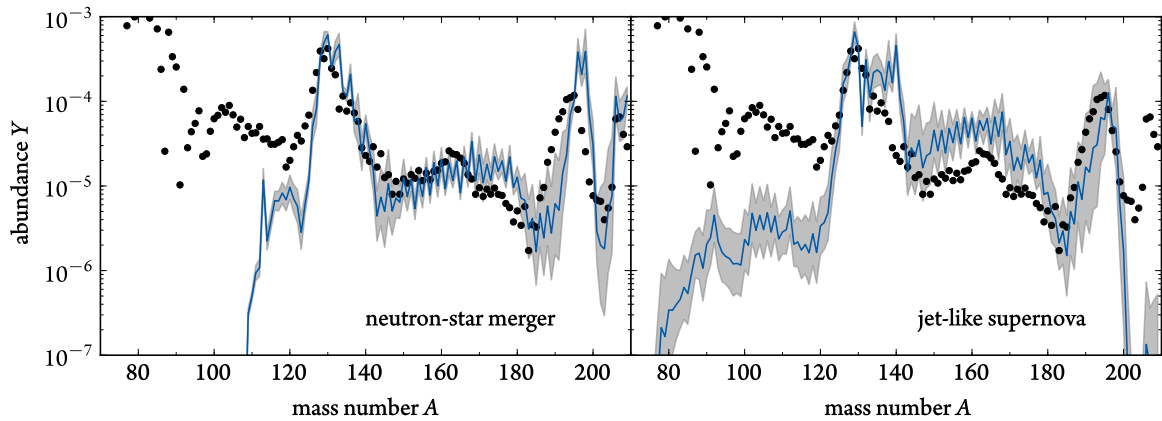


Figure 1.2: Solar system r-process abundances (black dots) for r-process nuclei with mass numbers A compared to predictions from r-process simulation using nuclear masses from Skyrme functionals (blue line). The grey band indicates the uncertainties stemming from different mass predictions. In the left figure the simulation assumes a neutron-star merger as astrophysical site while on the right a jet-like supernova is used. See Ref. [42] for details. Courtesy of Dirk Martin.

For simulations of the r-process precise knowledge of the nuclear masses and half-lives is of great importance [42], see Fig. 1.2 for a prediction of solar abundances of r-process nuclei. In particular, the masses of elements around magic numbers are critical since separation energies vary rapidly in these areas, due to shell closures. Currently almost all r-process simulations are based on empirical energy-density functionals and a reduction of their uncertainties will directly improve the simulations.

PAIRING IN NEUTRON-RICH NUCLEI

In 1957 John Bardeen, Leon N. Cooper, and John R. Schrieffer developed the theory of electron superconductivity, which is now referred to as BCS theory [43]. Superconductivity is explained by the formation of Cooper pairs [44] in the presence of the attractive phonon-mediated interaction between electrons. At critical temperatures [typically $\sim (1 - 10)$ K] a second-order phase transition occurs. The superconducting phase is characterised by the appearance of an energy gap Δ in the electron spectrum around the Fermi surface. Only a year later Aage Bohr, Ben R. Mottelson, and David Pines proposed a similar phenomenon in nuclei [45]. They found by analysing nuclear excitation spectra that the energies of the (lowest-lying) non-collective excited states in even-even nuclei exhibit a significant gap ~ 1 MeV. Another prominent evidence for pairing in nuclei is the so-called odd-even staggering: The binding energy of even- Z or even- N nuclei is significantly higher than those of neighbouring nuclides with odd number of protons or neutrons. Nucleons would form Cooper pairs due to the attractive part of the nucleon-nucleon interaction. Another year later Arkady B. Migdal applied BCS theory to nuclei [46].

Near the neutron drip line experiments have revealed large odd-even-staggering effects for the lighter

nuclei $^{18,19,20}\text{C}$, $^{28,29,30}\text{Ne}$, and $^{36,37,38}\text{Mg}$ [47]. These effects can be attributed to pairing and in particular to the pairing anti-halo effect, which prevents the formation of one-neutron halo nuclei [48]. Also for heavier nuclei precise knowledge about odd-even staggering is important to adjust nuclear physics models. In Ref. [49] mass-measurement experiments for even Z nuclei in the region $Z = 50 - 82$ have been performed on the neutron deficient side. Towards the proton drip line the odd-even-staggering effects increased for neutrons and protons. Similar effects have also been seen on the neutron-rich side but due to experimental limits by far not close to the neutron drip line. For a more elaborate discussion of pairing in (neutron-rich) nuclei see Refs. [50, 51].

EXPERIMENTAL ACCESS TO NEUTRON-RICH NUCLEI

The first identification of an atomic nucleus can be attributed to Ernest Rutherford and Hans Geiger, who concluded that the α -particle is a helium atom (at least when it has lost its charge) in 1908 [52], even before the famous Rutherford gold foil experiments, which established the picture of a ‘minute massive centre’ in atoms carrying positive charge [53]. In 1913 Joseph J. Thomson was the first to identify two isotopes of the same atom. Using mass spectroscopic methods he identified ‘two different types of neon’ with mass 20 and 22 [54]. The development of mass spectrographs, mainly driven by Francis W. Aston, led to the discovery of almost all stable nuclei by the end of the 1930s [55]. Since these discoveries more than 3000 nuclei have been identified and measured [5].

The measurement of radioactive short-lived nuclei is experimentally challenging. There are mainly two problems originating from the short lifetime of neutron- or proton-rich nuclei: Exotic nuclei do not exist in nature and have to be synthesised experimentally. Once produced they have to be identified and measured before their decay. The closer one gets to the drip line on either side of the nuclear chart the shorter lived are the nuclides.

On the proton-rich side the production is easier and the proton drip line has been established for most nuclei that exist on earth. This is due to the strong Coulomb repulsion that destabilises neutron-deficient nuclei shifting the proton drip line closer to the valley of stability. For neutron-rich nuclei the neutron drip line has not been reached experimentally for medium-mass to heavy nuclei. So far the heaviest nucleus which was shown to be unbound is ^{39}Mg [56].

For the production of neutron-rich nuclei target-fragmentation methods are used. A heavy, ideally neutron-rich nucleus is bombarded with lighter nuclei at high energies. This induces fragmentation, spallation, or fission reactions with neutron-rich nuclei as products. The setup can also be reversed with heavy projectiles shot on lighter targets. Currently these experiments are limited in beam intensities and energy. The construction of new facilities like FAIR or FRIB will help to overcome these limits and find nuclides closer to the neutron drip line [5]. After their production the nuclei of interest have to be separated and transported to the experimental setup. This can be done with both, the in-flight separation [57] or the isotope separation on line (ISOL) technique [58]. The nuclides are measured with different methods, *e.g.*, time of flight or Penning trap [59] measurements or by

storing them in large storage rings. For recent examples of precise measurements of neutron-rich ions see, *e.g.*, the works along the calcium isotopic chain [19, 20] measured at the TITAN setup at TRIUMF in Vancouver, Canada and at ISOLTRAP/ISOLDE at CERN in Geneva, Switzerland.

1.2.2 NEUTRON STARS

Neutron stars are very extreme, compact objects with typical masses of about $(1 - 2)M_{\odot}$, with M_{\odot} being the mass of our sun, but only radii of around 10 km, resulting in an average density of $\sim(2 - 3)n_0$ [7]. In their center, however, the density can even reach $8n_0$ [14]. Parts of this Section are based on Ref. [7], in which more details about neutron stars can be found.

Neutron stars are a product of core-collapse supernovae. Stars like our sun with masses up to $\sim 10M_{\odot}$ form white dwarfs at the end of their life cycle. For progenitor stars in a mass range of about $(10 - 25)M_{\odot}$ neutron stars are formed. Heavier stars will collapse into black holes.

In 1967 Jocelyn Bell, a graduate student of Antony Hewish, discovered a weak variable radio source with an extremely stable period of 1.337 s. It turned out that this rapidly pulsating source was far out of our solar system and was later named pulsar. Shortly after that discovery two other pulsars were observed and the results very published in Ref. [60]. After a strong competition pulsars were identified as rotating magnetised neutron stars [61]. The magnetic moment of neutron stars is inclined to their rotational axis. The radio emission, generated outside the star in its magnetosphere, is radiated along the magnetic axis. Due to its rotation the pulsar appears like a lighthouse for observers at earth explaining the regular detection of radio pulses.

Long before their discovery, and even before the discovery of the neutron by James Chadwick [1] in 1932, Lev D. Landau postulated the existence of stars heavier than white dwarfs in 1931 [62]. He concluded that in such stars the densities of nuclei could be reached such that a ‘gigantic nucleus’ would be formed. In 1934 Walter Baade and Fritz Zwicky were the first to predict ‘neutron stars’ consisting of ‘extremely closely packed neutrons’ as the product of supernovae [63–65].

The next step towards a better understanding of neutron stars was made by Richard C. Tolman and, independently of him, J. Robert Oppenheimer and George Volkoff, who derived an equation for spherical stars in hydrostatic equilibrium [66, 67]. The now called Tolman-Oppenheimer-Volkoff (TOV) equations are formulated in the framework of general relativity and give a one-to-one correspondence between the equation of state of neutron-star matter and their mass-radius relation. At that time one already expected neutron stars to consist mainly of neutrons with a small fraction of protons in β equilibrium (neutron β decay and proton electron capture are in equilibrium). However, since the interaction among neutrons was an unresolved problem at that time also the equation of state of neutron(-star) matter was unknown. One expected neutrons to form a noninteracting Fermi gas, which led to the conclusion that the maximal mass of neutron stars is around $0.7M_{\odot}$, the Oppenheimer-Volkoff limit.

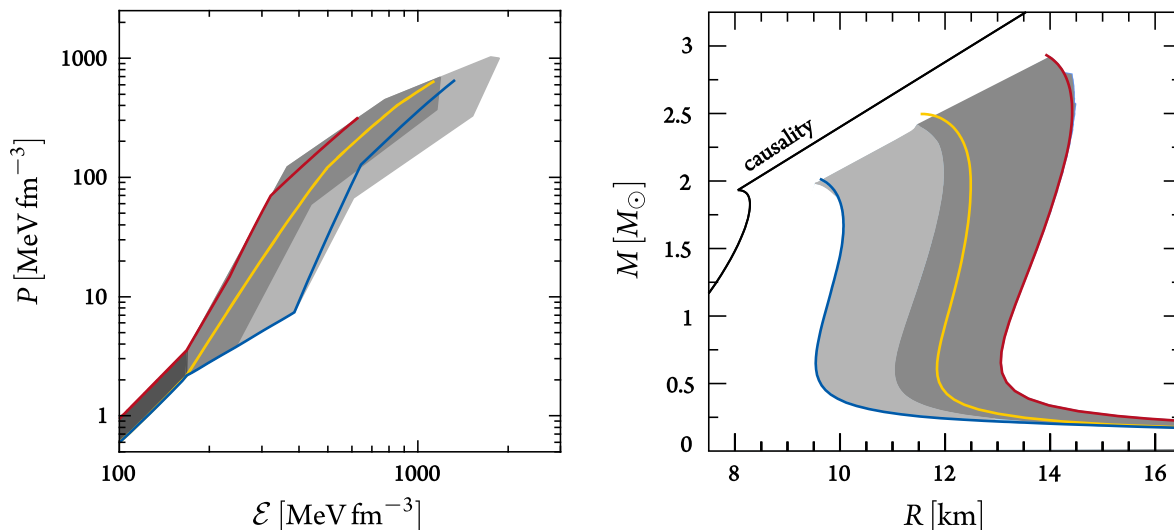


Figure 1.3: Left: Equation of state (pressure P versus energy density \mathcal{E}) of neutron-star matter based on perturbative calculations of neutron matter expanded to small proton fractions (dark grey band) and extrapolated to higher densities (lighter grey bands). The red, yellow, and blue line depict a stiff, intermediate, soft equation of state, respectively. They have been chosen as representatives.

Right: Corresponding predicted mass-radius range obtained with the TOV equations. All equations of state are chosen to support a $2M_\odot$ neutron star. If a heavier star is observed the soft equation of state (blue) would be ruled out. Figure taken from Ref. [14].

This picture was changed in the late 1950s, early 1960s when one hoped to discover neutron stars by observations. Alastair G. W. Cameron found that the nuclear interaction stiffens the equation of state [68] allowing for heavier neutron stars up to $\sim 2M_\odot$. He was also the first to point out the possible existence of hyperons in neutron-star cores, which also gave rise to more exotic equations of state and even speculations about a quark-matter core [69, 70].

With the help of the TOV equations, neutron matter calculations can be used to constrain the properties of neutron stars. In Fig. 1.3 the correspondence between the equation of state and a mass-radius relation is shown, based on perturbative calculations of neutron matter with chiral interactions and a general extension to high densities [13, 14].

INTERNAL STRUCTURE OF NEUTRON STARS

The current theories divide neutron stars into a thin atmosphere and four internal regions (see Fig. 1.4): The outer and inner crust as well as the outer and inner core [7].

The outer crust, or outer envelope has a width of only around a few hundred meters and densities up to $\sim 0.002n_0$. It consists of a crystal lattice of nuclei in the iron region, which are at the surface surrounded by a non-degenerate and deeper into the crust by a strongly degenerate electron gas. With increasing density the nuclei become more neutron rich because electron captures are induced

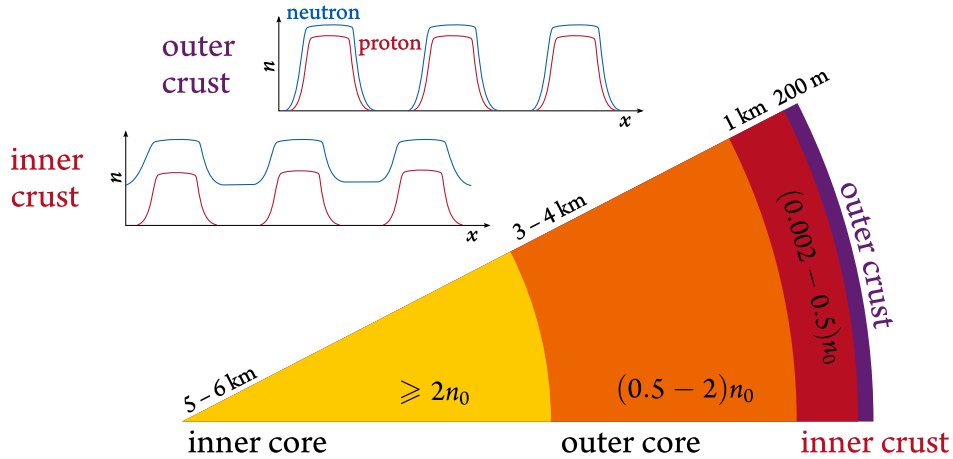


Figure 1.4: Schematic structure of a neutron star. The outer crust is formed by a lattice of neutron-rich nuclei. The corresponding density distribution functions are shown schematically in the upper plot with blue lines for the neutron and red lines for the proton density. Deeper into the interior the neutron density increases and the nuclei smear out as indicated in the lower plot. The background neutrons form a superfluid. In the outer core neutrons are in β equilibrium with a small fraction of protons and electrons. The composition of the inner core with densities of maybe severable times nuclear saturation density is not fully understood.

by the Fermi energy of the electron gas. At the transition to the inner crust neutrons start to drip out and form a free neutron gas in the background (see also the density sketches in Fig. 1.4).

In the inner crust the densities increase up to $\sim 0.5n_0$ and it has a width of around 1 km. The nuclei become more neutron rich and the fraction of the background neutrons increases. They can be in a superfluid state. At the crust-core boundary the nuclei disappear and neutron-rich matter is formed. The outer core is several kilometres thick and extends up to densities $\sim 2n_0$. It consists mainly of neutrons which are accompanied by a small fraction of protons ($\sim 5\%$) and the same number of electrons (and possibly muons) to ensure charge neutrality. This neutron-rich matter is in β equilibrium, *i.e.*, the β decay of the neutrons into protons and electrons (muons) is in equilibrium with its inverse process. The (anti)neutrinos are disregarded as they are weakly interacting and also emitted from the star. The electrons form an almost ideal Fermi gas and the nucleons a strongly interacting liquid. They can be in a superfluid state.

The inner core starts at densities around $2n_0$ and can reach up to $8n_0$ [14]. Its radius can be around a few kilometres. The composition is still unclear. There are hypotheses of Lee-Wick abnormal matter, pion- as well as kaon-condensed matter, hyperon matter, and even quark matter. The appearance of a new phase through a first- or second-order phase transition softens the equation of state and may not support heavy neutron stars beyond $2M_\odot$ [8–10].

PAIRING AND SUPERFLUIDITY IN NEUTRON STARS

After his application of BCS theory to nuclei in 1959, Arkady B. Migdal was the first to note that neutron superfluidity could occur in neutron stars with a gap $\Delta \approx 1$ MeV and critical temperature $T_c \approx 10^{10}$ K [46]. Vitaly L. Ginzburg and David A. Kirzhnits estimated a couple of years later the pairing gap from neutrons in a single state at neutron star densities [71, 72]. They found pairing gaps $\Delta \approx (5 - 20)$ MeV and also discussed various consequences of superfluidity in neutron stars.

In pioneering work by Richard A. Wolf in 1966 [73] and later by Mark Hoffberg *et al.* [74] pairing in neutron matter was analysed in detail in BCS theory. It was found that in the inner crust of neutron stars pairing in the 1S_0 channel was present but vanished at higher densities. At around a tenth of nuclear saturation density the pairing gap reaches its maximum of ~ 3 MeV and drops in the density region $\lesssim n_0$. At these densities pairing in the 3P_2 state is favoured, since it is more attractive due to the spin-orbit interaction among nucleons. Since only the total angular momentum J is a good quantum number, the channels 3P_2 and 3F_2 are coupled and can only be studied consistently together. The $^3P_2 - ^3F_2$ pairing gap is expected to reach its maximum around $2n_0$ and decreases until it vanishes in the inner core of neutron stars. The exact value of the $^3P_2 - ^3F_2$ pairing gap is a topic of current research (see Chapter 2).

In Fig. 1.5 we have plotted the phase shifts obtained from the Nijmegen partial-wave analysis [75] for the lowest partial waves contributing to neutron matter. This gives rise to a qualitative understanding of the pairing gap. Positive phase shifts indicate attractive interactions. The characteristics of the 1S_0 channel with positive phase shifts at low energies clearly indicates the possibility of pairing in that energy region. At lab energies $\gtrsim 260$ MeV it becomes negative implying a repulsive interaction. Thus, S-wave pairs form only at low energies/densities but are inhibited from forming around nuclear saturation density. The next candidate is the P-wave triplet since 3S_1 and 1P_1 are excluded by Pauli's principle for neutron-only systems. The phase shift in the 3P_0 partial wave shows the same characteristics as the 1S_0 wave but is much smaller. This hints that 1S_0 pairing is favoured. In the 3P_1 channel, the nuclear interaction is fully repulsive (negative phase shifts). The only candidate for pairing is thus the 3P_2 channel in which the phase shift is positive, even at high energies. In fact, it is the most attractive $T = 1$ channel at lab energies $E_{\text{lab}} = 2k_F^2/m \gtrsim 160$ MeV. This corresponds to Fermi momenta $k_F \approx 1.4 \text{ fm}^{-1}$. Due to spin-orbit interactions and tensor forces the 3P_2 channel is coupled to the 3F_2 channel and cannot be investigated independently. Hence, one expects a substantial pairing effect in the $^3P_2 - ^3F_2$ channel at densities around and above nuclear saturation density.

Pairing is a phenomenon which predominantly occurs at the Fermi surface and has only minor effects on the equation of state of neutron stars and thus on their radii. For a more detailed overview of superfluidity of nucleons in neutron stars see, *e.g.*, Ref. [76].

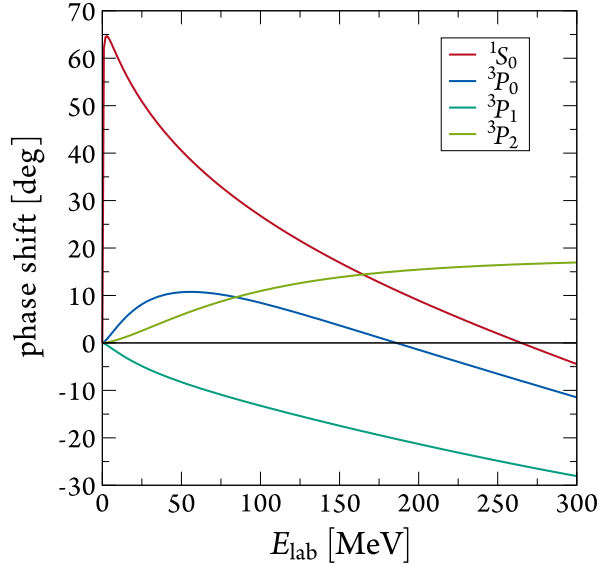


Figure 1.5: Neutron-proton phase shifts as a function of the laboratory energy $E_{\text{lab}} = 2k_{\text{F}}^2/m$ based on the Nijmegen partial-wave analysis [75] for the lowest contributing partial waves in neutron matter: 1S_0 (red line), 3P_0 (blue), 3P_1 (sea green), and 3P_2 (green). For laboratory energies $\gtrsim 160$ MeV (corresponding to $k_{\text{F}} \sim 1.4 \text{ fm}^{-1}$) the 3P_2 channel gives the dominant attractive contribution. Note that due to the only weakly broken isospin symmetry the neutron-proton phase shift approximates that of two neutrons scattering well.

COOLING OF NEUTRON STARS AND NEUTRINO EMISSION

Directly after a supernova in which a neutron star is born, this star is in a hot state and opaque to neutrinos. At this stage the star is referred to as a proto-neutron star. Only about one minute later it becomes transparent to neutrinos and cools down by two mechanisms [77–79]: For about the first 10^5 years neutrino emission from the entire star dominates. Later on the predominant cooling process is thermal photon emission which is supported by heat diffusion from the inner layers of the neutron star. We want to focus on neutrino cooling and discuss the most important neutrino processes in neutron stars.

Neutrinos are produced in many processes inside neutron stars [80, 81]. Whereas the neutrinos generated in a nearby core-collapse supernovae can be detected on earth in neutrino observatories, the neutrino flux of the neutrinos emitted from neutron stars is too small to be detected. At the beginning of their lifetime neutron stars have internal temperatures $\gtrsim 10^7$ K.

Inside the core the most energetic neutrinos with energies in the order of 1 K are produced in direct Urca processes. The Urca process consists for ordinary neutron-star matter of a neutron decay and the reverse process,

$$n \rightarrow p + l + \bar{\nu}_l, \quad p + l \rightarrow n + \nu_l, \quad (1.2)$$

where $l = e, \mu$ denotes electrons or muons, respectively. In both processes a neutrino is emitted. The direct Urca processes can possibly operate only in the inner core where the density of protons

and leptons is high enough [82, 83]. Assuming a non-superfluid core, one can calculate the neutron emissivity by

$$Q(T, \rho) = Q_0(\rho) \left(\frac{T}{10^9 \text{ K}} \right)^k \text{ erg cm}^{-3} \text{ s}^{-1}, \quad (1.3)$$

where $1 \text{ erg} = 10^{-7} \text{ J}$. For the direct Urca process with electrons and muons $k = 6$ and $Q_0 = (0.1 - 3) \times 10^{27}$ varies slowly with the density. Hence, the direct Urca process produces a strong neutrino cooling. A similar process can also act in exotic neutron-star matter with hyperons or pion and kaon condensates with comparable emissivities.

Another, weaker neutrino process cooling neutron stars is the modified Urca process. It can occur at lower electron fractions than the direct Urca process and can be dominant in low-mass neutron stars where the inner core is small or even non-existing. In this process another nucleon (N) is involved, which is required for momentum conservation,

$$n + N \rightarrow p + N + l + \bar{\nu}_l, \quad p + N + l \rightarrow n + N + \nu_l. \quad (1.4)$$

In these regions also bremsstrahlung processes are relevant,

$$N + N \rightarrow N + N + \nu + \bar{\nu}, \quad (1.5)$$

where the neutrino can have all flavours. The emissivity of these processes can again be calculated with Eq. (1.3) with $k = 8$ and $Q_0 \approx 10^{20} - 3 \times 10^{23}$ and $Q_0 \approx 10^{19} - 10^{20}$ for the modified Urca and bremsstrahlung process, respectively.

The neutrino processes discussed above are strongly effected by neutron and proton superfluidity [81, 84]. The nucleons are degenerate and they can only participate in a reaction if their energies lie within the thermal width of the Fermi levels. When the energy drops below the critical temperature pairing inhibits the nucleons from reacting and the processes are suppressed by a factor of the form $\exp[-\Delta(k_F)/T]$, where $\Delta(k_F)$ denotes the pairing gap at the Fermi surface. However, superfluidity triggers also a new neutrino cooling process [85]. The Cooper pairing of the nucleons produces neutrino pairs. This can be understood in the quasi-particle formalism. The annihilation of, e.g., two quasi-neutrons (\tilde{n}) produces two neutrinos, $\tilde{n} + \tilde{n} \rightarrow \nu + \bar{\nu}$, where ν can have all flavours. While this process starts at the critical temperature T_c it reaches its maximum around $0.8T_c$ and is exponentially suppressed for smaller temperatures. The neutrino luminosity originating from this process can be one to two orders of magnitude larger than that from the traditional neutrino processes discussed above. It was found recently that in particular the rapid cooling of the neutron star in Cassiopeia A is expected to be due to the neutrino emission from the formation and breaking of neutron pairs in the 3P_2 channel [86].

NEUTRON-STAR OBSERVATIONS

After the observation of the first pulsar in 1967, mentioned earlier, many more neutron stars have been found. In our galaxy about 2000 neutron stars have been observed, which is only a tiny fraction of the expected total population of $10^8 - 10^9$ neutron stars. The main route to investigate the properties of these stars follows observations in the electromagnetic spectrum but also the detection of neutrinos emitted during the lifetime of the proto-neutron star and of gravitational waves will provide useful insight into the physics of neutron stars.

Pulsars emit electromagnetic waves in a wide range of wavelengths: Radio, infrared, optical, ultraviolet, X-, and γ -rays. However, the emission mechanism is still poorly known. A possible explanation is curvature radiation originating from electrons trapped in the strong magnetic field [87]. On earth radio, infrared, and optical waves can only be detected with very large telescopes due to the weak emission in these channels. With space telescopes, *e.g.*, the ‘Hubble Space Telescope’ observations in the ultraviolet and optical regions are feasible. X- and γ -rays are also detected by space observatories, *e.g.*, the ‘X-ray Multi Mirror (XMM Newton)’ or ‘Chandra’, respectively.

As mentioned above, the magnetisation and rotational axis of neutron stars is in general misaligned, which causes a small decrease of the rotation. The rotation is, however, very stable and also its decrease can be calculated precisely. Thus, one can predict the detection of pulses with high accuracy and any small deviation caused from gravitational interaction with the companion can give information about the mass of the neutron star. The more compact the companion star is, the more precise measurements are possible. In neutron-star binaries the accuracy reaches even relative errors of the order of 10^{-4} (see Fig. 1.6). Neutron star masses can put constraints on their equation of state. As the TOV equations directly relate the equation of state to a mass-radius relation one can rule out models which do not support the recently precisely measured high-mass neutron stars with $M \approx 2M_{\odot}$ (PSR-J1614-2230 [8, 9], PSR-J0348+0432 [10]).

In principle, also measurements of the radius of neutron stars could put strong constraints on the equation of state, in particular if apart from the radius also the mass of a particular neutron star would be known. Nevertheless, radius measurements have low accuracies at the moment since neutron stars are so small, far away, and faint. The only access to radii at the moment is through high-order statistical analyses combining many observations, which predict radii for medium-mass neutron stars around 12 ± 1 km [12]. Another promising approach to access the radius is through the measurement of the moment of inertia of neutron stars which can constrain the radius while also knowing the mass precisely [90].

Neutrino measurement is experimentally very challenging because of their low interaction rate with ordinary matter. Huge experimental set-ups like the ‘Super-Kamioka Neutrino Detection Experiment’ in Japan still will only be able to measure the neutrino flux emitted during a supernova and from the proto-neutron star shortly after.

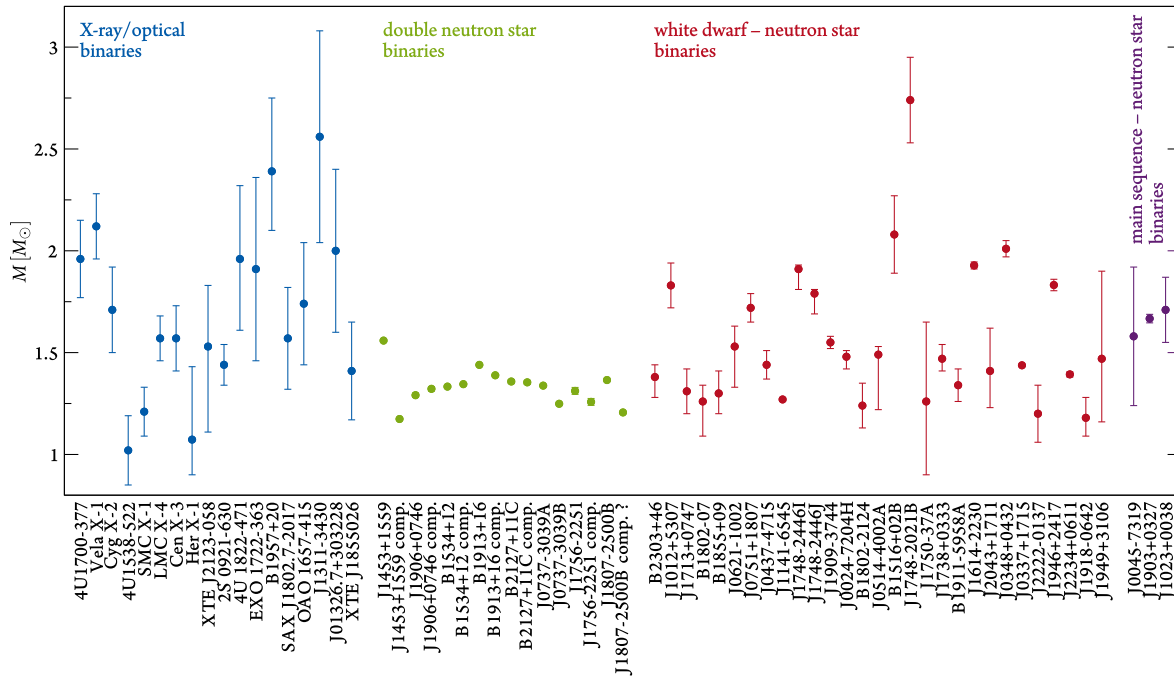


Figure 1.6: Overview of observed neutron-star masses with 1σ uncertainties, sorted with respect to the type of binary system the star resides in. Data taken from Refs. [88, 89].

The first direct detection of gravitational waves, which stretch and compress the spacetime and have been predicted within the framework of general relativity, gained enormous public interest in the beginning of this year [91]. The LIGO and Virgo Collaboration measured with the ‘Advanced LIGO’ detectors [92] the gravitational-wave signal originating from the merger of two black holes. It is also expected that the signal from neutron-star mergers inside our galaxy can be measured with these detectors. The signal from such a merger would have certain characteristics, which could determine parameters of the neutron-star equation of state [93–95].

1.3 ENERGY-DENSITY FUNCTIONALS

THE FIRST SIMPLE ENERGY FUNCTIONAL in nuclear physics was introduced by Carl F. von Weizsäcker within the theory of the liquid drop model in 1935 [2]. Hans A. Bethe was the first to calculate nuclear properties with it and it is thus often referred to as Bethe-Weizsäcker mass formula [96]. Strictly speaking it is not a functional but a function of the mass number $A = \int d^3x \rho(\mathbf{x})$, with density $\rho(\mathbf{x})$. It gives the binding energy of stable nuclei as a simple sum of five terms

$$E_B = a_V A - a_S A^{2/3} - a_C \frac{Z(Z-1)}{A^{1/3}} - a_A \frac{(N-Z)^2}{4A} + \delta(N, Z), \quad (1.6)$$

where the coefficients a_i have to be fitted to selected known nuclei. The first two terms are identified as volume (a_V) and surface (a_S) term. The power of A can easily be understood by the fact that the radius of nuclei to first approximation scales $\sim \sqrt[3]{A}$. The Coulomb term (a_C) accounts for the electric repulsion of the protons, while the asymmetry term (a_A) accounts for the different Fermi seas of neutrons and protons. Finally, $\delta(N, Z)$ is the pairing term which is needed to explain, e.g., odd-even staggering.

This semi-empirical mass formula has been used very successfully but the modern approach to the description of nuclei is more systematic through energy functionals of the density [97]. The foundations of density functional theory (DFT) have been led by Pierre Hohenberg and Walter Kohn in 1964.

1.3.1 HOHENBERG-KOHN THEOREM

As an introduction to DFT we want to start stating the famous theorem by Hohenberg and Kohn, originally developed for an interacting electron gas in an external potential $v(\mathbf{r})$ [98]:

There exists a universal functional of the density, $F[n(\mathbf{r})]$, independent of $v(\mathbf{r})$, such that the expression

$$E \equiv \int v(\mathbf{r})n(\mathbf{r})d\mathbf{r} + F[n(\mathbf{r})] \quad (1.7)$$

has as its minimum value the correct ground-state energy associated with $v(\mathbf{r})$.

In the literature the universal functional F is often named the Hohenberg-Kohn functional F_{HK} and is of the same form for any particle number. In a more mathematical manner we can write

$$\frac{\delta E}{\delta n(\mathbf{r})} = 0 \quad (1.8)$$

for the exact ground-state density $n(\mathbf{r})$. Note that the Hohenberg-Kohn theorem is only an existence theorem and does not provide a way to construct the universal functional.

The proof is simple and we want to sketch it in the following since it also provides better insights into the theorem. Assume that we have a system with Hamiltonian $H = H_{\text{int}} + V_{\text{ext}}$ with interaction part H_{int} and external part

$$V_{\text{ext}} = \int d^3r \psi^\dagger(\mathbf{r}) v(\mathbf{r}) \psi(\mathbf{r}). \quad (1.9)$$

For the ground state Ψ the density

$$n(\mathbf{r}) = \langle \Psi | \psi^\dagger(\mathbf{r}) \psi(\mathbf{r}) | \Psi \rangle \quad (1.10)$$

is a functional of $v(\mathbf{r})$ since the Hamiltonian depends on it. We now want to prove by contradiction that conversely $v(\mathbf{r})$ is a uniquely determined functional of $n(\mathbf{r})$. Thus, we assume that there exists another potential $v'(\mathbf{x})$ with corresponding ground state Ψ' that leads to the same ground state density $n(\mathbf{r})$. In general $\Psi' \neq \Psi$ since they solve different Schrödinger equations. Since the ground state minimises the energy it follows

$$\begin{aligned} E' = \langle \Psi' | H' | \Psi' \rangle &< \langle \Psi | H' | \Psi \rangle = \langle \Psi | H + V'_{\text{ext}} - V_{\text{ext}} | \Psi \rangle \\ &= E + \int d^3r [v'(\mathbf{r}) - v(\mathbf{r})] n(\mathbf{r}). \end{aligned} \quad (1.11)$$

On the other hand we can also conclude

$$E < E' + \int d^3r [v(\mathbf{r}) - v'(\mathbf{r})] n(\mathbf{r}). \quad (1.12)$$

By adding up the last two inequalities we obtain the contradiction

$$E + E' < E + E'. \quad (1.13)$$

Hence, we conclude that $v(\mathbf{r})$ is a unique functional of $n(\mathbf{r})$ and it follows that also F is a unique functional of the density. Note that $v(\mathbf{r})$ is only unique up to a constant, which directly follows from the proof.

Another, more constructive, proof of the Hohenberg-Kohn theorem is based on a constrained search of the ground state. It is discussed in detail in Refs. [34, 99]. Starting point is the general problem of nuclear many-body methods to find the ground-state energy of an N -particle system with Hamiltonian H , *i.e.*, the minimisation of the expectation value $\langle \Psi | H | \Psi \rangle$ with respect to the N -particle wave function Ψ . This minimisation is separated into two steps: (i) Minimisation over all Ψ but under

the constraint of a given density $n(\mathbf{r})$ and (ii) minimisation over $n(\mathbf{r})$ with fixed external potential $v(\mathbf{r})$.

For self-bound nuclei there is no external potential v , which makes Eq. (1.7) somewhat unclear. A calculation of neutron drops, however, requires an external potential for the system to be bound. But also for nuclei one can view the external potential more as a source that is varied and then set to zero which is of interest especially in the case for orbital-dependent functionals.

From the knowledge of the existence of a universal functional there is a long path to the construction of such a functional. A direct construction was pursued within Thomas-Fermi theory [100, 101] (even before the Hohenberg-Kohn theorem), of which only the kinetic term is still used in some modern functionals. Other approaches are the local density approximation (LDA) and, more sophisticated, the generalised gradient approximation (GGA) in which the exchange-correlation energy of the functional solely depends on the density or on the density and its gradients, respectively [102]. Rather than taking the path of a direct construction of a functional the more successful approach is orbital-based density functional theory. It is based on the ideas of Walter Kohn and Lu J. Sham.

1.3.2 KOHN-SHAM DENSITY FUNCTIONAL THEORY

Within Kohn-Sham density functional theory [103] one introduces single-particle orbitals, the Kohn-Sham orbitals φ_i , that solve the Kohn-Sham eigenvalue equation

$$\left[-\frac{\nabla^2}{2m} + v_{\text{KS}}(\mathbf{x}) \right] \varphi_i(\mathbf{x}) = \varepsilon_i \varphi_i(\mathbf{x}). \quad (1.14)$$

The local Kohn-Sham potential $v_{\text{KS}}(\mathbf{x})$ is constructed in a way such that the density of N non-interacting fermions in that system is equal to the density of N interacting fermions in an external potential $v_{\text{ext}}(\mathbf{x})$. This is illustrated for a system of 8 neutrons in a harmonic trap in Fig. 1.7. The density of the system is then given by

$$\rho(\mathbf{x}) = \sum_{i=1}^N |\varphi_i(\mathbf{x})|^2, \quad (1.15)$$

where the orbitals are summed over the lowest N states. The Kohn-Sham potential is obtained by variation of the interaction energy with respect to the density,

$$v_{\text{KS}}(\mathbf{x}) = \frac{\delta E_{\text{int}}}{\delta \rho(\mathbf{x})}. \quad (1.16)$$

Hence, the Kohn-Sham orbitals depend on the potential which itself depends on the density and thus on the orbitals. Consequently, one has to solve the system self-consistently.

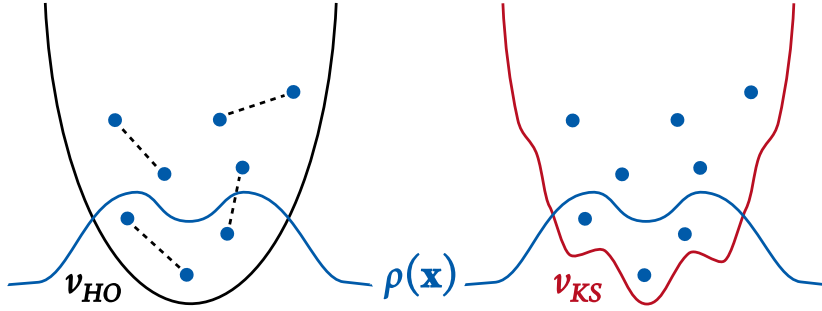


Figure 1.7: Illustration of Kohn-Sham density functional theory for a system of 8 neutrons in a harmonic trap. Left: The neutrons (blue dots) interact solely via two-body interactions (depicted as dashed lines) in a harmonic trap v_{HO} . Right: The external trap is transformed into the Kohn-Sham potential v_{KS} in a way such that the density $\rho(\mathbf{x})$ of the system stays the same but the interactions between the neutrons is absent. This figure is based on Fig. 1 of Ref. [34].

Note that the Kohn-Sham approach is not a mean-field approximation. It takes a mean-field state as reference state, which includes correlations in its solution. These correlations could be included from an organisation of many-body perturbation theory, *e.g.*, the optimised effective potential (OEP) method, which is used in this thesis.

DETAILS ON ORBITAL-DEPENDENT FUNCTIONALS

The subsequent discussion is based on the review article by Engel in Ref. [35], which discusses orbital-based DFT for electronic systems, and on the remarks by Drut *et al.* [34] for nuclear systems. For simplicity and clarity we omit any spin or isospin degrees of freedom.

In general the energy functional is given by

$$E[\rho] = T_{KS}[\rho] + E_{\text{ext}}[\rho] + E_H[\rho] + E_{\text{xc}}[\rho], \quad (1.17)$$

with the Kohn-Sham kinetic energy

$$T_{KS}[\rho] = - \sum_{i=1}^N \int d^3x \varphi_i^\dagger(\mathbf{x}) \frac{\nabla^2}{2m} \varphi_i(\mathbf{x}), \quad (1.18)$$

which is in general not equal to the kinetic energy of the system (since it depends on the Kohn-Sham orbitals and not on the non-local Hartree-Fock orbitals), the external-potential energy

$$E_{\text{ext}}[\rho] = \int d^3x v_{\text{ext}}(\mathbf{x}) \rho(\mathbf{x}), \quad (1.19)$$

Hartree energy

$$E_{\text{H}}[\rho] = \frac{1}{2} \int d^3x d^3y \rho(\mathbf{x}) V(\mathbf{x}, \mathbf{x}) \rho(\mathbf{y}), \quad (1.20)$$

and exchange-correlation term E_{xc} , which is implicitly defined via the decomposition of Eq. (1.17). For electronic systems there is also an additional term E_{ion} stemming from the electrostatic repulsion of the nucleus. This contribution, however, is irrelevant for the DFT formalism and is neglected.

Following Eq. (1.16) the Kohn-Sham potential can be splitted into three pieces

$$v_{\text{KS}}(\mathbf{x}) = v_{\text{ext}}(\mathbf{x}) + v_{\text{H}}(\mathbf{x}) + v_{\text{xc}}(\mathbf{x}), \quad (1.21)$$

where the Hartree potential can be calculated explicitly

$$v_{\text{H}}(\mathbf{x}) = \int d^3y V(\mathbf{x}, \mathbf{y}) \rho(\mathbf{y}), \quad (1.22)$$

and the derivation of the exchange-correlation potential is more tedious

$$v_{\text{xc}}(\mathbf{x}) = \frac{\delta E_{\text{xc}}[\rho]}{\delta \rho(\mathbf{x})}. \quad (1.23)$$

The isolation of E_{H} and E_{xc} of the functional is not necessary and for nuclear applications usually even involved. This is due to the fact that the nuclear interaction is more complicated than the simple Coulomb interaction in the electronic case. Combining the Hartree and exchange part enables also to use anti-symmetrised matrix elements (see Chapter 3 for a more detailed discussion). Thus, we have a Hartree–exchange–correlations potential

$$v_{\text{Hxc}}(\mathbf{x}) \equiv v_{\text{H}}(\mathbf{x}) + v_{\text{xc}}(\mathbf{x}) = \frac{\delta}{\delta \rho(\mathbf{x})} (E_{\text{H}}[\rho] + E_{\text{xc}}[\rho]) \equiv \frac{\delta E_{\text{Hxc}}[\rho]}{\delta \rho(\mathbf{x})}. \quad (1.24)$$

A self-consistent solution algorithm for orbital based DFT usually consists of two parts: A standard Schrödinger-equation solver for the orbitals and the construction of the functional or potential.

1.3.3 DENSITY MATRIX EXPANSION AND SKYRME FUNCTIONALS

Another direct approach to DFT based on microscopic interactions is the density matrix expansion (DME) introduced by John W. Negele and Dominique Vautherin [104, 105]. It is based on quasi-local expansions of the energy in terms of various densities, such that the functional derivatives for the construction of a Kohn-Sham potential are straightforward. It was originally constructed as an expansion of the Hartree-Fock energy using the nucleon-nucleon G matrix treated in a local approximation.

In a nuclear physics context it was revisited for spin-saturated nuclei using non-local low-momentum interactions in momentum space [106]. Employing soft, low-momentum interactions avoids the G -matrix summations. The DME applied to the Hartree-Fock energy leads to a functional similar to Skyrme energy functionals.

Skyrme functionals are widely used in nuclear physics, in particular also for predictions of neutron-rich nuclei [6, 107, 108]. The general form of Skyrme functionals consists of powers of various nuclear densities, restricted to be local. For simplicity we state a Skyrme functional for symmetric ($N = Z$) nuclei

$$E_{\text{Skyrme}}[\rho, \tau, \mathbf{J}] = \int d^3x \left[\frac{1}{2m} \tau + \frac{3}{8} t_0 \rho^2 + \frac{1}{16} (3t_1 + 5t_2) \rho \tau + \frac{1}{64} (9t_1 - 5t_2) (\nabla \rho)^2 - \frac{3}{4} W_0 \rho \nabla \cdot \mathbf{J} + \frac{1}{32} (t_1 - t_2) \mathbf{J}^2 \right], \quad (1.25)$$

with density ρ , kinetic density τ , and the spin-orbit density \mathbf{J} , as well as fit coefficients t_i and W_0 . Skyrme functionals can involve also more general densities, which are all expressed as sums of single-particle orbitals. As mentioned in Ref. [6] there are still large uncertainties in Skyrme functionals. A reduction of these was pursued using better fit technology within the UNEDF project [109, 110]. Other improvements may be achieved by modified structures of Skyrme functionals.

As mentioned above, the DME connects microscopic interactions to Skyrme-like functionals. The coefficients are replaced by density-dependent functions. A more detailed discussion how the DME can improve energy functionals can be found in Ref. [34].

1.3.4 ROUTE TO AB INITIO NUCLEAR ENERGY-DENSITY FUNCTIONALS

In Ref. [102] Perdew and Kurth described ‘Jacob’s ladder’ of Coulomb DFT approximations leading from empirical functionals to ‘the heaven of chemical accuracy’. From the lowest rung of local density approximations via generalised gradient approximations one can climb up to orbital-based DFT considering occupied and unoccupied orbitals.

Drut *et al.* transferred this idea to nuclear physics and suggested a five-rung ladder [34]:

1. Empirical Skyrme functionals fitted to properties of medium-mass to heavy nuclei.
2. Skyrme functionals enhanced by additional gradient and density dependences with input from microscopic calculations.
3. Functionals with long-range-physics input from density-matrix-expanded chiral interactions merged with Skyrme functionals refitted to experimental data or theoretical calculations.
4. Functionals entirely derived from DME applied to low-momentum chiral interactions.

5. Full orbital-dependent DFT using chiral interactions.

This ladder is not climbed step by step: At present there are efforts at all different rungs in order to improve nuclear energy-density functionals. In this thesis we directly address rung 5 with our calculations within the framework of the optimised effective potential method (see Chapters 3 and 4) and also calculate benchmark systems to improve Skyrme functionals in the sense of rung 2 (see our calculations for spin-polarised neutron matter in Chapter 2).

1.4 CHIRAL EFFECTIVE FIELD THEORY

THE DERIVATION OF RELIABLE NUCLEAR INTERACTIONS is a long-standing problem in nuclear physics. The modern approach is chiral effective field theory (EFT), which systematically connects the symmetries of the underlying theory, namely quantum chromodynamics (QCD), with nuclear forces. In this Section we first want to discuss the basic principles and symmetries of QCD. With these foundations we give an introduction to chiral EFT and its current developments.

1.4.1 INTRODUCTORY QCD AND SCALES IN NUCLEAR PHYSICS

QUANTUM CHROMODYNAMICS is the theory of the strong interaction, which binds nuclei. Its fundamental degrees of freedom are quarks and gluons. There exist six quark flavours in nature (see Table 1.1). They can be understood as matter fields carrying mass and electric charge and interacting via gluon exchanges, the gauge bosons of QCD. Both, quarks and gluons, carry also colour charge. This quantity was introduced in order to explain confinement: Quarks have not been observed as isolated particles. They are – at least at low temperatures – confined to colour-neutral particles, the hadrons. There are three kinds of colour charge: Red (r), green (g), and blue (b). Analogously to the additive colour mixing of light, the composition of three quarks with different colour charge is colour neutral. In addition to these three-quark states, called baryons, exist also states named mesons consisting of a quark and an antiquark, which carries anti-colour, *i.e.*, anti-red (\bar{r}), *etc.*). A colour–anti-colour duplet is also colour neutral. In recent measurements at the Large Hadron Collider (LHC) at CERN also a five-quark state, so-called pentaquark, was observed [111]. It consists of four quarks and an antiquark. Furthermore, there are speculations about a four-quark (tetraquark) state [112]. In QCD the quark masses are free parameters but in nature they are fixed to the values given in Table 1.1. For low-energy nuclear physics only the three lightest quarks are relevant: The up (u),

Table 1.1: Table of quarks and their electric charge, isospin z -projection, and approximate masses, adapted from the Particle Data Group [113].

Flavour (f)	symbol	electric charge	isospin	mass (m_f)
up	u	$+2/3e$	$+1/2$	$2.3^{+0.7}_{-0.5}$ MeV
down	d	$-1/3e$	$-1/2$	$4.8^{+0.5}_{-0.3}$ MeV
strange	s	$-1/3e$	0	95 ± 5 MeV
charm	c	$+2/3e$	0	$1\,275 \pm 25$ MeV
bottom	b	$-1/3e$	0	$4\,660 \pm 30$ MeV
top	t	$+2/3e$	0	$173\,210 \pm 510 \pm 710$ MeV

down (d), and strange (s) quark and we can neglect the heavy quarks. For details see Ref. [114], on which also the subsequent discussion is based.

In this light-quark approximation the QCD Lagrangian takes the form

$$\begin{aligned}\mathcal{L}_{\text{QCD}} &= \sum_{f=u,d,s} \bar{q}_f i\not{D} q_f - \bar{q}_f m_f q_f - \frac{1}{2} \text{tr}(G_{\mu\nu} G^{\mu\nu}) \\ &= \mathcal{L}_{\text{QCD}}^0 - \sum_{f=u,d,s} \bar{q}_f m_f q_f,\end{aligned}\quad (1.26)$$

with quark fields q_f and masses m_f . We have used the Feynman-slash notation for the covariant derivative $\not{D} \equiv \gamma^\mu D_\mu = \gamma^\mu (\partial_\mu + igA_\mu)$, where A_μ denotes the gluon field and

$$G_{\mu\nu}^a = \partial_\mu A_\nu^a - \partial_\nu A_\mu^a + g_s f^{abc} A_\mu^b A_\nu^c, \quad (1.27)$$

the gluon-field-strength tensor with colour indices $a, b, c = 1, \dots, 8$ corresponding to eight gluons, dimensionless coupling strength g_s , and $SU(3)$ structure constant f^{abc} .

One can describe light-quark QCD approximately by massless quarks. The corresponding Lagrangian $\mathcal{L}_{\text{QCD}}^0$ is invariant under separate unitary global transformations of the left- and right-handed quark fields, the so-called chiral rotations: $q_f \rightarrow V_{ff',i} q_{f'}$, where $V_{ff',i} \in SU(3)$, and $i = L, R$. One can write the kinetic term of the QCD Lagrangian as

$$\sum_{f=u,d,s} \bar{q}_f i\not{D} q_f = \sum_{f=u,d,s} \bar{q}_{Lf} i\not{D} q_{Lf} + \bar{q}_{Rf} i\not{D} q_{Rf}. \quad (1.28)$$

This term then fulfils the so-called chiral symmetry $SU(3)_L \times SU(3)_R$. However, chiral symmetry is not exact. It is explicitly broken due to the small quark masses. The quark-mass term couples left- and right-handed quarks,

$$\sum_{f=u,d,s} \bar{q}_f m_f q_f = \sum_{f=u,d,s} \bar{q}_{Rf} m_f q_{Lf} + \text{h.c.} . \quad (1.29)$$

In addition to this explicit breaking one also finds a spontaneous symmetry breaking, even for zero quark masses. This spontaneous symmetry breaking is reflected in the particle spectrum. If chiral symmetry were not broken spontaneously one would expect parity doublets, *i.e.*, particles with the same quantum numbers but opposite parity with the same mass. That this is not the case can be seen from the nucleon N with mass $m_N \approx 940$ MeV and its chiral partner N^* with $m_{N^*} \approx 1535$ MeV. The spontaneous symmetry breaking by the QCD vacuum gives rise to the chiral condensate $\langle \bar{q}q \rangle_0$. It is the expectation value of a quark-antiquark pair in vacuum and can be seen as the order parameter of spontaneous chiral symmetry breaking. It is zero if chiral symmetry is restored at high temperatures.

The spontaneous symmetry breaking has an important consequence. According to Goldstone's theorem, every generator of a spontaneously broken continuous symmetry corresponds to a massless excitation of the vacuum, a so-called Goldstone boson [115]. In the case of chiral symmetry breaking the Goldstone bosons are the pions, kaons, and the eta meson. Due to the explicit symmetry breaking by the quark masses also the Goldstone bosons carry small masses and are therefore called pseudo-Goldstone bosons.

AT LOW ENERGIES QCD is non-perturbative. This is due to the strong coupling strength α_s , which is connected to the coupling constant g_s and reads at one-loop order [116, 117]

$$\alpha_s \equiv \frac{g_s^2}{4\pi} = \frac{4\pi}{b_0} \log^{-1} \frac{Q}{\Lambda_{\text{QCD}}}, \quad (1.30)$$

where $b_0 = (33 - 2N_f)/(12\pi)$ with number of flavours N_f and $\Lambda_{\text{QCD}} \approx (200 - 400) \text{ MeV}$ is the characteristic scale of QCD. The coupling strength is dependent on the momentum Q and is thus often referred to as 'running coupling'. At low momenta $Q \lesssim 1 \text{ GeV}$ it becomes larger than 1, which makes QCD non-perturbative in this momentum regime. Thus, we cannot calculate the nuclear force directly from the QCD Lagrangian.

There are, however, efforts to calculate nuclear observables directly from QCD using lattice Monte-Carlo techniques. In lattice QCD one uses a four-dimensional lattice to discretise space-time with quarks on the vertices and gluons on the links. This problem can then be evaluated numerically and the results are extrapolated to infinite volume and vanishing lattice spacing. Nevertheless, lattice QCD calculations are computationally extremely expensive and for systems involving nucleons one presently needs to make various approximations.

Lattice QCD was used successfully to predict the masses of the lightest hadrons, using only the pion and kaon mass as input [118]. Physical calculations of nuclear systems are presently limited to very light systems and will most likely be limited to $A \lesssim 4$ in the foreseeable future [119]. However, it could also be used to predict coupling constants for nucleon-nucleon or pion-nucleon scattering [120], which could be used to constrain nuclear forces. For a detailed review on lattice QCD see Ref. [17].

Another approach to determine the nuclear interaction is chiral effective field theory. It is based on the separation of scales. For a better insight we briefly want to discuss the scales in nuclear physics.

The nuclear interaction can be understood by the exchange of light mesons. The average mass of the pion, the lightest meson, is $m_\pi \approx 138 \text{ MeV}$, which corresponds to a Compton wave length of about $\lambda_\pi = 1/m_\pi \approx 1.5 \text{ fm}$. Naïvely, one could assume that we can describe nuclear binding in terms of a pion-energy-scale expansion. However, the binding energies of nuclei ranges about $(1 - 8) \text{ MeV}$

per nucleon. The binding momentum of the deuteron, which is weakly bound, is

$$\Gamma_d = \sqrt{m_N E_B(d)} \approx 45 \text{ MeV} \ll m_\pi, \quad (1.31)$$

where $E_B(d) = 2.224 \text{ MeV}$ denotes the binding energy of the deuteron and $m_N = 938.92 \text{ MeV}$ is the mass of the nucleon. Hence, there exists a relevant energy scale much below that of the pion mass. This is also manifested in the S -wave neutron-proton-scattering lengths,

$$a(^1S_0) = -23.8 \text{ fm}, \quad a(^3S_1) = 5.4 \text{ fm} \gg \frac{1}{m_\pi}. \quad (1.32)$$

These different scales have to be treated properly to set-up an EFT for nuclear interactions. It is crucial that one chooses the correct energy scale, *e.g.*, in the case of large scattering lengths we restrict the region of interest to momenta $q_{\max} \sim |a(^1S_0)|^{-1} \sim 8 \text{ MeV} \ll m_\pi$, the so called pion-less EFT whose breakdown scale is the pion mass [121, 122]. When going to higher momenta one needs to include pions explicitly (chiral EFT) and when considering even higher energies one may include even heavier particles such as the delta isobar $\Delta(1232)$ in the EFT, often referred to as Δ -full chiral EFT.

1.4.2 FROM EFFECTIVE CHIRAL LAGRANGIANS TO INTERACTIONS

Chiral effective field theory was introduced by Steven Weinberg in the early 1990s [4, 123, 124]. In 1979, however, Weinberg already described the underlying principle of effective field theories in the following way [125]:

If one writes down the most general possible Lagrangian, including all terms consistent with assumed symmetry principles, and then calculates matrix elements with this Lagrangian to any given order of perturbation theory, the result will simply be the most general possible S -matrix consistent with analyticity, perturbative unitarity, cluster decomposition and the assumed symmetry principles.

Thus, to construct an effective Lagrangian we first need to specify the degrees of freedom and an expansion scheme. In chiral EFT the degrees of freedom are pions and nucleons. One expands in powers of a low-momentum scale over a high-momentum scale. The low-momentum scale Q is given by typical energies of the system, *i.e.*, $Q \sim m_\pi$. The high-momentum or breakdown scale is set by the energies where new physics comes into play. This is marked by heavier-meson exchanges, of which the ρ meson is the lightest with $m_\rho \approx 770 \text{ MeV}$. The breakdown scale is thus usually set $\Lambda_b \sim 500 \text{ MeV}$. This results in an expansion parameter $Q/\Lambda_b \sim 1/3$, meaning that the uncertainty of the interaction should be reduced by a factor of 3 when going to the next order.

The next step in the construction of the effective Lagrangian is the specification of a power-counting scheme. It defines a hierarchy for the importance of terms. Most widely used is Weinberg's power-counting scheme based on naïve dimensional analysis. The order ν of an A -nucleon diagram, which has L loops, C separately connected pieces, and V_i vertices of type i , is given by [4, 123, 124]:

$$\nu = -2 + 2A - 2C + 2L + \sum_i V_i \left(d_i + \frac{1}{2}n_i - 2 \right), \quad (1.33)$$

where n_i is the number of nucleon field operators and d_i the number of derivatives and/or insertions of the pion mass in the vertex i . Note that there exist also other approaches [126] and finding the right power counting is a topic of current research.

With that we can construct an effective Lagrangian systematically order by order. The lowest, with respect to symmetries, possible order ν is called leading order (LO), the next possible next-to-leading order (NLO), than next-to-next-to-leading order (N²LO), and so on. We state the LO and NLO chiral Lagrangians and refer to Ref. [127] for a detailed discussion and derivation. These Lagrangians describe vertices $\Delta_i = d_i + n_i/2 - 2$ with $i = 0, 1$:

$$\begin{aligned} \mathcal{L}^{(0)} = & \frac{1}{2}(\partial_\mu \boldsymbol{\pi} \cdot \partial^\mu \boldsymbol{\pi}) - \frac{1}{2}m_\pi^2 \boldsymbol{\pi}^2 + N^\dagger \left[i\partial_0 + \frac{g_A}{2f_\pi} \boldsymbol{\tau} \boldsymbol{\sigma} \cdot \boldsymbol{\nabla} \boldsymbol{\pi} - \frac{1}{4f_\pi^2} \boldsymbol{\tau} \cdot (\boldsymbol{\pi} \times \dot{\boldsymbol{\pi}}) \right] N \\ & - \frac{C_S}{2} (N^\dagger N)(N^\dagger N) - \frac{C_T}{2} (N^\dagger \boldsymbol{\sigma} N)(N^\dagger \boldsymbol{\sigma} N) + \dots, \end{aligned} \quad (1.34)$$

$$\begin{aligned} \mathcal{L}^{(1)} = & N^\dagger \left[4c_1 m_\pi^2 - \frac{2c_1}{f_\pi^2} m_\pi^2 \boldsymbol{\pi}^2 + \frac{c_2}{f_\pi^2} \dot{\boldsymbol{\pi}}^2 + \frac{c_3}{f_\pi^2} (\partial_\mu \boldsymbol{\pi} \cdot \partial^\mu \boldsymbol{\pi}) - \frac{c_4}{2f_\pi^2} \varepsilon_{ijk} \varepsilon_{abc} \sigma_i \tau_a (\nabla_j \pi_b) (\nabla_k \pi_c) \right] N \\ & - \frac{D}{4f_\pi} (N^\dagger N)(N^\dagger \boldsymbol{\sigma} \boldsymbol{\tau} N) \cdot \boldsymbol{\nabla} \boldsymbol{\pi} - \frac{E}{2} (N^\dagger N)(N^\dagger \boldsymbol{\tau} N) \cdot (N^\dagger \boldsymbol{\tau} N) + \dots, \end{aligned} \quad (1.35)$$

where $\boldsymbol{\pi}$ and N denote the pion and nucleon fields, respectively, g_A is the axial coupling and f_π the pion decay constant, $\boldsymbol{\sigma}/\boldsymbol{\tau}$ denote the Pauli spin/isospin matrices. Finally, the coefficients C_S , C_T , c_i , E , and D are low-energy couplings, or often called low-energy constants (LECs). Note that we have disregarded terms with more pion fields, indicated by ellipses.

All low-energy couplings in the Lagrangian are *a priori* unknown. They absorb high-momentum degrees of freedom, like heavier-meson exchanges or the Δ excitation. Through fits to low-energy scattering data like the NN phase shifts or pion-nucleon scattering the high-energy physics is included in the theory.

For the calculation of nuclear observables one needs to derive potentials from the Lagrangians. This problem was already studied for meson-exchange theories in the 1950s and a detailed discussion can be found in Ref. [128]. For a more recent, condensed discussion we again refer to Ref. [127].

With the Lagrangians in Eqs. (1.34), (1.35) one can determine the nuclear interaction up to N²LO, except for the contact NN interaction at NLO, which includes a vertex involving $\mathcal{L}^{(2)}$ [129].












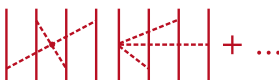


		NN	3N	4N
LO	$\mathcal{O}\left(\frac{Q^0}{\Lambda_b^0}\right)$			
NLO	$\mathcal{O}\left(\frac{Q^2}{\Lambda_b^2}\right)$			
N ² LO	$\mathcal{O}\left(\frac{Q^3}{\Lambda_b^3}\right)$			
N ³ LO	$\mathcal{O}\left(\frac{Q^4}{\Lambda_b^4}\right)$			
N ⁴ LO	$\mathcal{O}\left(\frac{Q^5}{\Lambda_b^5}\right)$			not yet developed

Figure 1.8: Hierarchy of nuclear forces in chiral effective field theory up to N⁴LO. Solid lines correspond to nucleons, while dashed lines depict pion exchanges. The low-energy couplings are indicated in the vertices. The dominant contribution is from nucleon-nucleon (NN) forces since they contribute already at leading order. At third order (N²LO) three-body (3N) forces emerge and at the next order also four-body (4N) forces. Note that the N⁴LO many-body forces have only been developed partially. A completely local representation of the chiral forces is (except for the non-local spin-orbit contribution) only possible from LO to N²LO.

In Fig. 1.8 we diagrammatically show nuclear forces up to order N⁴LO. These diagrams should not be understood as Feynman diagrams representing the scattering amplitude but rather as a schematic visualisation of the irreducible parts of it. The LO contribution (first line) consists of two parts, a contact and the one-pion-exchange interaction. As an example we quote the expression in momentum space here and refer to Refs. [130, 131] for the higher-order contributions:

$$V_{\text{LO}}(\mathbf{q}) = C_S + C_T \boldsymbol{\sigma}_1 \cdot \boldsymbol{\sigma}_2 - \frac{g_A^2}{4f_\pi^2} \frac{\boldsymbol{\sigma}_1 \cdot \mathbf{q} \boldsymbol{\sigma}_2 \cdot \mathbf{q}}{q^2 + m_\pi^2} \boldsymbol{\tau}_1 \cdot \boldsymbol{\tau}_2, \quad (1.36)$$

with the momentum transfer $\mathbf{q} = \mathbf{p}' - \mathbf{p}$ where \mathbf{p} and \mathbf{p}' are the initial and final relative momenta, respectively, and the same couplings as in Eq. (1.34).

The convergence of the chiral two-nucleon forces has been studied by analysing, *e.g.*, the neutron-proton phase shifts [127]. It was found that the long-range part of the chiral forces exhibits in various cases an unnatural convergence pattern. The sub-leading contributions had a larger effect than expected. This could be traced back to large low-energy constants c_3 and c_4 . These occur first in the N²LO two- and three-nucleon forces. The largest effect has its origin in the delta isobar $\Delta(1232)$. The corresponding excitation energy $\Delta = m_\Delta - m_N \approx 293$ MeV is lower than the breakdown scale

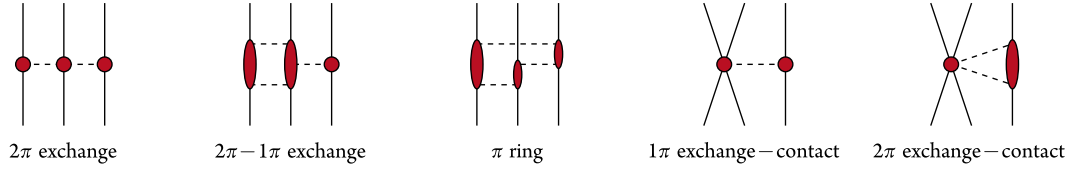


Figure 1.9: Sub-leading 3N topologies at $N^3\text{LO}$. The red ellipses indicate pion loops. In addition there exist relativistic $1/m_N$ corrections. Note that the 1π -exchange–contact topology vanishes at this order. The figure was taken from Ref. [142] and coloured.

of the theory and is known to play an important role in nuclear physics [130]. Schematically the absorption of the Δ excitation into the couplings c_3 and c_4 can be understood as:

$$\Delta \left[\begin{array}{c} | \\ | \\ | \end{array} \right] \rightarrow c_3, c_4 \left[\begin{array}{c} | \\ | \\ | \end{array} \right] \quad (1.37)$$

One expects that including Δ s explicitly in the effective theory leads to a better convergence pattern compared to a Δ -less theory. This is due to the shifting of effects from large long-range parts by one order. Even though such a theory is not well established yet, the effects of deltas on the couplings c_i were studied by Krebs *et al.* [132].

1.4.3 MANY-BODY FORCES

In chiral EFT also many-nucleon forces emerge naturally, as depicted in Fig. 1.8. They are a result of nucleons being composite particles with finite size. It can be understood in a simple picture: In presence of other nucleons they can be deformed. This leads to a modified interaction among the nucleons. These modifications are manifested in a residual many-nucleon force when the nucleons are treated as point-like particles. Since the nuclear interaction has a short range it becomes clear that many-nucleon forces are only relevant at sufficiently high densities. One can also conclude that many-body forces have to be repulsive – at least at high densities – as otherwise nuclei would collapse [16].

According to the power counting (1.33) it is clear that NN forces are most important since they occur already at LO ($\nu = 0$). Formally, the leading three-nucleon interaction appears at $\nu = 2$, *i.e.*, NLO. However, those contributions vanish and thus, three-nucleon forces occur first at $N^2\text{LO}$ [133]. Similarly, one would expect the leading four-nucleon forces already at NLO ($\nu = 2$) but through unitary transformation one can show that these contributions vanish. In fact, the leading four-nucleon forces appear at $N^3\text{LO}$ [134, 135]. Nevertheless, 3N forces play an important role in nuclear physics and they are crucial to predict the properties of nuclei, see *e.g.*, Refs. [19, 28, 136–138] and nuclear matter [139–141].

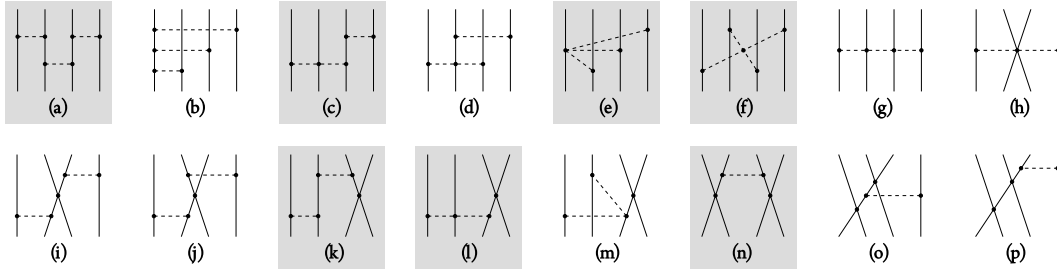


Figure 1.10: Leading 4N forces at $N^3\text{LO}$. The nomenclature follows Ref. [134]. Only the diagrams a, c, e, f, k, l, and n have non-vanishing contributions, highlighted with the shading.

We briefly want to discuss the individual contributions from 3N and 4N forces up to $N^3\text{LO}$, as they are included in our calculation presented in Chapter 2. The leading 3N forces at $N^2\text{LO}$ consists of three diagrams, depicted in Fig. 1.8: The two-pion-exchange, one-pion-contact, and three-nucleon-contact term. The first depends on the low-energy couplings c_1 , c_3 , and c_4 which are predicted from the NN sector [see Eq. (1.35)]. The latter two depend on the couplings c_D and c_E , respectively, which have to be fitted to three-body data. However, due to Pauli's principle they do not give contributions in neutron-only systems [139].

At $N^3\text{LO}$ one can group the 3N terms into 5 topologies, which we show schematically in Fig. 1.9. The long-range part is grouped into the 1π -exchange, 2π - 1π -exchange, and the π -ring topologies [142]. The shorter-range contributions are the 1π -exchange-contact and the 2π -exchange-contact topologies as well as the relativistic $1/m_N$ corrections [143]. One can show that the 1π -exchange-contact topology vanishes at this order. The long-range parts only include lowest-order pion-nucleon vertices and thus only depend on the constants g_A and f_π , while the 2π -exchange-contact term depends on the LO coupling C_T and the relativistic corrections also on C_S . Hence, no new low-energy couplings appear at this order and it is fully predicted from the NN sector.

The leading 4N interactions have been derived in Refs. [134, 135]. We show all diagrams in Fig. 1.10. All non-vanishing terms are indicated by the shaded regions. The long-range terms are parameter free and the short-range terms k, l, and n depend only on the NN coupling C_T . Thus, also the leading 4N forces are fully predicted.

1.4.4 REGULARISATION SCHEMES AND LOCAL INTERACTIONS

Chiral interactions lead to divergences in the high-energy (ultraviolet) regime when plugged into the Lippmann-Schwinger equation. These divergences are an intrinsic feature of chiral EFT [144]. A widely used approach to circumvent this problem is the introduction of an ultraviolet cutoff. The potential is then renormalised through the fits of the low-energy couplings to scattering data. However, this introduces cutoff artefacts in chiral potentials leading to cutoff dependences of the calculated nuclear observables. In a renormalisable theory one could take the cutoff large with only small

cutoff dependence, smaller than the error originating from the truncation in the EFT expansion. In chiral EFT with Weinberg power counting, however, at present cutoffs are of the order of the breakdown scale Λ_b .

Traditional chiral interactions have been formulated in momentum space [145–148], which is a natural choice as the chiral expansion is in powers of momentum scales. The most-widely used N³LO potential in nuclear structure calculations has been derived by Entem and Machleidt [145]. They employed a cutoff $\Lambda = 500$ MeV and we refer to it as EM 500 MeV in the following. There also exists a version of that potential with a cutoff $\Lambda = 600$ MeV [146]. Epelbaum, Glöckle, and Meißner derived multiple N²LO [147] and N³LO [148] potentials with a cutoff range $\Lambda = (450 - 600)$ MeV and used a different approach in the regularisation. They introduced additionally a regularisation of the spectral function of the sub-leading two-pion-exchange [149]. This makes the choice of the regulator function more flexible [144]. For this spectral-function regularisation they used $\tilde{\Lambda} = (500 - 700)$ MeV. We refer to these potentials as EGM $\Lambda/\tilde{\Lambda}$.

These rather low cutoffs limit the applicability of chiral interactions but with higher cutoffs the potentials are not renormalisable. Nuclear saturation density n_0 corresponds for isospin-symmetric systems to Fermi momenta $k_F \approx 1.35 \text{ fm}^{-1} \sim 270$ MeV and for neutron-only systems even to $k_F \approx 1.7 \text{ fm}^{-1} \sim 340$ MeV. Going to higher densities may not be in the range of these low-cutoff interactions. A larger range of applicability of chiral forces would thus be appealing.

A way to reduce cutoff artefacts originating from long-range pion exchanges was found in the development of local chiral coordinate-space interactions for quantum Monte Carlo calculations [150–152]. Locality means that the potential only depends on the particle separation $\mathbf{r} = \mathbf{r}_1 - \mathbf{r}_2$. When Fourier transforming the traditional momentum-space potentials into coordinate space there exist two sources of non-locality: Terms emerging from the regulator functions and genuine non-localities. In the contact interactions beyond LO arise dependences on the momentum transfer in the exchange channel $\mathbf{k} = (\mathbf{p}' + \mathbf{p})/2$. Also parts of the pion-exchanges at N³LO and beyond are \mathbf{k} dependent. The Fourier transform of these terms leads to these genuine non-localities, in contrast to the direct momentum transfers $\mathbf{q} = \mathbf{p}' - \mathbf{p}$, which are local.

The first non-locality can easily be circumvented by the use of different regulator functions or regulating the potential directly in coordinate space. Instead of regulator functions of the form $f(p) = \exp[-(p/\Lambda)^{2n}]$ one uses $f_{\text{long}}(r) = 1 - \exp[-(r/R_0)^m]$ for the long-range terms of the interaction. Now R_0 plays the role of the cutoff, suppressing contributions at $r < R_0$ [152]. These short-range components of the pion-exchange cause convergence problems in the chiral expansion [153]. In addition a spectral-function regularisation is used as in the momentum-space interactions. To avoid the genuine non-localities one can choose a different basis of short-range operators. This can be done for all contributions up to N²LO– except for the spin-orbit terms, which depend on $\mathbf{q} \times \mathbf{p}$. For a detailed discussion see Ref. [152]. As comparison to the momentum-space expressions (1.36) we

quote the LO potential in coordinate space (where we neglect the isospin-breaking terms),

$$V_{\text{LO}}(\mathbf{r}) = (C_S + C_T \boldsymbol{\sigma}_1 \cdot \boldsymbol{\sigma}_2) \delta^{(3)}(\mathbf{r}) + \frac{m_\pi^3 g_A^2 e^{-m_\pi r}}{12\pi 4f_\pi^2 m_\pi r} \left[\boldsymbol{\sigma}_1 \cdot \boldsymbol{\sigma}_2 + \left(1 + \frac{3}{m_\pi r} + \frac{3}{(m_\pi r)^2} \right) S_{12}(\hat{\mathbf{r}}) \right] \boldsymbol{\tau}_1 \cdot \boldsymbol{\tau}_2, \quad (1.38)$$

with the tensor operator $S_{12}(\hat{\mathbf{r}}) \equiv 3 \boldsymbol{\sigma}_1 \cdot \hat{\mathbf{r}} \boldsymbol{\sigma}_2 \cdot \hat{\mathbf{r}} - \boldsymbol{\sigma}_1 \cdot \boldsymbol{\sigma}_2$.

In the local interactions derived in Refs. [150, 151] a cutoff range $R_0 = (0.8 - 1.2)$ fm was employed, roughly corresponding to energies $(600 - 400)$ MeV. The long-range parts of these interactions show less cutoff artefacts than the non-local potentials. The spectral-function-regularisation cutoff was also varied $\tilde{\Lambda} = (1.0 - 1.4)$ GeV and only minor effects were observed.

Even though fully-local chiral interactions can only be derived up to N²LO, one can use the idea of local regularisation for higher-order potentials. This was pointed out in Ref. [144], in which Epelbaum, Krebs, and Meißner developed semi-local interactions. In these the long-range pion exchanges are regulated locally, while the short-range terms are regulated in the standard procedure in momentum space. The momentum-space cutoff is chosen as $\Lambda = 2R_0^{-1}$. In practice the local regulator function discussed above is Fourier transformed to momentum space and then applied to the long-range terms. Using this regularisation scheme also avoids the additional spectral-function regularisation. This also makes the inclusion of 3N forces at N³LO and beyond [132, 154] more consistent as they are derived only for infinite $\tilde{\Lambda}$.

Similarly to the local interactions, semi-local potentials with cutoffs in coordinate space $R_0 = (0.8 - 1.2)$ fm corresponding to momentum space cutoffs $\Lambda \approx (500 - 330)$ MeV have been derived. These potentials show significantly less cutoff artefacts and a more systematic convergence pattern.

2

Infinite neutron-rich systems

THE PHYSICS OF NEUTRON MATTER spans a wide density range. At low densities it exhibits universal properties due to the large neutron-neutron scattering length [155–157]. At intermediate density regions it is relevant for neutron-rich nuclei and at very high densities the physics of neutron stars is strongly determined by neutron-matter properties. Neutron matter also provides a unique laboratory to test nuclear forces because all low-energy couplings appearing in the many-body forces are predicted from the NN sector.

Neutron-matter calculations can be used to constrain the properties of neutron stars by predicting a range for allowed mass-radius relations [13, 14] (see Fig. 1.3). For that an extension to higher densities and an extrapolation to neutron-star matter with a small proton fraction is necessary. Such an extrapolation can be done with a quasi-parabolic expansion, which has been confirmed by actual asymmetric-nuclear-matter calculations [141, 158, 159].

At low densities ($n \lesssim n_0/10$) neutron matter has been studied with chiral effective field theory interactions using lattice simulations [24]. At nuclear densities there exist calculations in the in-medium chiral perturbation theory approach [160, 161], where the low-energy couplings have to be adjusted to empirical saturation properties. Other approaches used renormalisation group (RG) or similarity RG techniques [162, 163] to evolve chiral interactions to low momenta in order to perform perturbative calculations [139, 164–166]. A non-perturbative approach based on chiral interactions to calculate neutron matter is using Green’s functions and can be found in Refs. [159, 167].

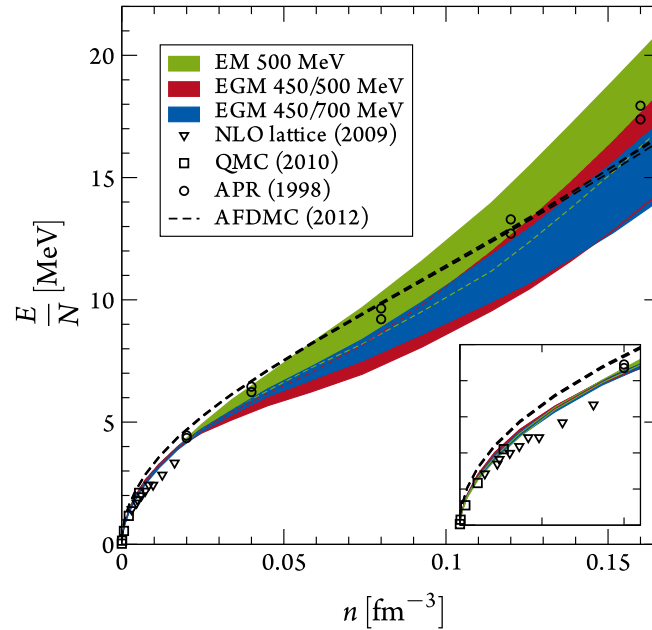


Figure 2.1: Neutron-matter energy per particle as a function of density including NN, 3N, and 4N interactions up to $N^3\text{LO}$. The overlapping bands correspond to different NN potentials [145, 146, 148] and include uncertainty estimates due to the many-body calculation, the low-energy couplings c_i , and by varying the 3N/4N cutoffs (see Refs. [140, 168]). For comparison we also show results at low densities (see also the inset) from NLO lattice [24] and Quantum Monte Carlo (QMC) simulations [173], and at nuclear densities from variational (APR, the different points are with or without boost corrections) [174] and auxiliary field diffusion Monte Carlo (AFDMC) [175] based on adjusted nuclear force models.

We have studied neutron matter using chiral effective field theory interactions including all many-body forces up to $N^3\text{LO}$ in a perturbative approach together with Ingo Tews and Kai Hebeler in Refs. [140, 168–170]. We show the main result for the equation of state of neutron matter using the traditional non-local interactions [145–148] in Fig. 2.1. The perturbative calculations are feasible due to effective-range effects weakening NN forces at higher densities [156] together with weaker tensor forces among neutrons and limited phase space due to Pauli blocking [171]. They have been confirmed by Quantum Monte Carlo (QMC) calculations with local chiral interactions [150–152, 172].

In this Chapter we want to study the properties of neutron matter further and calculate also other observables than the equation of state of neutron matter. In Section 2.1 we investigate the nuclear phase diagram and present calculations of the chiral condensate in neutron matter. In Section 2.2 we study the properties of spin-polarised neutron matter. This extreme system shows that the physics of neutron matter is similar to a unitary gas and we can use it to restrict energy-density functionals. In the last Section we investigate the pairing gap in neutron matter, which is important for the physics of neutron star crusts and outer cores as well as neutron-rich nuclei.

2.1 THE CHIRAL CONDENSATE IN NEUTRON MATTER

THE CHIRAL CONDENSATE is the order parameter of spontaneous chiral symmetry breaking. In this Section we present a calculation of the chiral condensate in neutron matter at zero temperature based on non-local chiral interactions. This project was carried out together with Ingo Tews, Bengt Friman, Kai Hebeler, and Achim Schwenk. Parts of it were already presented in Ref. [170] while it was completed throughout the work on this thesis. The results have been published in Ref. [176].

2.1.1 INTRODUCTION

THE UNDERSTANDING OF THE PHASE DIAGRAM OF MATTER is a current frontier in nuclear physics. At high temperatures and vanishing net baryon density, the properties of strongly interacting matter have been studied in first-principle lattice QCD calculations. It is found that at a temperature of 154 ± 9 MeV matter exhibits a chiral and deconfinement crossover transition from the low-temperature hadronic phase, where chiral symmetry is spontaneously broken, to the chirally symmetric high-temperature phase, the quark-gluon plasma [177]. An order parameter for characterising this transition is the chiral condensate. [178–180].

At zero baryon density the phase diagram of QCD can be calculated using, *e.g.*, perturbative or lattice QCD approaches. However, at finite densities this is not possible due to the running coupling of QCD and the fermion sign problem. As discussed in Section 1.2, the matter in neutron stars can reach several times nuclear saturation density and there have been speculations about exotic phases that may appear in the inner core of neutron stars. Furthermore, there are speculations about the occurrence of such exotic phases even below nuclear saturation density n_0 , see, *e.g.*, Fig. 1 in Ref. [15]. The observations of neutron stars with masses around $2M_\odot$ [8–10], however, put such exotic phases into question because they tend to soften equations of state, which do not support such heavy neutron stars. We study the chiral condensate in neutron matter at nuclear densities to further investigate the possibility of such phase transitions.

The chiral condensate can be obtained from the energy using the Hellman-Feynman theorem [161, 179, 181],

$$\langle \bar{q}q \rangle_n - \langle \bar{q}q \rangle_0 = n \frac{\partial}{\partial m_q} \left[\frac{E_{\text{free}}(m_q, k_F)}{N} + \frac{E_{\text{int}}(m_q, k_F)}{N} \right], \quad (2.1)$$

where $\langle \bar{q}q \rangle_n$ and $\langle \bar{q}q \rangle_0$ are the chiral condensates at finite baryon density $n = k_F^3/(3\pi^2)$ (with Fermi momentum k_F) and in vacuum, respectively. Moreover, $E_{\text{free}}/N = m_N + 3k_F^2/(10m_N)$ is the energy per particle of a system consisting of N non-interacting degenerate neutrons in the non-relativistic

limit, E_{int} is the corresponding interaction energy, m_q denotes the average of the u and d quark masses, $\bar{q}q = \bar{u}u + \bar{d}d$, and m_N is the nucleon mass.

The contribution from the nucleon mass to the chiral condensate is proportional to the pion-nucleon sigma term $\sigma_{\pi N}$, which accounts for the scalar quark density in the nucleon [179, 182]

$$\sigma_{\pi N} = \langle N | m_q \bar{q}q | N \rangle = m_q \frac{\partial m_N}{\partial m_q}. \quad (2.2)$$

Here $|N\rangle$ represents the state of a nucleon at rest. The value of the pion-nucleon sigma term has been determined within different frameworks [182–186]. As a baseline we use the value $\sigma_{\pi N} \approx 50$ MeV [161]. More recent high-precision determinations from Roy-Steiner equations suggest a value $\sigma_{\pi N} = (59.1 \pm 3.5)$ MeV [187]. The chiral condensate in neutron matter relative to the vacuum is then given by [179]

$$\frac{\langle \bar{q}q \rangle_n}{\langle \bar{q}q \rangle_0} = 1 - \frac{n}{f_\pi^2} \frac{\sigma_{\pi N}}{m_\pi^2} \left(1 - \frac{3k_F^2}{10m_N^2} + \dots \right) - \frac{n}{f_\pi^2} \frac{\partial E_{\text{int}}(m_\pi, k_F)}{\partial m_\pi^2} \frac{1}{N}, \quad (2.3)$$

where we have used the Gell-Mann–Oakes–Renner relation $m_q \langle \bar{q}q \rangle_0 = -f_\pi^2 m_\pi^2$.

The leading contribution (proportional to $\sigma_{\pi N}$) to the chiral condensate (2.3) stems from the quark- or pion-mass dependence of the nucleon mass, appearing in the energy of the free Fermi gas E_{free}/N . By extrapolating this linear density dependence, one finds restoration of chiral symmetry at a density around $(2.5 - 3)n_0$ [179, 181]. At the density ranges where chiral effective field theory is applicable ($n \lesssim 0.2 \text{ fm}^{-3}$) the correction from the kinetic-energy contribution to E_{free}/N gives only a 4% correction relative to the leading term. Higher-order contributions from relativistic corrections, indicated by the ellipses in Eq. (2.3), are negligible at these densities. The next term $9k_F^4/56m_N^4$ is only a 0.3% correction. While the first correction to the chiral condensate, proportional to $\sigma_{\pi N}$, in Eq. (2.3) is a consequence of the finite nucleon density, the long-range contributions from E_{int} can be attributed to the modification of the scalar pion density $\Delta n_\pi^s = n \partial(E_{\text{int}}/N)/\partial m_\pi$ due to the interactions between nucleons (*cf.* Ref. [188]).

2.1.2 CALCULATIONAL DETAILS

Based on our calculations for neutron matter [140, 168, 170] (see also Fig. 2.1) we calculate the interaction dependence of the chiral condensate. The pion-mass dependence of nuclear forces arises from two sources: First, due to the explicit m_π dependences in the long-range pion-exchange interactions, and second, implicitly, due to the quark-mass dependence of the pion-nucleon coupling g_A , the pion decay constant f_π , as well as the leading NN contact interactions C_S and C_T , and higher-order pion-nucleon and short-range NN and 3N contact interactions.

We calculate the explicit m_π dependence of nuclear forces by varying the value of the pion mass

in the pion-exchange NN, 3N, and 4N interactions. At the NN level, we use the N³LO potentials of Epelbaum, Glöckle, and Meißner (EGM) [147, 148] with cutoffs 450/500 and 450/700 MeV (and their N²LO versions to study the order-by-order convergence). With these NN interactions neutron matter is perturbative at the densities considered here [140, 168]. Note that we cannot use the EM 500 MeV potential [145, 146], which was also used for our neutron-matter calculations, because m_π cannot be changed in the potential routines provided by the authors.

We vary m_π by 0.5% in the corresponding potential routines using a C++ code for neutron matter developed by Kai Hebeler. In practice this is done by a variation of 10% in the original routines and a rescaling in our code. We found to good approximation a linear scaling with the pion mass in this region. A direct variation of m_π by 0.5% would be within the numerical uncertainty of the potential routines. The derivative of the interaction energy with respect to m_π^2 in Eq. (2.3) is then computed numerically for different densities.

We also estimate the impact of the quark-mass dependence of g_A and f_π using the results of Refs. [189, 190]. In a perturbative calculation, the interaction energy per particle E_{int}/N is a polynomial in g_A and in $1/f_\pi$. Consider a term in this polynomial, in which g_A enters with the power α , $[E_{\text{int}}/N]_\alpha$. For the corresponding contribution to the chiral condensate, due to the pion-mass dependence of g_A , we thus have at saturation density

$$\begin{aligned} -\frac{n}{f_\pi^2} \frac{\partial}{\partial m_\pi^2} \left[\frac{E_{\text{int}}}{N} \right]_\alpha &= -\frac{n}{f_\pi^2} \frac{\partial g_A}{\partial m_\pi^2} \frac{\alpha}{g_A} \left[\frac{E_{\text{int}}}{N} \right]_\alpha \\ &\approx -(4.4 - 5.7) \times 10^{-4} \text{ MeV}^{-1} \alpha \left[\frac{E_{\text{int}}}{N} \right]_\alpha. \end{aligned} \quad (2.4)$$

Here, we have used the range for $\partial g_A / \partial m_\pi^2$ from Ref. [190]. Similarly, an interaction term, in which $1/f_\pi$ enters with the power β , $[E_{\text{int}}/N]_\beta$, leads to a contribution to the chiral condensate

$$\begin{aligned} -\frac{n}{f_\pi^2} \frac{\partial}{\partial m_\pi^2} \left[\frac{E_{\text{int}}}{N} \right]_\beta &= -\frac{n}{f_\pi^2} \frac{\partial f_\pi}{\partial m_\pi^2} \frac{\partial}{\partial f_\pi} \left[\frac{E_{\text{int}}}{N} \right]_\beta \\ &\approx (2.6 - 5.0) \times 10^{-4} \text{ MeV}^{-1} \beta \left[\frac{E_{\text{int}}}{N} \right]_\beta, \end{aligned} \quad (2.5)$$

using $\partial f_\pi / \partial m_\pi^2$ from Ref. [190]. The uncertainty is larger in this case because of the c_3 and c_4 uncertainties, which are taken as in the N³LO calculations of neutron matter [140, 168] (see also Appendix A).

2.1.3 RESULTS

We show the final results including all explicit pion-mass dependences in Fig. 2.2. The leading term $\sigma_{\pi N}$ is shown as a black dashed line. In the left Figure we show the chiral condensate in neutron matter at N³LO, based on the two N³LO NN potentials and including 3N and 4N interactions to N³LO. The calculations include all interactions at the Hartree-Fock level plus N³LO NN and N²LO 3N interactions to second order and including particle-particle/hole-hole third-order contributions, using a free or a Hartree-Fock single-particle spectrum, as in our calculations of the neutron-matter equation of state [140, 168]. The bands include the uncertainties of the many-body calculation (*i.e.*, using a free and a Hartree-Fock single-particle spectrum), of the c_i couplings of 3N forces, and those resulting from the 3N/4N cutoff variation (see Refs. [140, 168] for details). The width of the bands are dominated by the uncertainties of the c_3 coupling and by the sensitivity of the many-body calculation on the single-particle spectrum used.

We find that the density dependence of the chiral condensate is dominated by the leading $\sigma_{\pi N}$ term and therefore the chiral condensate decreases almost linearly with increasing density. With this almost linear appearance in the density regions shown it is apparent that the relativistic corrections to the leading term neglected in Eq. (2.3) are not relevant in this density regime. The interaction contributions lead to a positive correction, thus impeding the restoration of chiral symmetry with increasing density. Consequently, for moderate densities, below say $n = 0.3 \text{ fm}^{-3}$, which is below the linear extrapolation $n = (2.5 - 3)n_0$, a chiral phase transition seems unlikely in neutron matter. However, we note that, based on calculations of the type presented here, where only the broken symmetry phase is considered, we cannot exclude the possibility of a first-order transition, where the order parameter changes discontinuously. If the transition occurs below $n = 0.3 \text{ fm}^{-3}$, this would have to be a relatively strong first-order transition.

The results for the chiral condensate in neutron matter based on the two EGM 450/500 MeV and 450/700 MeV N³LO potentials are in very good agreement within the uncertainty bands in Fig. 2.2. At nuclear saturation density, $\langle \bar{q}q \rangle_n / \langle \bar{q}q \rangle_0$ lies in the range $(67.3 - 69.8)\%$ and $(67.8 - 69.5)\%$, respectively. In comparison, the uncertainty of the leading $\sigma_{\pi N}$ term is much larger. Using $\Delta\sigma_{\pi N} = 8 \text{ MeV}$ [182], we find an uncertainty on the order of 10% at $n = 0.2 \text{ fm}^{-3}$.

The order-by-order convergence of the chiral EFT calculation for the chiral condensate is shown in the right panel of Fig. 2.2. Going from N²LO to N³LO, the enhancement of the condensate is weakly reduced and the width of the uncertainty band is reduced by roughly a factor of two. A similar reduction of the bands was found in our N³LO calculation of the equation of state [140, 168].

The results mentioned above were achieved only with a variation of the explicit pion-mass dependence of the nuclear forces. We now want to take a closer look into the implicit m_π dependence through the coupling constants. For the leading-order one-pion-exchange NN interaction, which is proportional to g_A^2/f_π^2 and contributes $\sim 10 \text{ MeV}$ per particle at n_0 , the terms (2.4) and (2.5) give

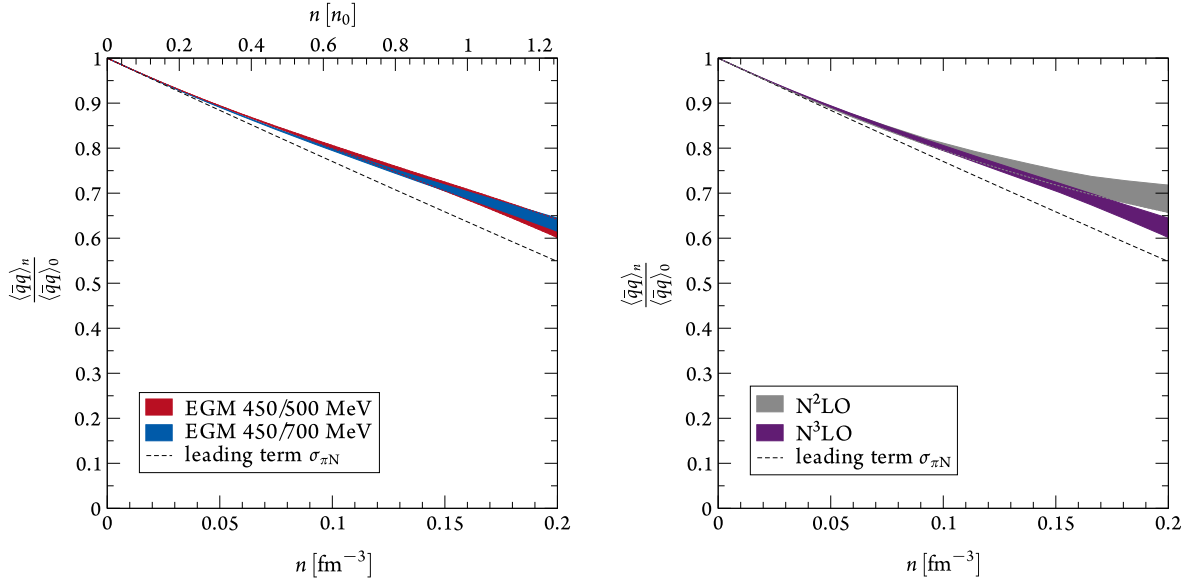


Figure 2.2: Chiral condensate $\langle \bar{q}q \rangle_n$ in neutron matter relative to vacuum $\langle \bar{q}q \rangle_0$ as a function of density. The dashed line is the leading pion-nucleon sigma-term contribution.

Left: The interaction contributions are obtained from the N³LO neutron-matter calculation of Refs. [140, 168], based on the EGM 450/500 MeV and 450/700 MeV N³LO NN potentials plus 3N and 4N interactions to N³LO, by varying the pion mass around the physical value. As in Refs. [140, 168], the bands for each NN potential include uncertainties of the many-body calculation, of the c_i couplings of 3N forces, and those resulting from the 3N/4N cutoff variation.

Right: Comparison of calculations at N²LO (grey) and N³LO (purple) using the same interactions and uncertainty estimates as in the left figure.

a contribution to the chiral condensate ranging from -0.006 to $+0.001$. The leading N²LO two-pion-exchange 3N forces also provide ~ 10 MeV per particle at n_0 . These terms are proportional to g_A^2/f_π^4 and the corresponding contribution to the chiral condensate lies in the range -0.001 to $+0.011$. Combined, these corrections amount to at most a 25% increase of the uncertainty band in Fig. 2.2.

We expect the contributions from the shorter-range interactions absorbed in the low-energy couplings to start at a similar level. However, the extrapolation of their m_π dependence from lattice QCD results at heavier pion masses to the physical point is uncertain. This will be improved in the future once lattice QCD results for NN and 3N interactions for physical pion masses will become available. Hence, we expect the estimated effects beyond the explicit m_π dependence to be small compared to the band in Fig. 2.2. This justifies our approach of not including these contributions in our calculations.

The individual interaction contributions to the chiral condensate are shown in Fig. 2.3. In the upper row, the Hartree-Fock N³LO NN, N²LO 3N, and N³LO 3N and 4N results are given. In the lower row, second-order and particle-particle/hole-hole third-order contributions beyond Hartree-Fock

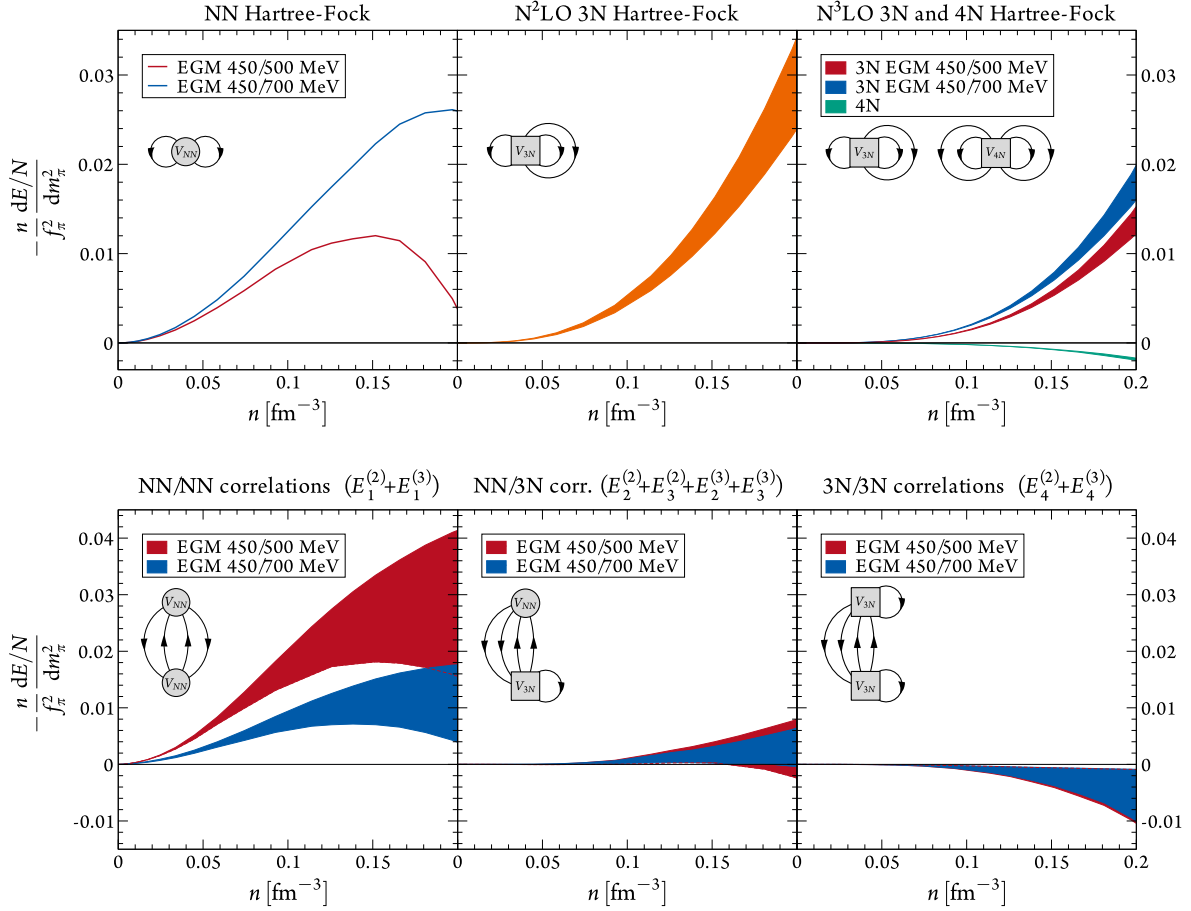


Figure 2.3: Individual interaction contributions to the chiral condensate in neutron matter as a function of density for the two $N^3\text{LO}$ NN potentials of Fig. 2.2. The upper row gives the NN, the $N^2\text{LO}$ 3N, and the $N^3\text{LO}$ 3N and 4N Hartree-Fock contributions. In the lower row, second-order and particle-particle/hole-hole third-order contributions beyond Hartree-Fock are shown, where the $N^2\text{LO}$ 3N forces are included as density-dependent two-body interactions. The various contributions are illustrated diagrammatically and the $E_i^{(2,3)}$ nomenclature follows Ref. [168]. The Hartree-Fock 3N- and 4N-force contributions include uncertainty estimates from the 3N/4N cutoff variation and from the c_i couplings of 3N forces. The higher-order bands also include uncertainties in the many-body calculation.

are shown, grouped into the different correlations where $N^2\text{LO}$ 3N forces are included as density-dependent two-body interactions. This follows the notation of Ref. [168]. The most important contributions are the NN and 3N Hartree-Fock terms as well as higher-order correlation effects due to NN interactions. The latter are sensitive to the single-particle spectrum used. This is because the Hartree-Fock single-particle energies depend on the pion mass, so that the derivative with respect to m_π^2 yields additional contributions. For the Hartree-Fock spectrum, the NN correlation contributions are then only about half as large as for the free spectrum. For the NN-3N and 3N-3N correlation contributions, we find a similar sensitivity, but they are relatively small.

As shown in Fig. 2.3, at nuclear saturation density the NN Hartree-Fock contribution of the EGM 450/500 MeV potential is by a factor two smaller than that of the EGM 450/700 MeV potential.

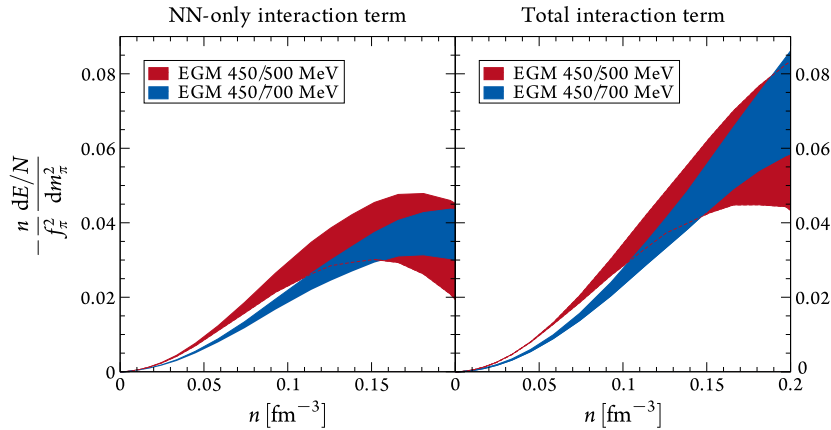


Figure 2.4: Sums of the NN-only and the total interaction contributions to the chiral condensate in neutron matter as a function of density. The bands are based on Fig. 2.3 and include the various uncertainty estimates.

However, for the higher-order correlations the situation is reversed, so that the sum of the Hartree-Fock and higher-order NN contributions of the two NN potentials are in very good agreement, as shown in the left panel of Fig. 2.4. The total interaction contribution, including 3N and 4N forces, is shown in the right panel of Fig. 2.4 and yields a $6 \pm 2\%$ enhancement of the chiral condensate at saturation density. We again find a very good agreement within the uncertainty bands of the two NN potentials.

We note that the increase of the chiral condensate due to interactions corresponds to a decrease of the scalar pion density in the interacting system. While the iterated NN one-pion-exchange interaction yields an enhancement of the scalar pion density [188], the interference between the one-pion-exchange and shorter-range NN parts induces the opposite effect. Thus, the sign of the interaction contribution to the chiral condensate is governed by a competition between these two contributions.

COMPARISON WITH OTHER RESULTS

Our results agree with those of Kaiser and Weise [191], who calculated the interaction corrections to the chiral condensate in chiral perturbation theory with explicit Δ 's including one- and two-pion exchange contributions up to three-loop order in the energy density. This leads to a $\sim 5\%$ contribution at n_0 . Extrapolating their results to higher densities, chiral symmetry restoration is found at $\sim 3n_0$. The chiral condensate in neutron matter was also calculated to NLO by Lacour *et al.* [192] using in-medium chiral perturbation theory [193]. They found only small interaction corrections, which reduce the chiral condensate at this level, inconsistent with our results. Lacour *et al.* also calculated the chiral condensate for the u and d quarks separately and showed that the condensate for the u quarks is larger than for the d quarks by $\sim 7\%$ at $n = 0.2 \text{ fm}^{-3}$. This difference is however smaller than the uncertainty from the $\sigma_{\pi N}$ term.

Finally, Kaiser *et al.* [160] also computed the interaction corrections to the chiral condensate in sym-

metric nuclear matter in the same scheme. Both in neutron and symmetric matter, they find a strong enhancement of the condensate owing to correlation diagrams involving the excitation of the Δ . In our work, the corresponding contribution is included mainly through 3N interactions. On a qualitative level, our results agree with those of Refs. [160, 180]. However, the various interaction contributions and the magnitude of the enhancement seem rather different. This may be due to differences in the calculational schemes, but also due to differences in the system considered (neutron matter versus symmetric nuclear matter). With a consistent study of symmetric matter a direct comparison could be made.

2.1.4 CONCLUSIONS

In summary, we find that nuclear interactions impede the restoration of chiral symmetry in neutron matter at zero temperature. The net effect of interactions remains below 10% for $n \lesssim 0.2 \text{ fm}^{-3}$, but grows with increasing density. The dominant source of uncertainty is the $\sigma_{\pi N}$ term. We conclude that for moderate densities, say $n \lesssim 0.3 \text{ fm}^{-3}$, a chiral phase transition in neutron-rich matter therefore seems unlikely, although we cannot exclude a strong first-order transition. For the densities considered here, we find a good convergence of the chiral condensate from N²LO to N³LO in chiral EFT. Clearly it would be very interesting to calculate the chiral condensate also for higher densities. While a systematic calculation in chiral effective field theory is difficult at densities much higher than $n = 0.2 \text{ fm}^{-3}$, astrophysical observations shed light on matter at high densities and at present there are no indications of quark matter in neutron stars (see Refs. [13, 14, 88, 161] for the equation of state).

2.2 SPIN-POLARISED NEUTRON MATTER

SPIN-POLARISED NEUTRON MATTER is an extreme system which, however, can be used to constrain other nuclear models and calculations. In this project, which was worked out in collaboration with Kai Hebeler and Achim Schwenk, we have studied the energy per particle to constrain energy-density functionals and we also investigated the pion-mass dependence of spin-polarised neutron matter in order to provide a benchmark system for lattice QCD. The results have been published in Ref. [194].

2.2.1 INTRODUCTION

As mentioned in the introductory remarks of this Chapter, neutron matter exhibits properties similar to a unitary Fermi gas, which is a consequence of the large neutron-neutron scattering length [155–157]. The energy of neutron matter is at nuclear densities approximately 0.4 times the energy of a free Fermi gas [195]. These benchmark results, combined with the possibility to simulate low-density neutron matter with ultra-cold atoms near a Feshbach resonance [196], have led to the inclusion of *ab initio* results for neutron matter into modern energy-density functionals for nuclei [197, 198].

We study the properties of spin-polarised neutron matter at N³LO in chiral effective field theory, including consistently NN, 3N, and 4N interactions, based on our calculations of unpolarised matter [140, 168]. Spin-polarised neutron matter may exist in very strong magnetic fields as they occur in the interior of magnetars (see Section 1.2). For a unitary Fermi gas, the spin-polarised system is an almost non-interacting gas, so we ask the question to which densities spin-polarised neutrons behave like a weakly interacting Fermi gas? The answer is simple at low densities relevant to ultra-cold atoms: Due to Pauli's principle polarised neutrons cannot interact through *S*-wave interactions, which are the dominant contribution to the nuclear force. *P*-wave interactions between neutrons are weaker and many-body forces are suppressed by a power of the density, which explains an almost non-interacting behaviour. However, we find the surprising result that the energy of spin-polarised neutrons is close to a non-interacting system at least up to nuclear saturation density n_0 , which is well beyond the large *S*-wave scattering-length regime $n \lesssim n_0/100$.

The physics of spin-polarised neutron matter is interesting, because it can provide an additional anchor point for energy-density functionals. To this end, we explore how our results compare with state-of-the-art functionals. In addition, spin-polarised matter is ferromagnetic, so that its energy compared to the spin-symmetric system determines whether a ferromagnetic transition in neutron stars is possible [199, 200]. Finally, due to the reduced spin/isospin degrees of freedom there are fewer non-trivial contractions for spin-polarised neutrons, so that the determination of this system is easier in lattice QCD than spin-symmetric nucleonic matter [201]. Therefore, we also study how our results depend on the pion mass and provide predictions that can be tested and refined with lat-

tice QCD, which is due to computational constraints currently limited to heavier (unphysical) pion masses.

Spin-polarised neutron matter has been studied before, *e.g.*, in Refs. [199, 200, 202, 203], however with NN interactions only, and without a focus on the subnuclear density region and the comparison to a weakly interacting Fermi gas.

2.2.2 CALCULATIONAL DETAILS

We calculate the energy per particle of spin-polarised matter in the Hartree-Fock approximation using the non-local chiral forces, as for our unpolarised-matter calculations [140, 168]. We also include many-body correlations for NN forces up to second order in many-body perturbation theory, as well as particle-particle/hole-hole diagrams to third order (see Ref. [139]). We expect this approximation to be reliable since we found only small contributions from 3N forces at second and third order in perturbation theory in spin-symmetric neutron matter [139]. This has also been verified by more recent calculations of neutron matter, which take the second- and third-order contributions of the sub-leading 3N forces into account [141, 159]. In the polarised case we expect even smaller contributions due to the enhanced Pauli-blocking effects.

The Hartree-Fock energy is given for an A -body interaction by

$$\begin{aligned} \frac{E_{AN}^{(1)}}{N} &= \frac{1}{n} \frac{1}{A!} \int \frac{d^3k_1}{(2\pi)^3} \cdots \frac{d^3k_A}{(2\pi)^3} f_R^2(\mathbf{k}_1, \dots, \mathbf{k}_A) \theta_{\mathbf{k}_1} \cdots \theta_{\mathbf{k}_A} \langle 1 \cdots A | \mathcal{A}_A \sum_{\text{all perm.}} V_{AN} | 1 \cdots A \rangle \\ &= \frac{1}{n} \int \frac{d^3k_1}{(2\pi)^3} \cdots \frac{d^3k_A}{(2\pi)^3} f_R^2(\mathbf{k}_1, \dots, \mathbf{k}_A) \theta_{\mathbf{k}_1} \cdots \theta_{\mathbf{k}_A} \langle V_{AN} \rangle, \end{aligned} \quad (2.6)$$

where we use the short-hand notation $i \equiv (\mathbf{k}_i \uparrow)$ in the bra and ket states, with the arrow indicating that only one spin species is considered. Further, \mathcal{A}_A denotes the A -body anti-symmetriser and $\theta_{\mathbf{k}_i} = \theta(k_F - k_i)$ is the Fermi-Dirac distribution function at zero temperature. We use a fully symmetric regulator function with respect to the exchange of particle momenta according to Refs. [139, 140, 168],

$$f_R(\mathbf{k}_1, \dots, \mathbf{k}_A) = \exp \left[- \left(\frac{\sum_{i=1}^A k_i^2 - \sum_{i,j}^A \mathbf{k}_i \cdot \mathbf{k}_j}{A\Lambda^2} \right)^{n_{\text{exp}}} \right], \quad (2.7)$$

with $n_{\text{exp}} = 4$ and 3N/4N cutoff $\Lambda = (2.0 - 2.5) \text{ fm}^{-1}$, which is varied in order to probe the cutoff dependence of our calculation.

The energy contributions from 3N and 4N forces up to N³LO [133–135, 142, 143] are calculated according to Eq. (2.6), where we have evaluated the spin by hand and used numerical integration methods of WOLFRAM MATHEMATICA for the momentum integrations. Note that due to the polarisation one cannot use spherical symmetry and has to perform all angular integrals explicitly.

In addition to the 3N and 4N topologies that do not contribute to the neutron-matter energy (see Refs. [139, 168]) for the spin-polarised system also the 3N N³LO two-pion-exchange–contact topology vanishes, as a consequence of the Pauli principle excluding all leading-order NN contacts C_S and C_T . Further, the 4N N³LO diagrams V^e and V^f (according to the nomenclature in Fig. 1.10) do not contribute in polarised matter. The C_S/C_T dependence of the N³LO 3N relativistic-corrections interaction is negligible and results only in energy differences at the 1 keV level at saturation density. Thus, the many-body forces essentially depend only on the low-energy couplings c_1 and c_3 , which are chosen according to Refs. [132, 204]: $c_1 = -(0.75 - 1.13) \text{ GeV}^{-1}$ and $c_3 = -(4.77 - 5.51) \text{ GeV}^{-1}$ as in Refs. [140, 168] (see also Appendix A).

As for our unpolarised-matter calculations, we use the N³LO NN potential of Entem and Machleidt (EM) with a cutoff 500 MeV [145, 146], and the potentials developed by Epelbaum, Glöckle, and Meißner (EGM) with cutoffs $\Lambda/\tilde{\Lambda} = 450/500$ and $450/700$ MeV [148]. These potentials were found to be perturbative in neutron matter [140, 150, 151, 168]. Spin-polarised matter is expected to converge even faster, because S -wave interactions among polarised neutrons vanish, P -wave interactions are weaker, and Pauli blocking becomes even more effective due to the larger Fermi momentum for a given density compared to spin-symmetric matter.

The NN contribution is calculated using a C++ code, which is based on the code used for the unpolarised matter calculations [140, 168], which also allows a calculation beyond the Hartree-Fock level. The second-order contribution to the energy per particle is given by

$$\frac{E_{\text{NN}}^{(2)}}{N} = \frac{1}{4} \left[\prod_{i=1}^4 \int \frac{d^3 k_i}{(2\pi)^3} \right] \frac{|\langle 12 | V_{\text{NN}} | 34 \rangle|^2 (2\pi)^3}{\varepsilon_{\mathbf{k}_1} + \varepsilon_{\mathbf{k}_2} - \varepsilon_{\mathbf{k}_3} - \varepsilon_{\mathbf{k}_4}} \theta_{\mathbf{k}_1} \theta_{\mathbf{k}_2} \bar{\theta}_{\mathbf{k}_3} \bar{\theta}_{\mathbf{k}_4} \delta(\mathbf{k}_1 + \mathbf{k}_2 - \mathbf{k}_3 - \mathbf{k}_4), \quad (2.8)$$

where $\bar{\theta}_{\mathbf{k}} = 1 - \theta_{\mathbf{k}}$. Taking a free or a Hartree-Fock spectrum for the single-particle energies $\varepsilon_{\mathbf{k}}$ changes the results only at the 10 keV level. This indicates that the many-body calculation is very well converged, and in the following results are given with a free spectrum. In order to simplify the numerical calculations, we average over the angles of initial and final relative momenta \mathbf{k} and \mathbf{k}' :

$$\begin{aligned} & \int \frac{d\mathbf{k} d\mathbf{k}'}{(4\pi)^2} |\langle \mathbf{k} S = 1 M_S = 1 | V_{\text{NN}} | \mathbf{k}' S = 1 M_S = 1 \rangle|^2 \\ &= \sum_{l, l', J, \tilde{J}} 4(4\pi)^2 C_{ll'}^{\tilde{J}} \langle k | V_{1l'l} | k' \rangle \langle k' | V_{1l'l} | k \rangle, \end{aligned} \quad (2.9)$$

where $V_{Sll'J}$ denote the neutron-neutron partial-wave matrix elements and $C_{ll'}^{\tilde{J}}$ is the sum of Clebsch-Gordan coefficients $C_{l_1 m_1 l_2 m_2}^{l_3 m_3}$

$$C_{ll'}^{\tilde{J}} = \sum_M C_{l'(M-1)11}^{JM} C_{l(M-1)11}^{JM} C_{l(M-1)11}^{\tilde{J}M} C_{l'(M-1)11}^{\tilde{J}M}. \quad (2.10)$$

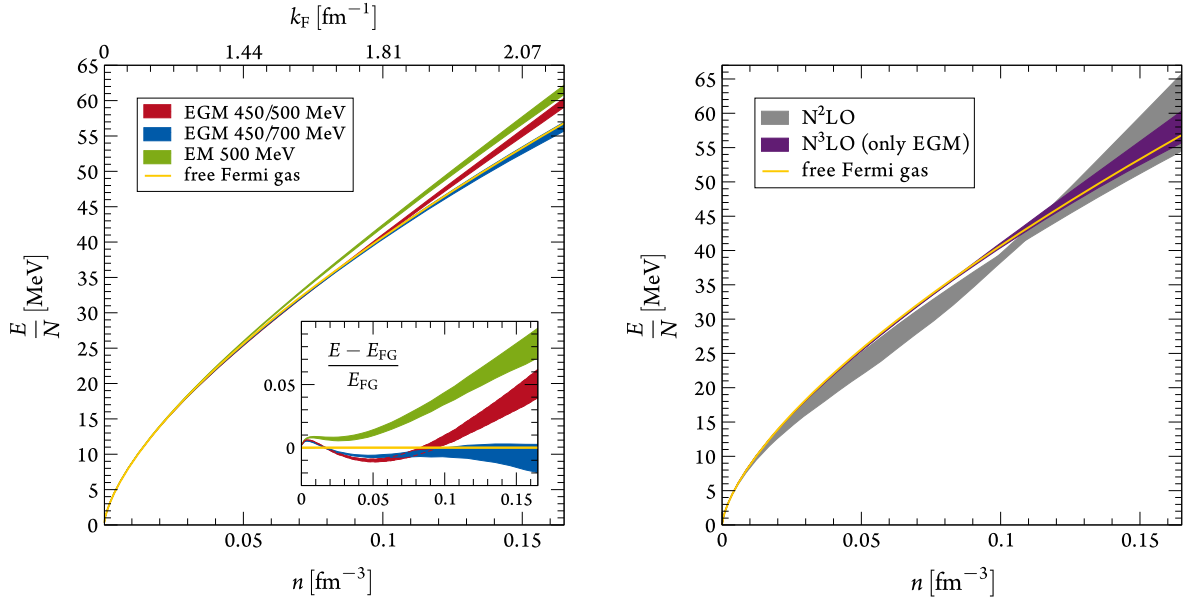


Figure 2.5: Energy of spin-polarised neutron matter as a function of density. The solid (yellow) line is the energy of a free Fermi gas (FG).

Left: The different bands correspond to the N^3 LO EM/EGM NN potentials and including 3N and 4N interactions up to N^3 LO. The bands provide an estimate of the uncertainty in 3N forces and in the many-body calculation (see text for details). The inset shows the relative size of the interaction contributions.

Right: Comparison of the N^2 LO to N^3 LO EGM potentials including the many-nucleon interactions up to that order.

Details on the partial-wave decomposition and this approximation can be found in Appendix B. The angular-averaging approximation has been demonstrated to be reliable for spin-symmetric matter [139] and only affects the small contributions beyond Hartree-Fock.

2.2.3 RESULTS AND DISCUSSIONS

We show as our central result the energy per particle of spin-polarised neutron matter as a function of density in Fig. 2.5. Compared to the non-interacting system (yellow line) we find that spin-polarised neutrons behave almost as a free Fermi gas. The interaction effects provide less than 10% corrections at n_0 (see the inset). The largest dependence of our calculations is on the NN interaction used. The EM 500 MeV potential (green band) leads to weakly repulsive interactions with $E/N \approx 60$ MeV at n_0 , compared to 55.7 MeV for a free Fermi gas. Using the EGM 450/500 (red) and 450/700 MeV (blue) potentials results in even weaker interactions with $E/N \approx 57$ MeV and ≈ 55 MeV, respectively. Because n_0 for polarised matter corresponds to a high Fermi momentum of 2.1 fm^{-1} , these small differences are due to the range in NN scattering predictions at these higher momenta (corresponding to laboratory energies of ~ 350 MeV). The bands include the 3N/4N cutoff variation, c_i range, and the difference between second- and third-order contributions on the NN level, as discussed above.

The dependence on the NN interaction can also be seen in the right panel of Fig. 2.5, where we show a comparison of a N²LO and N³LO calculation. As there does not exist an N²LO EM potential we only compare the EGM interactions. Note that the N²LO band (grey) results from the combination of the two different cutoffs and their different curvature leads to the bulbous appearance at intermediate densities. We attribute this effect to the poor description of the scattering phase shifts in the *P*-wave channels.

At very low densities, we can also compare our results to the dilute-gas expansion [205]

$$\begin{aligned} \frac{E}{N} = \frac{k_F^2}{2m_N} & \left\{ \frac{3}{5} + (g-1) \left[\frac{2}{3\pi}(k_F a_S) + \frac{4}{35\pi^2}(11 - 2 \ln 2)(k_F a_S)^2 + \frac{1}{10\pi}(k_F r_S)(k_F a_S)^2 \right. \right. \\ & + [0.076 + 0.057(g-3)](k_F a_S)^3 \left. \right] + (g+1) \frac{1}{5\pi}(k_F a_P)^3 \\ & \left. + (g-1)(g-2) \frac{16}{27\pi^3}(4\pi - 3\sqrt{3})(k_F a_S^4) \ln(k_F a_S) + \dots \right\}, \end{aligned} \quad (2.11)$$

where a_S and r_S are the *S*-wave scattering length and effective range, respectively, and a_P denotes the *P*-wave scattering length. For spin-polarised neutrons the spin degeneracy is $g = 1$ and we have

$$\frac{E}{N} = \frac{k_F^2}{2m_N} \left[\frac{3}{5} + \frac{2}{5\pi}(k_F a_P)^3 + \mathcal{O}(k_F^5) \right]. \quad (2.12)$$

The first non-vanishing interaction contribution is thus at k_F^5 from the *P*-wave scattering length, or the *P*-wave scattering volume a_P^3 . We have fitted the *P*-wave scattering length for $k_F < 0.3 \text{ fm}^{-1}$ to our equation of state and obtain a range $a_P = (0.50 - 0.52) \text{ fm}$ depending on the NN interaction used. This is consistent with $a_P = (0.44 - 0.47) \text{ fm}$ from the different NN interactions with small corrections due to Pauli blocking that render the *P*-wave scattering length more repulsive in the medium.

Figure 2.6 shows the individual interaction contributions. All energies are small compared to the spin-symmetric system [140, 168]. The left panel shows the NN contributions for the three N³LO potentials. The different behaviour can be traced back to different predictions for the scattering phase shifts. The EM 500 MeV potential gives a net repulsive contribution, with $E/N \approx 3.1 \text{ MeV}$ at n_0 (5.6% relative to E_{FG}). Up to densities $n \lesssim 0.1 \text{ fm}^{-3}$ the EGM 450/500 and 450/700 MeV potentials are in good agreement and provide only $E/N \approx -0.5 \text{ MeV}$ at $n = 0.08 \text{ fm}^{-3}$, and then start to differ. The middle panel of Fig. 2.6 shows the contributions from the leading N²LO 3N forces. The 3N interactions are, as in the spin-symmetric case, repulsive but with much smaller energies in the range $(0.8 - 1.9) \text{ MeV}$ at n_0 . In the right panel, we show all contributions from the N³LO many-body forces. The dominant contributions are from two-pion-exchange 3N forces with energies $-(0.9 - 1.6) \text{ MeV}$ at n_0 . This is almost as large as the leading contribution of the two-pion-exchange topology, and shows that one is pushing the chiral effective field theory expansion

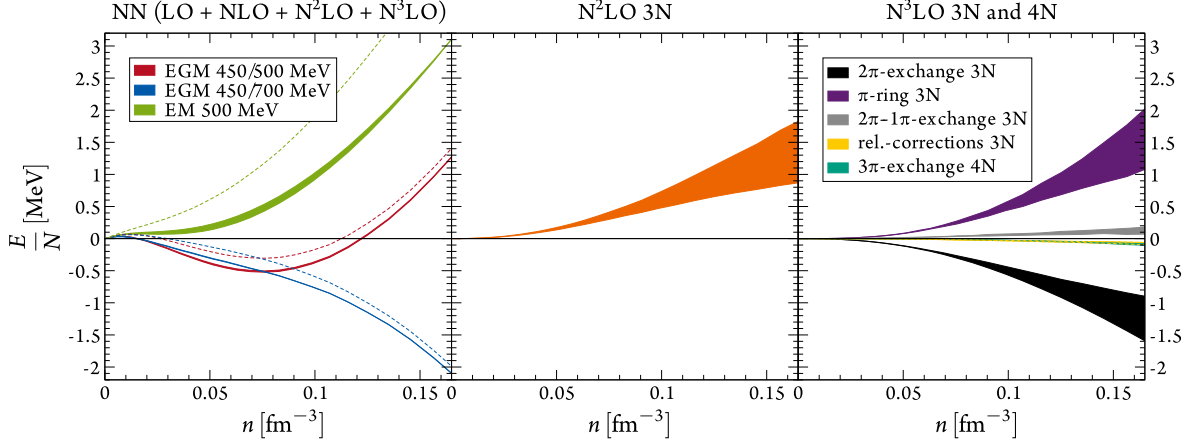


Figure 2.6: Interaction contributions to the energy of spin-polarised neutron matter as a function of density. The left panel shows the NN contributions for the three NN potentials. The width of the bands is given by the difference between second- and third-order contributions in the many-body calculation. The dashed lines are the Hartree-Fock energies. The middle panel shows the contribution from N^2LO 3N forces, where the band corresponds to the range of c_i couplings used and the 3N cutoff variation $\Lambda = (2.0 - 2.5) \text{ fm}^{-1}$. The right panel gives the different N^3LO 3N and 4N contributions, with corresponding c_i and cutoff variations. The 4N contributions overlap with the relativistic-corrections 3N energies.

to the limits. However, all these 3N contributions are still small. In addition, there are repulsive contributions from pion-ring 3N forces, which contribute $(1.1 - 2.1) \text{ MeV}$ at n_0 and counteract these. Finally, there are small repulsive contributions from the two-pion–one-pion-exchange 3N topology of $0.1 - 0.2 \text{ MeV}$ at n_0 , small attractive contributions from the relativistic-corrections 3N topology, while three-pion-exchange 4N interactions contribute only -0.1 MeV at n_0 . In total, the 3N+4N contributions provide a net repulsion of $E/N = (1.0 - 2.2) \text{ MeV}$ at n_0 . While it is known that P -wave interactions are weak it is remarkable that even contributions from many-body forces are small.

By comparing our results with the corresponding energy range for spin-symmetric matter, $E/N \approx 14 - 21 \text{ MeV}$ at n_0 (see Fig. 2.1) versus $(55 - 61) \text{ MeV}$ for polarised matter, it is clear that a phase transition to the ferromagnetic state is not possible for $n \lesssim n_0$. Further, we expect the energy of spin-polarised neutrons at higher densities to lie above the free Fermi gas due to repulsive 3N forces (see also Fig. 2.6). Assuming the energy of spin-polarised neutrons remains close to a free Fermi gas also for higher densities, we can use the general equation of state constraints of Ref. [14] to provide constraints for the onset of a possible ferromagnetic phase transition. Taking the three representative equations of state (see Fig. 1.3), a phase transition to a ferromagnetic state may be possible for $n/n_0 \gtrsim 6.1, 3.4,$ and 2.3 for the soft, intermediate, and stiff equations of state, respectively. At these densities the energy of the free Fermi gas is lower than that predicted by the representative equations of state. Note that if more massive neutron stars are discovered, e.g., with $2.4M_\odot$, the soft case is ruled out [14].

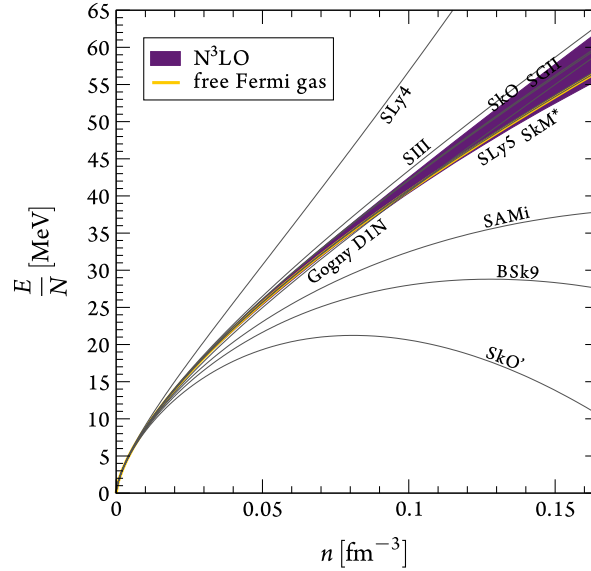


Figure 2.7: Energy of spin-polarised neutron matter from Fig. 2.5 compared to various energy-density functionals (see text) following Ref. [207].

CONSTRAINTS FOR ENERGY-DENSITY FUNCTIONALS

In Fig. 2.7 we compare our results with predictions based on state-of-the-art energy-density functionals (for early work on polarised neutron matter with Skyrme functionals see Ref. [206]), following Ref. [207]: SIII [208], SGII [209], SkM* [210], SLy4 and SLy5 [211], SkO and SkO' [212], BSk9 [213], as well as SAMi [32] and using the Gogny D1N interaction [33]. At low densities $n \lesssim 0.01 \text{ fm}^{-3}$ all functionals agree with a free Fermi gas. However, at higher densities we find significant deviations. In best agreement with our calculations are the functionals SIII, SkO, SGII, SkM*, and SLy5, whereas the latter two reproduce the free Fermi gas and the former provide small repulsive contributions. The predictions of the functionals SLy4, SAMi, BSk9, and SkO' differ significantly from our N³LO bands. Therefore, it will be interesting to use our results as additional neutron-matter constraint for modern functionals. Note that the above discussion of a possible transition to a ferromagnetic state is different to the spin instabilities caused by the polarised system to decrease unphysically in energy, as for the SkO' case, predicting a ferromagnetic state at sub-nuclear densities.

VARIATION OF THE PION MASS FOR LATTICE QCD

For comparison with lattice QCD simulations, we also vary the pion mass in NN, 3N, and 4N interactions. For this estimate we only take into account the explicit pion exchanges and do not vary the pion mass implicitly in the coupling constants, as we have done for the calculation of the chiral condensate in Section 2.1. This explicit pion-mass dependence is expected to be the dominant contribution in spin-symmetric neutron matter [176, 191, 192]. We emphasise, however, that for a high-

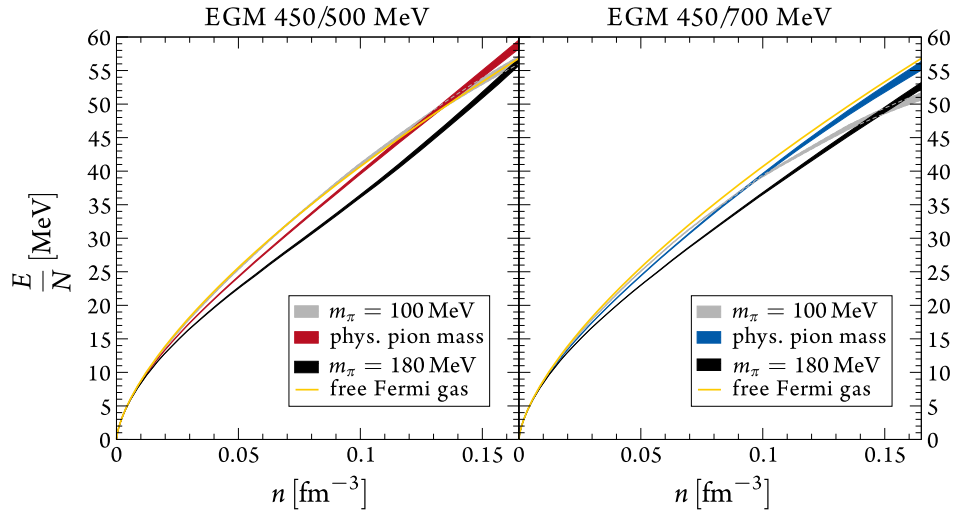


Figure 2.8: Energy of spin-polarised neutron matter as a function of density for the $N^3\text{LO}$ EGM potentials using different pion masses. The energy of the free Fermi gas is shown for comparison in the physical limit.

precision comparison, one would need to include this m_π dependence of the low-energy couplings. As mentioned in the previous Section, the pion mass variation can only be done for the EGM potentials.

In Fig. 2.8 we show the energy of polarised neutron matter for the potentials EGM 450/500 (left) and 450/700 MeV (right) for pion masses $m_\pi = 100, 138, 180$ MeV as grey, coloured, and black bands, respectively. For comparison we also show the energy of the non-interacting system in the physical limit. For both potentials we observe a similar behaviour: While higher pion masses lead to more attractive interactions lowering the total energy over the whole density region considered here, the picture is different for lower pion masses. At low and intermediate densities we find an increase of the total energy and a change of sign in the interaction energy in the higher-density regime.

We also study the dependence of the energy of the free Fermi gas, $E_{\text{FG}}/N = 3k_{\text{F}}^2/(10m_{\text{N}})$, on m_π . This is a result of the change of the nucleon mass with the pion mass. It varies as [190]

$$m_{\text{N}}(m_\pi) = m_0 - 4c_1 m_\pi^2 - \frac{3g_A^2}{32\pi f_\pi^2} m_\pi^3 + \mathcal{O}(m_\pi^4), \quad (2.13)$$

where m_0 is the nucleon mass in the chiral limit and c_1 is the same low-energy coupling that enters NN and 3N forces at $N^2\text{LO}$. We consistently also do not include the implicit pion-mass dependence of the coupling-constants in these estimates. For c_1 we use the same range as above, as in the 3N forces. Using the physical values of m_{N} , m_π , g_A , and f_π we can extract m_0 for the employed c_1 range. This range is consistent with the choice of the pion-nucleon sigma term $\sigma_{\pi\text{N}} \approx 50$ MeV as chosen in the previous Section. This leads to the yellow band in Fig. 2.9 at $n_0/2$ and corresponds to the range

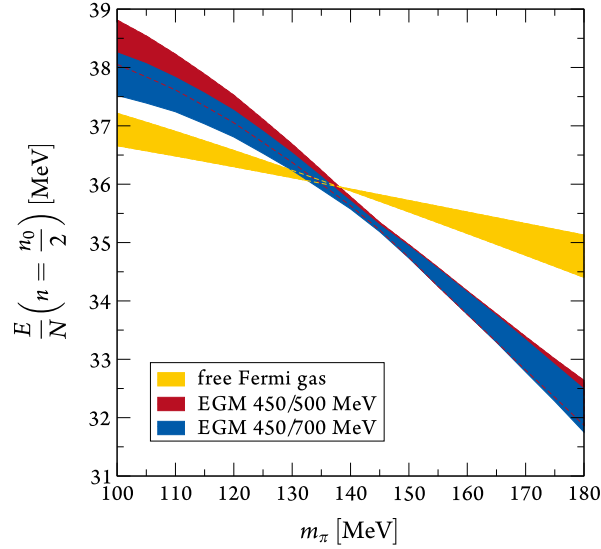


Figure 2.9: Dependence of the energy of spin-polarised neutron matter on the pion mass. The yellow band indicates the energy of a free Fermi gas. The red/blue bands correspond to the EGM NN potentials, including 3N and 4N interactions, at the same many-body calculational level as the results in Fig 2.5.

of the pion-nucleon sigma term $\sigma_{\pi N} = (34.9 - 63.9) \text{ MeV}$ (see Section 2.1 for details).

In Fig. 2.9 we show a systematic variation of the pion mass at fixed density $n = n_0/2$. As in Fig. 2.8, we find that including interactions gives a very similar m_π dependence, but away from the physical pion mass, the energy starts to deviate more from the free Fermi gas. As in spin-symmetric matter, the interaction contributions also increase the chiral condensate, as determined from the slope in m_π .

2.2.4 CONCLUSIONS

We have presented a complete N³LO calculation of spin-polarised neutron matter, where the dominant uncertainty is due to the NN potential used, as well as due to the uncertainty in 3N forces. The uncertainty from the many-body calculation is very small (shown by the bands in the left panel of Fig. 2.6). Our results show that the energy of spin-polarised neutrons is remarkably close to a non-interacting system. This shows that the physics of neutron matter is similar to a unitary gas well beyond the scattering-length regime. Moreover, our results provide constraints for energy-density functionals of nuclei and show that a phase transition to a ferromagnetic state is not possible for $n \lesssim n_0$. Finally, our predictions can be tested and refined with lattice QCD calculations of spin-polarised neutrons in a box.

2.3 THE PAIRING GAP IN NEUTRON MATTER

PAIRING IS A CENTRAL PHENOMENON IN A WIDE RANGE OF NUCLEAR SYSTEMS, from nuclei to nuclear matter. It is crucial to understand phenomena like the neutrino cooling mechanism and the rotational dynamics of neutron stars [77, 214], the shell structure and energies of neutron-rich nuclei [49], or the β decay of the two-neutron halo ^{11}Li [215]. In this project we studied in collaboration with Christian Drischler, Kai Hebeler, and Achim Schwenk the pairing gap in neutron matter at zero temperature in the BCS approximation in the spin singlet 1S_0 and triplet $^3P_2 - ^3F_2$ [216].

2.3.1 DERIVATION OF THE GAP EQUATION

We briefly want to derive the gap equation in BCS theory. This derivation is done for a system of unpolarised spin-1/2 particles interacting via a two-body potential. It is based on Ref. [76]. Another derivation can be found in Ref. [217] using the Gorkov approach to superfluidity, see also Ref. [218] for a derivation based on Weinberg eigenvalues.

The ground state of a superfluid system, *i.e.*, the BCS wave function is of the form

$$|\psi_{\text{BCS}}\rangle = \prod_{\mathbf{k}} (u_{\mathbf{k}} + v_{\mathbf{k}} a_{\mathbf{k}\uparrow}^\dagger a_{-\mathbf{k}\downarrow}^\dagger) |0\rangle, \quad (2.14)$$

with creation operators $a_{\mathbf{k}a}^\dagger$, which creates a particle with momentum \mathbf{k} and spin projection $a = \uparrow, \downarrow$. It describes pairing of particles with opposite spin and momentum (spin singlet). Since the BCS wave function is normalised, the coefficients $u_{\mathbf{k}}$ and $v_{\mathbf{k}}$ have to fulfil the condition $u_{\mathbf{k}}^2 + v_{\mathbf{k}}^2 = 1$ and can be chosen to be positive without loss of generality. The squares of these coefficients represent the probability of a Cooper-pair state to be occupied (v) or unoccupied (u).

Note that $|\psi_{\text{BCS}}\rangle$ is not an eigenstate of the particle number $\hat{N} = \sum_{\mathbf{k},a} a_{\mathbf{k}a}^\dagger a_{\mathbf{k}a}$. Thus, one usually works in the grand canonical ensemble with fixed average particle number

$$\langle \hat{N} \rangle \equiv \langle \psi_{\text{BCS}} | \sum_{\mathbf{k}} (a_{\mathbf{k}\uparrow}^\dagger a_{\mathbf{k}\uparrow} + a_{\mathbf{k}\downarrow}^\dagger a_{\mathbf{k}\downarrow}) | \psi_{\text{BCS}} \rangle = 2 \sum_{\mathbf{k}} v_{\mathbf{k}}^2. \quad (2.15)$$

In order to get the pairing gap in the BCS approximation of a system with Hamiltonian \hat{H} we need its expectation value with respect to the BCS wave function. In this expression occur factors of the form $u_{\mathbf{k}}^2 v_{\mathbf{k}}^2$, which correspond to the Hartree-Fock contribution, rather than to genuine pairing effects. They are neglected:

$$\langle \hat{H} - \mu \hat{N} \rangle = 2 \sum_{\mathbf{k}} \xi(\mathbf{k}) v_{\mathbf{k}}^2 + \sum_{\substack{\mathbf{k}, a, a' \\ \mathbf{k}', \beta, \beta'}} \langle \mathbf{k}a - \mathbf{k}a' | \hat{V} | \mathbf{k}'\beta - \mathbf{k}\beta' \rangle u_{\mathbf{k}} v_{\mathbf{k}} u_{\mathbf{k}'} v_{\mathbf{k}'}, \quad (2.16)$$

where $\mu = \varepsilon(k_F)$ denotes the chemical potential and $\xi(\mathbf{k}) = \varepsilon(k) - \mu$ is the kinetic energy relative to the Fermi surface; $\varepsilon(k)$ denotes the single-particle energy with momentum \mathbf{k} , which is given, *e.g.*, in a free spectrum as $\varepsilon(k) = k^2/(2m)$ with neutron mass m . Furthermore, $\langle \mathbf{k}\alpha - \mathbf{k}\alpha' | \widehat{V} | \mathbf{k}'\beta - \mathbf{k}'\beta' \rangle$ is the interaction matrix element for particles with opposite spin $\alpha, \alpha' / \beta, \beta'$ and momentum \mathbf{k}, \mathbf{k}' in the final and initial state, respectively. The BCS gap equation is then obtained by the minimisation of Eq. (2.16) under the constraint of normalisation. It reads in its self-consistent formulation

$$\Delta_{\alpha\alpha'}(\mathbf{k}) = - \sum_{\mathbf{k}', \beta, \beta'} \langle \mathbf{k}\alpha - \mathbf{k}\alpha' | \widehat{V} | \mathbf{k}'\beta - \mathbf{k}'\beta' \rangle \frac{\Delta_{\beta\beta'}(\mathbf{k}')}{2E(\mathbf{k}')}, \quad (2.17)$$

where the gap itself is defined via

$$\Delta_{\alpha\alpha'}(\mathbf{k}) = - \sum_{\mathbf{k}', \beta, \beta'} \langle \mathbf{k}\alpha - \mathbf{k}\alpha' | \widehat{V} | \mathbf{k}'\beta - \mathbf{k}'\beta' \rangle u_{\mathbf{k}'} v_{\mathbf{k}'}, \quad (2.18)$$

and $E(\mathbf{k}) = \sqrt{\xi^2(\mathbf{k}) + \frac{1}{2} \text{tr} [\Delta(\mathbf{k}) \Delta^\dagger(\mathbf{k})]}$ is the excitation energy of a quasiparticle, where tr denotes the trace in spin space.

CONTRIBUTIONS BEYOND THE BCS APPROXIMATION

The BCS approximation is not exact. There are important contributions originating from in-medium effects. The full pairing interaction V_{pairing} consists in addition to the standard nuclear interaction V_{NN} , which is used in the BCS approximation, of induced interactions V_{induced} [219, 220]. This induced interaction corresponds to a process where one fermion polarises the medium and a second fermion is influenced by this polarisation. The resulting interaction is analogous to the phonon-induced attraction causing the pairing of electrons in metallic superconductors. In Ref. [219] this effect was studied in a dilute Fermi gas of spin-1/2 particles. In this limit the BCS gap function in the 1S_0 channel takes the form

$$\Delta^{\text{BCS}}(k_F) = \frac{8\varepsilon_F}{e^2} \exp\left(\frac{\pi}{2k_F a_S}\right), \quad (2.19)$$

where a_S is the S-wave scattering length. In Ref. [219] was found that the inclusion of induced interactions reduces the gap

$$\Delta(k_F) = (4e)^{-\frac{1}{3}} \Delta^{\text{BCS}}(k_F), \quad (2.20)$$

corresponding to a numerical factor of ~ 2.2 . This indicates that the contribution of effects beyond the BCS approximation is substantial and should be investigated. The inclusion of these effects at higher densities is, however, a non-trivial problem. A step into that direction was taken, *e.g.*, recently

in Ref. [221] within the framework of the self-consistent Green's function method and Fermi liquid theory.

In this project we limit ourselves to the BCS approximation with a focus on the effects of different interactions and appropriate uncertainty estimates.

PARTIAL-WAVE DECOMPOSITION

The solution of Eq. (2.17) in partial waves requires a decomposition. Following, *e.g.*, Refs. [222–224], one decomposes the gap matrix

$$\Delta_{aa'}(\mathbf{k}) = \sum_{l,S,J,M} \sqrt{\frac{8\pi}{2J+1}} \Delta_{lS}^{JM}(k) [G_{lS}^{JM}(\hat{\mathbf{k}})]_{aa'}, \quad (2.21)$$

and the potential

$$\langle \mathbf{k}a - \mathbf{k}a' | V | \mathbf{k}'\beta - \mathbf{k}'\beta' \rangle = (4\pi)^2 \sum_{l,l',S,J,M} i^{l'-l} [G_{lS}^{JM}(\hat{\mathbf{k}})]_{aa'} [G_{l'S}^{JM}(\hat{\mathbf{k}}')]_{\beta\beta'}^* V_{l'S}^{J(M)}(k, k'), \quad (2.22)$$

in terms of the coefficients

$$[G_{lS}^{JM}(\hat{\mathbf{k}})]_{aa'} = \sum_{m,m_S} C_{1/2 a 1/2 a'}^{S m_S} C_{l m S m_S}^{JM} Y_l^m(\hat{\mathbf{k}}), \quad (2.23)$$

where $\Delta_{lS}^{JM}(k)$ and $V_{l'S}^{J(M)}(k, k')$ denote the gap and potential in partial waves, respectively. Note that the factor $\sqrt{8\pi/(2J+1)}$ in Eq. (2.21) is kept for simplifications later on. Inserting the expression for the gap (2.21) and the potential (2.22) in the gap equation (2.17) reads

$$\begin{aligned} \sum_{l,S,J,M} \frac{\Delta_{lS}^{JM}(k)}{\sqrt{2J+1}} [G_{lS}^{JM}(\hat{\mathbf{k}})]_{aa'} &= -(4\pi)^2 \int \frac{dk' k'^2}{(2\pi)^3} \sum_{\substack{l,l',J,M,S \\ l',J',M',S'}} i^{l'-l} [G_{lS}^{JM}(\hat{\mathbf{k}})]_{aa'} \\ &\times V_{l'S}^{J(M)}(k, k') \frac{\Delta_{l'S'}^{J'M'}(k')}{\sqrt{2J'+1}} \\ &\times \int d\hat{\mathbf{k}}' \frac{\sum_{\beta,\beta'} [G_{l'S}^{JM}(\hat{\mathbf{k}}')]_{\beta\beta'}^* [G_{l'S'}^{J'M'}(\hat{\mathbf{k}}')]_{\beta\beta'}}{2\sqrt{\xi^2(k') + \frac{1}{2}\text{tr}[\Delta(\mathbf{k}')\Delta^\dagger(\mathbf{k}')]} }. \end{aligned} \quad (2.24)$$

The angular integration is tedious because the denominator is angle dependent. By angle-averaging the denominator one can simplify the expression above tremendously:

$$\left\langle \frac{1}{2} \text{tr} [\Delta(\mathbf{k})\Delta^\dagger(\mathbf{k})] \right\rangle_{\hat{\mathbf{k}}} = \frac{1}{2} \int \frac{d\hat{\mathbf{k}}}{4\pi} \text{tr} [\Delta(\mathbf{k})\Delta^\dagger(\mathbf{k})] = \sum_{l,S,J} |\Delta_{lS}^J(k)|^2 \equiv D^2(k), \quad (2.25)$$

where we summed over all M states. The angular integration in the numerator can then be carried out explicitly, which we also used in the last step of the previous equation,

$$\int d\hat{\mathbf{k}} \sum_{\beta, \beta'} [G_{\nu S}^{JM}(\hat{\mathbf{k}}')]^*_{\beta\beta'} [G_{\nu' S'}^{J'M'}(\hat{\mathbf{k}}')]_{\beta\beta'} = \delta_{l, l'} \delta_{M, M'} \delta_{J, J'} \delta_{S, S'} . \quad (2.26)$$

Note that due to the choice of normalisation in Eq. (2.25) no additional pre-factor occurs. Multiplying Eq. (2.24) with $[G_{\nu S}^{JM}(\hat{\mathbf{k}})]_{aa'}$, and integrating over $\hat{\mathbf{k}}$ leads to the gap equation in partial-wave decomposition

$$\Delta_{\nu S}^J(k) = - \int_0^\infty \frac{dk' k'^2}{\pi} \sum_{l'} \frac{i^{l'-l} V_{\nu S}^J(k, k') \Delta_{\nu S}^J(k')}{\sqrt{\xi^2(k') + \sum_{\tilde{l}, \tilde{S}, \tilde{J}} |\Delta_{\tilde{l} \tilde{S}}^{\tilde{J}}(k')|^2}} , \quad (2.27)$$

with $l' = l$ for the spin singlet and $l' = l, |l \pm 2|$ for the coupled triplet states. Note that the solution of the gap in one channel is in general coupled to any other channel due to the sum over all gaps in the denominator. However, we assume that pairing in the given channel minimises the energy such that other gaps can appear only in different density regions and solve the gap equation for fixed spin and total angular momentum. This approach, including the angle averaging in Eq. (2.25), is taken in most other calculations, including the recent works in Refs. [225, 226]. For simplicity we drop the indices S and J and denote the components of the gap by Δ_l . The total gap function is given by $\Delta(k) = \sqrt{\sum_l \Delta_l^2(k)}$ and evaluated at the Fermi surface.

2.3.2 SOLVING THE GAP EQUATION

Since the gap equation (2.27) is a set of non-linear coupled equations one has to solve it with an iterative algorithm until a self-consistent solution is obtained. In previous attempts to solve the gap equation, in particular in the triplet channel, it was found that a simple algorithm which uses the bare output of a previous iteration as input for the next iterative step fails [227]. Such an algorithm for the m -th iteration,

$$\mathbf{\Delta}_{\text{out}}^{(m)} = I[\mathbf{\Delta}_{\text{in}}^{(m)}] , \quad \text{with} \quad \mathbf{\Delta}_{\text{in}}^{(m+1)} = \mathbf{\Delta}_{\text{out}}^{(m)} , \quad (2.28)$$

where $I[\cdot]$ is the update instruction, *i.e.*, the right-hand side of Eq. (2.27), tends to terminate at the (mathematically also valid) trivial solution $\Delta = 0$, especially if the nontrivial solution is small. As the gap is a function of the momentum, any numerical approach requires a discretisation. In practice we use a Gauß mesh with N_p points and construct a gap vector $\mathbf{\Delta}$ with components $\Delta_l(k_n)$, where $l = 1, 3$ for the triplet and $l = 0$ for the singlet case and $n = 1, \dots, N_p$. This mesh has to be chosen carefully because of the structure of the integrand in Eq. (2.27). If the total gap is small this integrand peaks around the Fermi surface resulting in a quasi-singularity. We use a combination of multiple in-

tegration meshes, concentrated around the peak position. This peak makes the solution also very sensitive to variations of $\Delta(k_F)$, leading to the convergence problems of the naïve self-consistent solution algorithm, discussed above.

These convergence issues have been studied extensively in the past and methods avoiding these have been developed. Khodel *et al.* [224] quasi-linearised the problem, Krotscheck [228] applied a full linearisation. Another approach is the instability analysis based on in-medium Weinberg eigenvalues [226, 229, 230], which is, however, only approximative. In the next Section we revise the basic concepts of ‘Khodel’s method’ and compare it to a new method which solves the problem by direct iteration with a modification of the iterative algorithm of Broyden [231], which is straightforward to implement.

At this point we briefly want to specify the above-mentioned term ‘convergence’, since it is central in the numerical algorithms discussed. An iterative algorithm is stable if the norm of the difference,

$$\mathbf{F}^{(m)} = \mathbf{\Delta}_{\text{out}}^{(m)} - \mathbf{\Delta}_{\text{in}}^{(m)}, \quad (2.29)$$

decreases. Here $\mathbf{\Delta}_{\text{out}}^{(m)}$ is the output in the m -th step where $\mathbf{\Delta}_{\text{in}}^{(m)}$ was used as input. Final convergence is achieved if $|\mathbf{F}^{(m)}| = 0$ although in practice a small finite threshold is used. After achieving convergence we check the condition by 5 to 10 additional iterative steps.

KHODEL’S METHOD

We first want to review Khodel’s method [224, 232], which is widely used to improve the convergence significantly. It is based on a reformulation of the gap equation (2.27) which avoids its quasi-singularity. One writes the potential $V_{ll'}(k, k')$ in a separable part,

$$\varphi_{ll'}(k) = \frac{V_{ll'}(k, k_F)}{v_{ll'}}, \quad \varphi_{ll'}^T(k') = \frac{V_{ll'}(k_F, k')}{v_{ll'}}, \quad (2.30)$$

where the definition $v_{ll'} \equiv V_{ll'}(k_F, k_F) \neq 0$ normalises $\varphi_{ll'}(k_F) = \varphi_{ll'}^T(k_F) \equiv 1$, and a remainder

$$W_{ll'}(k, k') \equiv V_{ll'}(k, k') - v_{ll'} \varphi_{ll'}(k) \varphi_{ll'}^T(k'), \quad (2.31)$$

which vanishes when at least one argument is at the Fermi surface. This property is key to remove the peak. By inserting $W_{ll'}(k, k')$ into the gap equation (2.27) we obtain

$$\Delta_l(k) + \sum_{l'} i^{l'-l} \int \frac{dk' k'^2}{\pi} W_{ll'}(k, k') \frac{\Delta_{l'}(k')}{\sqrt{\xi^2(k') + \Delta^2(k')}} = \sum_{l'} D_{ll'} \varphi_{ll'}(k), \quad (2.32)$$

where the coefficients are defined as

$$D_{l'l} = -i^{l'-l} v_{l'l} \int \frac{dk k^2}{\pi} \frac{\varphi_{l'l}^T(k) \Delta_{l'}(k)}{\sqrt{\xi^2(k) + \Delta^2(k)}}. \quad (2.33)$$

With that, the partial gaps Δ_l in Eq. (2.32) can be represented as linear combinations of shape functions $\chi_l^{l_1 l_2}(k)$

$$\Delta_l(k) = \sum_{l_1, l_2} D_{l_1 l_2} \chi_l^{l_1 l_2}(k), \quad (2.34)$$

which finally leads to an equation for the momentum dependence of the partial gaps

$$\chi_l^{l_1 l_2}(k) + \sum_{l'} i^{l'-l} \int \frac{dk' k'^2}{\pi} W_{l'l}(k, k') \frac{\chi_{l'}^{l_1 l_2}(k')}{\sqrt{\xi^2(k') + \Delta^2(k')}} = \delta_{l_1} \varphi_{l_1 l_2}(k). \quad (2.35)$$

This equation can be assumed as (quasi-)linear by, e.g., holding $\Delta(k)$ constant. The reason for that is the construction of $W_{l'l}$. As it vanishes if either argument is at the Fermi surface, the integral is mainly determined in momentum regions where $\xi^2(k)$ dominates $\Delta^2(k)$. Thus, the solution of the shape functions only weakly depends on $\Delta(k)$, motivating the approximation by a constant. With that, the iterative convergence is accelerated and it is almost independent of the magnitude of the gap.

The solution algorithm consists of three steps [224]: As initial condition we set $\Delta(k)$ to a small constant value, e.g., 1 keV. (i) With the gap vector from the previous iteration we solve Eq. (2.35) for the shape functions $\chi_l^{l_1 l_2}(k)$ using the method of matrix inversion. (ii) The coefficients $D_{l'l}$ are then calculated with Eqs. (2.33) and (2.34) using a non-linear solver, in particular the Newton-Raphson method. (iii) In the last step the partial gaps $\Delta_l(k)$ are updated with the new $D_{l'l}$ and $\chi_l^{l_1 l_2}(k)$ according to Eq. (2.34). Note that, since $\chi_l^{l_1 l_2}(k_F) = \delta_{l_1}$ for all l_2 , the gap at the Fermi momentum is just $\Delta_l(k_F) = \sum_{l_2} D_{l_2 l}$. These steps are repeated until we reach convergence as discussed earlier.

MODIFIED DIRECT-ITERATION METHOD

As confirmation and alternative we solve the gap equation with a new direct-iteration method based on a modified version [231] of Broyden's method for general non-linear equations, developed in Ref. [233]. This method to solve the gap equation was mainly derived by Christian Drischler and we briefly want to discuss it here. It uses as input for in the m -th iteration step not only the result obtained in the previous step but rather all other previous solutions, weighted appropriately. It is widely used in quantum chemistry and was introduced to nuclear physics in Ref. [234].

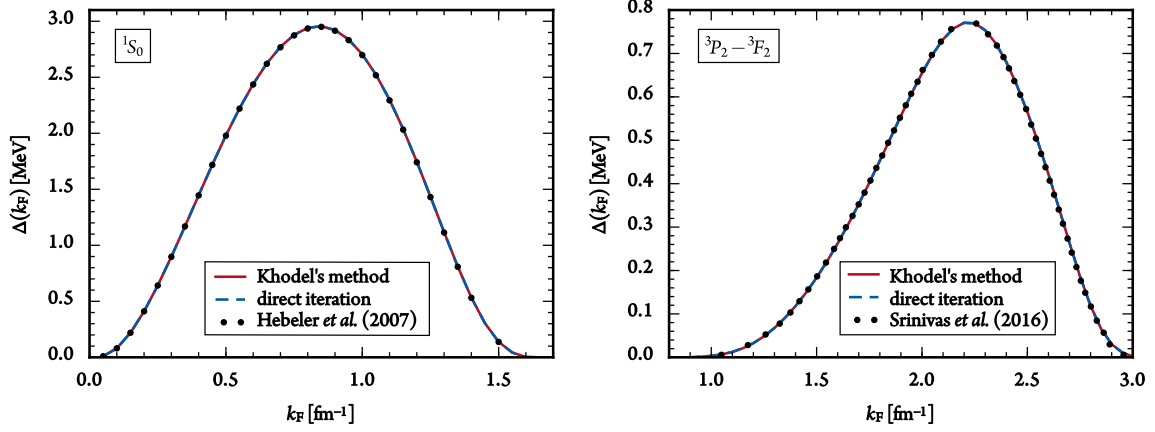


Figure 2.10: Comparison of the energy gaps in the 1S_0 (left) and $^3P_2 - ^3F_2$ (right panel) channel obtained using Khodel's (red) and via the modified direct-iteration method (blue dashed) with the $N^3\text{LO}$ NN potential EM 500 MeV. As reference we also show results (black dots) from Refs. [226, 235] obtained with Khodel's method. Both algorithms are in excellent agreement with each other (with differences on the ~ 10 eV level) and the reference calculations.

The update procedure for the gap vector after the m -th iteration is as follows

$$\Delta_{\text{in}}^{(m+1)} = \Delta_{\text{in}}^{(m)} + a\mathbf{F}^{(m)} - \sum_{n=1}^{m-1} w_n \gamma_{mn} \mathbf{u}^{(n)}, \quad (2.36)$$

where

$$\gamma_{mn} = \sum_{k=1}^{m-1} c_{km} \beta_{kn}, \quad \beta_{kn} = (Iw_0^2 + a)_{kn}^{-1}, \quad (2.37)$$

$$c_{km} = w_k \delta \mathbf{F}^{(k)\dagger} \mathbf{F}^{(m)}, \quad a_{kn} = w_k w_n \delta \mathbf{F}^{(n)\dagger} \delta \mathbf{F}^{(k)}. \quad (2.38)$$

Here, I denotes the identity matrix and

$$\mathbf{u}^{(n)} = a \delta \mathbf{F}^{(n)} + \delta \Delta^{(n)}, \quad \delta \Delta^{(n)} = \frac{\Delta_{\text{in}}^{(n+1)} - \Delta_{\text{in}}^{(n)}}{|\mathbf{F}^{(n+1)} - \mathbf{F}^{(n)}|}, \quad \delta \mathbf{F}^{(n)} = \frac{\mathbf{F}^{(n+1)} - \mathbf{F}^{(n)}}{|\mathbf{F}^{(n+1)} - \mathbf{F}^{(n)}|}, \quad (2.39)$$

where $\delta \mathbf{F}^{(n)\dagger} \delta \mathbf{F}^{(n)} = 1$ is normalised. In the m -th iteration step one has to store $\Delta_{\text{in}}^{(m)}$ and $\mathbf{F}^{(m)}$ as well as all $\mathbf{u}^{(m)}$ and $\delta \mathbf{F}^{(m)}$ of the previous iterations. For efficiency one should also store the $(m-1)$ -by- $(m-1)$ matrix with the entries a_{kn} . Note that this update procedure (2.36) includes simple mixing, however, the additional term favours accelerated convergence since it allows larger damping factors. In the first step one needs to guess $\Delta_{\text{in}}^{(1)}$, a , and the weights w_m . While $w_0 = 0.01$ should be small [231] we use $w_{(m-1)} = 1$ in the higher iterations similar to Ref. [234].

In Fig. 2.10 we show a benchmark calculation for the two solution algorithms discussed above. We in-

independently calculate the 1S_0 and $^3P_2-^3F_2$ gaps with both algorithms using the chiral N³LO nucleon-nucleon potential EM 500 MeV [145, 146]. Both methods are in excellent agreement, with deviations only on the 10 eV level. We also find a very good agreement with previous calculations using Khodel’s method by Hebeler *et al.* [235] in the singlet case and in the triplet channel with Srinivas *et al.* [226], especially in the computationally-involved region where the gap closes.

From these benchmark calculations we can conclude that both methods are competitive. All the following calculations have been done with both methods and we briefly want to revise their distinctive features: The modified direct-iteration method is straightforward to implement and does not require approximations like linearisation. Its computational runtime per iteration is faster but needs typically 2 – 3 times more steps than Khodel’s method. In rare cases the modified direct-iteration method leads to apparent discontinuities in the gap function. However, those could be recovered by fine tuning the damping factors α . Khodel’s method, on the other hand, is by construction unstable if $V_{ll'}(k, k)$ is close to zero. This could be avoided by using a modified version, discussed in Ref. [232].

2.3.3 CALCULATIONAL DETAILS: NN POTENTIALS, 3N FORCES, UNCERTAINTY ESTIMATES

We calculate the pairing gap in neutron matter in the spin singlet 1S_0 and triplet $^3P_2 - ^3F_2$, which are the relevant channels for pairing in neutron stars, as discussed in Section 1.2. For our calculations we use all three different kinds of chiral NN forces mentioned in Section 1.4: Local (up to N²LO) [150, 151], semi-local (up to N⁴LO) [144], and non-local (at N³LO) [145–148] interactions. We also study the influence of leading (N²LO) and sub-leading (N³LO) three-body forces on the gap equation. However, so far the inclusion 3N forces in a (semi-)locally regularised scheme is not feasible since the corresponding matrix elements have not been fully calculated, yet, but they will be available in the near future. We thus restrict ourselves for the inclusion of 3N forces to the traditional non-local interactions, which were also used in our calculations of polarised neutron matter (see previous Section). None of the interactions are evolved with renormalisation-group techniques.

INCLUSION OF 3N FORCES

The gap equation and its solution discussed above is formulated for two-body interactions only. We thus include 3N forces as normal-ordered, density dependent NN interactions, which also allows us to include correlations. Normal ordering with respect to a reference state is a widely used technique in nuclear physics [139, 141, 159, 167, 236, 237]. One particle is summed over all occupied states for the Fermi surface at zero temperature [13, 236], *i.e.*,

$$\bar{V}_{3N}^{\text{as}} = \text{tr}_{\sigma_3} \int \frac{d^3k_3}{(2\pi)^3} \mathcal{A}_{123} V_{3N} \theta_{\mathbf{k}_3} \Big|_{\text{nnn}}, \quad (2.40)$$

with the theta function $\theta_{\mathbf{k}} = \theta(k_F - |\mathbf{k}|)$ and the Fermi momentum k_F . The initial anti-symmetrised 3N forces $\mathcal{A}_{123}V_{3N}$ are regularised with the non-local regulator of Eq. (2.7).

In previous calculations of the energy gap [139, 225, 226, 238] the effects of 3N forces have already been studied. However, those calculations were limited to the leading (N^2 LO) 3N forces since the normal ordering was done on the operatorial level, which is not feasible for the sub-leading 3N forces with their rich structure. In our calculations we make use of recent developments, mainly by Kai Hebeler and Christian Drischler [141, 239] and evaluate the effective NN potentials (2.40) based on the partial-wave-decomposed matrix elements of the 3N forces rather than their analytic operator structure. With this method the only limiting factor is the availability of the partial-wave-decomposed 3N matrix elements, currently only for the non-local chiral interactions up to N^3 LO [239]. Note that these matrix elements are truncated at two- and three-body momenta of $J = 6$ and $\mathcal{J} = 9/2$, respectively, which was shown to be sufficient for nucleonic-matter calculations [141, 239]. The effective NN potential (2.40) depends in general on the total momentum \mathbf{P} of the two remaining particles in contrast to a Galilean-invariant NN interaction. In the BCS limit, however, the particles are assumed to be back-to-back at the Fermi surface and consequently $\mathbf{P} = 0$. For details of the normal-ordering process and the 3N matrix elements see Refs. [141, 159, 239].

The total interaction used in our calculations writes

$$V_{\text{NN}+3\text{N}}^{\text{as}} = V_{\text{NN}}^{\text{as}} + \zeta \bar{V}_{3\text{N}}^{\text{as}}, \quad (2.41)$$

where ζ is a combinatorial or symmetry factor depending on the type of quantity of interest [139]. For the solution of the gap equation we have $\zeta = 1$, similar to nuclear-matter calculations beyond the Hartree-Fock approximation. Note that this is consistent with Refs. [139, 226] and we discuss the derivation below.

SINGLE-PARTICLE SPECTRUM

The energy denominator of the gap equation (2.27) depends on the single-particle spectrum $\varepsilon(k)$. In our calculations of the gap we use both, a free spectrum and also take into account self-energy corrections caused by the interaction by employing a Hartree-Fock spectrum

$$\varepsilon(k) = \frac{k^2}{2m} + \Sigma^{(1)}(k), \quad (2.42)$$

where $\Sigma^{(1)}(k)$ is the spin-averaged self-energy at first order [139],

$$\Sigma^{(1)}(k_1) = \frac{1}{2\pi} \int dk_2 k_2^2 d \cos \theta_{\mathbf{k}_1, \mathbf{k}_2} n_{\mathbf{k}_2} \sum_{l, S, J} (2J+1) \langle k_{12}/2 | V_{llS}^J | k_{12}/2 \rangle [1 - (-1)^{l+S+1}], \quad (2.43)$$

with $k_{12} = |\mathbf{k}_1 - \mathbf{k}_2|$. Note that the combinatorial factor used to evaluate Eq. (2.43), $\zeta = 1/2$, also agrees with Refs. [139, 141, 226].

The effective neutron mass m^* at the Fermi surface is a measure of how the interaction affects the single-particle energy. It is given by

$$\frac{m^*(k_F)}{m} = \left(\frac{m}{k} \frac{d\varepsilon(k)}{dk} \right)^{-1} \Big|_{k=k_F}. \quad (2.44)$$

Our calculations of the effective masses are based on the Hartree-Fock energies. In Ref. [139] it was found that including contributions beyond the Hartree-Fock level gives higher effective masses $m^*/m > 1$ in density regions below and around nuclear saturation density. Effective masses $m^*/m < 1$ lead to a suppression of the energy gap while larger $m^*/m > 1$ cause an amplification as can be seen in the results section.

NORMAL-ORDERING SYMMETRY FACTORS

We briefly discuss how one obtains the symmetry factors for the energy gap Δ and self energy Σ . Consider a Hamiltonian of the form

$$\hat{H} = \hat{T} + \hat{V}_{\text{NN}} + \hat{V}_{\text{3N}}, \quad (2.45)$$

with kinetic energy \hat{T} and NN/3N interaction $\hat{V}_{\text{NN}/\text{3N}}$. With the help of Wick's theorem one can rewrite the Hamiltonian in an equivalent form by normal-ordering all operators with respect to a given reference state. For our pairing calculations it is convenient to choose the BCS state as reference. We can rewrite the interactions in terms of anti-symmetrised matrix elements,

$$\hat{V}_{\text{NN}} = \frac{1}{4} \sum_{i,j,k,l} \langle ij | V_{\text{NN}}^{\text{as}} | kl \rangle \hat{a}_i^\dagger \hat{a}_j^\dagger \hat{a}_k \hat{a}_l, \quad (2.46)$$

$$\hat{V}_{\text{3N}} = \frac{1}{36} \sum_{i,j,k,l,m,n} \langle ijk | V_{\text{3N}}^{\text{as}} | lmn \rangle \hat{a}_i^\dagger \hat{a}_j^\dagger \hat{a}_k^\dagger \hat{a}_l \hat{a}_m \hat{a}_n, \quad (2.47)$$

where the summation indices collect the single-particle quantum numbers. It is worth noticing that, applying Wick's theorem with respect to a BCS reference state, both normal contractions (connecting a creation operator with an annihilation operator) and anomalous contractions (connecting two creation or two annihilation operators) contribute. For the normal self energy Σ the relevant con-

tractions are of the form

$$\frac{1}{4} \sum_{i,j,k,l} \langle ij | V_{\text{NN}}^{\text{as}} | kl \rangle \widehat{a}_i^\dagger \widehat{a}_j^\dagger \widehat{a}_l \widehat{a}_k, \quad (2.48)$$

$$\frac{1}{36} \sum_{i,j,k,l,m,n} \langle ijk | V_{\text{3N}}^{\text{as}} | lmn \rangle \widehat{a}_i^\dagger \widehat{a}_j^\dagger \widehat{a}_k^\dagger \widehat{a}_n \widehat{a}_m \widehat{a}_l, \quad (2.49)$$

while for the energy gap Δ the relevant contractions take the form

$$\frac{1}{4} \sum_{i,j,k,l} \langle ij | V_{\text{NN}}^{\text{as}} | kl \rangle \widehat{a}_i^\dagger \widehat{a}_j^\dagger \widehat{a}_l \widehat{a}_k, \quad (2.50)$$

$$\frac{1}{36} \sum_{i,j,k,l,m,n} \langle ijk | V_{\text{3N}}^{\text{as}} | lmn \rangle \widehat{a}_i^\dagger \widehat{a}_j^\dagger \widehat{a}_k^\dagger \widehat{a}_n \widehat{a}_m \widehat{a}_l. \quad (2.51)$$

Since the interaction operators are represented in terms of anti-symmetrised matrix elements all different possible choices of picking creation or annihilation operators are equivalent and just lead to combinatoric factors. In order to determine ζ it is thus necessary to determine the number of different contractions c_N for Eqs. (2.48) to (2.51). We obtain: $c_N = 4$ for Eq. (2.48), $c_N = 18$ for Eq. (2.49), $c_N = 1$ for Eq. (2.50) and $c_N = 9$ for Eq. (2.51). Combining these combinatoric factors with the pre-factors $1/4$ and $1/36$ of the NN and 3N interactions we directly obtain $\zeta = 1/2$ for the self energy Σ and $\zeta = 1$ for gap Δ . We also note that in the present work we approximate the normal contractions in Eq. (2.51) by their contributions in normal systems. It has been shown in Ref. [167] that the inclusion of correlations in the reference state has only very small effects on the matrix elements of the normal ordered 3N interactions for nuclear-matter calculations. In addition to contributions from normal contractions in Eq. (2.51) we also obtain non-vanishing contributions from multiple anomalous contractions. However, these contributions are small since such terms only include contributions from momenta around the Fermi surface.

UNCERTAINTY ESTIMATES

In our calculations for neutron matter based on the traditional non-local chiral interactions (see Fig. 2.1) we used on the NN level a variation of the cutoff in the regulator as an uncertainty estimate, *i.e.*, using different NN potentials at the same order. With the development of the semi-local interactions a new uncertainty estimate has been suggested [131, 144].

This estimation is directly based on the principles of chiral effective field theory: The expansion in powers of a low momentum scale, the relevant energy scale Q or pion mass m_π , over a high momentum scale, the cutoff Λ . One naïvely expects a reduction of the uncertainty by a factor of $Q \approx m_\pi/\Lambda$ when going to the next order of the chiral expansion. The uncertainty is defined as the dif-

ference of the observable calculated at a specific order and at the previous order, multiplied with an appropriate power of Q . In our calculations of the energy gap these differences at chiral order ν read

$$d\Delta^{(\nu)} = \begin{cases} \Delta^{(0)} & \text{for } \nu = 0, \\ \Delta^{(2)} - \Delta^{(0)} & \text{for } \nu = 2, \text{ and} \\ \Delta^{(\nu)} - \Delta^{(\nu-1)} & \text{for } \nu \geq 3. \end{cases} \quad (2.52)$$

These are weighted with $Q^\nu(k_F)$, $\nu = 0, 2, 3, \dots$, where

$$Q(k_F) = \max\left(\frac{k_F}{\Lambda}, \frac{m_\pi}{\Lambda}\right), \quad (2.53)$$

with typical momentum cutoff scale

$$\Lambda = \begin{cases} 600 \text{ MeV} & \text{for } R_0 = 0.8, 0.9, 1.0 \text{ fm}, \\ 500 \text{ MeV} & \text{for } R_0 = 1.1 \text{ fm}, \text{ and} \\ 400 \text{ MeV} & \text{for } R_0 = 1.2 \text{ fm}, \end{cases} \quad (2.54)$$

which correlates with the local cutoff in the regulator of the NN forces. According to Refs. [131, 144], the theoretical uncertainty originating from the chiral expansion for the total gap at chiral order ν is given by

$$\delta\Delta^{(\nu)} = \begin{cases} 0 & \text{for } \nu = 0, 2, \text{ and} \\ \max_{3 \leq n \leq \nu} (Q^{\nu+1-n} |d\Delta^{(n)}|) & \text{for } \nu \geq 3. \end{cases} \quad (2.55)$$

Note that this is a modified estimation relative to Refs. [131, 144, 240]: We neglect LO contributions ($\nu = 0$) to the higher-order uncertainties ($\nu \geq 2$). Typically, LO potentials do not reproduce scattering phase shifts [131, 144] well, particularly not in the coupled ${}^3P_2 - {}^3F_2$ channel which is solely represented by the long-range one-pion exchange. Thus, the uncertainty estimation would be dominated by $d\Delta^{(0)}$ and would lose its predictive power. Hence, we neglect this term.

In Refs. [131, 144, 240] an additional term which assures that the next order always lies within the uncertainty band of the previous order was introduced. We also do not account for this term since it makes the uncertainty estimate more unnatural and less predictive. The reader can easily extend the provided uncertainty bands to all higher orders.

Note that this estimation of the chiral uncertainty is in principle only valid for a calculation which includes also many-nucleon forces. For inconsistent calculations with NN forces only this estimation could unnaturally increase the uncertainty band [240]. We do not find such effects.

In our calculations with 3N forces using the traditional non-local interactions we cannot use this uncertainty estimate due to the lack of potentials with consistent cutoffs at all previous orders. How-

ever, we account for uncertainties in the 3N forces by varying the 3N couplings c_1 , c_3 and cutoff $\Lambda_{3N} = (2.0 - 2.5) \text{ fm}^{-1}$ as well as the single-particle spectrum with NN and corresponding effective NN forces. Similarly to our previous matter calculations we use the recommended c_i values of Ref. [132], and take for calculations with N²LO 3N forces the ranges $c_1 = -(0.37 - 0.73) \text{ GeV}^{-1}$, $c_3 = -(2.71 - 3.38) \text{ GeV}^{-1}$ and with N³LO 3N forces $c_1 = -(0.75 - 1.13) \text{ GeV}^{-1}$, $c_3 = -(4.77 - 5.51) \text{ GeV}^{-1}$. The N³LO 3N contributions shift c_1 , c_3 and depend additionally on the LO NN low-energy constants which we consider consistently to the NN potentials. We quote their values in Appendix A.

2.3.4 RESULTS AND DISCUSSIONS

THE PAIRING GAP IN THE SINGLET 1S_0 CHANNEL

In Fig. 2.11 we show the results for the pairing gap as a function of the Fermi momentum in the spin singlet 1S_0 for the local chiral interactions with cutoffs $R_0 = 0.9, 1.0, 1.1, \text{ and } 1.2 \text{ fm}$ from row 1 to 4, respectively. The calculations at LO (blue), NLO (green), and N²LO (orange) are depicted with solid lines. We attach uncertainty estimates to the N²LO result as discussed above, depicted with a semi-transparent band limited by dashed lines. In the NLO and N²LO potential the spectral-function was regularised with a cutoff $\tilde{\Lambda} = 1000 \text{ MeV}$. In the first column we present results obtained with a free spectrum while in the second column a Hartree-Fock spectrum was used. In the last column we also show the calculation for the effective mass (2.44) corresponding to the Hartree-Fock spectrum. Note that we do not present calculations for the cutoff $R_0 = 0.8 \text{ fm}$, corresponding to the highest momentum-space cutoff, since there does not exist such a NLO potential and also at N²LO there seem to be deficiencies leading to a finite energy gap at $k_F = 0$ in the 1S_0 channel.

We find that the NLO and N²LO potentials agree up to momenta $k_F \approx (0.6 - 0.8) \text{ fm}^{-1}$ depending slightly on the regulator, while the best agreement is found for the highest cutoff. This agreement was also expected since the pairing gap is mainly determined by the phase shifts at low momenta. In Eq. (2.19) it was shown that the gap depends only on the S-wave scattering length, which is determined by the phase shifts. Both potentials describe the phase shifts appropriately well in the low-energy regions, while there are deficiencies at leading order [151]. This obviously motivates our modification to the error estimate, which does not take the LO results into account.

Using a Hartree-Fock spectrum weakly suppresses the energy gap due to the small effective masses $m^*/m < 1$. This is not the case for the LO potentials with cutoffs $R_0 \geq 1.1 \text{ fm}$, where the effective masses are large at high momenta. At N²LO we find the gap's maximum at $k_F \approx (0.8 - 0.9) \text{ fm}^{-1}$ with $\Delta \approx (3.05 - 3.15) \text{ MeV}$ and $\Delta \approx (2.65 - 2.85) \text{ MeV}$ for the free and Hartree-Fock spectrum, respectively, including the uncertainty estimates. Employing a free spectrum the pairing gap closure is found around $k_F = (1.6 - 1.7) \text{ fm}^{-1}$ where the lower bound corresponds to the lower cutoffs.

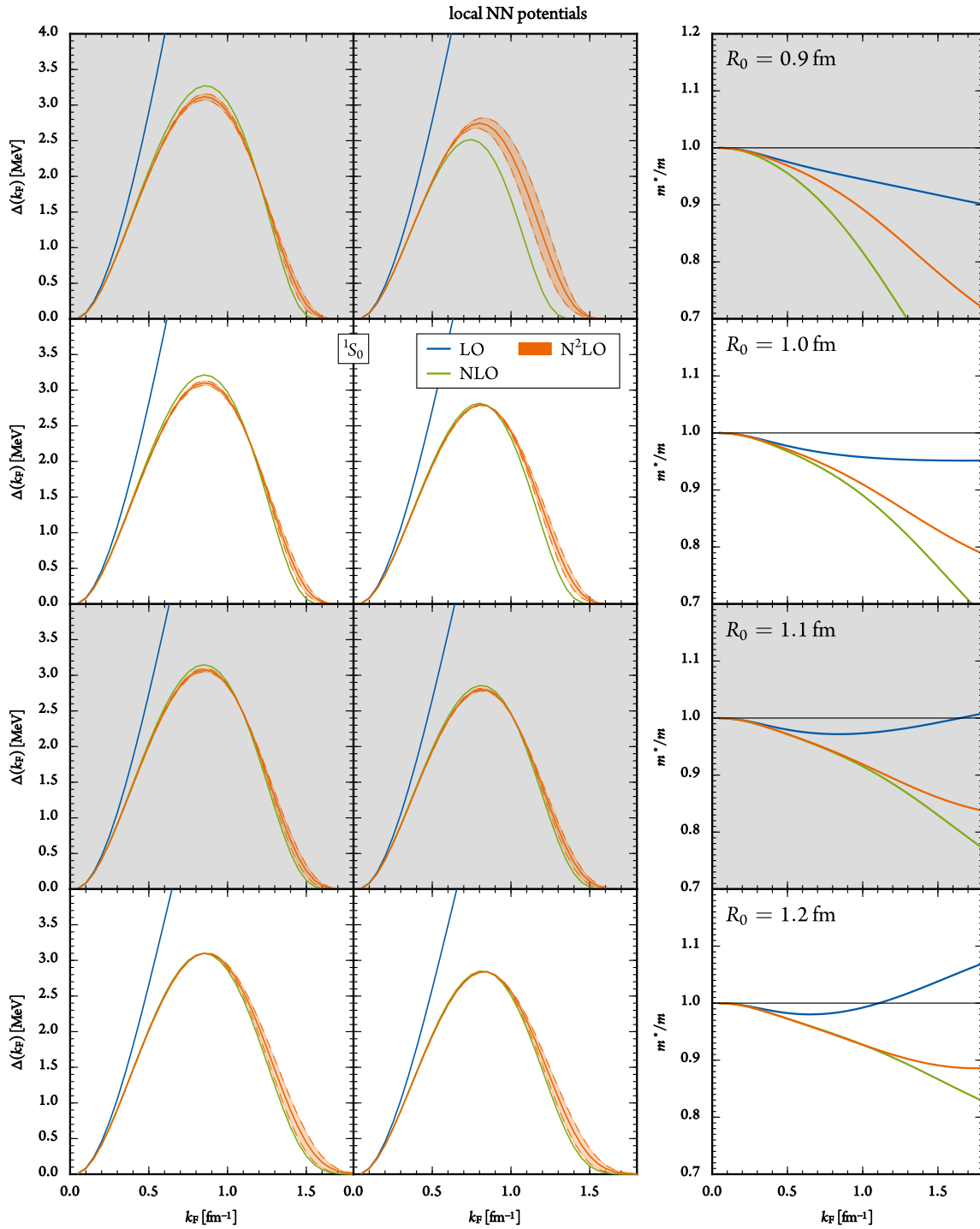


Figure 2.11: Energy gap in the 1S_0 channel for the local NN potentials with cutoffs $R_0 = (0.9-1.2)$ fm (rows) up to N²LO in a free (left) and in a Hartree-Fock spectrum (centre column). In the third column we show the effective masses at the Fermi surface corresponding to the Hartree-Fock spectrum. The uncertainty estimates discussed in the text are given by the coloured bands limited by dashed lines while the actual calculations are depicted by the solid lines. Note that we do not show uncertainties at LO and NLO.

Due to the suppression when using a Hartree-Fock spectrum the gap closes already at $k_F \approx 1.5 \text{ fm}^{-1}$ for the lower cutoffs but at similar values as with the free spectrum for $R_0 = 1.2 \text{ fm}$.

In Fig. 2.12 we again show results for the singlet 1S_0 gap but with semi-local interactions up to $N^4\text{LO}$. We use the same colour code as in Fig. 2.11 with the results at $N^3\text{LO}$ and $N^4\text{LO}$ in red and purple, respectively. As for $N^2\text{LO}$ we also attach uncertainty-estimate bands to the latter two. Again we do not show results for the potential with lowest cutoff $R_0 = 0.8 \text{ fm}$ since it is less perturbative.

As for the local interactions we find good agreement for the interactions at orders beyond NLO up to Fermi momenta around $k_F \approx 0.7 \text{ fm}^{-1}$. For the calculations at $N^3\text{LO}$ and $N^4\text{LO}$ we find very good agreement throughout the whole momentum range, except for maybe the smallest cutoff $R_0 = 0.9 \text{ fm}$, where we find a deviation of about 0.1 MeV at the maximum. This can also be explained by the excellent description of the phase shifts at these densities [131, 144]. Note that we show the uncertainty bands only in the physical region of positive gaps.

For the free spectrum we find maximum values $\Delta \approx (2.9 - 3.1) \text{ MeV}$ at $k_F \approx (0.80 - 0.85) \text{ fm}^{-1}$ for the $N^3\text{LO}/N^4\text{LO}$ potentials. The gap closure is found always around $k_F \approx 1.5 \text{ fm}^{-1}$ while the uncertainty estimate for $R_0 = 1.2 \text{ fm}$ suggests a range $k_F = (1.35 - 1.7) \text{ fm}^{-1}$. When using a Hartree-Fock spectrum we also find a small suppression of the gap with maximal values $\Delta \approx (2.80 - 2.95) \text{ MeV}$ around the same momenta as for the free spectrum. This suppression can also be seen in the effective masses which are always below 1 in these momentum ranges. For the gap closure we also find similar results with both the free and Hartree-Fock spectrum. It is worth noticing that the $N^4\text{LO}$ result lies for cutoffs $R_0 \geq 1.0 \text{ fm}$ always in the uncertainty band of the $N^3\text{LO}$ calculation, which thus could be interpreted as a reliable uncertainty estimate. Note however, that there are still deficiencies with the uncertainty estimation: The uncertainty band attached to the $N^2\text{LO}$ calculation is too narrow and when the calculations at different orders intersect at some point, *e.g.*, in the right flank of the calculation with the Hartree-Fock spectrum and $R_0 = 1.1 \text{ fm}$, the uncertainty estimate shrinks to zero.

When comparing the local and semi-local interactions we find very similar results for the free spectra but larger suppression effects in the local interactions when using a Hartree-Fock spectrum, which is also reflected by the smaller effective masses for the local interactions. However, one should keep in mind that the local interactions are only at $N^2\text{LO}$ while the semi-local forces are calculated up to $N^4\text{LO}$.

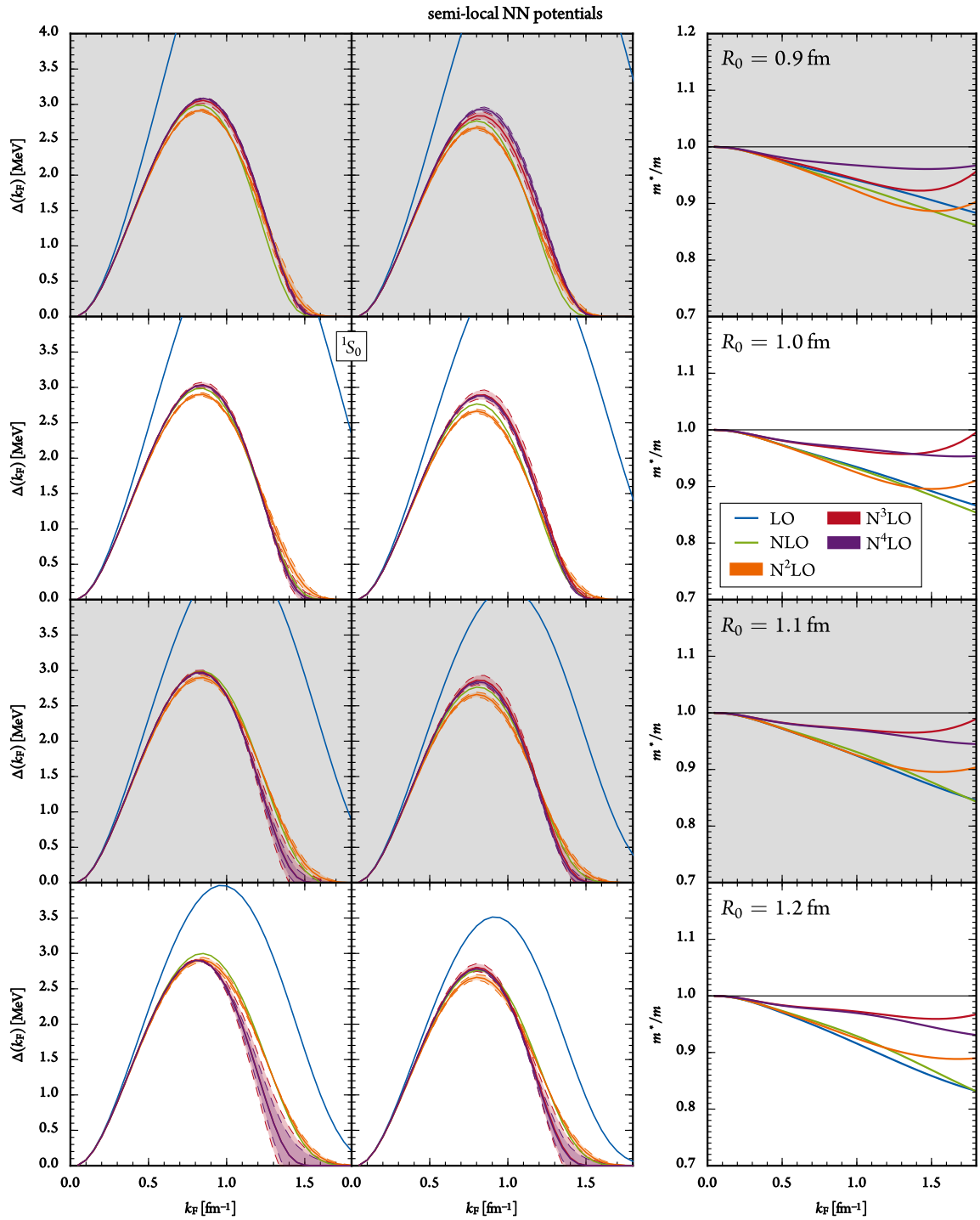


Figure 2.12: Energy gap in the 1S_0 channel for the semi-local NN potentials with cutoffs $R_0 = (0.9 - 1.2)$ fm (rows) up to N⁴LO in a free (left) and in a Hartree-Fock spectrum (centre column). In the third column we show the effective masses at the Fermi surface corresponding to the Hartree-Fock spectrum. The scheme is the same as in Fig. 2.11.

THE PAIRING GAP IN THE TRIPLET ${}^3P_2 - {}^3F_2$ CHANNEL

We show in Fig. 2.13 results for the pairing gap in the ${}^3P_2 - {}^3F_2$ channel using the same local interactions as for the singlet in Fig. 2.11. Note that the scale, however, is different and the pairing gaps in the triplet channels are much smaller.

For all cutoffs the energy gap opens at $k_F \approx 1.0 \text{ fm}^{-1}$, consistently predicted by the NLO and N²LO calculation. Note that at leading order the only contributions to the 3P_2 partial wave are from the regulator function and the long-range one-pion exchange interaction, which does not reproduce the 3P_2 phase shifts. Given the strong cutoff dependence of the LO calculations we attribute these effects mainly to the regulator.

With a free spectrum we find for the NLO and N²LO calculations similar predictions up to $k_F = (1.35 - 1.5) \text{ fm}^{-1}$ with larger ranges for the smaller cutoffs. At N²LO the maximal gap is reached at momenta $k_F \approx (1.85 - 2.0) \text{ fm}^{-1}$ and takes values $\Delta \approx (0.25 - 0.4) \text{ MeV}$ with uncertainty estimate range $\delta\Delta = (0.05 - 0.65) \text{ MeV}$. These values may not correspond to the actual physical maximum since at these high densities the chiral interactions lose their predictive power, which can also be seen by the strong cutoff dependence with much smaller values at the high coordinate-space cutoffs corresponding to low momentum-space values. Note that phase-shift equivalent potentials can be trusted only up to the Fermi momentum corresponding to the maximal laboratory energy at which the phase shifts are reproduced [227]. For usual fits up to 350 MeV this corresponds to $k_F \approx 2.1 \text{ fm}^{-1}$. The uncertainties in these density regimes are also reflected in the expansion parameter $Q(k_F)$, defined in Eq. (2.53). At $k_F = 2.0 \text{ fm}^{-1}$ it takes the values

$$Q(2.0 \text{ fm}^{-1}) = \begin{cases} 0.66 & \text{for } R_0 = 0.8, 0.9, 1.0 \text{ fm} , \\ 0.79 & \text{for } R_0 = 1.1 \text{ fm} , \text{ and} \\ 0.99 & \text{for } R_0 = 1.2 \text{ fm} , \end{cases} \quad (2.56)$$

which puts the efficiency of the chiral expansion into question at these high densities.

When using a Hartree-Fock spectrum we obtain much smaller pairing gaps. This suppression can also be seen in the small effective masses $m^*/m < 1$, especially for the smaller-cutoff potentials. The maximal gap is shifted to smaller momenta $k_F \approx (1.75 - 1.85) \text{ fm}^{-1}$ with values $\Delta \approx (0.05 - 0.15) \text{ MeV}$ with the largest values now corresponding to the largest cutoffs R_0 .

Figure 2.14 shows our results for the pairing gap in the triplet ${}^3P_2 - {}^3F_2$ using the same semi-local interactions as in Fig. 2.12. We do not show a curve for LO interactions since it is always zero. We attribute this effect to their poor description of the phase shifts in this channel. Note that due to the piecewise definition of the uncertainty estimate (2.55) the uncertainty bands are not always smooth, e.g., in the N³LO calculation with $R_0 = 0.9 \text{ fm}$ and a free spectrum.

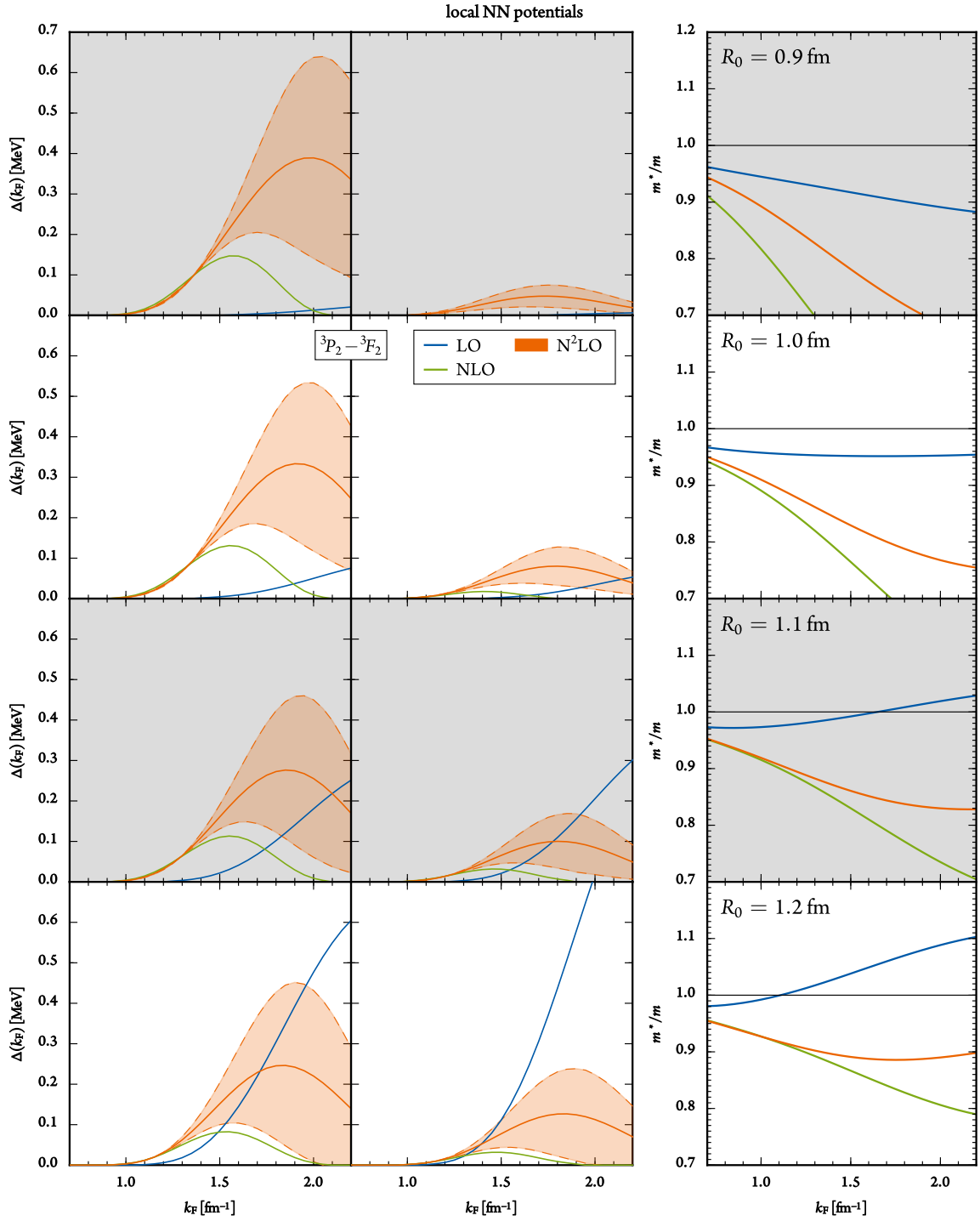


Figure 2.13: Energy gap in the ${}^3P_2 - {}^3F_2$ channel for the local NN potentials as in Fig. 2.11.

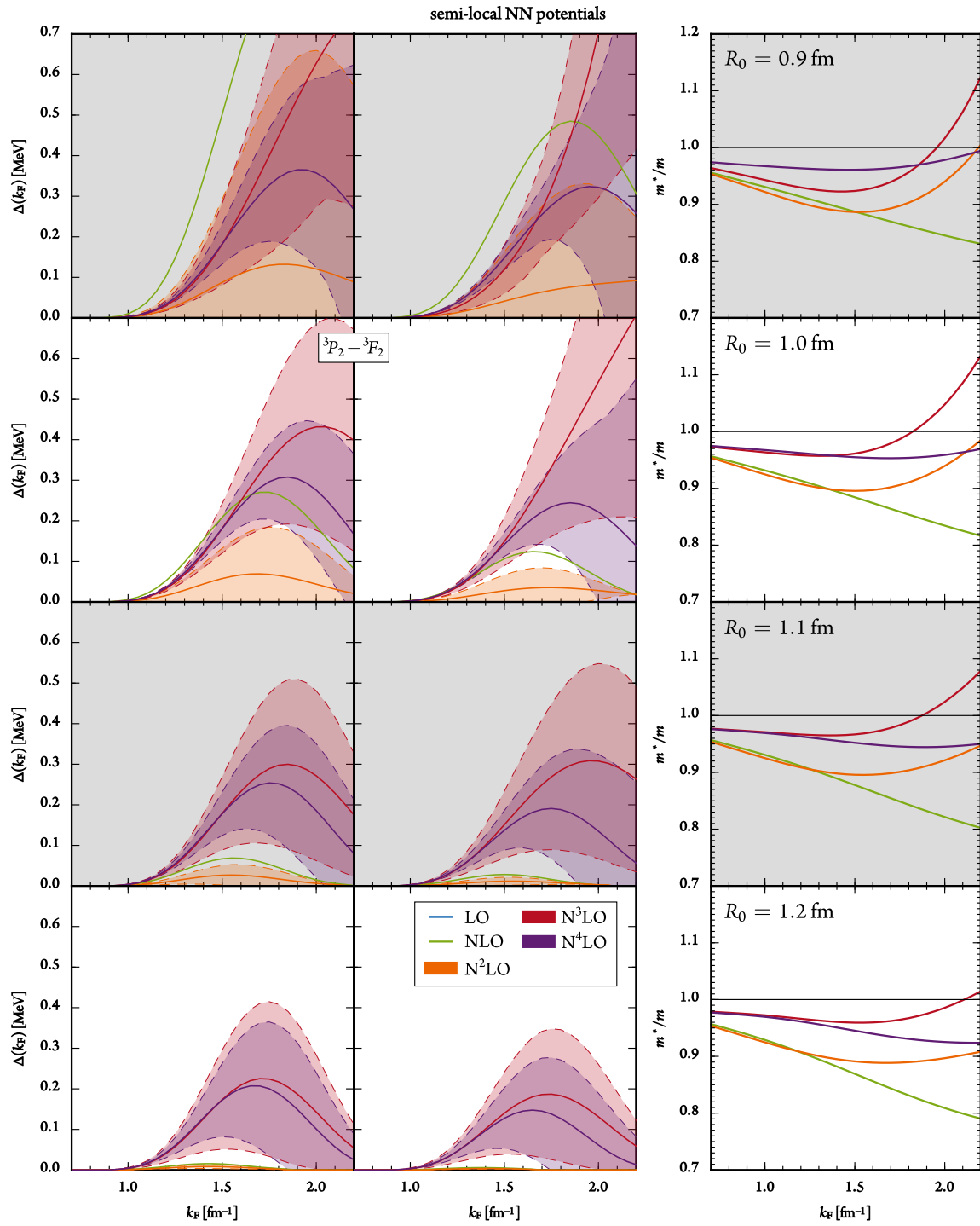


Figure 2.14: Energy gap in the ${}^3P_2 - {}^3F_2$ channel for the semi-local NN potentials as in Fig. 2.12.

For the semi-local potentials we find a much weaker dependence on the single-particle spectrum as for the local forces. This may also be seen in the effective masses, which are much closer to one for the semi-local potentials. Still there are small differences: With a free spectrum we find almost identical results for the N³LO and N⁴LO interactions up to $k_F \approx 1.55 \text{ fm}^{-1}$ while with the Hartree-Fock spectrum we find only up to around $k_F \approx (1.4 - 1.45) \text{ fm}^{-1}$ the same values and for the smallest-cutoff potential with $R_0 = 0.9 \text{ fm}$ this range is even smaller. This can be explained by comparing the predictions for the effective masses, which start to deviate at similar momenta.

The semi-local N⁴LO interactions predict the gap's maximum independent of the spectrum around $k_F \approx (1.65 - 1.95) \text{ fm}^{-1}$, similarly to the local interactions. It takes values $\Delta \approx (0.20 - 0.35) \text{ MeV}$ with a free spectrum and around 0.05 MeV smaller when using a Hartree-Fock spectrum. This is a similar range as predicted from the local interactions. Again, we want to mention that this may not be the physical maximum but may be explained from regulator effects.

Up to Fermi momenta $k_F \sim 2.0 \text{ fm}^{-1}$ the energy gaps obtained with the N⁴LO potential lies always within the uncertainty range of the N³LO calculation. From that we may conclude that higher-order potentials would lead to similar results. Given the fact that the results vary in good parts strongly when going from N²LO to N³LO, it is apparent that for an observable like the triplet-pairing gap, sensitive to only one higher partial wave, sophisticated high-order chiral interactions are crucial.

INCLUDING 3N INTERACTIONS

We also study the influence of 3N forces on the pairing gap but, as mentioned earlier, to be consistent we use the traditional non-local chiral interactions by Entem and Machleidt (EM) with cutoff 500 MeV [145, 146] and Epelbaum, Glöckle, and Meißner (EGM) with cutoff combinations 450/500 and 450/700 MeV [148]. We show results for both leading and sub-leading 3N forces with the c_i ranges discussed above.

In Fig. 2.15 we show the results for the pairing gap in the singlet 1S_0 . The NN-only calculation is depicted as a solid line. When including 3N forces we show uncertainty bands limited by dashed lines in grey for leading 3N forces only and in sea green when using also N³LO 3N interactions.

On the NN level we find the maximal gap at $k_F \approx (0.80 - 0.85) \text{ fm}^{-1}$ with values around $\Delta \approx 3.0 \text{ MeV}$ for the free and $\Delta \approx (2.7 - 2.9) \text{ MeV}$ with a Hartree-Fock spectrum. The gap closes around $k_F \approx 1.5 \text{ fm}^{-1}$ with the free and slightly below with a Hartree-Fock spectrum. These values are in good agreement with the calculations based on the local and semi-local interactions. This does not come as a surprise, given that the potentials reproduce the phase shifts well.

The inclusion of 3N forces lowers the pairing gap at momenta $k_F \gtrsim 0.6 \text{ fm}^{-1}$ and shifts the closure to lower $k_F \approx (1.3 - 1.4) \text{ fm}^{-1}$. The maximum is reduced by about 0.2 MeV but its position stays almost unchanged. This was expected since the 3N interactions are repulsive in this channel. For the EGM potentials we find about the same effects for the leading and sub-leading 3N interactions.

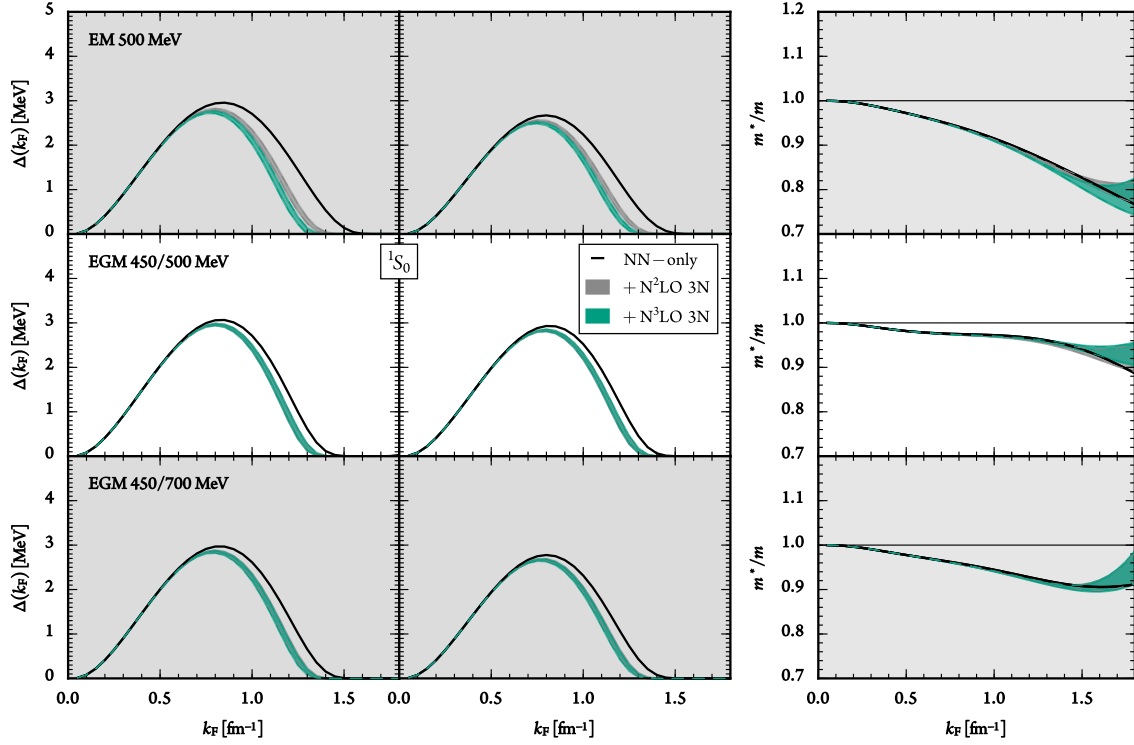


Figure 2.15: Pairing gap in the 1S_0 channel using a free (left column) and a Hartree-Fock spectrum (centre) for the non-local N^3LO NN potentials EM 500 MeV (first row), EGM 450/500 MeV (second) and EGM 450/700 MeV (third). The third column depicts the effective mass in a Hartree-Fock spectrum. The NN-only results are shown by the black-solid lines. The uncertainty bands for N^2LO and N^3LO are determined by variations of the 3N couplings c_1, c_3 and cutoff Λ_{3N} as discussed in the text.

For the EM potential the N^3LO 3N forces lead to slightly lower gaps which might be explained by the two-pion-exchange–contact topology at this order, which depends on the NN coupling C_T and is much stronger for the EM potential than for the EGM interactions [140]. Also with 3N forces the dependence on the single-particle spectrum is almost negligible, which can also be seen from the effective masses which only slightly vary when including 3N forces.

The pairing gap in the coupled triplet channel ${}^3P_2-{}^3F_2$ is shown in Fig. 2.16 using the same interactions and colour scheme as in Fig. 2.15.

Up to $k_F \approx 1.3 \text{ fm}^{-1}$ all three potentials lead to similar results on the NN level when using a free spectrum with $\Delta \approx 0.05 \text{ MeV}$. The EGM 450/500 MeV interaction reaches a maximum already at $k_F = 1.4 \text{ fm}^{-1}$ while the EGM 450/700 MeV peaks at $k_F \approx 1.65 \text{ fm}^{-1}$ and the EM potential not before $k_F = 2.2 \text{ fm}^{-1}$. This different behaviour is attributed to the smaller cutoff in the EGM potentials and their poor description of the phase shifts at high energies in comparison to the EM potential.

Due to the larger densities at which the ${}^3P_2-{}^3F_2$ pairing gap opens also 3N forces play a more dominant role. This is valid for both, pairing gaps and the effective masses. For the two EGM potentials we

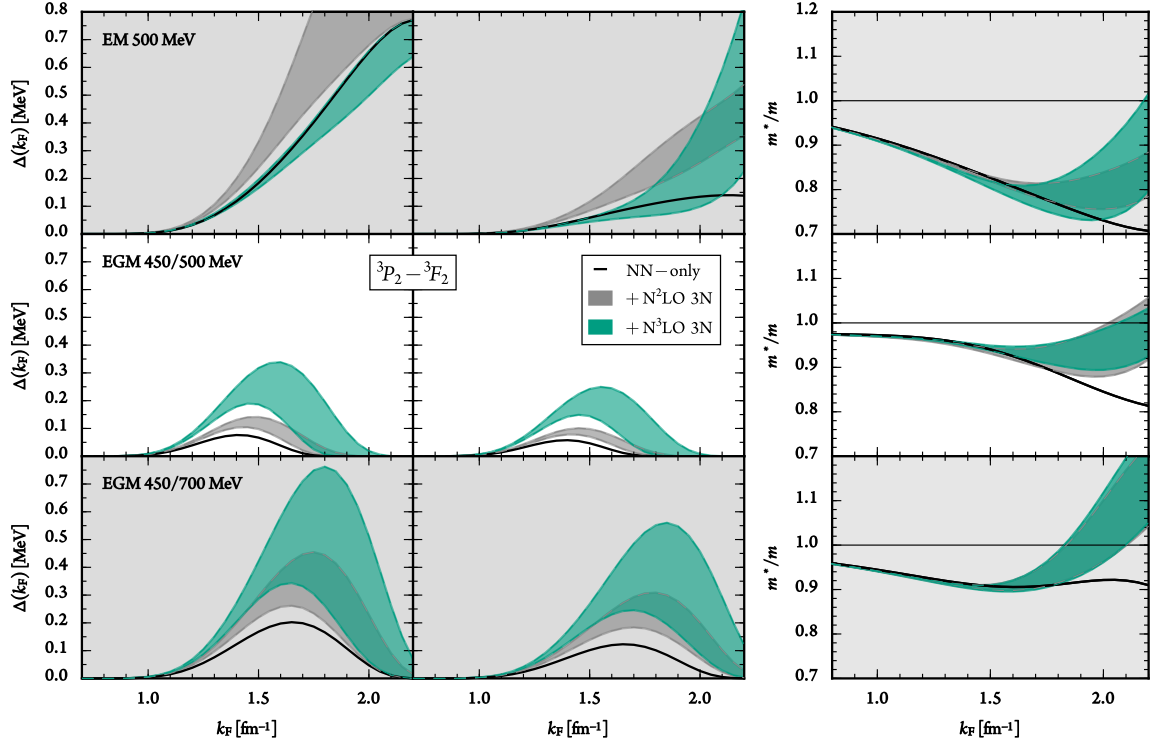


Figure 2.16: Pairing gap in the ${}^3P_2 - {}^3F_2$ channel obtained with non-local chiral N^3LO interactions. See Fig. 2.15 and the text for details.

find that the energy gaps are enlarged with 3N forces at N^2LO and even more at N^3LO . Also their maxima are shifted to higher Fermi momenta. We trace this back to attractive components of the, in total repulsive, 3N force in this channel. When using the EM potential the picture is slightly changed with still attractive leading 3N forces but almost negligible repulsive 3N interactions with the sub-leading 3N forces. We again attribute this to the different contribution in the two-pion–contact topology. For the EM potential we also find a much stronger dependence on the single-particle spectrum already on the NN level with strong suppression of the gap with a Hartree-Fock spectrum, which is reflected in the relatively small effective masses. Also the N^3LO 3N forces are strongly affected by the spectrum with now positive contributions for the energy gap at high momenta $k_F \gtrsim 1.7 \text{ fm}^{-1}$.

Note that, given the repulsive effects of sub-leading 3N forces for the EM potentials, we have investigated also other channels to find out if the ${}^3P_2 - {}^3F_2$ channel is still the dominant attractive interaction at the higher momenta $k_F \gtrsim 1.3 \text{ fm}^{-1}$. In fact, it is still the largest contribution and we conclude that 3N forces do not change the channel in which pairing is expected.

In conclusion we found substantial effects from 3N forces which may even more than double the ${}^3P_2 - {}^3F_2$ pairing gap. It is thus worthwhile investigating 3N forces with the newer semi-local and local forces. In particular the rich structure of the sub-leading 3N interactions can play an important role in that density region.

2.3.5 CONCLUSIONS

In summary, we made three advances within this project: (i) We have developed an independent method to solve the BCS gap equation, which does not require the introduction of an auxiliary potential and is straightforward to implement. (ii) We provide uncertainty estimates based on the chiral expansion and (iii) have studied the effect of sub-leading 3N forces.

In the 1S_0 channel the predictions of the interactions at highest chiral order agree for all cutoffs and in the entire density range. We find the maximum of the 1S_0 pairing around $k_F = (0.8 - 0.9) \text{ fm}^{-1}$ with $\Delta_{\text{max}} = (2.9 - 3.3) \text{ MeV}$ for a free single-particle spectrum and when including self-energy corrections in a Hartree-Fock spectrum suppressions of $\sim 0.3 \text{ MeV}$. The inclusion of 3N forces also leads to a small suppression but their effect is in general small.

In the triplet channel $^3P_2 - ^3F_2$ the global picture is less clear. For all potentials studied we find that the gap opens around $k_F \approx (0.9 - 1.0) \text{ fm}^{-1}$ and for the highest-chiral-order potentials we find a maximum of the $^3P_2 - ^3F_2$ gap in the region $k_F = (1.7 - 1.9) \text{ fm}^{-1}$ with $\Delta_{\text{max}} < 0.4 \text{ MeV}$. At these densities one pushes the chiral expansion to its limits and we find a strong scheme dependence. The inclusion of leading and sub-leading 3N forces can have a substantial attractive effect but should be studied further in the semi-local or local framework.

The inclusion of effects beyond the BCS approximation should be pursued in the future. For that the use of consistently evolved NN and 3N interactions via the similarity renormalisation group [166] is of great interest. These interactions are expected to exhibit a better many-body convergence in the expansion of the pairing interaction.

3

Towards *ab initio* energy-density functionals

CONNECTING NUCLEAR HAMILTONIANS TO ENERGY-DENSITY FUNCTIONALS is a major goal of nuclear theory. As discussed in Chapter 1, a promising step into the direction of *ab initio* DFT is orbital-based density functional theory and in particular the optimised effective potential (OEP) method. It provides a path from a general energy functional to a local Kohn-Sham potential [35].

The OEP method is similar to the Hartree-Fock approximation and many-body perturbation theory. In fact, the functional in the exchange-only approximation of the OEP method is the Hartree-Fock energy but the single-particle orbitals are exchanged by the Kohn-Sham orbitals such that the exchange term is transformed into a local potential. However, when we include correlations beyond Hartree-Fock, *e.g.*, from second-order perturbation theory the picture is not as simple.

In this Chapter we start with a short review of Hartree-Fock and many-body perturbation theory and then discuss the details of the OEP method and the differences to Hartree-Fock. We further discuss the inclusion of correlations. Computational details and results are presented in the next Chapter. This project was worked out in collaboration with Kai Hebel and Achim Schwenk.

3.1 HARTREE-FOCK AND MANY-BODY PERTURBATION THEORY

AS INTRODUCTION AND BENCHMARK SYSTEM we recapitulate the Hartree-Fock approximation and many-body perturbation theory. It is the simplest approach to solve the problem of finding the ground-state energy E_{gs} of a given A -particle Hamiltonian \widehat{H}_A by minimising over all normalised anti-symmetric A -body wave functions ψ

$$E_{\text{gs}} = \min_{\psi} \langle \psi | \widehat{H}_A | \psi \rangle. \quad (3.1)$$

In the Hartree-Fock approximation we minimize the energy over wavefunctions ψ_{HF} which are single Slater determinants of orbitals φ_i

$$|\psi_{\text{HF}}\rangle = |\varphi_1 \cdots \varphi_A\rangle_a. \quad (3.2)$$

3.1.1 DERIVATION OF THE HARTREE-FOCK EQUATIONS

Consider a many-body system in an external potential V_{ext} with the Hamiltonian $\widehat{H} = \widehat{H}_0 + \widehat{H}_I$,

$$\widehat{H}_0 = \sum_a \int d^3x \widehat{\psi}_a^\dagger(\mathbf{x}) \left[-\frac{\nabla^2}{2m} + V_{\text{ext}}(\mathbf{x}) \right] \widehat{\psi}_a(\mathbf{x}), \quad (3.3)$$

$$\widehat{H}_I = \frac{1}{2} \sum_{a,\beta,\alpha',\beta'} \int d^3x d^3y \widehat{\psi}_a^\dagger(\mathbf{x}) \widehat{\psi}_\beta^\dagger(\mathbf{y}) \langle \alpha\beta | V(\mathbf{x}, \mathbf{y}) | \alpha'\beta' \rangle \widehat{\psi}_{\beta'}(\mathbf{y}) \widehat{\psi}_{\alpha'}(\mathbf{x}), \quad (3.4)$$

where the greek indices collect the internal degrees of freedom, spin and isospin $a \equiv (m_s, m_t)$, and the states ψ are defined as

$$\widehat{\psi}_a(\mathbf{x}) = \sum_{i=1}^{k_{\text{max}}} \varphi_{ia}(\mathbf{x}) \widehat{a}_{ia}, \quad (3.5)$$

$$\widehat{\psi}_a^\dagger(\mathbf{x}) = \sum_{i=1}^{k_{\text{max}}} \varphi_{ia}^\dagger(\mathbf{x}) \widehat{a}_{ia}^\dagger, \quad (3.6)$$

where we have introduced a truncation of the basis states k_{max} .

The Hartree-Fock energy is then given by

$$\begin{aligned}
\langle \psi_{\text{HF}} | \hat{H} | \psi_{\text{HF}} \rangle &= \sum_a \sum_{i=1}^{N_a} \int d^3x \varphi_{ia}^\dagger(\mathbf{x}) \left[-\frac{\nabla^2}{2m} + V_{\text{ext}}(\mathbf{x}) \right] \varphi_{ia}(\mathbf{x}) \\
&+ \frac{1}{2} \sum_{a,\beta} \sum_{i=1}^{N_a} \sum_{j=1}^{N_\beta} \int d^3x d^3y \varphi_{ia}^\dagger(\mathbf{x}) \varphi_{j\beta}^\dagger(\mathbf{y}) \langle a\beta | V(\mathbf{x}, \mathbf{y}) | a\beta \rangle \varphi_{ia}(\mathbf{x}) \varphi_{j\beta}(\mathbf{y}) \\
&- \frac{1}{2} \sum_{a,\beta} \sum_{i=1}^{N_a} \sum_{j=1}^{N_\beta} \int d^3x d^3y \varphi_{ia}^\dagger(\mathbf{x}) \varphi_{j\beta}^\dagger(\mathbf{y}) \langle a\beta | V(\mathbf{x}, \mathbf{y}) | \beta a \rangle \varphi_{j\beta}(\mathbf{x}) \varphi_{ia}(\mathbf{y}), \quad (3.7)
\end{aligned}$$

where the sums are over occupied states only with $\sum_a N_a = A$. We minimise the energy by variation with respect to φ_{ia} using the single-particle energies ε_{ia} as Lagrange multipliers to ensure normalised orbitals:

$$\frac{\delta}{\delta \varphi_{ia}^\dagger(\mathbf{x})} \left[\langle \psi_{\text{HF}} | \hat{H} | \psi_{\text{HF}} \rangle - \sum_\beta \sum_{j=1}^{N_\beta} \varepsilon_{j\beta} \int d^3y |\varphi_{j\beta}(\mathbf{y})|^2 \right] = 0, \quad (3.8)$$

which leads to the Hartree-Fock equations in coordinate space

$$\begin{aligned}
&\left[-\frac{\nabla^2}{2m} + V_{\text{ext}}(\mathbf{x}) \right] \varphi_{ia}(\mathbf{x}) \\
&+ \sum_\beta \sum_{j=1}^{N_\beta} \int d^3y \varphi_{j\beta}^\dagger(\mathbf{y}) [\langle a\beta | V(\mathbf{x}, \mathbf{y}) | a\beta \rangle \varphi_{ia}(\mathbf{x}) \varphi_{j\beta}(\mathbf{y}) - \langle a\beta | V(\mathbf{x}, \mathbf{y}) | \beta a \rangle \varphi_{j\beta}(\mathbf{x}) \varphi_{ia}(\mathbf{y})] \\
&= \varepsilon_{ia} \varphi_{ia}(\mathbf{x}). \quad (3.9)
\end{aligned}$$

One defines the direct or Hartree potential,

$$\begin{aligned}
V_{\text{H}}^a(\mathbf{x}) &\equiv \sum_\beta \sum_{j=1}^{N_\beta} \int d^3y \langle a\beta | V(\mathbf{x}, \mathbf{y}) | a\beta \rangle \varphi_{j\beta}^\dagger(\mathbf{y}) \varphi_{j\beta}(\mathbf{y}) \\
&= \sum_\beta \int d^3y \langle a\beta | V(\mathbf{x}, \mathbf{y}) | a\beta \rangle \rho_\beta(\mathbf{y}), \quad (3.10)
\end{aligned}$$

and exchange or Fock potential,

$$\begin{aligned}
V_{\text{F}}^a(\mathbf{x}, \mathbf{y}) &\equiv - \sum_\beta \sum_{j=1}^{N_\beta} \langle a\beta | V(\mathbf{x}, \mathbf{y}) | \beta a \rangle \varphi_{j\beta}^\dagger(\mathbf{y}) \varphi_{j\beta}(\mathbf{x}) \\
&= - \sum_\beta \langle a\beta | V(\mathbf{x}, \mathbf{y}) | \beta a \rangle \rho_\beta(\mathbf{x}, \mathbf{y}), \quad (3.11)
\end{aligned}$$

where we have introduced the spin/isospin densities

$$\rho_\beta(\mathbf{x}) = \sum_{j=1}^{N_\beta} \varphi_{j\beta}^\dagger(\mathbf{x}) \varphi_{j\beta}(\mathbf{x}), \quad (3.12)$$

$$\rho_\beta(\mathbf{x}, \mathbf{y}) = \sum_{j=1}^{N_\beta} \varphi_{j\beta}^\dagger(\mathbf{y}) \varphi_{j\beta}(\mathbf{x}). \quad (3.13)$$

With the definitions above we can rewrite Eq. (3.9) into a non-local Schrödinger-like equation

$$\left[-\frac{\nabla^2}{2m} + V_{\text{ext}}(\mathbf{x}) + V_{\text{H}}^\alpha(\mathbf{x}) \right] \varphi_{ia}(\mathbf{x}) + \int d^3y V_{\text{F}}^\alpha(\mathbf{x}, \mathbf{y}) \varphi_{ia}(\mathbf{y}) = \varepsilon_{ia} \varphi_{ia}(\mathbf{x}). \quad (3.14)$$

Both, the Hartree and the Fock potential, depend on the solution of the orbitals φ_{ia} . Thus, the Hartree-Fock equations form a set of A coupled equations and one has to solve them self-consistently.

3.1.2 SOLUTION OF THE HARTREE-FOCK EQUATIONS

In the following we assume the external trap to be a 3d-harmonic-oscillator potential

$$V_{\text{ext}}(\mathbf{x}) \equiv V_{\text{HO}}(\mathbf{x}) = \frac{1}{2} m^2 \omega^2 \mathbf{x}^2. \quad (3.15)$$

For the self-consistent solution of the Hartree-Fock equations we work in a harmonic oscillator basis, *i.e.*, the eigenbasis of the external potential, in order to reduce the calculation to a simple eigenvalue problem. Hence, we introduce the basis states

$$\varphi_{aa}^0 = \frac{u_{n_a l_a}^0(x)}{x} Y_{l_a}^{m_a}(\hat{\mathbf{x}}) \chi_a, \quad \text{with} \quad \left[-\frac{\nabla^2}{2m} + V_{\text{ext}}(\mathbf{x}) \right] \varphi_{aa}^0(\mathbf{x}) = \varepsilon_{aa}^0 \varphi_{aa}^0(\mathbf{x}), \quad (3.16)$$

with collective index $a \equiv (n_a, l_a, m_a)$, spin function χ_a , $n = 2k + l$, and radial wavefunction

$$u_{nl}^0(x) = \sqrt{\frac{\sqrt{\frac{\omega^3}{\pi}} \omega^l 2^{k+l+2k}!}{(2k+2l+1)!!}} x^l \exp\left(-\frac{1}{2} \omega x^2\right) L_k^{l+\frac{1}{2}}(\omega x^2). \quad (3.17)$$

We expand the orbitals $\varphi_{ia} = u_{n_i l_i}(x)/x Y_{l_i}^{m_i}(\hat{\mathbf{x}})$ with collective index i as above in terms of the free-harmonic-oscillator orbitals φ^0

$$\varphi_{ia}(\mathbf{x}) = \varphi_{(n_i, l_i, m_i)_a}(\mathbf{x}) = \sum_{n_a} a_{n_i n_a, a} \varphi_{(n_a, l_i, m_i)_a}^0(\mathbf{x}) \equiv \sum_a a_{ia, a} \varphi_{aa}^0(\mathbf{x}), \quad (3.18)$$

where we have introduced the expansion coefficients $a_{ia,a} \equiv a_{n_i n_a, a} \delta_{l_i, l_a} \delta_{m_i, m_a}$ for simplicity. With this expansion we can cast Eq. (3.14) into

$$\sum_a a_{ia,a} \varepsilon_{aa}^0 \varphi_{aa}^0(\mathbf{x}) + \sum_a a_{ia,a} \left[V_H^a(\mathbf{x}) \varphi_{aa}^0(\mathbf{x}) + \int d^3 y V_F^a(\mathbf{x}, \mathbf{y}) \varphi_{aa}^0(\mathbf{y}) \right] = \varepsilon_{ia} \sum_a a_{ia,a} \varphi_{aa}^0(\mathbf{x}). \quad (3.19)$$

Multiplying with $\varphi_{ba}^{0\dagger}(\mathbf{x})$ and integrating over \mathbf{x} gives

$$\begin{aligned} 0 &= a_{ib,a} \varepsilon_{ba}^0 - \varepsilon_{ia} a_{ib,a} + \int d^3 x \varphi_{ba}^{0\dagger}(\mathbf{x}) \sum_a a_{ia,a} \left[V_H^a(\mathbf{x}) \varphi_{aa}^0(\mathbf{x}) + \int d^3 y V_F^a(\mathbf{x}, \mathbf{y}) \varphi_{aa}^0(\mathbf{y}) \right] \\ &= a_{ib,a} \varepsilon_{ba}^0 - \varepsilon_{ia} a_{ib,a} + \sum_a a_{ia,a} (I_H^{ab,a} + I_F^{ab,a}), \end{aligned} \quad (3.20)$$

with the Hartree term,

$$\begin{aligned} I_H^{ab,a} &= \sum_\beta \sum_{j=1}^{N_\beta} \int d^3 x d^3 y \varphi_{ba}^{0\dagger}(\mathbf{x}) \varphi_{j\beta}^\dagger(\mathbf{y}) \langle a\beta | V(\mathbf{x}, \mathbf{y}) | a\beta \rangle \varphi_{aa}^0(\mathbf{x}) \varphi_{j\beta}(\mathbf{y}) \\ &= \sum_\beta \sum_{j=1}^{N_\beta} \sum_{c,d} a_{jc,\beta}^\dagger a_{jd,\beta} \int d^3 x d^3 y \varphi_{ba}^{0\dagger}(\mathbf{x}) \varphi_{c\beta}^{0\dagger}(\mathbf{y}) \langle a\beta | V(\mathbf{x}, \mathbf{y}) | a\beta \rangle \varphi_{aa}^0(\mathbf{x}) \varphi_{d\beta}^0(\mathbf{y}) \\ &= \sum_\beta \sum_{c,d} \rho_{cd,\beta} \int d^3 x d^3 y \varphi_{ba}^{0\dagger}(\mathbf{x}) \varphi_{c\beta}^{0\dagger}(\mathbf{y}) \langle a\beta | V(\mathbf{x}, \mathbf{y}) | a\beta \rangle \varphi_{aa}^0(\mathbf{x}) \varphi_{d\beta}^0(\mathbf{y}), \end{aligned} \quad (3.21)$$

and Fock term,

$$\begin{aligned} I_F^{ab,a} &= - \sum_\beta \sum_{j=1}^{N_\beta} \int d^3 x d^3 y \varphi_{ba}^{0\dagger}(\mathbf{x}) \varphi_{j\beta}^\dagger(\mathbf{y}) \langle a\beta | V(\mathbf{x}, \mathbf{y}) | \beta a \rangle \varphi_{j\beta}(\mathbf{x}) \varphi_{aa}^0(\mathbf{y}) \\ &= - \sum_\beta \sum_{j=1}^{N_\beta} \sum_{c,d} a_{jc,\beta}^\dagger a_{jd,\beta} \int d^3 x d^3 y \varphi_{ba}^{0\dagger}(\mathbf{x}) \varphi_{c\beta}^{0\dagger}(\mathbf{y}) \langle a\beta | V(\mathbf{x}, \mathbf{y}) | \beta a \rangle \varphi_{d\beta}^0(\mathbf{x}) \varphi_{aa}^0(\mathbf{y}) \\ &= - \sum_\beta \sum_{c,d} \rho_{cd,\beta} \int d^3 x d^3 y \varphi_{ba}^{0\dagger}(\mathbf{x}) \varphi_{c\beta}^{0\dagger}(\mathbf{y}) \langle a\beta | V(\mathbf{x}, \mathbf{y}) | \beta a \rangle \varphi_{d\beta}^0(\mathbf{x}) \varphi_{aa}^0(\mathbf{y}). \end{aligned} \quad (3.22)$$

Here we have introduced the harmonic-oscillator density matrix

$$\rho_{cd,a} = \sum_{j=1}^{N_a} a_{jc,a}^\dagger a_{jd,a}. \quad (3.23)$$

Equation (3.20) can be read as an eigenvalue equation for the i -th eigenvector $\mathbf{a}_{ia} = (a_{i1,a}, a_{i2,a}, \dots)^T$ and eigenvalue ε_{ia}

$$\sum_a a_{ia,a} M_{ab,a} = \varepsilon_{ia} a_{ib,a} \quad \Leftrightarrow \quad M_a \mathbf{a}_{ia} = \varepsilon_{ia} \mathbf{a}_{ia}, \quad (3.24)$$

with the matrix

$$M_{ab,a} = \delta_{ab} \varepsilon_{ba}^0 + I_{\text{H}}^{ab,a} + I_{\text{F}}^{ab,a}. \quad (3.25)$$

We solve this equation for the expansion coefficients and energies with standard linear-algebra algorithms. The Hartree-Fock energy is then calculated using Eq. (3.7).

3.1.3 DETAILS OF THE HARTREE-FOCK SOLUTION

In practice, we use anti-symmetrised matrix elements in a jj -coupled single-particle harmonic-oscillator basis with neutron-proton formalism. Therefore, we have basis states

$$|n_a n_b [(l_a s) j_a (l_b s) j_b] J M t m_{t_a} t m_{t_b}\rangle = \sum_{m_{j_a}, m_{j_b}} C_{j_a m_{j_a} j_b m_{j_b}}^{JM} |n_a (l_a s) j_a m_{j_a} t m_{t_a}\rangle |n_b (l_b s) j_b m_{j_b} t m_{t_b}\rangle, \quad (3.26)$$

with Clebsch-Gordan coefficients $C_{l_1 m_1 l_2 m_2}^{l_3 m_3}$ and

$$|n (l s) j m_j t m_t\rangle = \sum_{m, m_s} C_{l m s m_s}^{j m_j} |n l m s m_s t m_t\rangle, \quad (3.27)$$

with spin $s = 1/2$, isospin $t = 1/2$ and isospin projection $m_t = -1/2$ for neutrons and $m_t = 1/2$ for protons. In order to use those matrix elements in our calculation we need to decouple, *i.e.*, sum over the total single-particle angular momentum j ,

$$|n l m s m_s t m_t\rangle = \sum_{j, m_j} C_{l m s m_s}^{j m_j} |n (l s) j m_j t m_t\rangle, \quad (3.28)$$

and

$$|n_a (l_a s) j_a m_{j_a} t m_{t_a}\rangle |n_b (l_b s) j_b m_{j_b} t m_{t_b}\rangle = \sum_{J, M} C_{j_a m_{j_a} j_b m_{j_b}}^{JM} |n_a n_b [(l_a s) j_a (l_b s) j_b] J M t m_{t_a} t m_{t_b}\rangle. \quad (3.29)$$

Since the matrix elements are independent of the total-angular-momentum projection M we drop the index from now. However, we have to ensure that M in the bra and in the ket state are equal. For

simplicity and clarity we further drop the indices s and t . We thus get

$$\begin{aligned} |n_a l_a m_a m_{s_a} m_{t_a}\rangle |n_b l_b m_b m_{s_b} m_{t_b}\rangle &= \sum_{J, j_a, j_b} \mathcal{C}_{j_a(m_a+m_{s_a})j_b(m_b+m_{s_b})}^{J(m_a+m_{s_a}+m_b+m_{s_b})} \mathcal{C}_{l_a m_a s_{m_a}}^{j_a(m_a+m_{s_a})} \mathcal{C}_{l_b m_b s_{m_b}}^{j_b(m_b+m_{s_b})} \\ &\times |n_a l_a j_a m_{t_a} n_b l_b j_b m_{t_b} J\rangle. \end{aligned} \quad (3.30)$$

For an arbitrary matrix element we have

$$\begin{aligned} &\int d^3x d^3y \varphi_{a\alpha}^{0\dagger}(\mathbf{x}) \varphi_{b\beta}^{0\dagger}(\mathbf{y}) \langle \alpha\beta | V(\mathbf{x}, \mathbf{y}) | \gamma\delta \rangle \varphi_{c\gamma}^0(\mathbf{x}) \varphi_{d\delta}^0(\mathbf{y}) \\ &= \sum_{J, j_a, j_b, j_c, j_d} \mathcal{C}_{j_a(m_a+m_{s_a})j_b(m_b+m_{s_b})}^{J(m_a+m_{s_a}+m_b+m_{s_b})} \mathcal{C}_{j_c(m_c+m_{s_c})j_d(m_d+m_{s_d})}^{J(m_c+m_{s_c}+m_d+m_{s_d})} \mathcal{C}_{l_a m_a s_{m_a}}^{j_a(m_a+m_{s_a})} \mathcal{C}_{l_b m_b s_{m_b}}^{j_b(m_b+m_{s_b})} \mathcal{C}_{l_c m_c s_{m_c}}^{j_c(m_c+m_{s_c})} \mathcal{C}_{l_d m_d s_{m_d}}^{j_d(m_d+m_{s_d})} \\ &\times \delta_{m_a+m_{s_a}+m_b+m_{s_b}, m_c+m_{s_c}+m_d+m_{s_d}} \langle n_a l_a j_a m_{t_a} n_b l_b j_b m_{t_b} J | V | n_c l_c j_c m_{t_c} n_d l_d j_d m_{t_d} J \rangle. \end{aligned} \quad (3.31)$$

This leads to the following expressions for the Hartree and Fock term

$$\begin{aligned} I_H^{ab,a} &= \sum_{\beta} \sum_{c,d} \rho_{cd,\beta} \sum_{J, j_b, j_c, j_a, j_d} \mathcal{C}_{j_b(m_b+m_{s_b})j_c(m_c+m_{s_c})}^{J(m_b+m_{s_b}+m_c+m_{s_c})} \mathcal{C}_{j_a(m_a+m_{s_a})j_d(m_d+m_{s_d})}^{J(m_a+m_{s_a}+m_d+m_{s_d})} \\ &\times \mathcal{C}_{l_b m_b s_{m_b}}^{j_b(m_b+m_{s_b})} \mathcal{C}_{l_c m_c s_{m_c}}^{j_c(m_c+m_{s_c})} \mathcal{C}_{l_a m_a s_{m_a}}^{j_a(m_a+m_{s_a})} \mathcal{C}_{l_d m_d s_{m_d}}^{j_d(m_d+m_{s_d})} \\ &\times \langle n_b l_b j_b m_{t_b} n_c l_c j_c m_{t_c} J | V | n_a l_a j_a m_{t_a} n_d l_d j_d m_{t_d} J \rangle, \end{aligned} \quad (3.32)$$

$$\begin{aligned} I_F^{ab,a} &= - \sum_{\beta} \sum_{c,d} \rho_{cd,\beta} \sum_{J, j_b, j_c, j_a, j_d} \mathcal{C}_{j_b(m_b+m_{s_b})j_c(m_c+m_{s_c})}^{J(m_b+m_{s_b}+m_c+m_{s_c})} \mathcal{C}_{j_d(m_d+m_{s_d})j_a(m_a+m_{s_a})}^{J(m_d+m_{s_d}+m_a+m_{s_a})} \\ &\times \mathcal{C}_{l_b m_b s_{m_b}}^{j_b(m_b+m_{s_b})} \mathcal{C}_{l_c m_c s_{m_c}}^{j_c(m_c+m_{s_c})} \mathcal{C}_{l_d m_d s_{m_d}}^{j_d(m_d+m_{s_d})} \mathcal{C}_{l_a m_a s_{m_a}}^{j_a(m_a+m_{s_a})} \\ &\times \langle n_b l_b j_b m_{t_b} n_c l_c j_c m_{t_c} J | V | n_d l_d j_d m_{t_d} n_a l_a j_a m_{t_a} J \rangle, \end{aligned} \quad (3.33)$$

where the M delta function from Eq. (3.31) is automatically ensured by the expansion coefficients, which imply $m_a = m_b$ and $m_c = m_d$. For anti-symmetrised matrix elements we have

$$\begin{aligned} &\langle n_a l_a j_a m_{t_a} n_b l_b j_b m_{t_b} J | V_{as} | n_c l_c j_c m_{t_c} n_d l_d j_d m_{t_d} J \rangle \\ &= \langle n_a l_a j_a m_{t_a} n_b l_b j_b m_{t_b} J | V(1 + \mathcal{P}_{12}) | n_c l_c j_c m_{t_c} n_d l_d j_d m_{t_d} J \rangle \\ &= \langle n_a l_a j_a m_{t_a} n_b l_b j_b m_{t_b} J | V | n_c l_c j_c m_{t_c} n_d l_d j_d m_{t_d} J \rangle + \langle n_a l_a j_a m_{t_a} n_b l_b j_b m_{t_b} J | V | n_d l_d j_d m_{t_d} n_c l_c j_c m_{t_c} J \rangle, \end{aligned} \quad (3.34)$$

and thus we can combine the Hartree and Fock term to

$$\begin{aligned}
I_{\text{HF}}^{ab,a} &= \sum_{\beta} \sum_{c,d} \rho_{cd,\beta} \sum_{J,j_b,j_c,j_a,j_d} \mathcal{C}_{j_b(m_b+m_{s_a})j_c(m_c+m_{s_\beta})}^{J(m_b+m_{s_a}+m_c+m_{s_\beta})} \mathcal{C}_{j_a(m_a+m_{s_a})j_d(m_d+m_{s_\beta})}^{J(m_a+m_{s_a}+m_d+m_{s_\beta})} \\
&\times \mathcal{C}_{l_b m_b m_{s_a}}^{j_b(m_b+m_{s_a})} \mathcal{C}_{l_c m_c m_{s_\beta}}^{j_c(m_c+m_{s_\beta})} \mathcal{C}_{l_a m_a m_{s_a}}^{j_a(m_a+m_{s_a})} \mathcal{C}_{l_d m_d m_{s_\beta}}^{j_d(m_d+m_{s_\beta})} \\
&\times \langle n_b l_b j_b m_{t_a} n_c l_c j_c m_{t_\beta} J | V_{\text{as}} | n_a l_a j_a m_{t_a} n_d l_d j_d m_{t_\beta} J \rangle, \tag{3.35}
\end{aligned}$$

where the minus sign of the Fock term is incorporated due to the exchange of indices in the Clebsch-Gordan coefficients.

For closed-shell systems, *i.e.*, $A = 2, 8, 20, 40, \dots$, we can also work in an ls -coupled single-particle basis to avoid decoupling of the matrix elements. The expansion coefficients and single-particle energies are independent of the total angular momentum projection m_j . We can thus work in a restricted basis with index $a \equiv (n, l, j)$. The density matrix then becomes

$$\rho_{ab,m_t} = \sum_c^{\text{occ.}} (2j+1) a_{ac,m_t}^\dagger a_{bc,m_t}, \tag{3.36}$$

where the factor $(2j+1)$ originates from the m degeneracy in the basis states (n_a, l, j) . The Hartree-Fock term then writes

$$\begin{aligned}
I_{\text{HF}}^{ab,m_t} &= \sum_{m'_t} \sum_{c,d} \rho_{cd,m'_t} \frac{1}{(2j_a+1)(2j_c+1)} \sum_{m_{j_a},m_{j_c}} \sum_{J,M} \mathcal{C}_{j_a m_{j_a} j_c m_{j_c}}^{JM} \mathcal{C}_{j_a m_{j_a} j_c m_{j_c}}^{JM} \\
&\times \langle n_b l_a j_a m_t n_c l_c j_c m'_t J | V_{\text{as}} | n_a l_a j_a m_t n_d l_c j_c m'_t J \rangle \\
&= \sum_{m'_t} \sum_{c,d} \rho_{cd,m'_t} \frac{(2J+1)}{(2j_a+1)(2j_c+1)} \sum_J \langle n_b l_a j_a m_t n_c l_c j_c m'_t J | V_{\text{as}} | n_a l_a j_a m_t n_d l_c j_c m'_t J \rangle, \tag{3.37}
\end{aligned}$$

where we have used the completeness of the Clebsch-Gordan coefficients and that the matrix elements are independent of the total angular momentum projection M .

3.1.4 SECOND-ORDER CONTRIBUTION TO THE HARTREE-FOCK ENERGY

As mentioned above, the many-body states of the Hartree-Fock approximation are single Slater determinants, *i.e.*, independent particle states. Thus, they are not capable of describing correlations. As seen in Chapter 2 for neutron matter, there are large contributions originating from correlations. We thus calculate also contributions at second order in many-body perturbation theory.

In the ls -coupled single-particle basis the energy contribution is

$$\begin{aligned} E^{(2)} &= \frac{1}{4} \sum_{m_i, m_j, m_a, m_b} \sum_{i, j, a, b} \theta_{im_i} \theta_{jm_j} \bar{\theta}_{am_a} \bar{\theta}_{bm_b} \frac{|(im_t j m_t | V | am_t a b m_t) - (im_t j m_t | V | b m_t a m_t)|^2}{\varepsilon_{im_t} + \varepsilon_{jm_t} - \varepsilon_{am_t} - \varepsilon_{bm_t}} \\ &= \frac{1}{4} \sum_{m_i, m_j, m_a, m_b} \sum_{i, j, a, b} \theta_{im_i} \theta_{jm_j} \bar{\theta}_{am_a} \bar{\theta}_{bm_b} \frac{|(im_t j m_t | V_{as} | am_t a b m_t)|^2}{\varepsilon_{im_t} + \varepsilon_{jm_t} - \varepsilon_{am_t} - \varepsilon_{bm_t}}, \end{aligned} \quad (3.38)$$

with collective indices $i = (n_i, l_i, j_i, m_i)$ and where we have defined the matrix elements

$$\begin{aligned} (im_t j m_t | V_{as} | am_t a b m_t) &= \int d^3x d^3y \varphi_{im_t}^\dagger(\mathbf{x}) \varphi_{jm_t}^\dagger(\mathbf{y}) V_{as}(\mathbf{x} - \mathbf{y}) \varphi_{am_t}(\mathbf{x}) \varphi_{bm_t}(\mathbf{y}) \\ &= (am_t a b m_t | V_{as} | im_t j m_t) \\ &= (j m_t i m_t | V_{as} | b m_t a m_t), \end{aligned} \quad (3.39)$$

and occupation-number functions

$$\theta_{im_t} = \theta(\varepsilon_{F, m_t} - \varepsilon_{im_t}) = \begin{cases} 1 & \text{for } \varepsilon_{im_t} \leq \varepsilon_{F, m_t}, \\ 0 & \text{else,} \end{cases} \quad (3.40)$$

$\bar{\theta}_{am_t} = 1 - \theta_{am_t}$. For clarity we denote particles with indices a, b, \dots and holes with i, j, \dots . We expand the matrix elements in the free orbitals,

$$(im_t j m_t | V_{as} | am_t a b m_t) = \sum_{n'_i, n'_j, n'_a, n'_b} a_{n'_i, n'_i, m_t}^\dagger a_{n'_j, n'_j, m_t}^\dagger a_{n'_a, n'_a, m_t} a_{n'_b, n'_b, m_t} \langle i' m_t j' m_t | V_{as} | a' m_t a b' m_t \rangle, \quad (3.41)$$

where i' indicates (n'_i, l_i, j_i, m_i) matrix elements with respect to the free orbitals,

$$\langle i' m_t j' m_t | V_{as} | a' m_t a b' m_t \rangle = \int d^3x d^3y \varphi_{im_t}^{0\dagger}(\mathbf{x}) \varphi_{jm_t}^{0\dagger}(\mathbf{y}) V_{as}(\mathbf{x} - \mathbf{y}) \varphi_{am_t}^0(\mathbf{x}) \varphi_{bm_t}^0(\mathbf{y}). \quad (3.42)$$

This expansion and jj coupling leads to the following expression for the second-order energy

$$\begin{aligned} E^{(2)} &= \frac{1}{4} \sum_{m_i, m_j, m_a, m_b} \sum_{i, j, a, b} \frac{\theta_{im_t} \theta_{jm_t} \bar{\theta}_{am_t} \bar{\theta}_{bm_t}}{\varepsilon_{im_t} + \varepsilon_{jm_t} - \varepsilon_{am_t} - \varepsilon_{bm_t}} \\ &\times \left[\sum_{n'_i, n'_j, n'_a, n'_b, J, M} a_{n'_i, n'_i, m_t}^\dagger a_{n'_j, n'_j, m_t}^\dagger a_{n'_a, n'_a, m_t} a_{n'_b, n'_b, m_t} C_{j_i m_i j_i m_i}^{JM} C_{j_a m_a j_b m_b}^{JM} \right. \\ &\quad \left. \times \langle n'_i l_i j_i m_t n'_j l_j j_i m_t J | V_{as} | n'_a l_a j_a m_t n'_b l_b j_b m_t J \rangle \right]^2. \end{aligned} \quad (3.43)$$

Since θ_{im_t} and ε_{im_t} are independent of m_j , we can simplify the expression above as follows, where we redefine the collective index without the total-angular-momentum projection m_j : $i = (n_i, l_i, j_i)$

$$\begin{aligned}
E^{(2)} &= \frac{1}{4} \sum_{m_i, m_j, m_{t_a}, m_{t_b}} \sum_{i, j, a, b} \frac{\theta_{im_i} \theta_{jm_j} \bar{\theta}_{am_{t_a}} \bar{\theta}_{bm_{t_b}}}{\varepsilon_{im_i} + \varepsilon_{jm_j} - \varepsilon_{am_{t_a}} - \varepsilon_{bm_{t_b}}} \\
&\times \sum_{\substack{n'_i, n'_j, n'_a, n'_b, J, M \\ n''_i, n''_j, n''_a, n''_b, J', M'}} a_{n_i n'_i, m_i}^\dagger a_{n_j n'_j, m_j}^\dagger a_{n_a n'_a, m_{t_a}} a_{n_b n'_b, m_{t_b}} a_{n_i n''_i, m_i}^\dagger a_{n_j n''_j, m_j}^\dagger a_{n_a n''_a, m_{t_a}} a_{n_b n''_b, m_{t_b}} \\
&\times \sum_{m_{j_i}, m_{j_j}, m_{j_a}, m_{j_b}} C_{j_i m_{j_i}, j_i m_{j_i}}^{JM} C_{j_a m_{j_a}, j_b m_{j_b}}^{JM} C_{j_i m_{j_i}, j_i m_{j_i}}^{J'M'} C_{j_a m_{j_a}, j_b m_{j_b}}^{J'M'} \\
&\times \langle n'_i l_{j_i} m_{t_i} n'_j l_{j_j} m_{t_j} J | V_{as} | n'_a l_{j_a} m_{t_a} n'_b l_{j_b} m_{t_b} J \rangle \\
&\times \langle n''_i l_{j_i} m_{t_i} n''_j l_{j_j} m_{t_j} J' | V_{as} | n''_a l_{j_a} m_{t_a} n''_b l_{j_b} m_{t_b} J' \rangle \\
&= \frac{1}{4} \sum_{m_i, m_j, m_{t_a}, m_{t_b}} \sum_{i, j, a, b} \frac{\theta_{im_i} \theta_{jm_j} \bar{\theta}_{am_{t_a}} \bar{\theta}_{bm_{t_b}}}{\varepsilon_{im_i} + \varepsilon_{jm_j} - \varepsilon_{am_{t_a}} - \varepsilon_{bm_{t_b}}} \sum_J (2J + 1) \\
&\times \sum_{\substack{n'_i, n'_j, n'_a, n'_b \\ n''_i, n''_j, n''_a, n''_b}} a_{n_i n'_i, m_i}^\dagger a_{n_j n'_j, m_j}^\dagger a_{n_a n'_a, m_{t_a}} a_{n_b n'_b, m_{t_b}} a_{n_i n''_i, m_i}^\dagger a_{n_j n''_j, m_j}^\dagger a_{n_a n''_a, m_{t_a}} a_{n_b n''_b, m_{t_b}} \\
&\times \langle n'_i l_{j_i} m_{t_i} n'_j l_{j_j} m_{t_j} J | V_{as} | n'_a l_{j_a} m_{t_a} n'_b l_{j_b} m_{t_b} J \rangle \langle n''_i l_{j_i} m_{t_i} n''_j l_{j_j} m_{t_j} J | V_{as} | n''_a l_{j_a} m_{t_a} n''_b l_{j_b} m_{t_b} J \rangle \\
&= \frac{1}{4} \sum_{m_i, m_j, m_{t_a}, m_{t_b}} \sum_{i, j, a, b} \frac{\theta_{im_i} \theta_{jm_j} \bar{\theta}_{am_{t_a}} \bar{\theta}_{bm_{t_b}}}{\varepsilon_{im_i} + \varepsilon_{jm_j} - \varepsilon_{am_{t_a}} - \varepsilon_{bm_{t_b}}} \sum_J (2J + 1) \tag{3.44} \\
&\times \left[\sum_{n'_i, n'_j, n'_a, n'_b} a_{n_i n'_i, m_i}^\dagger a_{n_j n'_j, m_j}^\dagger a_{n_a n'_a, m_{t_a}} a_{n_b n'_b, m_{t_b}} \langle n'_i l_{j_i} m_{t_i} n'_j l_{j_j} m_{t_j} J | V_{as} | n'_a l_{j_a} m_{t_a} n'_b l_{j_b} m_{t_b} J \rangle \right]^2.
\end{aligned}$$

3.2 THE OPTIMISED EFFECTIVE POTENTIAL METHOD

IN CONTRAST TO THE HARTREE-FOCK approach, the optimised effective potential (OEP) method transforms the exchange or Fock term to a local multiplicative potential using a functional derivative. Thus, it involves an additional step in the solution algorithm. In this Section we will first derive the OEP integral equation in the exchange-only approximation. We then discuss the algorithm to solve this equation. We follow the discussions by Engel in Ref. [35] and Drut *et al.* [34].

3.2.1 DERIVATION OF THE OEP EQUATION

The optimised effective potential consists of two parts: Hartree and exchange correlations. The Hartree or direct potential v_H , corresponding to the Hartree term in Eq. (3.21) is already a multiplicative potential,

$$v_H(\mathbf{x}) = \int d^3x' \rho(\mathbf{x}') V(\mathbf{x}, \mathbf{x}'). \quad (3.45)$$

Thus, the term of interest is the exchange-correlation potential, denoted v_{xc} . Since we will use anti-symmetrised nuclear matrix elements in our calculation we will not (and in fact cannot) separate Hartree and exchange part in the derivation of the OEP equation. Note however, that for the inclusion of correlations the separation of exchange and correlations part is crucial, which is discussed in the next Section. Thus, we want to derive $v_{Hxc} = v_H + v_{xc}$ rather than v_{xc} only. As in the previous Section, we use a general basis with quantum numbers (k, a) , where the greek index collects all internal degrees of freedom like spin and/or isospin.

$$v_{Hxc,a}(\mathbf{x}) = \frac{\delta E_{Hxc}[\rho]}{\delta \rho_a(\mathbf{x})}. \quad (3.46)$$

In order to evaluate the derivatives we apply the chain rule of functional differentiation

$$\begin{aligned} \frac{\delta E_{Hxc}[\varphi_{ka}, \varepsilon_{ka}]}{\delta \rho_a(\mathbf{x})} &= \sum_k \int d^3x' \left[\frac{\delta E_{Hxc}}{\delta \varphi_{ka}(\mathbf{x}')} \frac{\delta \varphi_{ka}(\mathbf{x}')}{\delta \rho_a(\mathbf{x})} + \frac{\delta E_{Hxc}}{\delta \varphi_{ka}^\dagger(\mathbf{x}')} \frac{\delta \varphi_{ka}^\dagger(\mathbf{x}')}{\delta \rho_a(\mathbf{x})} + \frac{\partial E_{Hxc}}{\partial \varepsilon_{ka}} \frac{\delta \varepsilon_{ka}}{\delta \rho_a(\mathbf{x}')} \right] \\ &= \sum_k \int d^3x' d^3x'' \left[\frac{\delta E_{Hxc}}{\delta \varphi_{ka}(\mathbf{x}')} \frac{\delta \varphi_{ka}(\mathbf{x}')}{\delta v_{KS,a}(\mathbf{x}'')} \frac{\delta v_{KS,a}(\mathbf{x}'')}{\delta \rho_a(\mathbf{x})} + \text{c.c.} \right. \\ &\quad \left. + \frac{\partial E_{Hxc}}{\partial \varepsilon_{ka}} \frac{\delta \varepsilon_{ka}}{\delta v_{KS,a}(\mathbf{x}'')} \frac{\delta v_{KS,a}(\mathbf{x}'')}{\delta \rho_a(\mathbf{x})} \right]. \end{aligned} \quad (3.47)$$

Note that we allow for complex orbitals to keep the derivation as general as possible.

In principle we would also have a term accounting for the occupation-number dependence,

$$\frac{\partial E_{\text{Hxc}}}{\partial \theta_{ka}} \frac{\delta \theta_{ka}}{\delta v_{\text{KS},a}(\mathbf{x}'')} \frac{\delta v_{\text{KS},a}(\mathbf{x}'')}{\delta \rho_a(\mathbf{x})}. \quad (3.48)$$

However, in the Kohn-Sham framework the occupation number, $\theta_{ka} \equiv \Theta(\varepsilon_{\text{F},a} - \varepsilon_{ka})$, is always a Heaviside function and we obtain [241]

$$\begin{aligned} \frac{\delta \theta_{ka}}{\delta v_{\text{KS},a}(\mathbf{x})} &= \frac{\partial \Theta(\varepsilon_{\text{F},a} - \varepsilon_{ka})}{\partial \varepsilon_{\text{F},a}} \frac{\delta \varepsilon_{\text{F},a}}{\delta v_{\text{KS},a}(\mathbf{x})} + \frac{\partial \Theta(\varepsilon_{\text{F},a} - \varepsilon_{ka})}{\partial \varepsilon_{ka}} \frac{\delta \varepsilon_{ka}}{\delta v_{\text{KS},a}(\mathbf{x})} \\ &= \delta^{(1)}(\varepsilon_{\text{F},a} - \varepsilon_{ka}) [|\varphi_{\text{F},a}(\mathbf{x})|^2 - |\varphi_{ka}(\mathbf{x})|^2] = 0, \end{aligned} \quad (3.49)$$

where the Fermi energy $\varepsilon_{\text{F},a}$ and orbital $\varphi_{\text{F},a}$ correspond to the highest occupied state. For the calculation of the functional derivatives of the single-particle energies with respect to the Kohn-Sham potential see below. Hence, we can neglect these terms.

Following first-order perturbation theory we can evaluate the functional derivative with respect to infinitesimal variations of $\delta v_{\text{KS},a}$ ¹:

$$\delta \varepsilon_{ka} [\delta v_{\text{KS},a}] = \int d^3 x \varphi_{ka}^\dagger(\mathbf{x}) \delta v_{\text{KS},a}(\mathbf{x}) \varphi_{ka}(\mathbf{x}), \quad (3.50)$$

$$\delta \varphi_{ka}(\mathbf{x}) = \sum_{l \neq k} \int d^3 x' \frac{\varphi_{la}^\dagger(\mathbf{x}') \delta v_{\text{KS},a}(\mathbf{x}') \varphi_{ka}(\mathbf{x}')}{\varepsilon_{ka} - \varepsilon_{la}} \varphi_{la}(\mathbf{x}), \quad (3.51)$$

$$\delta \varphi_{ka}^\dagger(\mathbf{x}) = \sum_{l \neq k} \int d^3 x' \frac{\varphi_{ka}^\dagger(\mathbf{x}') \delta v_{\text{KS},a}(\mathbf{x}') \varphi_{la}(\mathbf{x}')}{\varepsilon_{ka} - \varepsilon_{la}} \varphi_{la}^\dagger(\mathbf{x}), \quad (3.52)$$

from which directly follows

$$\frac{\delta \varepsilon_{ka}}{\delta v_{\text{KS},a}(\mathbf{x})} = \varphi_{ka}^\dagger(\mathbf{x}) \varphi_{ka}(\mathbf{x}), \quad (3.53)$$

$$\frac{\delta \varphi_{ka}(\mathbf{x})}{\delta v_{\text{KS},a}(\mathbf{x}')} = \sum_{l \neq k} \frac{\varphi_{la}(\mathbf{x}) \varphi_{la}^\dagger(\mathbf{x}')}{\varepsilon_{ka} - \varepsilon_{la}} \varphi_{ka}(\mathbf{x}') = -G_{ka}(\mathbf{x}, \mathbf{x}') \varphi_{ka}(\mathbf{x}'), \quad (3.54)$$

$$\frac{\delta \varphi_{ka}^\dagger(\mathbf{x})}{\delta v_{\text{KS},a}(\mathbf{x}')} = \varphi_{ka}^\dagger(\mathbf{x}') \sum_{l \neq k} \frac{\varphi_{la}(\mathbf{x}') \varphi_{la}^\dagger(\mathbf{x})}{\varepsilon_{ka} - \varepsilon_{la}} = -\varphi_{ka}^\dagger(\mathbf{x}') G_{ka}(\mathbf{x}', \mathbf{x}), \quad (3.55)$$

¹For a Hamiltonian $H = H_0 + \lambda v_{\text{KS},a}$ the eigenvalues ε_k and eigenvectors $|k\rangle$ are given by

$$\begin{aligned} \varepsilon_i &= \varepsilon_k^{(0)} + \langle k^{(0)} | \lambda v_{\text{KS},a} | k^{(0)} \rangle + \dots, \\ |k\rangle &= |k^{(0)}\rangle + \sum_{l \neq k} \frac{\langle l^{(0)} | \lambda v_{\text{KS},a} | k^{(0)} \rangle}{\varepsilon_k^{(0)} - \varepsilon_l^{(0)}} |l^{(0)}\rangle + \dots, \end{aligned}$$

where $\varepsilon_k^{(0)}$ and $|k^{(0)}\rangle$ are the eigenvalues and eigenvectors of the unperturbed Hamiltonian H_0 , respectively.

with the propagator

$$G_{ka}(\mathbf{x}, \mathbf{x}') = \sum_{l \neq k} \frac{\varphi_{la}^\dagger(\mathbf{x}') \varphi_{la}(\mathbf{x})}{\varepsilon_{la} - \varepsilon_{ka}}. \quad (3.56)$$

The single-particle energies correspond to the Kohn-Sham energies ε_{ia} , since in our ansatz $H_0 = H_{\text{KS}}$ is the unperturbed Hamiltonian. For the evaluation of Eq. (3.47) we further need to evaluate $\delta v_{\text{KS}}/\delta \rho$, which we can do via its inverse:

$$\begin{aligned} \frac{\delta \rho_a(\mathbf{x})}{\delta v_{\text{KS},a}(\mathbf{x}')} &= \sum_k \theta_{ka} \frac{\delta[\varphi_{ka}(\mathbf{x}) \varphi_{ka}^\dagger(\mathbf{x}')] }{\delta v_{\text{KS},a}(\mathbf{x}')} \\ &= - \sum_k \theta_{ka} \varphi_{ka}^\dagger(\mathbf{x}) G_{ka}(\mathbf{x}, \mathbf{x}') \varphi_{ka}(\mathbf{x}') + \text{c.c.} \\ &\equiv \chi_a(\mathbf{x}, \mathbf{x}'), \end{aligned} \quad (3.57)$$

where χ_a is the static response function of the Kohn-Sham system.

By inserting these relations into the right-hand side of Eq. (3.47), multiplying the equation by $\chi_a(\mathbf{x}, \mathbf{x}')$, and integrating over \mathbf{x} we obtain an expression for $\delta E_{\text{Hxc}}/\delta v_{\text{KS},a}$, the OEP equation,

$$\int d^3 x' v_{\text{Hxc},a}(\mathbf{x}') \chi_a(\mathbf{x}', \mathbf{x}) = \Lambda_{\text{Hxc},a}(\mathbf{x}), \quad (3.58)$$

with

$$\begin{aligned} \Lambda_{\text{Hxc},a}(\mathbf{x}) &= \sum_k \left\{ - \int d^3 x' \left[\frac{\delta E_{\text{Hxc}}}{\delta \varphi_{ka}(\mathbf{x}')} G_{ka}(\mathbf{x}', \mathbf{x}) \varphi_{ka}(\mathbf{x}) + \text{c.c.} \right] + |\varphi_{ka}(\mathbf{x})|^2 \frac{\partial E_{\text{Hxc}}}{\partial \varepsilon_{ka}} \right\} \\ &= \sum_k \left\{ - \int d^3 x' [\varphi_{ka}^\dagger(\mathbf{x}') u_{ka}^{\text{Hxc}}(\mathbf{x}') G_{ka}(\mathbf{x}', \mathbf{x}) \varphi_{ka}(\mathbf{x}) + \text{c.c.}] + |\varphi_{ka}(\mathbf{x})|^2 \frac{\partial E_{\text{Hxc}}}{\partial \varepsilon_{ka}} \right\}, \end{aligned} \quad (3.59)$$

and

$$u_{ka}^{\text{Hxc}}(\mathbf{x}) = \frac{1}{\varphi_{ka}^\dagger(\mathbf{x})} \frac{\delta E_{\text{Hxc}}}{\delta \varphi_{ka}(\mathbf{x})}. \quad (3.60)$$

In terms of the orbital shifts,

$$\begin{aligned} \psi_{ka}^\dagger(\mathbf{x}) &= \int d^3 x' \varphi_{ka}^\dagger(\mathbf{x}') [u_{ka}^{\text{Hxc}}(\mathbf{x}') - \theta_{ka} v_{\text{Hxc},a}(\mathbf{x}')] G_{ka}(\mathbf{x}', \mathbf{x}) \\ &= \sum_{l \neq k} \int d^3 x' \frac{\varphi_{ka}^\dagger(\mathbf{x}') [u_{ka}^{\text{Hxc}}(\mathbf{x}') - \theta_{ka} v_{\text{Hxc},a}(\mathbf{x}')] \varphi_{la}(\mathbf{x}') \varphi_{la}^\dagger(\mathbf{x})}{\varepsilon_{la} - \varepsilon_{ka}}, \end{aligned} \quad (3.61)$$

we can compactly write the OEP equation in the form

$$\sum_k [\psi_{ka}^\dagger(\mathbf{x})\varphi_{ka}(\mathbf{x}) + \text{c.c.}] = \sum_k |\varphi_{ka}(\mathbf{x})|^2 \frac{\partial E_{\text{Hxc}}}{\partial \varepsilon_{ka}}. \quad (3.62)$$

The OEP equation is linear in E , so that one can treat each component of E individually. We want to take a closer look at the orbital shifts. It is of the form of first-order perturbation theory with perturbations $u_{ka}^{\text{Hxc}}(\mathbf{x}') - \theta_{ka} v_{\text{Hxc},a}(\mathbf{x}')$. Hence, ψ_{ka}^\dagger describes the first-order change of the Kohn-Sham orbital φ_{ka}^\dagger when the Kohn-Sham potential is replaced by u_{ka}^{Hxc} . The OEP equation thus states that first-order perturbations of the Kohn-Sham potential do not change the density. Furthermore, we want to mention that the orbital shifts are orthogonal to the Kohn-Sham orbitals, *i.e.*, $\int d^3x \psi_{ka}^\dagger(\mathbf{x})\varphi_{ka}(\mathbf{x})$, which is clear from their definition [242].

SPECIAL CASE: THE EXACT-EXCHANGE FUNCTIONAL

The exact-exchange functional E_x [243, 244] is one of the most simple functionals of DFT and is defined as the Fock expression in Eq. (3.7)

$$E_x \equiv -\frac{1}{2} \sum_{\alpha,\beta} \sum_{k,l} \theta_{ka} \theta_{l\beta} \int d^3x d^3y \varphi_{ka}^\dagger(\mathbf{x})\varphi_{l\beta}^\dagger(\mathbf{y}) \langle \alpha\beta | V(\mathbf{x}, \mathbf{y}) | \beta\alpha \rangle \varphi_{l\beta}(\mathbf{x})\varphi_{ka}(\mathbf{y}). \quad (3.63)$$

Note that this is not equal to the Fock energy in Hartree-Fock theory since the orbitals satisfy the Kohn-Sham equation but not the Hartree-Fock equations. The difference, as well as the difference between Kohn-Sham kinetic energy and full kinetic energy, is accounted for in $E_c \equiv E_{\text{Hxc}} - E_{\text{Hx}}$. The expression above is in fact an (implicit) functional of the density since the Kohn-Sham orbitals are uniquely determined by the density. The Hohenberg-Kohn theorem guarantees that the density uniquely determines the Kohn-Sham potential v_{KS} which itself determines the orbitals φ_{ka} .

The functional derivative of the exchange functional with respect to the orbitals is

$$\frac{\delta E_x}{\delta \varphi_{ka}^\dagger(\mathbf{x})} = -\theta_{ka} \sum_{\beta} \sum_l \theta_{l\beta} \varphi_{l\beta}(\mathbf{x}) \int d^3y \varphi_{l\beta}^\dagger(\mathbf{y}) \langle \alpha\beta | V(\mathbf{x}, \mathbf{y}) | \beta\alpha \rangle \varphi_{ka}(\mathbf{y}), \quad (3.64)$$

and since E_x does not explicitly depend on the single-particle energies it follows $\partial E_{\text{Hx}} / \partial \varepsilon_{ka} = 0$.

DETAILS ON THE OEP EQUATION

From the OEP integral equation (3.59) one can derive an important consistency criterion for the exchange-correlation energy [245]. We integrate over \mathbf{x}' , use the projection property of Green's functions,

$$\int d^3x \varphi_{ka}^\dagger(\mathbf{x}) G_{ka}(\mathbf{x}, \mathbf{x}') = 0 = \int d^3x' G_{ka}(\mathbf{x}, \mathbf{x}') \varphi_{ka}(\mathbf{x}'), \quad (3.65)$$

and get for the left-hand side

$$\begin{aligned} \int d^3x d^3x' v_{\text{Hxc},a}(\mathbf{x}') \chi_a(\mathbf{x}', \mathbf{x}) &= - \sum_k \theta_{ka} \int d^3x d^3x' v_{\text{Hxc},a}(\mathbf{x}') [\varphi_{ka}^\dagger(\mathbf{x}') G_{ka}(\mathbf{x}', \mathbf{x}) \varphi_{ka}(\mathbf{x}) + \text{c.c.}] \\ &= 0, \end{aligned} \quad (3.66)$$

and the right-hand side

$$\begin{aligned} \int d^3x \Lambda_{\text{Hxc},a}(\mathbf{x}) &= - \sum_k \int d^3x d^3x' \varphi_{ka}^\dagger(\mathbf{x}') u_{ka}^{\text{Hxc}}(\mathbf{x}') G_{ka}(\mathbf{x}', \mathbf{x}) \varphi_{ka}(\mathbf{x}) + \text{c.c.} + |\varphi_{ka}(\mathbf{x})|^2 \frac{\partial E_{\text{Hxc}}}{\partial \varepsilon_{ka}} \\ &= - \sum_k \frac{\partial E_{\text{Hxc}}}{\partial \varepsilon_{ka}}. \end{aligned} \quad (3.67)$$

Hence, we have derived a sum rule for any E_{Hxc} :

$$\sum_k \frac{\partial E_{\text{Hxc}}}{\partial \varepsilon_{ka}} = 0. \quad (3.68)$$

For the exchange-only potential this is obviously fulfilled, since E_x does not depend explicitly on the single-particle energies.

3.2.2 SOLUTION OF THE OEP EQUATION

In principle, there are many ways to solve the OEP equation. We follow, similarly to Drut and Platner [36], an iterative algorithm originally developed by Stephan Kümmel and John P. Perdew [246, 247].

Starting point for this iterative solution is a differential equation for the orbital shifts ψ_{ka}^\dagger . Using the Kohn-Sham equation,

$$H_{\text{KS},a}(\mathbf{x}) \varphi_{ka}(\mathbf{x}) \equiv \left[-\frac{\nabla^2}{2m} + v_{\text{KS},a}(\mathbf{x}) \right] \varphi_{ka}(\mathbf{x}) = \varepsilon_{ka} \varphi_{ka}(\mathbf{x}), \quad (3.69)$$

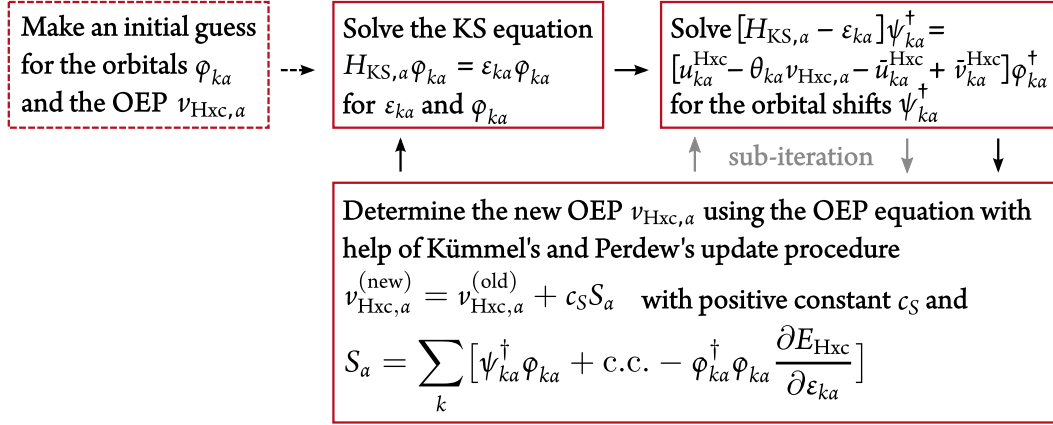


Figure 3.1: Schematic view of the algorithm to solve the OEP equations using the method developed by Kümmel and Perdew in Ref. [246].

we can show

$$\begin{aligned} [H_{KS,a}(\mathbf{x}) - \varepsilon_{ka}] \psi_{ka}^\dagger(\mathbf{x}) &= \sum_{l \neq k} \int d^3 x' \frac{\varphi_{ka}^\dagger(\mathbf{x}') [u_{ka}^{Hxc}(\mathbf{x}') - \theta_{ka} v_{Hxc,a}(\mathbf{x}')] \varphi_{la}(\mathbf{x}') [H_{KS,a}(\mathbf{x}) - \varepsilon_{ka}] \varphi_{la}^\dagger(\mathbf{x})}{\varepsilon_{la} - \varepsilon_{ka}} \\ &= \sum_l \int d^3 x' \varphi_{ka}^\dagger(\mathbf{x}') [u_{ka}^{Hxc}(\mathbf{x}') - \theta_{ka} v_{Hxc,a}(\mathbf{x}')] \varphi_{la}(\mathbf{x}') \varphi_{la}^\dagger(\mathbf{x}) \\ &\quad - \int d^3 x' \varphi_{ka}^\dagger(\mathbf{x}') [u_{ka}^{Hxc}(\mathbf{x}') - \theta_{ka} v_{Hxc,a}(\mathbf{x}')] \varphi_{ka}(\mathbf{x}') \varphi_{ka}^\dagger(\mathbf{x}), \end{aligned} \quad (3.70)$$

which gives finally

$$[H_{KS,a}(\mathbf{x}) - \varepsilon_{ka}] \psi_{ka}^\dagger(\mathbf{x}) = [u_{ka}^{Hxc}(\mathbf{x}) - \theta_{ka} v_{Hxc,a}(\mathbf{x}) - \bar{u}_{ka}^{Hxc} + \bar{v}_{ka}^{Hxc}] \varphi_{ka}^\dagger(\mathbf{x}), \quad (3.71)$$

where we have used the definitions

$$\bar{u}_{ka}^{Hxc} = \int d^3 x' \varphi_{ka}^\dagger(\mathbf{x}') u_{ka}^{Hxc}(\mathbf{x}') \varphi_{ka}(\mathbf{x}'), \quad (3.72)$$

$$\bar{v}_{ka}^{Hxc} = \int d^3 x' \varphi_{ka}^\dagger(\mathbf{x}') \theta_{ka} v_{Hxc,a}(\mathbf{x}') \varphi_{ka}(\mathbf{x}'). \quad (3.73)$$

In the last step we have used the completeness relation of the Kohn-Sham orbitals:

$$\sum_l \varphi_{la}^\dagger(\mathbf{x}) \varphi_{la}(\mathbf{x}') = \delta^{(3)}(\mathbf{x} - \mathbf{x}'). \quad (3.74)$$

The solution algorithm consists of three steps, which are schematically shown in Fig. 3.1.

INITIALISATIONS

As initial condition we make a guess for the orbitals φ_{ka} , e.g., free harmonic-oscillator or Hartree-Fock orbitals. With these orbitals we calculate the corresponding u_{ka}^{Hxc} . Finally, we need a guess for the OEP $v_{\text{Hxc},a}$ and for simplicity set it to zero.

FIRST STEP: SOLVING THE KOHN-SHAM EQUATION

With the (new) OEP we can solve the Kohn-Sham equation (3.69) for the orbitals and energies using the same linear-algebra algorithms as in the Hartree-Fock calculation: We expand the orbitals in terms of the free orbitals φ_{ja}^0

$$\varphi_{ia}(\mathbf{x}) = \sum_j a_{ij,a} \varphi_{ja}^0(\mathbf{x}), \quad (3.75)$$

which fulfil

$$\left[-\frac{\nabla^2}{2m} + v_{\text{ext},a}(\mathbf{x}) \right] \varphi_{ka}^0(\mathbf{x}) = \varepsilon_{ka}^0 \varphi_{ka}^0(\mathbf{x}). \quad (3.76)$$

Hence, following the derivation of the Hartree-Fock equations, the equation for the expansion coefficients $a_{ij,a}$ reads:

$$a_{ik,a} \varepsilon_{ka}^0 + \sum_j \theta_{ja} a_{ij,a} \int d^3x v_{\text{Hxc},a}(\mathbf{x}) \varphi_{ja}^0(\mathbf{x}) \varphi_{ka}^0(\mathbf{x}) = \varepsilon_{ia} a_{ik,a}, \quad (3.77)$$

where we need the matrix

$$M_{jk,a}^{\text{Hxc}} = \int d^3x v_{\text{Hxc},a}(\mathbf{x}) \varphi_{ja}^0(\mathbf{x}) \varphi_{ka}^0(\mathbf{x}). \quad (3.78)$$

This step is skipped in the first iteration, since we do not make a reasonable choice for the OEP.

SECOND STEP: DETERMINE THE ORBITAL SHIFTS

We use the OEP and in the last step obtained orbitals to solve Eq. (3.71) for the orbital shifts ψ_{ka}^\dagger . In practice, one also expands the orbital in some basis, e.g., the harmonic-oscillator orbitals,

$$\psi_{ka}^\dagger(\mathbf{x}) = \sum_l b_{kl,a}^\dagger \varphi_{la}^{0\dagger}(\mathbf{x}), \quad (3.79)$$

and solves a system of linear equations of the form

$$M_a \mathbf{b}_{ka}^\dagger = \mathbf{c}_{ka}, \quad (3.80)$$

where \mathbf{b}_k is a vector collecting the expansion coefficients of the orbital shifts; M and \mathbf{c}_k contain the left- and right-hand side of the orbital-shift equation, respectively:

$$M_{kl,mi} = \varepsilon_{ka}^0 \delta_{kl} + \int d^3x \varphi_{ka}^0(\mathbf{x}) \nu_{\text{Hxc},a}(\mathbf{x}) \varphi_{la}^{0\dagger}(\mathbf{x}) - \varepsilon_{ka} \delta_{kl}, \quad (3.81)$$

$$c_{ki,a} = \sum_m \left[\int d^3x \varphi_{ia}^0(\mathbf{x}) [u_{ka}^{\text{Hxc}}(\mathbf{x}) - \theta_{ka} \nu_{\text{Hxc},a}(\mathbf{x})] \varphi_{ma}^{\dagger 0}(\mathbf{x}) - (\bar{u}_{ka}^{\text{Hxc}} - \bar{v}_{ka}^{\text{Hxc}}) \delta_{im} \right] a_{km,a}^\dagger. \quad (3.82)$$

We need an expression for u_{ka}^{Hxc} but the division by the orbitals might be problematic. However, in the numerical calculation it only appears with a factor of φ_{ka}^\dagger such that we define $\tilde{u}_{ka}^{\text{Hxc}}(\mathbf{x}) \equiv \varphi_{ka}^\dagger(\mathbf{x}) u_{ka}^{\text{Hxc}}(\mathbf{x})$. In practice we calculate the expression (in the exact-exchange approximation)

$$\begin{aligned} u_{kla}^{\text{Hx}} &\equiv \int d^3x \tilde{u}_{ka}^{\text{Hx}}(\mathbf{x}) \varphi_{la}^0(\mathbf{x}) \\ &= \sum_i a_{ki,a}^\dagger \int d^3x \varphi_{ia}^{0\dagger}(\mathbf{x}) \theta_{ka} \sum_{j,\beta} \theta_{j\beta} \int d^3x' \varphi_{j\beta}^\dagger(\mathbf{x}') V_{\text{as}}(\mathbf{x} - \mathbf{x}') \varphi_{j\beta}(\mathbf{x}') \varphi_{la}^0(\mathbf{x}) \\ &= \theta_{ka} \sum_i a_{ki,a}^\dagger I_{\text{HF}}^{il,a}, \end{aligned} \quad (3.83)$$

with the Hartree-Fock term as in Eq. (3.37).

As mentioned in Ref. [246] the orbital-shift equation (3.71) is singular. When adding the Kohn-Sham orbitals φ_{ka} multiplied by an arbitrary constant to the orbital shifts ψ_{ka}^\dagger one obtains a new solution. Nevertheless, one can solve the equation due to two facts: (i) It is clear from the definition of the orbital shifts that the relevant solution must be orthogonal to the Kohn-Sham orbitals. (ii) Since the right-hand side of Eq. (3.71) is orthogonal to the Kohn-Sham orbitals φ_{ka} one can use the conjugate-gradient method [248], as suggested by Kümmel and Perdew.

We found a simpler approach by using the Moore–Penrose pseudo inverse of the matrix M_a , denoted M_a^+ . The minimal solution (with respect to the Euclidian norm) of the system of linear equations (3.80) is then given by

$$\mathbf{b}_{ka}^\dagger = M_a^+ \mathbf{c}_{ka}. \quad (3.84)$$

Since the ‘correct’ orbital shifts are orthogonal to the orbitals this will always give the intended solution. As the Moore–Penrose pseudo inverse is a standard algorithm in linear algebra libraries this method is easier and more straightforward to implement and numerically more stable.

THIRD STEP: UPDATE THE OEP

The new OEP is obtained using a method by Kümmel and Perdew [246, 247]. For the update procedure,

$$v_{\text{Hxc},a}^{(\text{new})}(\mathbf{x}) = v_{\text{Hxc},a}^{(\text{old})}(\mathbf{x}) + c_S S_a(\mathbf{x}), \quad (3.85)$$

we make use of the OEP equation (3.62) via the definition of

$$S_a(\mathbf{x}) \equiv \sum_k \left[\psi_{ka}^\dagger(\mathbf{x}) \varphi_{ka}(\mathbf{x}) + \text{c.c.} - |\varphi_{ka}(\mathbf{x})|^2 \frac{\partial E_{\text{Hxc}}}{\partial \varepsilon_{ka}} \right]. \quad (3.86)$$

The positive constant c_S has to be chosen by trial and error. Larger values lead to faster convergence but with too large values the algorithm does not converge. If the algorithm converges the solution is independent of c_S . We discuss the role of c_S more detailed in the following but let us first motivate that the update procedure indeed makes sense. If the new OEP solves the OEP equation, S_a vanishes and we reach convergence. On the other hand S_a is an indicator for the error of the OEP and it is thus straightforward to use it to construct the new OEP.

The new $v_{\text{Hxc},a}$ is then reinserted into the Kohn-Sham equation and the self-consistency cycle is started over until convergence in the energies is reached. In practice however, the iteration algorithm is slightly modified to speed up convergence: Steps two and three are repeated multiple times within one iteration cycle without updating the Kohn-Sham orbitals. The benefit of this modification is that we only need to calculate the numerically costly u_{ka}^{Hxc} once before each sub-iteration cycle. With only 5 to 10 sub-iterations we can reduce the number of iterations by up to a factor of 5.

We determine S_a by expanding ψ_{ka}^\dagger and φ_{ka} in terms of the free orbitals as in the previous step, which gives

$$\begin{aligned} S_{ij,a} &\equiv \int d^3x \varphi_{ia}^{0\dagger}(\mathbf{x}) \tilde{S}_a(\mathbf{x}) \varphi_{ja}^0(\mathbf{x}) \\ &= \int d^3x \varphi_{ia}^{0\dagger}(\mathbf{x}) \sum_k \left[\psi_{ka}^\dagger(\mathbf{x}) \varphi_{ka}(\mathbf{x}) + \text{c.c.} - |\varphi_{ka}(\mathbf{x})|^2 \frac{\partial E_{\text{Hxc}}}{\partial \varepsilon_{ka}} \right] \varphi_{ja}^0(\mathbf{x}) \\ &= \sum_k \sum_{l,m} \left[b_{kl,a}^\dagger a_{km,a} + \text{c.c.} - a_{kl,a}^\dagger a_{km,a} \frac{\partial E_{\text{Hxc}}}{\partial \varepsilon_{ka}} \right] \int d^3x \varphi_{ia}^{0\dagger}(\mathbf{x}) \varphi_{la}^{0\dagger}(\mathbf{x}) \varphi_{ma}^0(\mathbf{x}) \varphi_{ja}^0(\mathbf{x}), \quad (3.87) \end{aligned}$$

where the integral can be simplified by

$$\begin{aligned}
& \int d^3x \varphi_{ia}^{0\dagger}(\mathbf{x}) \varphi_{ia}^{0\dagger}(\mathbf{x}) \varphi_{ma}^0(\mathbf{x}) \varphi_{ja}^0(\mathbf{x}) \\
&= \int d\mathbf{x} x^2 \frac{u_{n_i l_i}^{0\dagger}(\mathbf{x})}{x} \frac{u_{n_l l_l}^{0\dagger}(\mathbf{x})}{x} \frac{u_{n_m l_m}^0(\mathbf{x})}{x} \frac{u_{n_j l_j}^0(\mathbf{x})}{x} \int d\widehat{\mathbf{x}} \mathcal{Y}_{j_i m_i}^{l_i s \dagger}(\widehat{\mathbf{x}}) \mathcal{Y}_{j_l m_l}^{l_l s \dagger}(\widehat{\mathbf{x}}) \mathcal{Y}_{j_m m_m}^{l_m s}(\widehat{\mathbf{x}}) \mathcal{Y}_{j_j m_j}^{l_j s}(\widehat{\mathbf{x}}) \\
&= \int d\mathbf{x} \frac{1}{x^2} u_{n_i l_i}^{0\dagger}(\mathbf{x}) u_{n_l l_l}^{0\dagger}(\mathbf{x}) u_{n_m l_m}^0(\mathbf{x}) u_{n_j l_j}^0(\mathbf{x}) \\
&\times \sum_L (-1)^{j_i+m_i+j_l+m_l+j_m+m_m+j_j+1} \begin{Bmatrix} l_i & l_l & L \\ j_l & j_i & \frac{1}{2} \end{Bmatrix} \begin{Bmatrix} l_m & l_j & L \\ j_j & j_m & \frac{1}{2} \end{Bmatrix} C_{l_i 0 l_0}^{L0} C_{l_m 0 l_0}^{L0} C_{j_i(-m_i) j_l m_l}^{L(m_i-m_i)} C_{l_m(-m_m) j_j m_j}^{L(m_j-m_m)} \\
&\times \frac{\sqrt{(2j_i+1)(2j_l+1)(2j_m+1)(2j_j+1)(2l_i+1)(2l_l+1)(2l_m+1)(2l_j+1)}}{4\pi(2L+1)}, \quad (3.88)
\end{aligned}$$

with tensor spherical harmonics

$$\mathcal{Y}_{jm}^{ls}(\widehat{\mathbf{x}}) = \sum_{m_l, m_s} C_{l m_l m_s}^{jm} Y_l^{m_l}(\widehat{\mathbf{x}}) \chi_{s, m_s}, \quad (3.89)$$

and where we have used [249, p. 206]:

$$\begin{aligned}
\mathcal{Y}_{j_1 m_1}^{l_1 \frac{1}{2}}(\widehat{\mathbf{x}}) \mathcal{Y}_{j_2 m_2}^{l_2 \frac{1}{2}}(\widehat{\mathbf{x}}) &= \sum_{L, M} (-1)^{j_1+m_1+j_2+L+\frac{1}{2}} \begin{Bmatrix} l_1 & l_2 & L \\ j_2 & j_1 & \frac{1}{2} \end{Bmatrix} \\
&\times \sqrt{\frac{(2j_1+1)(2j_2+1)(2l_1+1)(2l_2+1)}{4\pi(2L+1)}} C_{l_1 0 l_2 0}^{L0} C_{j_1(-m_1) j_2 m_2}^{LM} Y_L^M(\widehat{\mathbf{x}}). \quad (3.90)
\end{aligned}$$

We now want to come back to the role of the constant c_s . For deeper insights we briefly want to review the direct update procedure for the OEP which was widely used before Kümmel and Perdew introduced their algorithm.

To obtain an expression for $v_{\text{Hxc},a}$ one solves the orbital-shift equation (3.71) for

$$v_{\text{KS},a}(\mathbf{x}) \psi_{ka}^\dagger(\mathbf{x}) = [u_{ka}^{\text{Hxc}}(\mathbf{x}) - \theta_{ka} v_{\text{Hxc},a}(\mathbf{x}) - \bar{u}_{ka}^{\text{Hxc}} + \bar{v}_{ka}^{\text{Hxc}}] \varphi_{ka}^\dagger(\mathbf{x}) + \left[\frac{\nabla^2}{2m} + \varepsilon_{ka} \right] \psi_{ka}^\dagger(\mathbf{x}), \quad (3.91)$$

plugs it into the OEP equation (3.62) multiplied by $v_{\text{KS},a}$,

$$\begin{aligned}
& \sum_k \left\{ [u_{ka}^{\text{Hxc}}(\mathbf{x}) - \theta_{ka} v_{\text{Hxc},a}(\mathbf{x}) - \bar{u}_{ka}^{\text{Hxc}} + \bar{v}_{ka}^{\text{Hxc}}] |\varphi_{ka}(\mathbf{x})|^2 + \left(\frac{\nabla^2}{2m} + \varepsilon_{ka} \right) \psi_{ka}^\dagger(\mathbf{x}) \varphi_{ka}(\mathbf{x}) + \text{c.c.} \right\} \\
&= \sum_k |\varphi_{ka}(\mathbf{x})|^2 \frac{\partial E_{\text{Hxc}}}{\partial \varepsilon_{ka}} v_{\text{KS},a}(\mathbf{x}), \quad (3.92)
\end{aligned}$$

and solves for the OEP

$$v_{\text{Hxc},a}(\mathbf{x}) = \frac{1}{2\rho_a(\mathbf{x})} \sum_k \left\{ [u_{ka}^{\text{Hxc}}(\mathbf{x}) - \bar{u}_{ka}^{\text{Hxc}} + \bar{v}_{ka}^{\text{Hxc}}] |\varphi_{ka}(\mathbf{x})|^2 + \left(\frac{\nabla^2}{2m} + \varepsilon_{ka} \right) \psi_{ka}^\dagger(\mathbf{x}) \varphi_{ka}(\mathbf{x}) + \text{c.c.} - \frac{\partial E_{\text{Hxc}}}{\partial \varepsilon_{ka}} v_{\text{KS},a}(\mathbf{x}) |\varphi_{ka}(\mathbf{x})|^2 \right\}. \quad (3.93)$$

This also shows that the OEP can be expressed explicitly in terms of the (occupied) Kohn-Sham orbitals and the orbital shifts. And one also sees that for finite systems the division by the density can be numerically cumbersome since it goes to zero for large distances x .

In order to understand Kümmel's and Perdew's update procedure we solve the orbital-shift equation for $[\nabla^2/(2m) + \varepsilon_{ka}] \psi_{ka}^\dagger$, insert it into Eq. (3.93), and obtain

$$v_{\text{Hxc},a}(\mathbf{x}) = v_{\text{Hxc},a}(\mathbf{x}) + \frac{v_{\text{KS},a}(\mathbf{x})}{2\rho_a(\mathbf{x})} S_a(\mathbf{x}), \quad (3.94)$$

which obviously is an identity if the OEP equation is fulfilled as we inserted the orbital-shift equation into itself and $S_a = 0$. During an iterative solution process, where one only has approximations of the orbitals and the orbital shifts, the second term on the right-hand side is nonzero and rather is an error term. Since S_a contains all the information of the OEP equation it is most important. For a better approximation of the OEP we rather have to subtract this error term

$$v_{\text{Hxc},a}^{(\text{new})}(\mathbf{x}) = v_{\text{Hxc},a}^{(\text{old})}(\mathbf{x}) - \frac{v_{\text{Hxc},a}^{(\text{old})}(\mathbf{x})}{2\rho_a(\mathbf{x})} S_a(\mathbf{x}), \quad (3.95)$$

where one also replaces the full Kohn-Sham potential by the OEP $v_{\text{Hxc},a}$ for stability reasons (see Ref [247] for details). One could also use the iteration procedure above rather than Eq. (3.85). However, this still involves a division by the density and it is easier to approximate the term $-v_{\text{Hxc},a}/(2\rho)$ by the constant c_S . As mentioned earlier, it has to be chosen by trial and error but we found our calculations to be pretty robust in a range $c_S = (10 - 30) \text{ MeV fm}^3$.

3.2.3 THE KRIEGER-LI-IAFRATE APPROXIMATION

Before we discuss the details of OEP solution and the inclusion of correlations we want to discuss the approximation by Joseph B. Krieger, Yan Li, and Gerald J. Iafrate (KLI) [250, 251]. It has been found in the exchange-only case for Coulomb systems to be quite accurate.

The presence of the Green's function in the left- and right-hand side of OEP equation (3.58), *i.e.*, in the response function χ_a and the inhomogeneity $\Lambda_{\text{Hxc},a}$, is a source of inefficiency. It depends on the complete Kohn-Sham spectrum (and not only the occupied states). The KLI approximation expounds a way to avoid this evaluation. It is based on a closure approximation for the Green's

function: The energy difference in the denominator is replaced by an averaged difference,

$$G_{ka}(\mathbf{x}, \mathbf{x}') \approx \sum_{l \neq k} \frac{\varphi_{la}^\dagger(\mathbf{x}') \varphi_{la}(\mathbf{x})}{\Delta \bar{\varepsilon}} = \frac{1}{\Delta \bar{\varepsilon}} [\delta^{(3)}(\mathbf{x} - \mathbf{x}') - \varphi_{ka}^\dagger(\mathbf{x}') \varphi_{ka}(\mathbf{x})]. \quad (3.96)$$

We insert this expression into the OEP integral equation (3.58) and obtain for the left-hand side

$$\begin{aligned} \int d^3 x' v_{\text{Hxc},a}(\mathbf{x}') \chi_a(\mathbf{x}', \mathbf{x}) &= - \sum_k \int d^3 x' v_{\text{Hxc},a}(\mathbf{x}') \theta_{ka} \varphi_{ka}^\dagger(\mathbf{x}') G_{ka}(\mathbf{x}', \mathbf{x}) \varphi_{ka}(\mathbf{x}) + \text{c.c.} \\ &\stackrel{\text{KLI}}{\approx} - \frac{2}{\Delta \bar{\varepsilon}} v_{\text{Hxc},a}(\mathbf{x}) \rho_a(\mathbf{x}) \\ &\quad + \frac{1}{\Delta \bar{\varepsilon}} \sum_k \int d^3 x' [v_{\text{Hxc},a}(\mathbf{x}') \theta_{ka} |\varphi_{ka}(\mathbf{x}')|^2 |\varphi_{ka}(\mathbf{x})|^2 + \text{c.c.}], \end{aligned} \quad (3.97)$$

and for the right-hand side

$$\begin{aligned} \Lambda_{\text{Hxc},a}(\mathbf{x}) &= \sum_k \left\{ - \int d^3 x' [\varphi_{ka}^\dagger(\mathbf{x}') u_{ka}^{\text{Hxc}}(\mathbf{x}') G_{ka}(\mathbf{x}', \mathbf{x}) \varphi_{ka}(\mathbf{x}) + \text{c.c.}] + |\varphi_{ka}(\mathbf{x})|^2 \frac{\partial E_{\text{Hxc}}}{\partial \varepsilon_{ka}} \right\} \\ &\stackrel{\text{KLI}}{\approx} - \frac{1}{\Delta \bar{\varepsilon}} \sum_k [\varphi_{ka}^\dagger(\mathbf{x}) u_{ka}^{\text{Hxc}}(\mathbf{x}) \varphi_{ka}(\mathbf{x}) + \text{c.c.}] \\ &\quad + \frac{1}{\Delta \bar{\varepsilon}} \sum_k |\varphi_{ka}(\mathbf{x})|^2 \int d^3 x' [\varphi_{ka}^\dagger(\mathbf{x}') u_{ka}^{\text{Hxc}}(\mathbf{x}') \varphi_{ka}(\mathbf{x}') + \text{c.c.}] \\ &\quad + \sum_k |\varphi_{ka}(\mathbf{x})|^2 \frac{\partial E_{\text{Hxc}}}{\partial \varepsilon_{ka}}, \end{aligned} \quad (3.98)$$

which solved for the OEP gives

$$v_{\text{Hxc},a}(\mathbf{x}) = \frac{1}{2\rho_a(\mathbf{x})} \sum_k \left\{ \frac{\delta E_{\text{Hxc}}}{\delta \varphi_{ka}(\mathbf{x})} \varphi_{ka}(\mathbf{x}) + \text{c.c.} + |\varphi_{ka}(\mathbf{x})|^2 \left[\Delta v_{ka} - \Delta \bar{\varepsilon} \frac{\partial E_{\text{Hxc}}}{\partial \varepsilon_{ka}} \right] \right\}, \quad (3.99)$$

with

$$\Delta v_{ka} = \int d^3 x' \left[\theta_{ka} |\varphi_{ka}(\mathbf{x}')|^2 v_{\text{Hxc},a}(\mathbf{x}') - \frac{\delta E_{\text{Hxc}}}{\delta \varphi_{ka}(\mathbf{x}')} \varphi_{ka}(\mathbf{x}') \right] + \text{c.c.} \quad (3.100)$$

Note that the energy average only appears in front of the derivatives of E_{Hxc} with respect to the single-particle energies, introducing a new energy scale. If the energy does not explicitly depend on ε_{ka} , *e.g.*, in the exact-exchange approximation, the KLI approximation becomes unambiguous. However, in the KLI approximation one always neglects this term to be consistent with the closure approximation. The effect of neglecting this term, especially when including correlations, has to be investigated in detail. For Coulomb systems it has been found for the relativistic exchange that this approximation

is excellent [245]. The OEP in the KLI approximation is thus given by

$$\begin{aligned} v_{\text{Hxc},a}^{\text{KLI}}(\mathbf{x}) &= \frac{1}{2\rho_a(\mathbf{x})} \sum_k \left\{ \frac{\delta E_{\text{Hxc}}}{\delta \varphi_{ka}(\mathbf{x})} \varphi_{ka}(\mathbf{x}) + \text{c.c.} + |\varphi_{ka}(\mathbf{x})|^2 \Delta v_{ka}^{\text{KLI}} \right\} \\ &= \frac{1}{2\rho_a(\mathbf{x})} \sum_k |\varphi_{ka}(\mathbf{x})|^2 [u_{ka}^{\text{Hxc}}(\mathbf{x}) + \bar{v}_{ka}^{\text{KLI,Hxc}} - \bar{u}_{ka}^{\text{Hxc}} + \text{c.c.}], \end{aligned} \quad (3.101)$$

with the same definitions for u , \bar{u} , and \bar{v} as above. As $v_{\text{Hxc},a}^{\text{KLI}}$ appears on the right-hand side through the definition of $\Delta v_{ka}^{\text{KLI}}$ we have not found a solution, yet. However, we can iterate Eq. (3.101) in a self-consistency loop until we reach convergence.

Comparing the KLI approximation to Eq. (3.93), with the orbital shifts $\psi_{ka}^\dagger = 0$ set to zero, indicates it to be some sort of mean-field approximation for the full OEP [251, 252].

The results obtained in the KLI approximation will always be above the full OEP result, since the OEP energy is a minimum for local potentials. For the energy of Coulomb systems it was found that the difference between the KLI and full OEP result was systematically around 1/3 of the difference between OEP and Hartree-Fock [34].

Since we use nuclear matrix elements in a harmonic-oscillator basis and cannot divide by the density we need to derive a similar solution algorithm by Kümmel and Perdew: If one adds and subtracts $\theta_{ka} v_{\text{Hxc},a}^{\text{KLI}}(\mathbf{x})$ to the summand in Eq. (3.101) one obtains a similar update expression as in Eq. (3.94)

$$v_{\text{Hxc},a}^{\text{KLI}}(\mathbf{x}) = v_{\text{Hxc},a}^{\text{KLI}}(\mathbf{x}) + \frac{1}{2\rho_a(\mathbf{x})} \sum_k |\varphi_{ka}(\mathbf{x})|^2 [u_{ka}^{\text{Hxc}}(\mathbf{x}) - \theta_{ka} v_{\text{Hxc},a}^{\text{KLI}}(\mathbf{x}) + \bar{v}_{ka}^{\text{KLI,Hxc}} - \bar{u}_{ka}^{\text{Hxc}} + \text{c.c.}]. \quad (3.102)$$

We further define the quantity

$$\eta_{ka}^\dagger(\mathbf{x}) = \varphi_{ka}^\dagger(\mathbf{x}) [u_{ka}^{\text{Hxc}}(\mathbf{x}) - \theta_{ka} v_{\text{Hxc},a}^{\text{KLI}}(\mathbf{x}) + \bar{v}_{ka}^{\text{KLI,Hxc}} - \bar{u}_{ka}^{\text{Hxc}}], \quad (3.103)$$

and expand it in harmonic-oscillator orbitals

$$\eta_{ka}^\dagger(\mathbf{x}) = \sum_l e_{kl,a}^\dagger \varphi_{la}^{0\dagger}. \quad (3.104)$$

For the calculation of the expansion coefficients $e_{kl,a}^\dagger$ we do not need to solve a system of linear equations as in the full OEP solution. They are straightforwardly given by

$$\begin{aligned} e_{km,a}^\dagger &= \int d^3x \eta_{ka}^\dagger(\mathbf{x}) \varphi_{ma}^0(\mathbf{x}) \\ &= \sum_l a_{kl,a}^\dagger \left\{ \int d^3x \varphi_{la}^{0\dagger}(\mathbf{x}) [u_{ka}^{\text{Hxc}}(\mathbf{x}) - \theta_{ka} v_{\text{Hxc},a}^{\text{KLI}}(\mathbf{x})] \varphi_{ma}^0(\mathbf{x}) + \delta_{lm} (\bar{v}_{ka}^{\text{KLI,Hxc}} - \bar{u}_{ka}^{\text{Hxc}}) \right\}. \end{aligned} \quad (3.105)$$

With that definition we introduce

$$T_a(\mathbf{x}) = \sum_k \varphi_{ka}(\mathbf{x}) \eta_{ka}^\dagger(\mathbf{x}) + \text{c.c.}, \quad (3.106)$$

and rewrite Eq. (3.102) as follows

$$v_{\text{Hxc},a}^{\text{KLI}}(\mathbf{x}) = v_{\text{Hxc},a}^{\text{KLI}}(\mathbf{x}) + \frac{1}{2\rho_a(\mathbf{x})} T_a(\mathbf{x}). \quad (3.107)$$

Similarly to Kümmel and Perdew we approximate the density with a constant c_T and use the update procedure

$$v_{\text{Hxc},a}^{\text{KLI},(\text{new})}(\mathbf{x}) = v_{\text{Hxc},a}^{\text{KLI},(\text{old})}(\mathbf{x}) - c_T T_a(\mathbf{x}). \quad (3.108)$$

3.3 INCLUDING CORRELATIONS AT SECOND ORDER

AS SEEN IN CHAPTER 2 FOR MATTER, contributions beyond the Hartree-Fock level play an important role in nuclear physics. Due to the similarities of Hartree-Fock and the exact-exchange functional one can conclude that correlations are crucial here as well. In the following we first want to derive an exact formula for E_{Hxc} using many-body perturbation theory and then study the contributions at second order in detail. This Section follows the discussion of Ref. [35], where more details can be found.

3.3.1 DERIVATION OF AN EXACT EXPRESSION FOR E_{Hxc}

For this derivation we start with the Kohn-Sham Hamiltonian as the unperturbed system. Assuming the Kohn-Sham potential is known, this Hamiltonian reads

$$\hat{H}_{\text{KS}} = \sum_a \hat{H}_{\text{KS},a} = \hat{T} + \sum_a \int d^3x \hat{\rho}_a(\mathbf{x}) v_{\text{KS},a}(\mathbf{x}), \quad (3.109)$$

with ground-state energy E_{KS} and ground state $|\Phi_{\text{KS}}\rangle$, written as a Slater determinant in second quantisation,

$$|\Phi_{\text{KS}}\rangle = \prod_{\epsilon_{ka} \leq \epsilon_{\text{F}}} \hat{a}_{ka}^\dagger |0\rangle. \quad (3.110)$$

Here \hat{a}_{ka} and \hat{a}_{ka}^\dagger denote the annihilation and creation operator for the single-particle states φ_{ka} , respectively, and $|0\rangle$ the Kohn-Sham vacuum, *i.e.*, $\hat{a}_{ka}|0\rangle = 0$. The Kohn-Sham energy and density (being equal to the density of the interacting system by construction) read

$$E_{\text{KS}} = T_{\text{KS}} + \sum_a \int d^3x \rho_a(\mathbf{x}) v_{\text{KS},a}(\mathbf{x}) = \sum_{k,a} \theta_{ka} \epsilon_{ka}, \quad (3.111)$$

$$\rho_a(\mathbf{x}) = \langle \Phi_{\text{KS}} | \hat{\rho}_a(\mathbf{x}) | \Phi_{\text{KS}} \rangle = \sum_k \theta_{ka} |\varphi_{ka}(\mathbf{x})|^2. \quad (3.112)$$

From the Kohn-Sham Hamiltonian we also obtain the explicit form of the field operator in the Heisenberg picture,

$$\hat{\psi}_{\text{KS},a}(\mathbf{x}, t) = \exp(i\hat{H}_{\text{KS},a}t) \hat{\psi}_a \exp(-i\hat{H}_{\text{KS},a}t) = \sum_k \hat{a}_{ka} \varphi_{ka}(\mathbf{x}) e^{-i\epsilon_{ka}t}, \quad (3.113)$$

from which we can evaluate the Kohn-Sham Green's function,

$$\begin{aligned}
G_a(\mathbf{x}, t; \mathbf{x}', t') &= i\theta(t' - t) \sum_{\varepsilon_{ka} \leq \varepsilon_F} \varphi_{ka}(\mathbf{x}) \varphi_{ka}^\dagger(\mathbf{x}') e^{-i\varepsilon_{ka}(t-t')} \\
&\quad - i\theta(t - t') \sum_{\varepsilon_{ka} > \varepsilon_F} \varphi_{ka}(\mathbf{x}) \varphi_{ka}^\dagger(\mathbf{x}') e^{-i\varepsilon_{ka}(t-t')}. \tag{3.114}
\end{aligned}$$

As mentioned above, we want to take \widehat{H}_{KS} as reference and decompose the full Hamiltonian of the interacting system $\widehat{H} = \widehat{T} + \widehat{V} + \widehat{V}_{\text{ext}}$ into \widehat{H}_{KS} and a remainder (perturbation) \widehat{H}_1 . Thus, \widehat{H}_1 compensates for the interaction parts which are not present in the Kohn-Sham Hamiltonian, *i.e.*,

$$\widehat{H}_1 = \widehat{V} - \sum_a \int d^3x \widehat{\rho}_a(\mathbf{x}) v_{\text{Hxc},a}(\mathbf{x}), \tag{3.115}$$

where $v_{\text{Hxc},a} = v_{\text{KS},a} - v_{\text{ext}}$, as in the previous Section.

Following the standard derivations of many-body perturbation theory one finally obtains an expression for the full Hartree-exchange-correlation energy, including correlations

$$\begin{aligned}
E_{\text{Hxc}} &= E_1 + \sum_a \int d^3x \rho_a(\mathbf{x}) v_{\text{Hxc},a}(\mathbf{x}) \\
&= -\frac{1}{2} \sum_{a,\beta} \int d^3x d^3y \langle \Phi_{\text{KS}} | \widehat{\psi}_a^\dagger(\mathbf{x}) \widehat{\psi}_\beta^\dagger(\mathbf{y}) \widehat{V}(\mathbf{x}, \mathbf{y}) \widehat{\psi}_\beta(\mathbf{y}) \widehat{\psi}_a(\mathbf{x}) | \Phi_{\text{KS}} \rangle \\
&\quad + \lim_{\varepsilon \rightarrow 0} \sum_{n=0}^{\infty} \frac{(-i)^n}{(n+1)!} \int_{-\infty}^{\infty} dt_1 \cdots dt_n e^{-\varepsilon(|t_1| + \dots + |t_n|)} \\
&\quad \times : \langle \Phi_{\text{KS}} | T[\widehat{H}_{1,I}(0) \widehat{H}_{1,I}(t_1) \cdots \widehat{H}_{1,I}(t_n)] | \Phi_{\text{KS}} \rangle :, \tag{3.116}
\end{aligned}$$

where the $:$ correspond to summing only over connected diagrams according to Wick's theorem. Note that the first term is the first-order contribution corresponding to the exchange-only energy (3.63). The second term corresponds to the correlation energy E_c , for which we need the Green's function (3.114) and v_{Hxc} . Thus, the correlation energy depends on φ_{ka} , ε_{ka} and v_{Hxc} . The dependence on v_{Hxc} shows that E_c is a non-linear functional – it depends on its own functional derivative. There are two ways to solve this problem: Either one solves the non-linear equation directly or one tries to linearise it first. Since the first is a highly non-trivial task we pursue the latter strategy [243].

3.3.2 THE CORRELATION ENERGY AT SECOND ORDER

The linearisation of the OEP equation based on Eq. (3.116) motivates an expansion in interaction vertices (in Coulomb systems that corresponds to an expansion in powers of the coupling e^2). The first order is the exchange-only energy and all higher terms contribute to E_c . Thus, we decompose

the energy and the potential as follows

$$E_{\text{Hxc}} = E_{\text{Hx}} + E_{\text{c}}^{(2)} + \dots, \quad (3.117)$$

$$v_{\text{Hxc},a}(\mathbf{x}) = v_{\text{Hx},a}(\mathbf{x}) + v_{\text{c},a}^{(2)}(\mathbf{x}) + \dots. \quad (3.118)$$

Inserting these series into the OEP equation (3.58) leads to a power series with respect to the potential vertex on both the left- and right-hand side. At the lowest order, *i.e.*, terms containing only one potential matrix element, the left-hand side contains only v_{Hx} and the right-hand side is solely determined by the functional derivative of E_{Hx} with respect to the orbitals. Hence, we end up with only the OEP equations in the exact-exchange approximation. At second order, however, the non-linearity shows up for the first time. Considering terms where the potential matrix elements appear twice, we find that the second-order correlation functional is given by two terms

$$E_{\text{c}}^{(2)} = E_{\text{c}}^{\text{MBPT}(2)} + E_{\text{c}}^{\Delta\text{HF}}. \quad (3.119)$$

The first contribution is given by the second-order many-body perturbation theory expression as in Eq. (3.38) with the Hartree-Fock orbitals and energies replaced by the Kohn-Sham orbitals and energies. The second term accounts for the systematic error using the Kohn-Sham Hamiltonian in the perturbative expansion rather than the commonly used reference – the Hartree-Fock Hamiltonian. At lowest order this difference is given by

$$E_{\text{c}}^{\Delta\text{HF}} = \sum_{\sigma,a} \sum_{i,a} \frac{\theta_{i\sigma} \bar{\theta}_{aa}}{\varepsilon_{i\sigma} - \varepsilon_{aa}} \left| \int d^3x \varphi_{i\sigma}^\dagger(\mathbf{x}) v_{\text{Hx},a}(\mathbf{x}) \varphi_{aa}(\mathbf{x}) - \sum_{j,\tau} \theta_{j\tau} (i\sigma j\tau | V | j\tau aa) \right|^2, \quad (3.120)$$

where the matrix element $(\cdot | V | \cdot)$ is defined as in Eq. (3.39). As the OEP energy is always higher than the Hartree-Fock energy this contribution is always negative.

In order to use the correlation-energy functional (3.119) in a self-consistent solution of the OEP equation, as discussed in the previous Section, we need to evaluate the functional derivative with respect to the density to obtain the correlation part of the potential,

$$v_{\text{c},a}^{(2)}(\mathbf{x}) = \frac{\delta E_{\text{c}}^{(2)}[\varphi_{ka}, \varepsilon_{ka}, v_{\text{Hx},a}]}{\delta \rho_a(\mathbf{x})}. \quad (3.121)$$

The first term $E_{\text{c}}^{\text{MBPT}(2)}$ does not depend on v_{Hx} and the evaluation is straightforward. We discuss the details below. The second term, however, depends on the Hartree-exchange potential explicitly and thus involves not only derivatives with respect to the orbitals and energies when using the chain rule of functional differentiation in Eq. (3.47) but also with respect to the potential. Though fundamentally not different from the other differentiations, this calculation is rather cumbersome in-

cluding also differentiations of the response function and inhomogeneity of the OEP equation. For Coulomb systems the total contribution of $E_c^{\Delta\text{HF}}$ was found to be rather small and also for nuclear systems we find only little difference between the Hartree-Fock and OEP result, as can be seen in the next Chapter. The uncertainties of the second-order MBPT result are, especially for unevolved nuclear forces, larger than this difference. We thus neglect $E_c^{\Delta\text{HF}}$ in these first explorations.

FUNCTIONAL DERIVATIVES OF THE CORRELATION ENERGY

According to many-body perturbation theory the correlations contribution writes [see Eq. (3.38)]

$$\begin{aligned} E_c[\varphi, \varepsilon, \theta] &= \frac{1}{4} \sum_{a_i, a_j, a_a, a_b} \sum_{i, j, a, b} \theta_{ia_i} \theta_{ja_j} \bar{\theta}_{aa_a} \bar{\theta}_{ba_b} \frac{|(ia_i ja_j | V | aa_a ba_b) - (ia_i ja_j | V | ba_b aa_a)|^2}{\varepsilon_{ia_i} + \varepsilon_{ja_j} - \varepsilon_{aa_a} - \varepsilon_{ba_b}} \\ &= \frac{1}{2} \sum_{a_i, a_j, a_a, a_b} \sum_{i, j, a, b} \frac{\theta_{ia_i} \theta_{ja_j} \bar{\theta}_{aa_a} \bar{\theta}_{ba_b}}{\varepsilon_{ia_i} + \varepsilon_{ja_j} - \varepsilon_{aa_a} - \varepsilon_{ba_b}} \\ &\quad \times (ia_i ja_j | V | aa_a ba_b) [(aa_a ba_b | V | ia_i ja_j) - (ba_b aa_a | V | ja_i ia_i)], \end{aligned} \quad (3.122)$$

where the matrix elements are defined as in Eq. (3.41). Accordingly to the case without correlations, the orbital shifts are given by

$$\begin{aligned} \psi_{ka}^\dagger(\mathbf{x}) &= \int d^3 \mathbf{x}' \varphi_{ka}^\dagger(\mathbf{x}') [u_{ka}^{\text{Hx}}(\mathbf{x}') + u_{ka}^c(\mathbf{x}') - \theta_{ka} \nu_{\text{Hxc}, a}(\mathbf{x}')] G_{km_t}(\mathbf{x}', \mathbf{x}) \\ &= \sum_{l \neq k} \int d^3 \mathbf{x}' \frac{\varphi_{ka}^\dagger(\mathbf{x}') [u_{ka}^{\text{Hx}}(\mathbf{x}') + u_{ka}^c(\mathbf{x}') - \theta_{ka} \nu_{\text{Hxc}, a}(\mathbf{x}')] \varphi_{la}(\mathbf{x}') \varphi_{la}^\dagger(\mathbf{x})}{\varepsilon_{la} - \varepsilon_{ka}}, \end{aligned} \quad (3.123)$$

and the orbital-shift equation now reads

$$[H_{\text{KS}, a}(\mathbf{x}) - \varepsilon_{ka}] \psi_{ka}^\dagger(\mathbf{x}) = [u_{ka}^{\text{Hx}}(\mathbf{x}) + u_{ka}^c(\mathbf{x}) - \theta_{ka} \nu_{\text{Hxc}, a}(\mathbf{x}) - \bar{u}_{ka}^{\text{Hx}} - \bar{u}_{ka}^c + \bar{v}_{ka}^{\text{Hxc}}] \varphi_{ka}^\dagger(\mathbf{x}), \quad (3.124)$$

where we calculate the u -functions

$$u_{ka}^{\text{Hx}/c}(\mathbf{x}) = \frac{1}{\varphi_{ka}^\dagger(\mathbf{x})} \frac{\delta E_{\text{Hx}/c}}{\delta \varphi_{ka}(\mathbf{x})}, \quad (3.125)$$

using

$$\begin{aligned} \frac{\delta (aa_a ba_b | V | ca_c da_d)}{\delta \varphi_{ka}(\mathbf{x})} &= \delta_{ck} \delta_{aa_c} \int d^3 \mathbf{x}' \varphi_{aa_a}^\dagger(\mathbf{x}) \varphi_{ba_b}^\dagger(\mathbf{x}') V(\mathbf{x} - \mathbf{x}') \varphi_{da_d}(\mathbf{x}') \\ &\quad + \delta_{dk} \delta_{aa_d} \int d^3 \mathbf{x}' \varphi_{ba_b}^\dagger(\mathbf{x}) \varphi_{aa_a}^\dagger(\mathbf{x}') V(\mathbf{x} - \mathbf{x}') \varphi_{ca_c}(\mathbf{x}'), \end{aligned} \quad (3.126)$$

and find for the correlation term

$$\begin{aligned}
u_{ka}^c(\mathbf{x}) &= \frac{1}{2} \frac{1}{\varphi_{ka}^\dagger(\mathbf{x})} \sum_{\alpha_i, \alpha_j, \alpha_a, \alpha_b} \sum_{i, j, a, b} \theta_{\alpha_i} \theta_{\alpha_j} \bar{\theta}_{\alpha_a} \bar{\theta}_{\alpha_b} \\
&\times \frac{(aa_a ba_b | V | ia_j \alpha_j) - (aa_a ba_b | V | ja_j \alpha_i)}{\varepsilon_{\alpha_i} + \varepsilon_{\alpha_j} - \varepsilon_{\alpha_a} - \varepsilon_{\alpha_b}} \\
&\times \left[\delta_{ka} \delta_{aa_a} \int d^3 \mathbf{x}' \varphi_{\alpha_i}^\dagger(\mathbf{x}) \varphi_{\alpha_j}^\dagger(\mathbf{x}') V(\mathbf{x} - \mathbf{x}') \varphi_{\alpha_b}(\mathbf{x}') \right. \\
&\quad \left. + \delta_{kb} \delta_{aa_b} \int d^3 \mathbf{x}' \varphi_{\alpha_j}^\dagger(\mathbf{x}) \varphi_{\alpha_i}^\dagger(\mathbf{x}') V(\mathbf{x} - \mathbf{x}') \varphi_{\alpha_a}(\mathbf{x}') \right] \\
&+ \frac{1}{2} \frac{1}{\varphi_{ka}^\dagger(\mathbf{x})} \sum_{\alpha_i, \alpha_j, \alpha_a, \alpha_b} \sum_{i, j, a, b} \theta_{\alpha_i} \theta_{\alpha_j} \bar{\theta}_{\alpha_a} \bar{\theta}_{\alpha_b} \frac{(ia_j \alpha_j | V | aa_a ba_b)}{\varepsilon_{\alpha_i} + \varepsilon_{\alpha_j} - \varepsilon_{\alpha_a} - \varepsilon_{\alpha_b}} \\
&\times \left[\delta_{ik} \delta_{aa_i} \int d^3 \mathbf{x}' \varphi_{\alpha_a}^\dagger(\mathbf{x}) \varphi_{\alpha_b}^\dagger(\mathbf{x}') V(\mathbf{x} - \mathbf{x}') \varphi_{\alpha_j}(\mathbf{x}') \right. \\
&\quad \left. + \delta_{jk} \delta_{aa_j} \int d^3 \mathbf{x}' \varphi_{\alpha_b}^\dagger(\mathbf{x}) \varphi_{\alpha_a}^\dagger(\mathbf{x}') V(\mathbf{x} - \mathbf{x}') \varphi_{\alpha_i}(\mathbf{x}') \right. \\
&\quad \left. - \delta_{jk} \delta_{aa_j} \int d^3 \mathbf{x}' \varphi_{\alpha_a}^\dagger(\mathbf{x}) \varphi_{\alpha_b}^\dagger(\mathbf{x}') V(\mathbf{x} - \mathbf{x}') \varphi_{\alpha_i}(\mathbf{x}') \right. \\
&\quad \left. - \delta_{ik} \delta_{aa_i} \int d^3 \mathbf{x}' \varphi_{\alpha_b}^\dagger(\mathbf{x}) \varphi_{\alpha_a}^\dagger(\mathbf{x}') V(\mathbf{x} - \mathbf{x}') \varphi_{\alpha_j}(\mathbf{x}') \right] \\
&= \frac{1}{2} \frac{\bar{\theta}_{ka}}{\varphi_{ka}^\dagger(\mathbf{x})} \sum_{\alpha_i, \alpha_j, \alpha_a} \sum_{i, j, b} \theta_{\alpha_i} \theta_{\alpha_j} \bar{\theta}_{\alpha_a} \frac{(kaba_b | V_{as} | ia_j \alpha_j)}{\varepsilon_{\alpha_i} + \varepsilon_{\alpha_j} - \varepsilon_{ka} - \varepsilon_{ba_b}} \\
&\times \int d^3 \mathbf{x}' \varphi_{\alpha_i}^\dagger(\mathbf{x}) \varphi_{\alpha_j}^\dagger(\mathbf{x}') V_{as}(\mathbf{x} - \mathbf{x}') \varphi_{\alpha_b}(\mathbf{x}') \\
&+ \frac{1}{2} \frac{\theta_{ka}}{\varphi_{ka}^\dagger(\mathbf{x})} \sum_{\alpha_j, \alpha_a, \alpha_b} \sum_{j, a, b} \theta_{\alpha_j} \bar{\theta}_{\alpha_a} \bar{\theta}_{\alpha_b} \frac{(kaja_j | V_{as} | aa_a ba_b)}{\varepsilon_{ka} + \varepsilon_{\alpha_j} - \varepsilon_{aa_a} - \varepsilon_{ba_b}} \\
&\times \int d^3 \mathbf{x}' \varphi_{\alpha_a}^\dagger(\mathbf{x}) \varphi_{\alpha_b}^\dagger(\mathbf{x}') V_{as}(\mathbf{x} - \mathbf{x}') \varphi_{\alpha_j}(\mathbf{x}'). \tag{3.127}
\end{aligned}$$

The Hartree-exchange term u_{ka}^{Hx} is given as in the exact-exchange approximation, Eq. (3.64). Except for theta function θ_{ka} it is independent of the quantum numbers (k, α) . In contrast, u_{ka}^c has a non-trivial dependence on the orbital quantum numbers. Furthermore, in the orbital-shift equation we also get a non-vanishing term $\partial E_c / \partial \varepsilon_{ka}$ since the correlation energy explicitly depends on the single-particle energies:

$$\sum_k [\psi_{ka}^\dagger(\mathbf{x}) \varphi_{ka}(\mathbf{x}) + \text{c.c.}] = \sum_k \varphi_{ka}^\dagger(\mathbf{x}) \varphi_{ka}(\mathbf{x}) \frac{\partial E_c}{\partial \varepsilon_{ka}}. \tag{3.128}$$

For the derivative on the right hand side we obtain

$$\begin{aligned} \frac{\partial E_c}{\partial \varepsilon_{ka}} &= -\frac{1}{4} \sum_{a_i, a_j, a_a, a_b} \sum_{i, j, a, b} \theta_{ia_i} \theta_{ja_j} \bar{\theta}_{aa_a} \bar{\theta}_{ba_b} (\delta_{ki} \delta_{aa_i} + \delta_{kj} \delta_{aa_j} - \delta_{ka} \delta_{aa_a} - \delta_{kb} \delta_{aa_b}) \\ &\times \frac{|(ia_j ia_j | V_{as} | a \alpha_a b \alpha_b)|^2}{(\varepsilon_{ia_i} + \varepsilon_{ja_j} - \varepsilon_{aa_a} - \varepsilon_{ba_b})^2}. \end{aligned} \quad (3.129)$$

From this equation we can easily verify the consistency criterion for the energy functional, which was derived in Eq. (3.68):

$$\sum_{k,a} \frac{\partial E_c}{\partial \varepsilon_{ka}} = 0. \quad (3.130)$$

DETAILS ON THE SECOND-ORDER CALCULATION

The solution algorithm is the same as discussed above. However, in addition to the exact-exchange term (3.83) we need to calculate u_{ka}^c . In practice we only need $\tilde{u}_{ka}^c \equiv \varphi_{ka}^\dagger u_{k,a}^c$ in terms of the harmonic-oscillator basis:

$$\begin{aligned} \tilde{u}_{kl,a}^c &\equiv \int d^3x \tilde{u}_{ka}^c(\mathbf{x}) \varphi_{la}^0(\mathbf{x}) \\ &= \frac{1}{2} \theta_{k\sigma} \sum_{a_j, a_a, a_b} \sum_{j, a, b} \frac{\theta_{ja_j} \bar{\theta}_{aa_a} \bar{\theta}_{ba_b}}{\varepsilon_{ka} + \varepsilon_{ja_j} - \varepsilon_{aa_a} - \varepsilon_{ba_b}} A_{kjab, aa_j a_a a_b} M_{baj, a_b a_a a_j}^{la} \\ &+ \frac{1}{2} \bar{\theta}_{ka} \sum_{a_i, a_j, a_b} \sum_{i, j, b} \frac{\theta_{ia_i} \theta_{ja_j} \bar{\theta}_{ba_b}}{\varepsilon_{ia_i} + \varepsilon_{ja_j} - \varepsilon_{ka} - \varepsilon_{ba_b}} B_{kbij, aa_b a_i a_j} M_{jib, a_j a_i a_b}^{la}, \end{aligned} \quad (3.131)$$

where we have defined

$$M_{abc, a_a a_b a_c}^{da_d} \equiv \sum_{n'_a, n'_b, n'_c} a_{n_a n'_a, a_a}^\dagger a_{n_b n'_b, a_b}^\dagger a_{n_c n'_c, a_c} \langle a' a_a b' a_b | V_{as} | c' a_c d a_d \rangle, \quad (3.132)$$

and

$$A_{kjab, aa_j a_a a_b} \equiv \sum_{n'_b} a_{n_b n'_b, a_b} M_{kja, aa_j a_a}^{b' a_b}, \quad (3.133)$$

$$B_{kbij, aa_b a_i a_j} \equiv \sum_{n'_j} a_{n_j n'_j, a_j} M_{kbi, aa_b a_i}^{j' a_j}. \quad (3.134)$$

WITH THIS WE CONCLUDE the discussion of the formalism and present numerical details and calculations for neutron drops in the next Chapter.

4

Finite neutron-rich systems

NEUTRON DROPS ARE A UNIQUE LABORATORY to test and improve empirical energy-density functionals and to develop *ab initio* functionals. Empirical functionals have to be fitted to data but on the neutron-rich side there are weaker constraints from experiments. One approach to improve the functional's predictions on the neutron-rich side are fits to infinite neutron matter (see, *e.g.*, Ref. [253]). Such fits to infinite systems, however, may only improve the bulk properties of the functional and cannot constrain, *e.g.*, gradient terms. A more straightforward approach would be fits to neutron drops (for recent calculations using quasi-exact methods see, *e.g.*, Refs. [172, 254, 255]). As neutron-only systems are unbound one calculates neutron drops in external traps, typically harmonic-oscillator or Wood-Saxon potentials. Such calculations can then be used to calibrate energy-density functionals [254] or as input for fits.

For the construction of non-empirical functionals neutron drops in external potentials are ideal [256]. The external potential plays a central role in the Hohenberg-Kohn theorem as the unique energy-density functional is independent of it (see. Section 1.3). By varying the external potential one can probe the functional. This makes neutron drops preferred to self-bound nuclei, which also feature problems with symmetry breaking [257].

In this Chapter we present calculations for neutron drops using many-body perturbation theory and the optimised effective potential method (see Chapter 3). We start with calculational details and benchmark studies and then show results obtained with local chiral interactions.

4.1 CALCULATIONAL DETAILS, APPROXIMATIONS, AND BENCHMARKS

STARTING POINT FOR OUR STUDIES OF NEUTRON DROPS are the calculations by Drut and Platter in Ref. [36]. They calculated neutron drops in a harmonic-oscillator potential using the exact-exchange (EEX) approximation of the OEP method. These were the first calculations in nuclear physics within this method and they compared their results to Hartree-Fock (HF) calculations finding a remarkable agreement. Their calculations were done in a cartesian harmonic-oscillator basis using the trap frequency also for the basis, such that it forms an eigenbasis of the non-interacting system.

Drut and Platter used a simple toy model for the interaction among the neutrons: The Minnesota interaction. It is a soft local NN-only interaction consisting of three Gaussians [258]. In coordinate space it takes the form

$$V(\mathbf{r}, \mathbf{r}') = \frac{1}{2} \left[V_R(r) + \frac{1}{2}(1 + \mathcal{P}_\sigma)V_t(r) + \frac{1}{2}(1 - \mathcal{P}_\sigma)V_s(r) \right] (1 + \mathcal{P}_r)\delta^{(3)}(\mathbf{r} - \mathbf{r}'), \quad (4.1)$$

with spin-exchange operator $\mathcal{P}_\sigma = \frac{1}{2}(1 + \boldsymbol{\sigma}_1 \cdot \boldsymbol{\sigma}_2)$, coordinate-space exchange operator \mathcal{P}_r , and the functions $V_i(r) = V_{0i} \exp(-\kappa_i r^2)$, where $i = R, t, s$ and the coefficients V_{0i} and κ_i are chosen to reproduce the scattering length and effective-range parameters of NN scattering. We list their values in Appendix C. The simple form of the Minnesota interaction makes it easy to implement and is on the other hand semi-realistic with reasonable results for the binding energies of light nuclei. It was also used in test calculations of the density-matrix expansion (DME) in Ref. [256] because its softness somewhat imitates renormalisation-group-evolved potentials, which are ideal to use in the DME [34].

We also performed calculations in a cartesian basis and could reproduce the results of Ref. [36]. An advantage of a cartesian basis is that one can calculate arbitrary particle numbers and spin states. However, it is computationally expensive, especially when using more advanced potentials and also including correlations at second order. As the Minnesota potential has no spin-orbit or tensor terms one can perform the calculations mainly in one direction only and easily extend it to three dimensions. This is not possible for chiral interactions, which makes the use of a cartesian basis much more expensive for these interactions. We thus work in a spherical basis, in which we can make use of the symmetries of the system. However, this limits us to spherical closed-shell systems with neutron numbers $N = 2, 8, 20, \dots$ and symmetric spin distributions.

The numerical calculations are performed in a C++ code that allows Hartree-Fock and second-order many-body-perturbation-theory calculations as well as calculations in the exact-exchange approximation of the OEP method with and without correlations at second order. The inclusion of correlations, however, is limited to the approximations discussed below. Main output observable is the total energy E and the individual contributions to it (kinetic energy E_{kin} , external energy from the trap E_{ext} ,

and the interaction contributions $E_{\text{HF}}, E^{(2)}$ or E_{HX}, E_c). We also can calculate the root-mean-square (rms) radius $\sqrt{\langle r^2 \rangle}$ with

$$\langle r^2 \rangle = \frac{1}{N} \int d^3r r^2 \rho(\mathbf{r}), \quad (4.2)$$

and the density profile $\rho(r)$.

4.1.1 MATRIX-ELEMENTS IN SINGLE-PARTICLE BASIS

The derivations in Chapter 3 make use of an expansion of the orbitals in single-particle harmonic-oscillator states. The calculations thus require the potential matrix elements in the corresponding harmonic-oscillator single-particle basis. Nuclear interactions, however, are usually formulated in a relative basis, either in momentum or coordinate space. A widely used method to transform the relative potential matrix elements in a single-particle basis is the Talmi-Moshinsky transformation and corresponding harmonic-oscillator brackets. For details on this transformation see, *e.g.*, Ref. [259]. We use a FORTRAN code provided by Morten Hjorth-Jensen with modifications from Johannes Simonis to transform the matrix elements given in a relative momentum-space basis into a single-particle harmonic-oscillator basis. It requires partial-wave decomposed matrix elements in momentum space as input. We thus first Fourier transform the Minnesota and local chiral interactions and decompose them into partial waves. For details on the partial-wave decomposition of the Minnesota potential see Appendix C and for the local chiral interactions see Ref. [152]. The integrals in the Fourier transformation are performed in a C++ routine using the adaptive integration algorithm QAG of the GNU Scientific Library (GSL) [260]. The local chiral interactions are provided by Ingo Tews and have been tested in neutron-matter calculations [150, 151]. We have tested the partial-wave-decomposed matrix elements of the Minnesota potential in Faddeev calculations of ${}^3\text{H}$ and ${}^3,4\text{He}$ and found good agreement with Ref. [258].

4.1.2 MODEL SPACE TRUNCATION AND APPROXIMATIONS

In the numerical calculations the expansion of the orbitals in harmonic-oscillator states needs to be truncated. The limit $e_{\text{max}} \geq 2k + l$ assures a truncation at shell closures. Here, k denotes the radial quantum number and l the angular momentum of the shells included in the model space. Due to runtime (and memory) constraints we are limited to $e_{\text{max}} \leq 10$. In the cartesian calculations Drut and Platter found reasonable convergence on the Hartree-Fock/ exact-exchange level at model-space sizes of $N_{\text{max}} = k_{\text{max},x}^3 = 216$, where $k_{\text{max},x}$ is the truncation of the one-dimensional harmonic-oscillator basis. These 216 basis states are reached in a spherical basis at $e_{\text{max}} = 7$, which corresponds to 240 single-particle states. However, due to the different symmetries a direct comparison may not be possible.

WE HAVE STUDIED THE KLI APPROXIMATION, discussed in Section 3.2.3, which is widely used in quantum chemistry. For small model spaces we find a good agreement with the exact-exchange results obtained without the KLI approximation. However, it requires more iterative steps in the solution algorithm and in our calculations of, *e.g.*, 8 neutrons in an $\hbar\omega = 10$ MeV trap we do not obtain converged results for $e_{\max} \gtrsim 5$. This comes as a result of the solution algorithm used for the KLI approximation. As discussed in Section 3.2.3, we cannot evaluate Eq. (3.101) directly, when using nuclear matrix elements expanded in some basis because it involves a division by the density $\rho(\mathbf{x})$. In quantum chemistry the interaction is much simpler and one does not need this expansion and can thus easily evaluate Eq. (3.101). When using the solution algorithm developed in Sec. 3.2.3, which is based on the standard algorithm by Kümmel and Perdew, we cannot perform the sub-iteration loop, iterating the OEP with the same orbitals (see Fig. 3.1). This sub-iteration, however, stabilises and speeds up the convergence of the solution algorithm. We thus conclude that the KLI approximation does not bring any benefits for nuclear systems – at least with the current solution algorithm and implementation.

When including correlations at second order we observe convergence problems in the solution algorithm. To avoid these problems we make two approximations: We (i) limit the solution for the orbital shifts to occupied orbitals and (ii) neglect the derivatives with respect to the single-particle energies in the update of the matrix S_a in Eq. (3.86). The latter is standard within the KLI approximation. When we do not limit the second step of OEP iteration to occupied orbitals (which is exact in the first-order exact-exchange approximation) we find very unnatural mixture of the single-particle levels leading to the non-convergent behaviour.

4.1.3 BENCHMARK CALCULATIONS

In order to test the calculational routines we make benchmark calculations with the Minnesota interaction for 8 neutrons in a trap with frequency $\hbar\omega = 10$ MeV and compare it to the cartesian calculations of Ref. [36]. In Fig. 4.1 we show results for the total energy (left) and the radius (right) versus basis truncation e_{\max} . While Drut and Platter found differences of the exact-exchange (dashed orange line) and Hartree-Fock (solid orange line) result of the order of ~ 10 keV, we find a remarkable agreement of both methods (filled blue and open red circles, respectively) for all e_{\max} , and converged results in agreement with Drut and Platter at $e_{\max} = 7$. We further agree with Hartree-Fock calculations of Ref. [256] (black dots). The very small deviations may be traced back to the only one-digit precision given in this Reference. Within Ref. [256] also no-core full-configuration (NCFC) calculations were performed, which we show as a solid black line with uncertainty estimates as shaded region. These non-perturbative results are assumed to be quasi exact. At first order (HF and EXX) the converged results for the energy are about 4 MeV off from the NCFC calculations but the results for the radius lies within the NCFC uncertainty band.

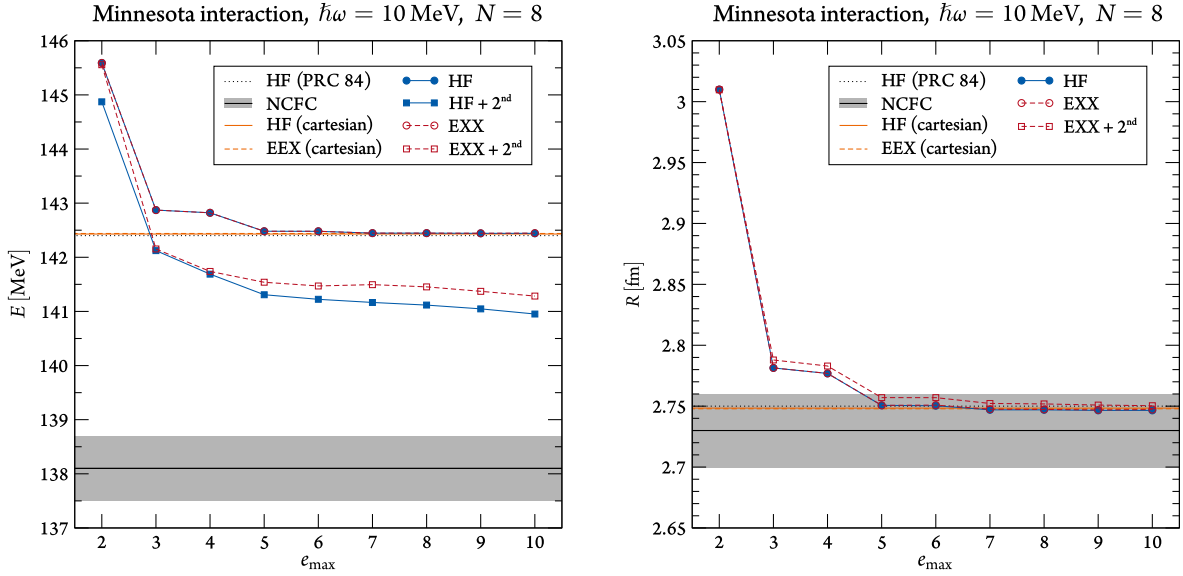


Figure 4.1: Total energy (left) and radius (right) of 8 neutrons in a harmonic-oscillator potential with $\hbar\omega = 10$ MeV as a function of the model-space size e_{\max} employing the Minnesota interaction. We show our calculations in many-body perturbation theory (blue) at Hartree-Fock level (filled circles) and second order (filled squares) and using the OEP (red) in the exact-exchange approximation (open circles) and with correlations at second order (open squares). For comparison we also show Hartree-Fock (black dots) and no-core full-configuration (solid black line with uncertainty estimate as grey band) calculations from Ref. [256] and the Hartree-Fock (solid orange line) and exact-exchange (dashed orange line) calculations from Ref. [36], which were obtained in a cartesian basis.

The inclusion of correlations at second order (squares) changes the convergence pattern of the energy. The calculations in many-body perturbation theory (blue) do not plateau within the model spaces investigated and the results are also still far off (> 2 MeV) from the NCFC calculation. This comes as a surprise as the Minnesota potential is very soft and one expects good perturbative convergence for such interactions [162]. Including correlations to the exact-exchange approximation (red) seems to be systematically worse than the second-order many-body perturbation-theory calculation, even though the orbitals are varied within this method. This can also be seen in the calculation of the radius which is more sensitive to the orbitals. However, the effect is much smaller for this observable and seems to improve with e_{\max} .

To study these effects further we also performed calculations with larger trap frequency $\hbar\omega = 20$ MeV. The results are shown in Fig. 4.2. At first order we still find for $e_{\max} \gtrsim 7$ remarkable agreement with Drut and Platter and within the numerical precision with the Hartree-Fock calculations of Ref. [256]. The second-order results show a very unnatural pattern and are clearly not converged. Note that due to runtime constraints we could not perform second-order OEP calculations for $e_{\max} = 10$. These involve a calculation of the second-order energy in every iterative step and are thus computationally much more expensive than many-body perturbation theory. These much more pronounced effects might be caused by higher densities in this more compressed system.

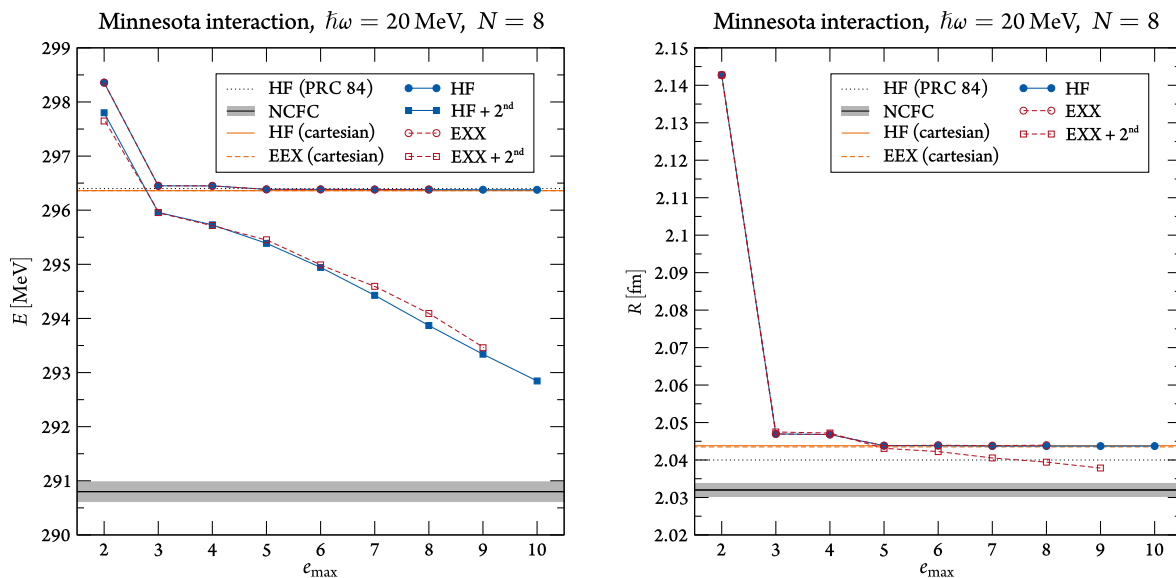


Figure 4.2: Total energy (left) and radius (right) of 8 neutrons in a harmonic-oscillator potential with $\hbar\omega = 20$ MeV as a function of the model-space size e_{\max} employing the Minnesota interaction. See Fig. 4.1 for details.

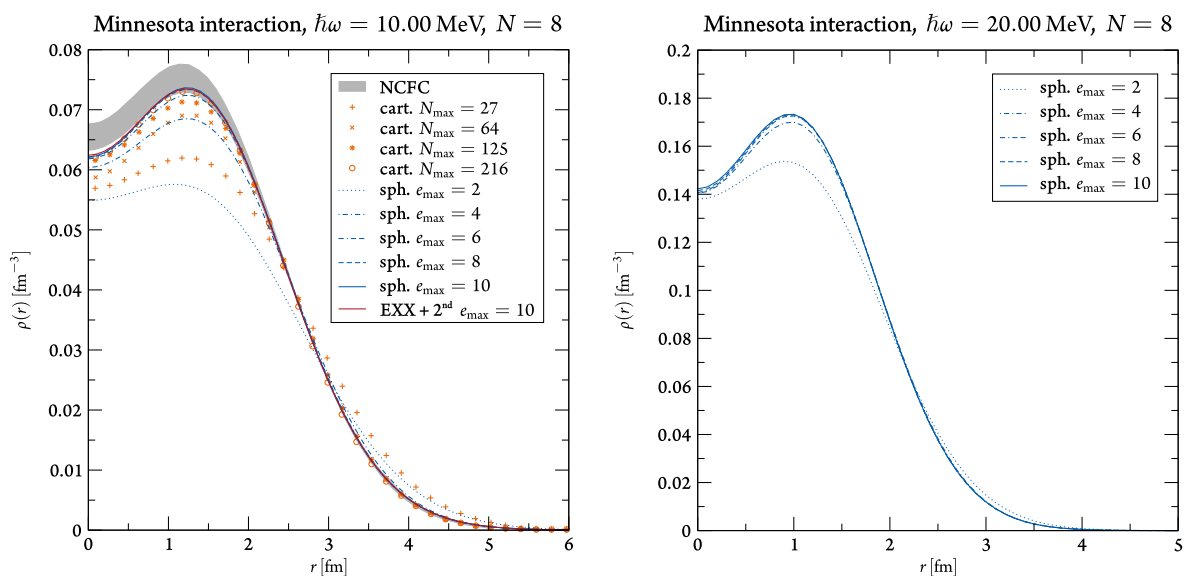


Figure 4.3: Density profile of 8 neutrons in a harmonic-oscillator potential with $\hbar\omega = 10$ MeV (left) and $\hbar\omega = 20$ MeV (right). We compare our spherical Hartree-Fock calculations (blue lines) to the cartesian Hartree-Fock calculations (orange symbols) of Ref. [36] at various model-space sizes e_{\max} and N_{\max} , respectively. Note that both the Hartree-Fock and exact-exchange approximation lead to almost identical density profiles for the spherical and cartesian bases. This also holds when including correlations at second order to the exact-exchange approximation (see solid red line obtained at $e_{\max} = 10$). As reference we show results obtained with the no-core full-configuration calculation of Ref. [256] with uncertainty estimates (grey band).

In Fig. 4.3 we show the density profiles for both trap frequencies at different e_{\max} . At $\hbar\omega = 10$ MeV we can compare to the cartesian calculations of Ref. [36] (orange symbols) and the NCFC results of Ref. [256] (grey band). For clarity we do not show results for both Hartree-Fock and exact-exchange as the density profiles are almost exactly identical. This is still true when including correlations which we indicate by showing results at $e_{\max} = 10$ (red line), which lie almost on top of the first-order results (solid blue line). Comparing the cartesian to the spherical calculations at different basis sizes is only possible at the converged level, *i.e.*, for $N_{\max} \geq 125$ and $e_{\max} \geq 7$. The small deviations from the NCFC results observed in the radius calculations are also reflected in the density profile with slightly larger central densities for the NCFC calculations, resulting in a smaller rms radius.

For trap frequency $\hbar\omega = 20$ MeV we find much higher central densities around and slightly above nuclear saturation density. Note that to our knowledge there do not exist published results against which we could benchmark this density profile. Perturbative calculations of neutron matter up to $\rho = 0.2 \text{ fm}^{-3}$, however, showed a systematic convergence pattern. And the second-order contributions were of the order of 1 MeV per nucleon at nuclear saturation density compared to the total energy of ~ 12 MeV per nucleon.

We could not resolve the issue of the unnatural convergence pattern for the Minnesota interaction in the second-order calculations but we find no such behaviour for the local chiral interactions, which we discuss in the next Section.

4.2 NEUTRON DROPS BASED ON LOCAL CHIRAL INTERACTIONS

WE HAVE CALCULATED NEUTRON DROPS in a harmonic-oscillator potential using local chiral interactions with cutoffs $R_0 = 1.0$ and 1.2 fm and cutoff $\tilde{\Lambda} = 1000$ MeV in the regularisation of the spectral function in the two-pion exchanges at NLO. These potentials have also been employed in neutron drop calculations of Ref. [172] using the quasi-exact auxiliary-field diffusion Monte Carlo (AFDMC) method. In Figs. 4.4 and 4.5 we show the total energy (first row), rms radius (centre), and density profile (bottom) of 8 neutrons in a trap with frequency $\hbar\omega = 10$ MeV for model space sizes $e_{\max} = 2 - 10$. From left to right we show calculations at LO, NLO, and N²LO, respectively. As in the benchmark calculations, we compare the Hartree-Fock (filled blue circles/ lines) to the exact-exchange approximation of the OEP method (open red circles/ lines). The second-order contributions are depicted as squares: Filled blue for many-body perturbation theory and open red for the OEP method. As reference we show the AFDMC results as black line with its calculational uncertainty as grey band. Note that due to runtime constraints we did not obtain fully converged results in the largest model spaces ($e_{\max} = 10$) for the second-order contributions to the exact-exchange approximation for some potentials. With e_{\max} the runtime of each iterative step of the OEP solution algorithm increases and also more iterations are needed to achieve convergence.

As a general trend we find very natural convergence patterns of the second-order calculations for both cutoffs at all chiral orders when compared to the Minnesota interaction. We also find that the potential with the lower coordinate-space cutoff $R_0 = 1.0$ fm is less perturbative with our results more off from the AFDMC calculations and a slower second-order convergence with respect to the model-space size. This matches our expectations as the low coordinate-space cutoff corresponds to higher momentum-space cutoffs. This was also seen in calculations of neutron matter [150–152, 172] where many-body perturbation theory was benchmarked to AFDMC simulations.

For both cutoffs the LO calculations show the worst convergence pattern which may be traced back to higher central densities reflected in smaller radii. This may be a result of stronger S-wave attraction at this order. Even at large e_{\max} we find strong changes in the orbitals, which can be seen in the density profile. For the LO potentials we also find large orbital changes in the second-order OEP calculations. For $R_0 = 1.2$ fm this can be seen at $e_{\max} = 10$ in the radius with ~ 0.1 fm difference between the exact-exchange or Hartree-Fock and the second-order OEP results and also in the density profile where the orbital variation at second order leads to an increase of the central density of ~ 0.015 fm⁻³.

Similarly to the benchmark calculations with the Minnesota interaction we find at first order for the NLO and N²LO potentials converged results for $e_{\max} \gtrsim 6$. This holds for the energy and the radius and we find only minor changes in the density at low r . Including second-order contribu-

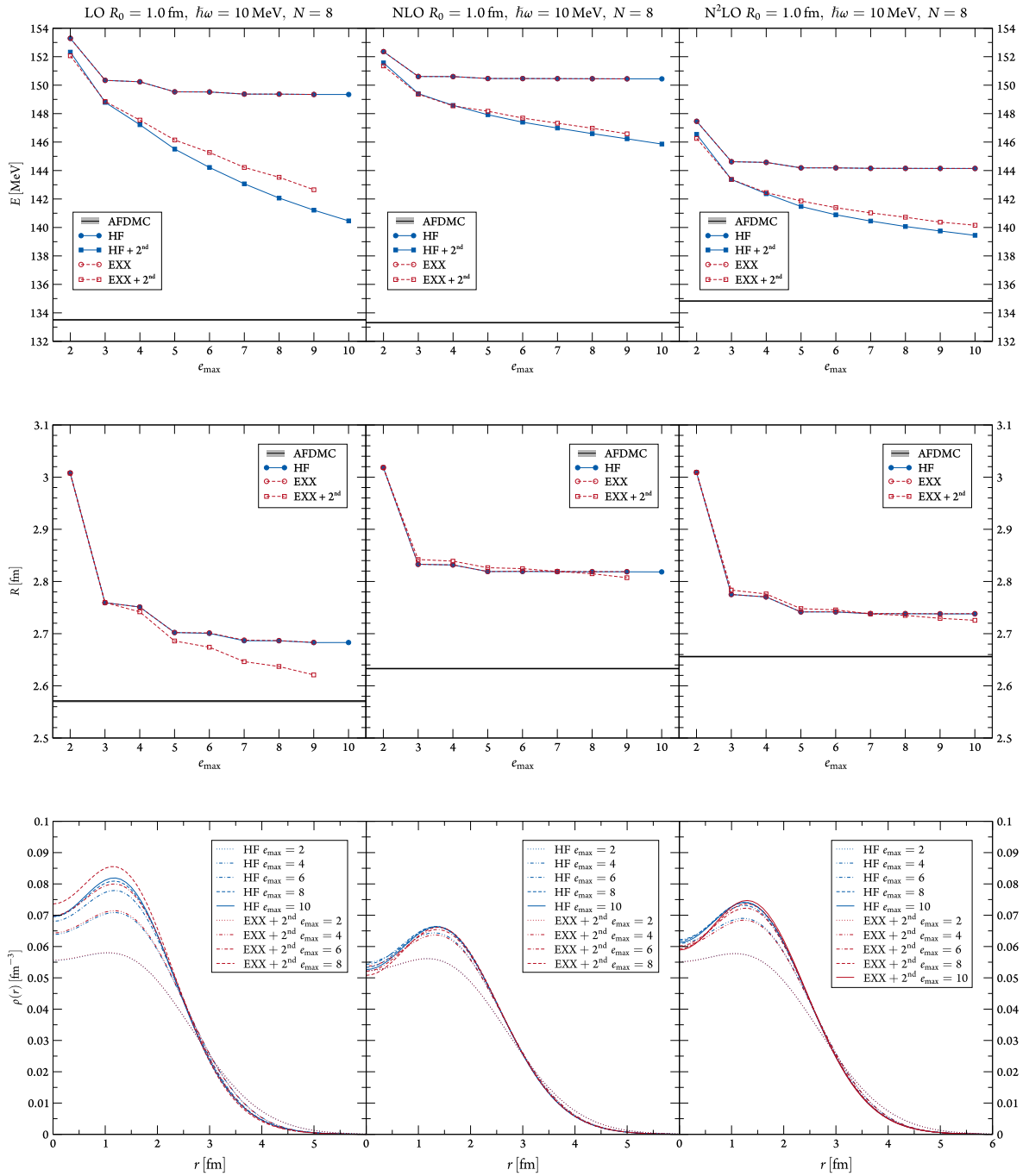


Figure 4.4: Energy (top row), radius (centre), and density profile (bottom) for different model-space sizes ϵ_{\max} for 8 neutrons in a harmonic-oscillator trap with $\hbar\omega = 10$ MeV obtained with local chiral interactions with $R_0 = 1.0$ fm and SFR cutoff $\tilde{\Lambda} = 1000$ MeV. From left to right column we show LO, NLO, and N²LO results, respectively.

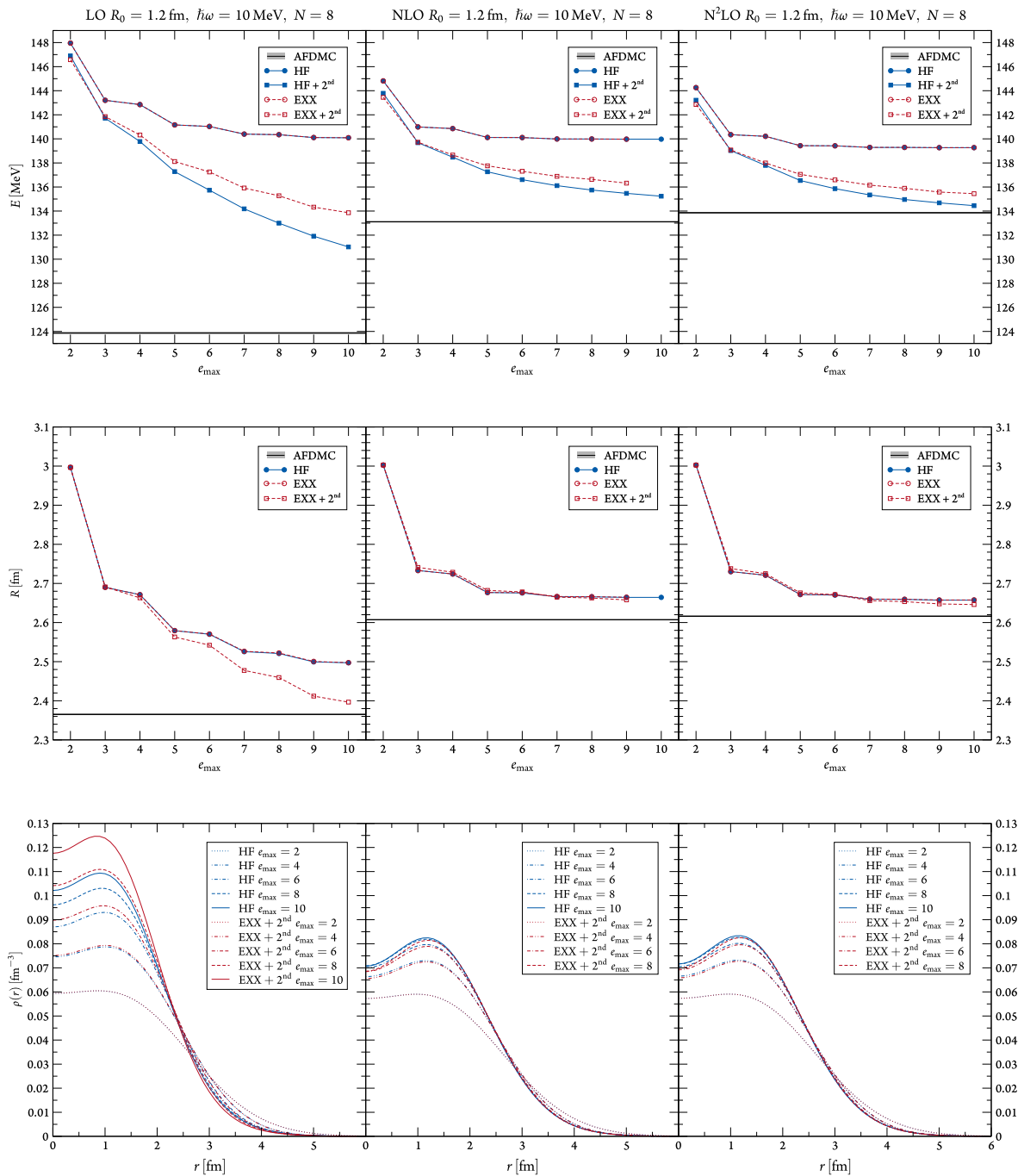


Figure 4.5: Energy (top row), radius (centre), and density profile (bottom) for different model-space sizes ϵ_{\max} for 8 neutrons in a harmonic-oscillator trap with $\hbar\omega = 10$ MeV obtained with local chiral interactions with $R_0 = 1.2$ fm and SFR cutoff $\tilde{\Lambda} = 1000$ MeV. From left to right column we show LO, NLO, and N²LO results, respectively.

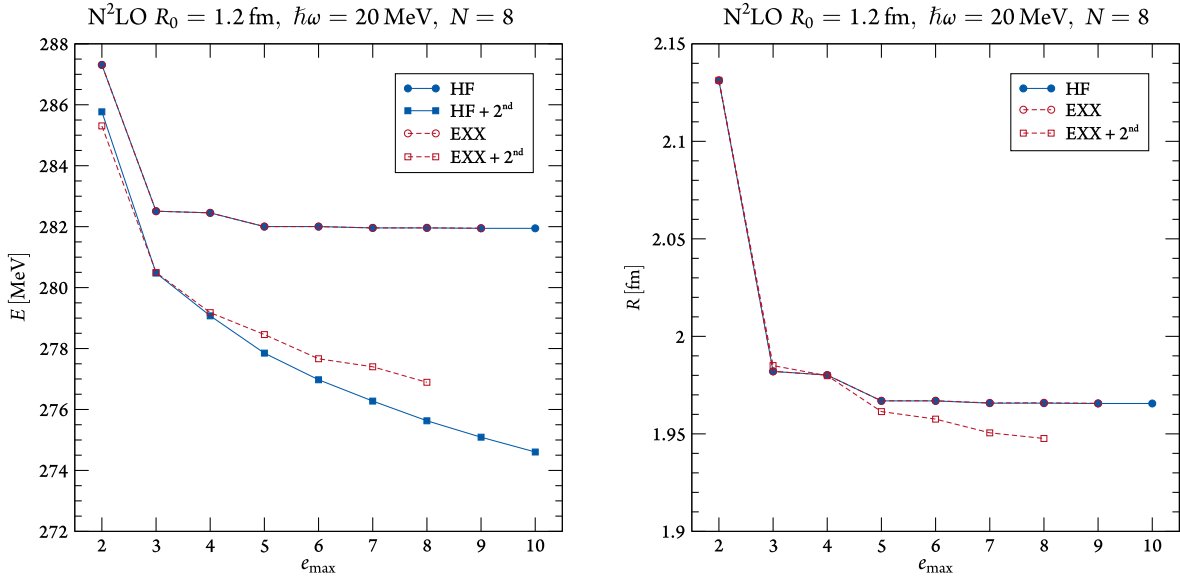


Figure 4.6: Total energy (left) and radius (right) of 8 neutrons in a harmonic-oscillator potential with $\hbar\omega = 20 \text{ MeV}$ as a function of the model-space size e_{max} employing the local chiral $N^2\text{LO}$ interaction with $R_0 = 1.2 \text{ fm}$. See Fig. 4.5 and text for details.

tions changes the picture. We did not obtain full-converged results in any potential. The best in this sense might be the $N^2\text{LO } R_0 = 1.2 \text{ fm}$ potential, where we would assume converged energies around $e_{\text{max}} = 12$ when naively following the trend. This would also agree nicely with the AFDMC calculation. A way to improve the convergence would be through the use of renormalisation-group techniques to evolve the potentials to lower momenta, which would improve the convergence [162]. This would in particular be relevant when calculating larger systems.

For the NLO and $N^2\text{LO}$ potentials we also find only small variations in the orbitals, when including second-order correlations in the OEP calculations. The radii and central densities slightly decrease at large e_{max} and for the energies we systematically find smaller second-order contributions than from many-body perturbation theory for all $e_{\text{max}} \geq 3$. This might be an indication that the approximation of varying only the occupied orbitals is not sufficient and one needs to develop another method to circumvent the convergence problems, discussed in the previous Section.

Note that for a consistent calculation at $N^2\text{LO}$ one would also need to include leading 3N forces, which our formalism and code is currently not capable of. The inclusion of 3N forces would be a natural next step and can either be done directly by extending the formalism of Chapter 3 or indirectly via normal-ordered 3N forces, where the Hartree-Fock state could be used as reference in a first-order approximation.

WE HAVE ALSO CALCULATED the system of 8 neutrons in a trap with $\hbar\omega = 20 \text{ MeV}$ using the $N^2\text{LO}$ potential with $R_0 = 1.2 \text{ fm}$. We show the total energy and radius in Fig. 4.6 using the same definitions as in the previous Figures. At this trap frequency we do not have results from an AFDMC calculation

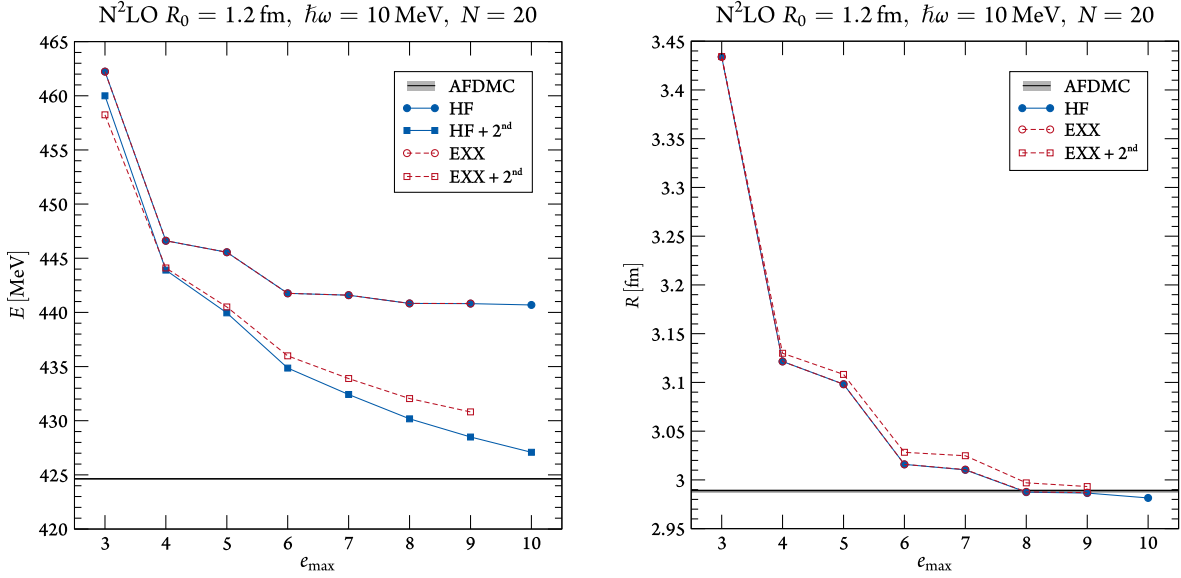


Figure 4.7: Total energy (left) and radius (right) of 20 neutrons in a harmonic-oscillator potential with $\hbar\omega = 10$ MeV as a function of the model-space size e_{\max} employing the local chiral N²LO interaction with $R_0 = 1.2$ fm. See Fig. 4.5 and text for details.

as reference. When comparing the second-order curves with those obtained with the Minnesota potential (see Fig. 4.2) we observe a completely different picture. With the chiral interaction the convergence pattern appears much more natural, even though the calculations are not converged with respect to the model-space size. The general trends of the results agree with those obtained in a trap with $\hbar\omega = 10$ MeV.

When calculating larger systems the model-space limitations become more apparent. We show in Fig. 4.7 calculations of 20 neutrons in a trap with $\hbar\omega = 10$ MeV using the same N²LO $R_0 = 1.2$ fm interaction. Especially the radius seems not to be converged, even at first order. We also find minor changes in the energy when going from $e_{\max} = 9$ to 10. For such systems clearly using a renormalisation-group evolved potential would be more efficient and could speed up the convergence.

IN SUMMARY WE STATE OUR MAIN FINDINGS and conclusions: The calculations of neutron drops with the Minnesota and the chiral interactions confirm the excellent agreement of the exact-exchange approximation of OEP and Hartree-Fock. However, we have found that the energies obtained in the second-order OEP calculations are systematically worse than those from second-order many-body perturbation theory. This was not expected but might be caused by the approximations made. Further studies avoiding these approximations may resolve these issues.

The convergence with respect to the model-space size might be addressed using renormalisation-group-evolved interactions and for a consistent and more realistic calculation the inclusion of 3N forces should be pursued.

The next steps towards the construction of an *ab initio* energy-density functional should be twofold: One can use our calculations to constrain empirical functionals, similarly to our approach in spin-polarised neutron matter (see Section 2.2), and one should extend the calculations to other systems. The inclusion of protons is straightforward in the OEP method by extending the spin degrees of freedom to isospin. With that a calculation of actual nuclei should be possible when one (gradually) switches off the external potential. However, due to larger tensor forces and fewer Pauli blocking effects in systems with neutrons and protons we expect worse convergence behaviours. Thus, using renormalisation-group evolved potentials will be key. From a computationally point of view one should also further optimise the OEP algorithm and code to go to larger model spaces or even use a cartesian basis in order to calculate also non-spherical systems. One approach could be the use of Broyden's method, which we applied in the calculations of the pairing gap (see Section 2.3). Another exciting direction could be comparisons with results from the density-matrix expansion, which is also structurally easier for local interactions [256].

5

Conclusions

IN THIS THESIS WE HAVE STUDIED a range of phenomena of finite and infinite neutron-rich systems. We first addressed the physics of neutron stars by studying the chiral condensate in neutron matter, spin-polarised neutron matter, and the pairing gap in neutron matter. In the second part we focused on finite systems by taking a step towards the development of *ab initio* energy-density functionals. In particular, we calculated neutron drops within the optimised effective potential (OEP) method. To study whether there exists a phase transition in neutron stars to exotic phases at nuclear densities, we have calculated the chiral condensate in neutron matter. Our perturbative calculations using non-local chiral interactions up to N³LO including all many-body forces show that the interaction among neutrons impedes the restoration of chiral symmetry. We do not expect a phase transition at densities $n \lesssim 0.3 \text{ fm}^{-3}$. The uncertainties are, however, dominated by the pion-nucleon sigma term $\sigma_{\pi N}$, which accounts for the quark-mass dependences of the nucleon mass.

Spin-polarised neutron matter is an extreme system which we found to behave almost like a non-interacting Fermi gas up to nuclear saturation density. We have performed perturbative calculations consistently up to N³LO, taking into account many-body forces at the Hartree-Fock level. We found very small contributions from leading and, in particular, sub-leading 3N forces. With the assumption that spin-polarised neutron matter behaves like a free Fermi gas even at higher densities, we have predicted the densities at which such a polarised phase could appear in neutron stars. We also compared our calculations of spin-polarised neutron matter to predictions from energy-density functionals and

found good agreement with the Gogny D1N interaction as well as the Skyrme functionals SGII, SIII, SkM*, SkO, and Sly5. It will be interesting to use our results as additional neutron-matter constraint for modern functionals. Spin-polarised matter can also be used as a benchmark system for lattice QCD. For that we have varied the pion mass in our calculations, which makes it easier to calculate the system in lattice QCD and provide results in a range $m_\pi = (100 - 180)$ MeV.

We have also studied the pairing gap in neutron matter in the BCS approximation in the 1S_0 and $^3P_2 - ^3F_2$ channel using two independent solution algorithms: A new modified direct-iteration method and the so-called Khodel method. On the NN level, using local and semi-local chiral interactions we found similar results for the 1S_0 pairing gap and also at lower momenta in the triplet channel $^3P_2 - ^3F_2$ for the highest chiral-order potentials (N^2 LO for local and N^4 LO for semi-local potentials). We also provided an uncertainty estimate that gives a confidence level at which especially the highest-order calculations may be trusted. The inclusion of many-body forces, at present limited to the traditional non-local interactions, up to N^3 LO decreased the 1S_0 pairing gap to a small extent. In the $^3P_2 - ^3F_2$ channel the picture is not as clear, with different predictions for the NN potentials used, especially at high densities. Further investigations with non-local and (semi-)local many-body forces will shed light towards a better understanding of triplet pairing in neutron matter.

Current nuclear energy-density functionals are based on empirical parametrisation and fits to stable nuclei. The construction of an *ab initio* functional directly connected to the nuclear interaction is an important goal of nuclear physics. A promising approach is the use of orbital-dependent functionals within the framework of Kohn-Sham theory. We pursued the method of optimised effective potentials. For that we have developed the inclusion of second-order correlations to the exact-exchange approximation and the use of chiral interactions in a spherical harmonic-oscillator basis.

In our calculations of neutron drops in external harmonic-oscillator traps using local chiral interactions on the NN level we confirmed that the first-order exact-exchange approximation of the OEP method gives almost identical results as the Hartree-Fock approximation. At second order we were limited to approximations, making the results obtained within the OEP formalism not competitive with second-order many-body perturbation-theory calculations. We also studied the KLI approximation, which is widely used in quantum chemistry and found good agreement at small model spaces but no benefits for a nuclear-physics calculation. In the future further studies on how to include the second-order correlations into the OEP method are crucial for the derivation of an *ab initio* energy-density functional within this framework. Also the inclusion of low-momentum interactions using renormalisation-group techniques and the inclusion of 3N forces will be exciting topics.

Acknowledgements

AN ERSTER STELLE DANKE ICH Achim Schwenk für die Betreuung meiner Dissertation. Die Zusammenarbeit der letzten sechs Jahre seit dem Beginn meiner Bachelorarbeit fand ich immer spannend und habe die Zeit genossen. Danke für die guten Diskussionen, Ratschläge und Deine Hilfe.

Ebenso danke ich Kai Hebeler für die gute Zusammenarbeit und immerwährende Unterstützung bei allen Projekten dieser Dissertation. Danke für Deine großartige Hilfe, vor allem auch bei den numerischen Berechnungen. Danke auch an Ingo Tews für die gute Zusammenarbeit bei den Projekten zu Neutronenmaterie und Christian Drischler für die beeindruckende Arbeit bezüglich der Gap-Gleichung. Darüber hinaus möchte ich mich auch bei Johannes Simonis für die Unterstützung im Matricelementbusiness bedanken. Ihr alle wart mir eine große Hilfe und ich habe sehr gerne mit Euch zusammengearbeitet.

Meinen Bürokollegen Klaus Vobig, Philipp Klos, Rodric Seutin und Stefan Schulz sowie den ehemaligen Kollegen Angelo Calci, Joachim Langhammer, Maximilian Jacobi, Sebastian Dietz und Sven Binder danke ich für die lebhaften Diskussionen und die freundliche Unterstützung bei physikalischen und *computational* Problemen – *Nuclear Dankos*.

Für das Lesen und die hilfreichen Kommentare zu dieser Dissertation danke ich Achim Schwenk, Alexander Bartl, Christian Drischer, Ingo Tews, Johannes Simonis und Kai Hebeler.

MANY THANKS GO ALSO TO the other members of the strongint group: Arianna Carbone, Joel Lynn, Kyle Wendt, Lukas Huth, Svenja Greif, Toño Coello Pérez, and Victoria Durant, as well as to the former members: Alexandros Gezerlis, Andreas Kleiner, Anja Schuster, Anton Cyrol, David Volk, Dmitry Kobayakov, Gang Shen, Jan Hoppe, Jason D. Holt, Javier Menéndez, Laura Vietze, Liliana Caballero, Marc Schönborn, Maria Voskresenskaya, Martin Hoferichter, Philipp Bischoff, Sabrina Schäfer, Ubbi Sauerwein, Vittorio Somà. I had a great time with all of you.

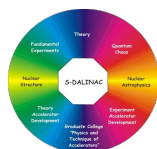
In addition I want to mention all other colleagues of the Theory Centre and in particular the people in Robert Roth's group. I enjoyed the discussions and chats in the numerous coffee breaks.

In the beginning of my doctoral research I had the great opportunity to participate in the ECT* Doctoral Training Programme ‘Neutron-rich matter: Constraints from nuclear physics and astrophysics’. I liked the programme very much and met many fascinating people. Thanks to all of you!

TEILE DIESER ARBEIT habe ich im Rahmen des Sonderforschungsbereichs 634 der Deutschen Forschungsgemeinschaft ‘Nuclear Structure, Nuclear Astrophysics and Fundamental Experiments at Low Momentum Transfer at the Superconducting Darmstadt Accelerator (S-DALINAC)’ erstellt. Außerdem bedanke ich mich für die Unterstützung im Rahmen des ExtreMe Matter Institute EMMI der Helmholtzgemeinschaft (HA216/EMMI), des ERC-Grants Nr. 307986 STRONGINT des Europäischen Forschungsrats, der Promotionsförderung der Studienstiftung des deutschen Volkes, sowie der Wilhelm und Else Heraeus-Stiftung für die Teilnahme an Konferenzen und Workshops.

NATÜRLICH GEBÜHRT AUCH EIN GROSSER DANK meiner Familie. Meine Eltern haben mich stets auf allen meinen Wegen begleitet und mich in all meinen Vorhaben unterstützt. Ohne Euch stünde ich nicht da, wo ich heute bin. Meine Brüder und viele Freunde gaben mir ebenso immer Halt und Unterstützung.

Zuletzt danke ich Swetlana, die mich an meiner Seite stets unterstützt, mir den Rücken frei gehalten und mir immer Halt gegeben hat, auch wenn es gerade in den letzten Wochen und Monaten sicherlich anstrengend war. Ich bin froh Dich als treue Partnerin an meiner Seite zu haben und freue mich mit Dir die Zukunft zu bestreiten.



SFB 634



European Research Council
Established by the European Commission



Appendices

A

Numerical details

THE NUMERICAL VALUES of constants and low-energy couplings used throughout this thesis are summarised in this Appendix.

Table A.1: Values of physical constant used in the numerical calculations.

Constant	symbol	numerical value
nucleon mass	m_N	938.92 MeV
average pion mass	m_π	138.04 MeV
pion decay constant	f_π	92.4 MeV
axial coupling constant	g_A	1.29
conversion factor	$\hbar c$	197.327 MeV fm

Table A.2: Low-energy couplings appearing in the NN sector 3N forces of the non-local chiral interactions used in the calculations of neutron matter.

NN potential	C_S [fm ²]	C_T [fm ²]	c_1 [GeV ⁻¹]	c_3 [GeV ⁻¹]
N ³ LO EM 500 MeV [145, 146]	-4.19	-0.45	-0.81	-3.20
N ³ LO EGM 450/500 MeV [148]	-4.71	-0.24	-0.81	-3.40
N ³ LO EGM 450/700 MeV [148]	3.90	0.22	-0.81	-3.40

Table A.3: Values of couplings c_1 , c_3 recommended for 3N calculations at order N²LO/N³LO from Krebs, Gasparyan, and Epelbaum (KGE, Ref. [132]), and the range adopted in the calculation of neutron matter of this thesis.

NN potential	c_1 [GeV ⁻¹]	c_3 [GeV ⁻¹]
N ² LO KGE [132]	-(0.26 – 0.58)	-(2.80 – 3.14)
N ² LO KGE (recommended) [132]	-(0.37 – 0.73)	-(2.71 – 3.38)
N ³ LO KGE [132]	-(0.75 – 1.13)	-(4.77 – 5.51)
N ² LO this work	-(0.37 – 0.81)	-(2.71 – 3.40)
N ³ LO this work	-(0.75 – 1.13)	-(4.77 – 5.51)

B

Details on the polarised-neutron-matter calculation

IN THIS APPENDIX we give details about the partial-wave decomposition of the NN interactions and the angle-averaging used in the calculation of spin-polarised neutron matter.

For a general two-body state with relative momentum \mathbf{k} , spin S and spin-projection m_S ,

$$|\mathbf{k}Sm_S\rangle = \sum_{l,m_l} (4\pi)^l Y_l^{m_l^\dagger}(\hat{\mathbf{k}}) |k\rangle |lm_lSm_S\rangle \quad (\text{B.1})$$

one decomposes the NN interaction V_{NN}

$$\begin{aligned} \langle \mathbf{k}Sm_S | V_{\text{NN}}(1 - \mathcal{P}_{12}) | \mathbf{k}Sm_S \rangle &= \sum_{\substack{l,l',m_l,m_l' \\ J,m_j}} (4\pi)^2 i^{l-l'} C_{l'm_l'Sm_S}^{Jm_j} C_{lm_lSm_S}^{Jm_j} Y_{l'}^{m_l'}(\hat{\mathbf{k}}) Y_l^{m_l^\dagger}(\hat{\mathbf{k}}) \\ &\times \langle k | V_{\text{NN}}^{JSl} | k \rangle [1 - (-1)^{l+S+1}]. \end{aligned} \quad (\text{B.2})$$

In spin-polarised neutron matter with, *e.g.*, $S = m_S = 1$, the anti-symmetry of the wave function requires $l = 1, 3, 5, \dots$. Thus, we obtain

$$\begin{aligned}
\langle k11 | V_{\text{NN}}(1 - \mathcal{P}_{12}) | k11 \rangle &\equiv \int d\hat{\mathbf{k}} \langle \mathbf{k}11 | V_{\text{nn}}(1 - \mathcal{P}_{12}) | \mathbf{k}11 \rangle \\
&= \int d\hat{\mathbf{k}} \sum_{\substack{l,l',m_l,m_{l'} \\ J,m_J}} (4\pi)^2 i^{l-l'} \mathcal{C}_{l'm_{l'}11}^{Jm_J} \mathcal{C}_{lm_l11}^{Jm_J} Y_{l'}^{m_{l'}}(\hat{\mathbf{k}}) Y_l^{m_l \dagger}(\hat{\mathbf{k}}) \langle k | V_{\text{NN}}^{J1l'l} | k \rangle [(1 - (-1))] \\
&= \sum_{l,J} 2(4\pi)^2 \frac{2J+1}{3} \langle k | V_{\text{NN}}^{J1l'l} | k \rangle, \tag{B.3}
\end{aligned}$$

where we used the orthogonality of the Clebsch-Gordan coefficients and the spherical harmonics and summed over m_J .

At second order the matrix elements are decomposed as follows

$$\begin{aligned}
&|\langle \mathbf{k}' S m'_S | V_{\text{NN}}(1 - \mathcal{P}_{12}) | \mathbf{k} S m_S \rangle|^2 \\
&= \sum_{\substack{l,l',\tilde{l},\tilde{l}',J,\tilde{J} \\ m_l,m_{l'},\tilde{m}_l,\tilde{m}_{l'},m_J,\tilde{m}_J}} (4\pi)^4 i^{l-l'+\tilde{l}-\tilde{l}'} \mathcal{C}_{l'm_{l'}S m_S}^{Jm_J} \mathcal{C}_{\tilde{l}\tilde{m}_{l'}S m_S}^{\tilde{J}\tilde{m}_{\tilde{J}}} \mathcal{C}_{l'\tilde{m}_{l'}S m_S}^{\tilde{J}\tilde{m}_{\tilde{J}}} \mathcal{C}_{\tilde{l}\tilde{m}_{l'}S m_S}^{\tilde{J}\tilde{m}_{\tilde{J}}} Y_{l'}^{m_{l'}}(\hat{\mathbf{k}}) Y_l^{m_l \dagger}(\hat{\mathbf{k}}) Y_{\tilde{l}'}^{\tilde{m}_{l'}}(\hat{\mathbf{k}}') Y_{\tilde{l}}^{\tilde{m}_{\tilde{l}} \dagger}(\hat{\mathbf{k}}') \\
&\times \langle k | V_{\text{NN}}^{JSl'l} | k' \rangle \langle k' | V_{\text{NN}}^{\tilde{J}\tilde{S}\tilde{l}\tilde{l}'} | k \rangle [1 - (-1)^{l+S+1}] [1 - (-1)^{\tilde{l}+S+1}]. \tag{B.4}
\end{aligned}$$

And for spin-polarised neutron matter we obtain

$$\begin{aligned}
&|\langle k'11 | V_{\text{nn}}(1 - \mathcal{P}_{12}) | k11 \rangle|^2 = |\langle \mathbf{k}'11 | V_{\text{NN}}(1 - \mathcal{P}_{12}) | \mathbf{k}11 \rangle|^2 \\
&= \sum_{\substack{l,l',\tilde{l},\tilde{l}',J,\tilde{J} \\ m_l,m_{l'},\tilde{m}_l,\tilde{m}_{l'},m_J,\tilde{m}_J}} 4(4\pi)^4 i^{l-l'+\tilde{l}-\tilde{l}'} \mathcal{C}_{l'm_{l'}11}^{Jm_J} \mathcal{C}_{\tilde{l}\tilde{m}_{l'}11}^{\tilde{J}\tilde{m}_{\tilde{J}}} \mathcal{C}_{l'\tilde{m}_{l'}11}^{\tilde{J}\tilde{m}_{\tilde{J}}} \mathcal{C}_{\tilde{l}\tilde{m}_{l'}11}^{\tilde{J}\tilde{m}_{\tilde{J}}} \\
&\times Y_{l'}^{m_{l'}}(\hat{\mathbf{k}}) Y_l^{m_l \dagger}(\hat{\mathbf{k}}) Y_{\tilde{l}'}^{\tilde{m}_{l'}}(\hat{\mathbf{k}}') Y_{\tilde{l}}^{\tilde{m}_{\tilde{l}} \dagger}(\hat{\mathbf{k}}') \langle k | V_{\text{NN}}^{J1l'l} | k' \rangle \langle k' | V_{\text{NN}}^{\tilde{J}1\tilde{l}\tilde{l}'} | k \rangle \\
&= \sum_{\substack{l,l',\tilde{l},\tilde{l}' \\ J,\tilde{J},m_J,\tilde{m}_J}} 4(4\pi)^4 i^{l-l'+\tilde{l}-\tilde{l}'} \mathcal{C}_{l'(m_J-1)11}^{Jm_J} \mathcal{C}_{\tilde{l}(\tilde{m}_J-1)11}^{\tilde{J}\tilde{m}_{\tilde{J}}} \mathcal{C}_{l'(m_J-1)11}^{\tilde{J}\tilde{m}_{\tilde{J}}} \mathcal{C}_{\tilde{l}(\tilde{m}_J-1)11}^{\tilde{J}\tilde{m}_{\tilde{J}}} \\
&\times Y_{l'}^{m_J-1}(\hat{\mathbf{k}}) Y_l^{m_J-1 \dagger}(\hat{\mathbf{k}}) Y_{\tilde{l}'}^{\tilde{m}_J-1}(\hat{\mathbf{k}}') Y_{\tilde{l}}^{\tilde{m}_J-1 \dagger}(\hat{\mathbf{k}}') \langle k | V_{\text{NN}}^{J1l'l} | k' \rangle \langle k' | V_{\text{NN}}^{\tilde{J}1\tilde{l}\tilde{l}'} | k \rangle. \tag{B.5}
\end{aligned}$$

We average over all angles,

$$\begin{aligned}
\frac{\int d\hat{\mathbf{k}} d\hat{\mathbf{k}}'}{(4\pi)^2} |\langle k'11 | V_{\text{NN}}(1 - \mathcal{P}_{12}) | k11 \rangle|^2 &= \sum_{l,l',J,\tilde{J},m_J} 4(4\pi)^2 \mathcal{C}_{l'(m_J-1)11}^{Jm_J} \mathcal{C}_{l(m_J-1)11}^{Jm_J} \mathcal{C}_{l(m_J-1)11}^{\tilde{J}\tilde{m}_{\tilde{J}}} \mathcal{C}_{l'(m_J-1)11}^{\tilde{J}\tilde{m}_{\tilde{J}}} \\
&\times \langle k | V_{\text{NN}}^{J1l'l} | k' \rangle \langle k' | V_{\text{NN}}^{\tilde{J}1\tilde{l}\tilde{l}'} | k \rangle, \\
&= \sum_{l,l',J,\tilde{J}} 4(4\pi)^2 \mathcal{C}_{l'l}^{\tilde{J}\tilde{J}} \langle k | V_{\text{nn}}^{J1l'l} | k' \rangle \langle k' | V_{\text{nn}}^{\tilde{J}1\tilde{l}\tilde{l}'} | k \rangle, \tag{B.6}
\end{aligned}$$

where we used the orthogonality of the Clebsch-Gordan coefficients and the spherical harmonics and performed the m_j sum implicitly, using the definition

$$\mathcal{C}_{l'l'}^{\tilde{J}} = \sum_{m_j} \mathcal{C}_{l'(m_j-1)11}^{Jm_j} \mathcal{C}_{l(m_j-1)11}^{Jm_j} \mathcal{C}_{l(m_j-1)11}^{\tilde{J}m_j} \mathcal{C}_{l'(m_j-1)11}^{\tilde{J}m_j}. \quad (\text{B.7})$$

Without angle averaging one can rewrite Eq. (B.5) using the (anti-)symmetry and the following relation for spherical harmonics [249, p. 144]

$$Y_l^{m_l}(\hat{\mathbf{k}}) Y_{l'}^{m_{l'}}(\hat{\mathbf{k}}) = \sum_{L,M} \sqrt{\frac{(2l+1)(2l'+1)}{4\pi(2L+1)}} \mathcal{C}_{l0l'0}^{L0} \mathcal{C}_{lm_l l' m_{l'}}^{LM} Y_L^M(\hat{\mathbf{k}}). \quad (\text{B.8})$$

With that we obtain

$$\begin{aligned} & |\langle k'11 | V_{\text{NN}}(1 - \mathcal{P}_{12}) | k11 \rangle|^2 \\ &= \sum_{\substack{l,l',\tilde{l},\tilde{l}' \\ J,\tilde{J},m_j,\tilde{m}_j \\ L,L',M,M'}} 4(4\pi)^4 i^{l-l'+\tilde{l}-\tilde{l}'} \mathcal{C}_{l'(m_j-1)11}^{Jm_j} \mathcal{C}_{l(m_j-1)11}^{Jm_j} \mathcal{C}_{l'(\tilde{m}_j-1)11}^{\tilde{J}\tilde{m}_j} \mathcal{C}_{l(\tilde{m}_j-1)11}^{\tilde{J}\tilde{m}_j} \langle k | V_{\text{NN}}^{J1l'l} | k' \rangle \langle k' | V_{\text{NN}}^{\tilde{J}1\tilde{l}\tilde{l}'} | k \rangle \\ &\times (-1)^{\tilde{m}_j-1} \sqrt{\frac{(2l'+1)(2\tilde{l}+1)}{4\pi(2L+1)}} \mathcal{C}_{l'0\tilde{l}0}^{L0} \mathcal{C}_{l'(m_j-1)\tilde{l}(1-\tilde{m}_j)}^{LM} Y_L^M(\hat{\mathbf{k}}) \\ &\times (-1)^{m_j-1} \sqrt{\frac{(2l+1)(2\tilde{l}'+1)}{4\pi(2L'+1)}} \mathcal{C}_{l0\tilde{l}'0}^{L'0} \mathcal{C}_{l(1-m_j)\tilde{l}'(\tilde{m}_j-1)}^{L'M'} Y_{L'}^{M'}(\hat{\mathbf{k}}') \\ &= \sum_{\substack{l,l',\tilde{l},\tilde{l}' \\ J,\tilde{J},L,L'}} 4(4\pi)^3 i^{l-l'+\tilde{l}-\tilde{l}'} \sqrt{\frac{(2l'+1)(2\tilde{l}+1)(2l+1)(2\tilde{l}'+1)}{(2L+1)(2L'+1)}} \mathcal{C}_{l'0\tilde{l}0}^{L0} \mathcal{C}_{l0\tilde{l}'0}^{L'0} \langle k | V_{\text{NN}}^{J1l'l} | k' \rangle \langle k' | V_{\text{NN}}^{\tilde{J}1\tilde{l}\tilde{l}'} | k \rangle \\ &\times \sum_{m_j,\tilde{m}_j} \mathcal{C}_{l'(m_j-1)11}^{Jm_j} \mathcal{C}_{l(m_j-1)11}^{Jm_j} \mathcal{C}_{l'(\tilde{m}_j-1)11}^{\tilde{J}\tilde{m}_j} \mathcal{C}_{l(\tilde{m}_j-1)11}^{\tilde{J}\tilde{m}_j} \mathcal{C}_{l'(m_j-1)\tilde{l}(1-\tilde{m}_j)}^{L(\tilde{m}_j-m_j)} \mathcal{C}_{l(1-m_j)\tilde{l}'(\tilde{m}_j-1)}^{L'(\tilde{m}_j-m_j)} Y_L^{\tilde{m}_j-m_j}(\hat{\mathbf{k}}) Y_{L'}^{\tilde{m}_j-m_j}(\hat{\mathbf{k}}'). \end{aligned} \quad (\text{B.9})$$

We can rewrite the expression above into the angle-averaged equation (B.6) by restricting $L = L' = 0$. This implies $m_j = \tilde{m}_j$ and $l = \tilde{l}'$, $l' = \tilde{l}$ and we write

$$\begin{aligned} & |\langle k'11 | V_{\text{NN}}(1 - \mathcal{P}_{12}) | k11 \rangle|^2 \\ &\approx 4(4\pi)^2 \sum_{l,l',\tilde{J}} (2l'+1)(2l+1) \mathcal{C}_{l'0l'0}^{00} \mathcal{C}_{l0l0}^{00} \langle k | V_{\text{nn}}^{J1l'l} | k' \rangle \langle k' | V_{\text{nn}}^{\tilde{J}1\tilde{l}\tilde{l}'} | k \rangle \\ &\times \sum_{m_j} \mathcal{C}_{l'(m_j-1)11}^{Jm_j} \mathcal{C}_{l(m_j-1)11}^{Jm_j} \mathcal{C}_{l(m_j-1)11}^{\tilde{J}m_j} \mathcal{C}_{l'(m_j-1)11}^{\tilde{J}m_j} \mathcal{C}_{l'(m_j-1)l'(1-m_j)}^{00} \mathcal{C}_{l(1-m_j)l(m_j-1)}^{00}. \end{aligned} \quad (\text{B.10})$$

Using $C_{ml-m}^{00} = (-1)^{l-m} 1/\sqrt{2l+1}$ leads to

$$\sum_{l,l',j,\tilde{j}} 4(4\pi)^2 \langle k | V_{nn}^{l'l} | k' \rangle \langle k' | \tilde{V}_{nn}^{l'l'} | k \rangle \sum_{mj} C_{l'(m_j-1)11}^{lm_j} C_{l(m_j-1)11}^{jm_j} C_{l(m_j-1)11}^{\tilde{j}m_j} C_{l'(m_j-1)11}^{\tilde{j}m_j}, \quad (\text{B.11})$$

which verifies Eq. (B.6).

C

Partial-wave decomposition of the Minnesota interaction

THE MINNESOTA INTERACTION is a local nucleon-nucleon potential of the form

$$V(\mathbf{r}, \mathbf{r}') = \frac{1}{2} \left[V_R(r) + \frac{1}{2}(1 + \mathcal{P}_\sigma)V_t(r) + \frac{1}{2}(1 - \mathcal{P}_\sigma)V_s(r) \right] (1 + \mathcal{P}_r)\delta^{(3)}(\mathbf{r} - \mathbf{r}'), \quad (\text{C.1})$$

with spin-exchange operator $\mathcal{P}_\sigma = \frac{1}{2}(1 + \boldsymbol{\sigma}_1 \cdot \boldsymbol{\sigma}_2)$, coordinate-space exchange operator \mathcal{P}_r , and the functions

$$V_i(r) = V_{0i} \exp(-\kappa_i r^2), \quad (\text{C.2})$$

where $i = R, t, s$ and the coefficients V_{0i} and κ_i are given in Table C.1.

Table C.1: Coefficients of the Minnesota interaction according to Ref. [258].

i	R	t	s
V_{0i}	200.0 MeV	-178.0 MeV	-91.85 MeV
κ_i	1.487 fm ⁻²	0.639 fm ⁻²	0.465 fm ⁻²

Using $\boldsymbol{\sigma}_1 \cdot \boldsymbol{\sigma}_2 = 2S(S+1) - 3$, since

$$\mathbf{S}^2 = (\mathbf{s}_1 + \mathbf{s}_2)^2 = \mathbf{s}_1^2 + \mathbf{s}_2^2 + 2\mathbf{s}_1 \cdot \mathbf{s}_2 = \frac{3}{4} + \frac{3}{4} + \frac{1}{2}\boldsymbol{\sigma}_1 \cdot \boldsymbol{\sigma}_2, \quad (\text{C.3})$$

we can write

$$\begin{aligned} V_S(r)(1 + \mathcal{P}_r)\delta^{(3)}(\mathbf{r} - \mathbf{r}') &= \langle SM'_S | V(r)(1 + \mathcal{P}_r)\delta^{(3)}(\mathbf{r} - \mathbf{r}') | SM_S \rangle \\ &= \frac{1}{2} [V_R(r) + S V_t(r) + (1 - S) V_s(r)] (1 + \mathcal{P}_r)\delta^{(3)}(\mathbf{r} - \mathbf{r}'), \end{aligned} \quad (\text{C.4})$$

where we have introduced $V(r)$ via $V(\mathbf{r}, \mathbf{r}') = V(r)(1 + \mathcal{P}_r)\delta^{(3)}(\mathbf{r} - \mathbf{r}')$.

We Fourier transform the potential into momentum space:

$$\begin{aligned} \langle \mathbf{k}' SM'_S | V | \mathbf{k} SM_S \rangle &= \int d^3r d^3r' \langle SM'_S | \langle \mathbf{k}' | \mathbf{r}' \rangle V(\mathbf{r}, \mathbf{r}') \langle \mathbf{r} | \mathbf{k} \rangle | SM_S \rangle \\ &= \int d^3r (\langle \mathbf{k}' | \mathbf{r} \rangle + \langle \mathbf{k}' | -\mathbf{r} \rangle) V_S(r) \langle \mathbf{r} | \mathbf{k} \rangle \\ &= \int d^3r 4\pi \sum_{L', M'_L} i^{-L'} j_{L'}(k'r) Y_{L'}^{M'_L}(\hat{\mathbf{k}}') [Y_{L'}^{M'_L \dagger}(\hat{\mathbf{r}}) + Y_{L'}^{M'_L \dagger}(-\hat{\mathbf{r}})] V_S(r) \\ &\quad \times 4\pi \sum_{L, M_L} i^L j_L(kr) Y_L^{M_L \dagger}(\hat{\mathbf{k}}) Y_L^{M_L}(\hat{\mathbf{r}}) \\ &= (4\pi)^2 \sum_{L, L', M_L, M'_L} i^{L-L'} \int d\hat{\mathbf{r}} Y_{L'}^{M'_L \dagger}(\hat{\mathbf{r}}) Y_L^{M_L}(\hat{\mathbf{r}}) \\ &\quad \times \int r^2 dr j_{L'}(k'r) j_L(kr) Y_{L'}^{M'_L}(\hat{\mathbf{k}}') Y_L^{M_L \dagger}(\hat{\mathbf{k}}) [1 + (-1)^{L'}] V_S(r) \\ &= (4\pi)^2 \sum_{L, M_L} [1 + (-1)^L] \int r^2 dr j_L(k'r) j_L(kr) Y_L^{M_L}(\hat{\mathbf{k}}') Y_L^{M_L \dagger}(\hat{\mathbf{k}}) V_S(r), \end{aligned} \quad (\text{C.5})$$

where we have used in the first step that $\mathcal{P}_r \delta^{(3)}(\mathbf{r} - \mathbf{r}') = \delta^{(3)}(\mathbf{r} + \mathbf{r}')$. On the other hand we can write

$$\begin{aligned} &\langle \mathbf{k}' SM'_S | V | \mathbf{k} SM_S \rangle \\ &= \sum_{L, L', M_L, M'_L} \langle SM'_S | \langle \mathbf{k}' | L' M'_L \rangle \langle L' M'_L | V | L M_L \rangle \langle L M_L | \mathbf{k} \rangle | SM_S \rangle \\ &= \sum_{L, L', M_L, M'_L} Y_{L'}^{M'_L}(\hat{\mathbf{k}}') Y_L^{M_L \dagger}(\hat{\mathbf{k}}) \langle L', M'_L SM'_S | \langle k' | V | k \rangle | L M_L SM_S \rangle \\ &= \sum_{J, M} \sum_{L, L', M_L, M'_L} Y_{L'}^{M'_L}(\hat{\mathbf{k}}') Y_L^{M_L \dagger}(\hat{\mathbf{k}}) \mathcal{C}_{L' M'_L SM'_S}^{JM} \mathcal{C}_{L M_L SM_S}^{JM} \langle (L' S) JM | \langle k' | V | k \rangle | (L S) JM \rangle. \end{aligned} \quad (\text{C.6})$$

Thus,

$$V_{LL'S}^{J(M)}(k, k') = \sum_{\substack{M_L, M'_L \\ M_S, M'_S}} \int \widehat{\mathbf{k}} \widehat{\mathbf{k}}' Y_{L'}^{M'_L \dagger}(\widehat{\mathbf{k}}') Y_L^{M_L}(\widehat{\mathbf{k}}) \mathcal{C}_{L'M'_L S M'_S}^{JM} \mathcal{C}_{LM_L S M_S}^{JM} \langle SM'_S | \langle \mathbf{k}' | V | \mathbf{k} \rangle | SM_S \rangle. \quad (\text{C.7})$$

Plugging in Eq. (C.5) we obtain the Minnesota interaction in partial-wave decomposition:

$$\begin{aligned} V_{LL'S}^{J(M)}(k, k') &= (4\pi)^2 \sum_{\substack{M_L, M'_L \\ M_S, M'_S}} \sum_{L'', M''_L} [1 + (-1)^{L''}] \int \widehat{\mathbf{k}} \widehat{\mathbf{k}}' Y_{L'}^{M'_L \dagger}(\widehat{\mathbf{k}}') Y_L^{M_L}(\widehat{\mathbf{k}}) \mathcal{C}_{L'M'_L S M'_S}^{JM} \mathcal{C}_{LM_L S M_S}^{JM} \\ &\quad \times \int r^2 \mathbf{d}r j_{L''}(k'r) j_{L''}(kr) Y_{L''}^{M''_L}(\widehat{\mathbf{k}}') Y_{L''}^{M''_L \dagger}(\widehat{\mathbf{k}}) V_S(r) \\ &= (4\pi)^2 \delta_{LL'} [1 + (-1)^L] \sum_{M_L, M_S} \mathcal{C}_{LM_L S M_S}^{JM} \mathcal{C}_{LM_L S M_S}^{JM} \int r^2 \mathbf{d}r j_L(k'r) j_L(kr) V_S(r) \\ &= (4\pi)^2 \delta_{LL'} [1 + (-1)^L] \int r^2 \mathbf{d}r j_L(k'r) j_L(kr) V_S(r). \end{aligned} \quad (\text{C.8})$$

Bibliography

- [1] J. Chadwick, *Possible Existence of a Neutron*, Nature **129**, 312 (1932).
- [2] C. F. von Weizsäcker, *Zur Theorie der Kernmassen*, Z. Phys. **96**, 431 (1935).
- [3] H. Yukawa, *On the Interaction of Elementary Particles. I*, Proceedings of the Physico-Mathematical Society of Japan. 3rd Series **17**, 48 (1935).
- [4] S. Weinberg, *Nuclear forces from chiral Lagrangians*, Phys. Lett. B **251**, 288 (1990).
- [5] M. Thoennessen, *Current status and future potential of nuclide discoveries*, Rep. Prog. Phys. **76**, 056301 (2013).
- [6] J. Erler, N. Birge, M. Kortelainen, W. Nazarewicz, E. Olsen, A. M. Perhac, and M. Stoitsov, *The limits of the nuclear landscape*, Nature **486**, 509 (2012).
- [7] P. Haensel, A. Y. Potekhin, and D. G. Yakovlev, *Neutron Stars 1*, vol. 326 of *Astrophysics and Space Science Library* (Springer-Verlag, New York, 2007).
- [8] P. Demorest, T. Pennucci, S. Ransom, M. Roberts, and J. Hessels, *Shapiro Delay Measurement of A Two Solar Mass Neutron Star*, Nature **467**, 1081 (2010).
- [9] E. Fonseca *et al.*, *The NANOGrav Nine-year Data Set: Mass and Geometric Measurements of Binary Millisecond Pulsars*, arXiv:1603.00545.
- [10] J. Antoniadis *et al.*, *A Massive Pulsar in a Compact Relativistic Binary*, Science **340**, 1233232 (2013).
- [11] S. Guillot, R. E. Rutledge, and E. F. Brown, *Neutron Star Radius Measurement with the Quiescent Low-Mass X-ray Binary U24 in NGC 6397*, Astrophys. J. **732**, 88 (2011).
- [12] A. W. Steiner, J. M. Lattimer, and E. F. Brown, *The Neutron Star Mass-Radius Relation and the Equation of State of Dense Matter*, Astrophys. J. **765**, L5 (2013).
- [13] K. Hebeler, J. M. Lattimer, C. J. Pethick, and A. Schwenk, *Constraints on Neutron Star Radii Based on Chiral Effective Field Theory Interactions*, Phys. Rev. Lett. **105**, 161102 (2010).
- [14] K. Hebeler, J. M. Lattimer, C. J. Pethick, and A. Schwenk, *Equation of state and neutron star properties constrained by nuclear physics and observation*, Astrophys. J. **773**, 11 (2013).
- [15] I. Sagert, T. Fischer, M. Hempel, G. Pagliara, J. Schaffner-Bielich, A. Mezzacappa, F.-K. Thielemann, and M. Liebendörfer, *Signals of the QCD Phase Transition in Core-Collapse Supernovae*, Phys. Rev. Lett. **102**, 081101 (2009).

- [16] H.-W. Hammer, A. Nogga, and A. Schwenk, *Three-body forces: From cold atoms to nuclei*, Rev. Mod. Phys. **85**, 197 (2013).
- [17] S. R. Beane, W. Detmold, K. Orginos, and M. J. Savage, *Nuclear Physics from Lattice QCD*, Prog. Part. Nucl. Phys. **66**, 1 (2011).
- [18] M. Arnould, S. Goriely, and K. Takahashi, *The r-process of stellar nucleosynthesis: Astrophysics and nuclear physics achievements and mysteries*, Phys. Rep. **450**, 97 (2007).
- [19] A. T. Gallant *et al.*, *New Precision Mass Measurements of Neutron-Rich Calcium and Potassium Isotopes and Three-Nucleon Forces*, Phys. Rev. Lett. **109**, 032506 (2012).
- [20] F. Wienholtz *et al.*, *Masses of exotic calcium isotopes pin down nuclear forces*, Nature **498**, 346 (2013).
- [21] B. R. Barrett, P. Navrátil, and J. P. Vary, *Ab initio no core shell model*, Prog. Part. Nucl. Phys. **69**, 131 (2013).
- [22] P. Navrátil, V. G. Gueorguiev, J. P. Vary, W. E. Ormand, and A. Nogga, *Structure of $A = 10 - 13$ Nuclei with Two- Plus Three-Nucleon Interactions from Chiral Effective Field Theory*, Phys. Rev. Lett. **99**, 042501 (2007).
- [23] S. C. Pieper and R. B. Wiringa, *Quantum Monte Carlo calculations of light nuclei*, Ann. Rev. Nucl. Part. Sci. **51**, 53 (2001).
- [24] E. Epelbaum, H. Krebs, D. Lee, and U.-G. Meißner, *Ground state energy of dilute neutron matter at next-to-leading order in lattice chiral effective field theory*, Eur. Phys. J. A **40**, 199 (2009).
- [25] E. Epelbaum, H. Krebs, T. A. Lähde, D. Lee, and U.-G. Meißner, *Structure and Rotations of the Hoyle State*, Phys. Rev. Lett. **109**, 252501 (2012).
- [26] K. Kowalski, D. J. Dean, M. Hjorth-Jensen, T. Papenbrock, and P. Piecuch, *Coupled Cluster Calculations of Ground and Excited States of Nuclei*, Phys. Rev. Lett. **92**, 132501 (2004).
- [27] G. Hagen, T. Papenbrock, M. Hjorth-Jensen, and D. J. Dean, *Coupled-cluster computations of atomic nuclei*, Rep. Prog. Phys. **77**, 096302 (2014).
- [28] T. Otsuka, T. Suzuki, J. D. Holt, A. Schwenk, and Y. Akaishi, *Three-Body Forces and the Limit of Oxygen Isotopes*, Phys. Rev. Lett. **105**, 032501 (2010).
- [29] T. Otsuka and A. Schwenk, *Shell Evolution in Exotic Nuclei and Nuclear Forces*, Nuclear Physics News **22(4)**, 22 (2012).
- [30] K. Tsukiyama, S. K. Bogner, and A. Schwenk, *In-medium Similarity Renormalization Group for Nuclei*, Phys. Rev. Lett. **106**, 222502 (2011).
- [31] K. Tsukiyama, S. K. Bogner, and A. Schwenk, *In-medium similarity renormalization group for open-shell nuclei*, Phys. Rev. C **85**, 061304(R) (2012).
- [32] X. Roca-Maza, G. Colò, and H. Sagawa, *New Skyrme interaction with improved spin-isospin properties*, Phys. Rev. C **86**, 031306(R) (2012).

- [33] F. Chappert, M. Girod, and S. Hilaire, *Towards a new Gogny force parameterization: Impact of the neutron matter equation of state*, Phys. Lett. B **668**, 420 (2008).
- [34] J. E. Drut, R. J. Furnstahl, and L. Platter, *Toward ab initio density functional theory for nuclei*, Prog. Part. Nucl. Phys. **64**, 120 (2010).
- [35] E. Engel, *Orbital-Dependent Functionals for the Exchange-Correlation Energy: A Third Generation of Density Functionals*, C. Fiolhais, F. Nogueira, and M. A. L. Marques (eds.), *A Primer in Density Functional Theory*, vol. 620 of *Lecture Notes in Physics*, chap. 2, p. 56 (Springer-Verlag, Berlin Heidelberg, 2003).
- [36] J. E. Drut and L. Platter, *Exact-exchange density functional theory for neutron drops*, Phys. Rev. C **84**, 014318 (2011).
- [37] A. Gezerlis and J. Carlson, *Strongly paired fermions: Cold atoms and neutron matter*, Phys. Rev. C **77**, 032801 (2008).
- [38] O. Kamigaito *et al.*, *Present Status and Future Plan of RIKEN RI Beam Factory*, *Proceedings, 7th International Particle Accelerator Conference (IPAC 2016), Busan, Korea, May 8-13, 2016*, p. 1281 (2016).
- [39] O. Kester, P. Spiller, and H. Stöcker, *FAIR project at GSI, Challenges and Goals for Accelerators in the XXI Century*, chap. 32, p. 611 (World Scientific, Singapore, 2016).
- [40] J. Wei *et al.*, *FRIB Accelerator: Design and Construction Status*, *Proceedings, 13th Heavy Ion Accelerator Technology Conference (HIAT2015), Yokohama, Japan, September 7-11, 2015*, p. MOM1102 (2016).
- [41] M. Wang, G. Audi, A. H. Wapstra, F. G. Kondev, M. MacCormick, X. Xu, and B. Pfeiffer, *The AME2012 atomic mass evaluation*, Chin. Phys. C **36**, 1603 (2012).
- [42] D. Martin, A. Arcones, W. Nazarewicz, and E. Olsen, *Impact of Nuclear Mass Uncertainties on the r Process*, Phys. Rev. Lett. **116**, 121101 (2016).
- [43] J. Bardeen, L. N. Cooper, and J. R. Schrieffer, *Theory of Superconductivity*, Phys. Rev. **108**, 1175 (1957).
- [44] L. N. Cooper, *Bound Electron Pairs in a Degenerate Fermi Gas*, Phys. Rev. **104**, 1189 (1956).
- [45] A. Bohr, B. R. Mottelson, and D. Pines, *Possible Analogy between the Excitation Spectra of Nuclei and Those of the Superconducting Metallic State*, Phys. Rev. **110**, 936 (1958).
- [46] A. B. Migdal, *Superfluidity and the Moments of Inertia of Nuclei*, Zh. Eksp. Teor. Fiz. **37**, 249 (1959).
- [47] H. Sagawa and K. Hagino, *Pairing correlations in exotic nuclei*, *Proceedings of the International Summer School for Advanced Studies 'Dynamics of open nuclear systems' (PREDEAL12), Predeal, Romania, July 6-20, 2012*, vol. 413, p. 012008 (IOP Publishing, 2013).
- [48] K. Bennaceur, J. Dobaczewski, and M. Płoszajczak, *Pairing anti-halo effect*, Phys. Lett. B **496**, 154 (2000).

- [49] Y. A. Litvinov *et al.*, *Isospin Dependence in the Odd-Even Staggering of Nuclear Binding Energies*, Phys. Rev. Lett. **95**, 042501 (2005).
- [50] D. J. Dean and M. Hjorth-Jensen, *Pairing in nuclear systems: from neutron stars to finite nuclei*, Rev. Mod. Phys. **75**, 607 (2003).
- [51] D. M. Brink and R. A. Broglia, *Nuclear Superfluidity: Pairing in Finite Systems*, vol. 24 of *Cambridge Monographs on Particle Physics, Nuclear Physics and Cosmology* (Cambridge University Press, 2005).
- [52] E. Rutherford and H. Geiger, *The Charge and Nature of the α -Particle*, Proc. R. Soc. A **81**, 162 (1908).
- [53] H. Geiger and E. Marsden, *The Laws of Deflexion of α -Particles through Large Angles*, Philos. Mag. **25**, 604 (1913).
- [54] J. J. Thomson, *Bakerian Lecture: Rays of Positive Electricity*, Proc. R. Soc. A **89**, 1 (1913).
- [55] F. W. Aston, *Mass spectra and isotopes* (E. Arnold & co., New York, 1942).
- [56] M. Notani *et al.*, *New neutron-rich isotopes, ^{34}Ne , ^{37}Na and ^{43}Si , produced by fragmentation of a 64 A MeV ^{48}Ca beam*, Phys. Lett. B **542**, 49 (2002).
- [57] D. J. Morrissey and B. M. Sherrill, *In-Flight Separation of Projectile Fragments*, J. Al-Khalili and E. Roeckl (eds.), *The Euroschool Lectures on Physics with Exotic Beams, Vol. I*, vol. 651 of *Lecture Notes in Physics*, p. 113 (Springer, Berlin, Heidelberg, 2004).
- [58] M. Huyse, *The Why and How of Radioactive-Beam Research*, J. Al-Khalili and E. Roeckl (eds.), *The Euroschool Lectures on Physics with Exotic Beams, Vol. I*, vol. 651 of *Lecture Notes in Physics*, p. 1 (Springer, Berlin, Heidelberg, 2004).
- [59] K. Blaum, *High-accuracy mass spectrometry with stored ions*, Phys. Rep. **425**, 1 (2006).
- [60] A. Hewish, S. J. Bell, J. D. H. Pilkington, P. F. Scott, and R. A. Collins, *Observation of a Rapidly Pulsating Radio Source*, Nature **217**, 709 (1968).
- [61] T. Gold, *Rotating Neutron Stars as the Origin of the Pulsating Radio Sources*, Nature **218**, 731 (1968).
- [62] L. D. Landau, *On the theory of stars*, Phys. Z. Sowjetunion **1**, 285 (1932).
- [63] W. Baade and F. Zwicky, *On Super-Novae*, Proc. National Akad. Sci. **20**, 254 (1934).
- [64] W. Baade and F. Zwicky, *Cosmic Rays from Super-Novae*, Proc. National Akad. Sci. **20**, 259 (1934).
- [65] W. Baade and F. Zwicky, *Remarks on Super-Novae and Cosmic Rays*, Phys. Rev. **46**, 76 (1934).
- [66] R. C. Tolman, *Static Solutions of Einstein's Field Equations for Spheres of Fluid*, Phys. Rev. **55**, 364 (1939).

- [67] J. R. Oppenheimer and G. M. Volkoff, *On Massive Neutron Cores*, Phys. Rev. **55**, 374 (1939).
- [68] A. G. W. Cameron, *Pycnonuclear Reactions and Nova Explosions*, Astrophys. J. **130**, 916 (1959).
- [69] D. D. Ivanenko and D. F. Kurdgelaidze, *Hypothesis concerning quark stars*, Astrofizika **1**, 479 (1965).
- [70] D. D. Ivanenko and D. F. Kurdgelaidze, *Remarks on Quark Stars*, Lettere al Nuovo Cimento **2**, 13 (1969).
- [71] V. L. Ginzburg and D. A. Kirzhnits, *On the Superfluidity of Neutron Stars*, Zh. Eksp. Teor. Fiz. **47**, 2006 (1964).
- [72] V. L. Ginzburg and D. A. Kirzhnits, *Superfluidity and Superconductivity in the Universe*, Usp. Fiz. Nauk **97**, 601 (1969).
- [73] W. R. A., *Some Effects of the Strong Interactions on the Properties of Neutron-Star Matter*, Astrophys. J. **145**, 834 (1966).
- [74] M. Hoffberg, A. E. Glassgold, R. W. Richardson, and M. Ruderman, *Anisotropic Superfluidity in Neutron Star Matter*, Phys. Rev. Lett. **24**, 775 (1970).
- [75] V. G. J. Stoks, R. A. M. Klomp, M. C. M. Rentmeester, and J. J. de Swart, *Partial wave analysis of all nucleon-nucleon scattering data below 350 MeV*, Phys. Rev. C **48**, 792 (1993).
- [76] A. Gezerlis, C. J. Pethick, and A. Schwenk, *Pairing and superfluidity of nucleons in neutron stars*, K.-H. Bennemann and J. B. Ketterson (eds.), *Novel Superfluids: Volume 2*, vol. 157 of *International Series of Monographs on Physics*, chap. 22, p. 580 (Oxford University Press, Oxford, 2014).
- [77] D. G. Yakovlev and C. J. Pethick, *Neutron star cooling*, Ann. Rev. Astron. Astrophys. **42**, 169 (2004).
- [78] D. Page, J. M. Lattimer, M. Prakash, and A. W. Steiner, *Minimal cooling of neutron stars: A New paradigm*, Astrophys. J. Suppl. Ser. **155**, 623 (2004).
- [79] D. Page and A. Cumming, *Superbursts from Strange Stars*, Astrophys. J. **635**, L157 (2005).
- [80] C. J. Pethick, *Cooling of neutron stars*, Rev. Mod. Phys. **64**, 1133 (1992).
- [81] D. G. Yakovlev, A. D. Kaminker, O. Y. Gnedin, and P. Haensel, *Neutrino emission from neutron stars*, Phys. Rep. **354**, 1 (2001).
- [82] J. Boguta, *Remarks on the beta stability in neutron stars*, Phys. Lett. B **106**, 255 (1981).
- [83] J. M. Lattimer and F. D. Swesty, *A generalized equation of state for hot, dense matter*, Nucl. Phys. A **535**, 331 (1991).
- [84] D. G. Yakovlev, K. P. Levenfish, and Yu. A. Shibano, *Cooling neutron stars and superfluidity in their cores*, Phys. Usp. **42**, 737 (1999).

- [85] E. Flowers and N. Itoh, *Transport properties of dense matter*, *Astrophys. J.* **206**, 218 (1976).
- [86] D. Page, M. Prakash, J. M. Lattimer, and A. W. Steiner, *Rapid Cooling of the Neutron Star in Cassiopeia A Triggered by Neutron Superfluidity in Dense Matter*, *Phys. Rev. Lett.* **106**, 081101 (2011).
- [87] J. M. Lattimer, *Neutron Stars*, J. Hewett, J. Jaros, T. Kamae, and C. Prescott (eds.), *33rd SLAC Summer Institute on Particle Physics (SSI 2005): Gravity in the Quantum World and the Cosmos Menlo Park, California, July 25-August 5, 2005*, vol. Co507252, p. L007 (eConf, 2005).
- [88] J. M. Lattimer, *The nuclear equation of state and neutron star masses*, *Ann. Rev. Nucl. Part. Sci.* **62**, 485 (2012).
- [89] J. M. Lattimer, *Observed Neutron Star Masses*, <https://stellarcollapse.org/nsmasses>, accessed September 16, 2016.
- [90] S. K. Greif, *Constraining the radius of neutron stars through the moment of inertia*, Master's thesis, Technische Universität Darmstadt (2016).
- [91] B. P. Abbott *et al.* (LIGO Scientific Collaboration and Virgo Collaboration), *Observation of Gravitational Waves from a Binary Black Hole Merger*, *Phys. Rev. Lett.* **116**, 061102 (2016).
- [92] J. Aasi *et al.* (LIGO Scientific Collaboration), *Advanced LIGO*, *Class. Quant. Grav.* **32**, 074001 (2015).
- [93] A. Bauswein and H.-T. Janka, *Measuring Neutron-Star Properties via Gravitational Waves from Neutron-Star Mergers*, *Phys. Rev. Lett.* **108**, 011101 (2012).
- [94] A. Bauswein, H.-T. Janka, K. Hebeler, and A. Schwenk, *Equation-of-state dependence of the gravitational-wave signal from the ring-down phase of neutron-star mergers*, *Phys. Rev. D* **86**, 063001 (2012).
- [95] A. Bauswein, N. Stergioulas, and H.-T. Janka, *Revealing the high-density equation of state through binary neutron star mergers*, *Phys. Rev. D* **90**, 023002 (2014).
- [96] H. A. Bethe and R. F. Bacher, *Nuclear Physics A. Stationary States of Nuclei*, *Rev. Mod. Phys.* **8**, 82 (1936).
- [97] M. Bender, P.-H. Heenen, and P.-G. Reinhard, *Self-consistent mean-field models for nuclear structure*, *Rev. Mod. Phys.* **75**, 121 (2003).
- [98] P. Hohenberg and W. Kohn, *Inhomogeneous Electron Gas*, *Phys. Rev.* **136**, B864 (1964).
- [99] M. Levy, *Electron densities in search of Hamiltonians*, *Phys. Rev. A* **26**, 1200 (1982).
- [100] L. H. Thomas, *The calculation of atomic fields*, *Proc. Cambridge Philos. Soc.* **23**, 542 (1927).
- [101] E. Fermi, *Eine statistische Methode zur Bestimmung einiger Eigenschaften des Atoms und ihre Anwendung auf die Theorie des periodischen Systems der Elemente*, *Z. Phys.* **48**, 73 (1928).

- [102] J. P. Perdew and S. Kurth, *Density Functionals for Non-relativistic Coulomb Systems in the New Century*, C. Fiolhais, F. Nogueira, and M. A. L. Marques (eds.), *A Primer in Density Functional Theory*, vol. 620 of *Lecture Notes in Physics*, chap. 1, p. 1 (Springer-Verlag, Berlin Heidelberg, 2003).
- [103] W. Kohn and L. J. Sham, *Self-Consistent Equations Including Exchange and Correlation Effects*, *Phys. Rev.* **140**, A1133 (1965).
- [104] J. W. Negele and D. Vautherin, *Density-Matrix Expansion for an Effective Nuclear Hamiltonian*, *Phys. Rev. C* **5**, 1472 (1972).
- [105] J. W. Negele and D. Vautherin, *Density-matrix expansion for an effective nuclear Hamiltonian. II*, *Phys. Rev. C* **11**, 1031 (1975).
- [106] S. K. Bogner, R. J. Furnstahl, and L. Platter, *Density matrix expansion for low-momentum interactions*, *Eur. Phys. J. A* **39**, 219 (2009).
- [107] J. Dobaczewski, W. Nazarewicz, and P. G. Reinhard, *Pairing interaction and self-consistent densities in neutron-rich nuclei*, *Nucl. Phys. A* **693**, 361 (2001).
- [108] M. V. Stoitsov, J. Dobaczewski, W. Nazarewicz, S. Pittel, and D. J. Dean, *Systematic study of deformed nuclei at the drip lines and beyond*, *Phys. Rev. C* **68**, 054312 (2003).
- [109] T. Kortelainen, M. Lesinski, J. Moré, W. Nazarewicz, J. Sarich, N. Schunck, M. V. Stoitsov, and S. Wild, *Nuclear energy density optimization*, *Phys. Rev. C* **82**, 024313 (2010).
- [110] M. Kortelainen *et al.*, *Nuclear energy density optimization: Shell structure*, *Phys. Rev. C* **89**, 054314 (2014).
- [111] R. Aaij *et al.* (LHCb Collaboration), *Observation of $J/\psi p$ Resonances Consistent with Pentaquark States in $\Lambda_b^0 \rightarrow J/\psi K^- p$ Decays*, *Phys. Rev. Lett.* **115**, 072001 (2015).
- [112] A. Esposito, A. L. Guerrieri, F. Piccinini, A. Pilloni, and A. D. Polosa, *Four-quark hadrons: An updated review*, *Int. J. Mod. Phys. A* **30**, 1530002 (2015).
- [113] K. A. Olive *et al.* (Particle Data Group), *Review of Particle Physics*, *Chin. Phys. C* **38**, 090001 (2014), and 2015 update.
- [114] D. B. Kaplan, *Five lectures on effective field theory, Lectures delivered at the 17th National Nuclear Physics Summer School 2015, Berkeley, June 6-17, 2005* (2005), nucl-th/0510023.
- [115] J. Goldstone, A. Salam, and S. Weinberg, *Broken Symmetries*, *Phys. Rev.* **127**, 965 (1962).
- [116] D. J. Gross and F. Wilczek, *Ultraviolet Behavior of Non-Abelian Gauge Theories*, *Phys. Rev. Lett.* **30**, 1343 (1973).
- [117] H. D. Politzer, *Reliable Perturbative Results for Strong Interactions?*, *Phys. Rev. Lett.* **30**, 1346 (1973).
- [118] S. Dürr *et al.*, *Ab Initio Determination of Light Hadron Masses*, *Science* **322**, 1224 (2008).

- [119] S. R. Beane, E. Chang, S. Cohen, W. Detmold, H. W. Lin, K. Orginos, A. Parreño, M. J. Savage, and B. C. Tiburzi (NPLQCD Collaboration), *Magnetic Moments of Light Nuclei from Lattice Quantum Chromodynamics*, Phys. Rev. Lett. **113**, 252001 (2014).
- [120] S. R. Beane *et al.* (NPLQCD Collaboration), *Nucleon-nucleon scattering parameters in the limit of SU(3) flavor symmetry*, Phys. Rev. C **88**, 024003 (2013).
- [121] P. F. Bedaque and U. van Kolck, *Nucleon deuteron scattering from an effective field theory*, Phys. Lett. B **428**, 221 (1998).
- [122] D. B. Kaplan, M. J. Savage, and M. B. Wise, *A New expansion for nucleon-nucleon interactions*, Phys. Lett. B **424**, 390 (1998).
- [123] S. Weinberg, *Effective chiral Lagrangians for nucleon - pion interactions and nuclear forces*, Nucl. Phys. B **363**, 3 (1991).
- [124] S. Weinberg, *Three body interactions among nucleons and pions*, Phys. Lett. B **295**, 114 (1992).
- [125] S. Weinberg, *Phenomenological Lagrangians*, Physica A **96**, 327 (1979).
- [126] D. B. Kaplan, M. J. Savage, and M. B. Wise, *Two nucleon systems from effective field theory*, Nucl. Phys. B **534**, 329 (1998).
- [127] E. Epelbaum, *Few-nucleon forces and systems in chiral effective field theory*, Prog. Part. Nucl. Phys. **57**, 654 (2006).
- [128] R. J. N. Phillips, *The two-nucleon interaction*, Rep. Prog. Phys. **22**, 562 (1959).
- [129] E. Epelbaum and U.-G. Meißner, *Isospin-violating nucleon-nucleon forces using the method of unitary transformation*, Phys. Rev. C **72**, 044001 (2005).
- [130] E. Epelbaum, H.-W. Hammer, and U.-G. Meißner, *Modern Theory of Nuclear Forces*, Rev. Mod. Phys. **81**, 1773 (2009).
- [131] E. Epelbaum, H. Krebs, and U.-G. Meißner, *Precision Nucleon-Nucleon Potential at Fifth Order in the Chiral Expansion*, Phys. Rev. Lett. **115**, 122301 (2015).
- [132] H. Krebs, A. Gasparyan, and E. Epelbaum, *Chiral three-nucleon force at N⁴LO: Longest-range contributions*, Phys. Rev. C **85**, 054006 (2012).
- [133] U. van Kolck, *Few nucleon forces from chiral Lagrangians*, Phys. Rev. C **49**, 2932 (1994).
- [134] E. Epelbaum, *Four-nucleon force in chiral effective field theory*, Phys. Lett. B **639**, 456 (2006).
- [135] E. Epelbaum, *Four-nucleon force using the method of unitary transformation*, Eur. Phys. J. A **34**, 197 (2007).
- [136] R. Roth, S. Binder, K. Vobig, A. Calci, J. Langhammer, and P. Navrátil, *Ab Initio Calculations of Medium-Mass Nuclei with Normal-Ordered Chiral NN+3N Interactions*, Phys. Rev. Lett. **109**, 052501 (2012).

- [137] H. Hergert, S. K. Bogner, S. Binder, A. Calci, J. Langhammer *et al.*, *In-Medium Similarity Renormalization Group with Chiral Two- Plus Three-Nucleon Interactions*, Phys. Rev. C **87**, 034307 (2013).
- [138] S. Binder, J. Langhammer, A. Calci, and R. Roth, *Ab initio path to heavy nuclei*, Phys. Lett. B **736**, 119 (2014).
- [139] K. Hebeler and A. Schwenk, *Chiral three-nucleon forces and neutron matter*, Phys. Rev. C **82**, 014314 (2010).
- [140] I. Tews, T. Krüger, K. Hebeler, and A. Schwenk, *Neutron Matter at Next-to-Next-to-Next-to-Leading Order in Chiral Effective Field Theory*, Phys. Rev. Lett. **110**, 032504 (2013).
- [141] C. Drischler, K. Hebeler, and A. Schwenk, *Asymmetric nuclear matter based on chiral two- and three-nucleon interactions*, Phys. Rev. C **93**, 054314 (2016).
- [142] V. Bernard, E. Epelbaum, H. Krebs, and U.-G. Meißner, *Subleading contributions to the chiral three-nucleon force. I. Long-range terms*, Phys. Rev. C **77**, 064004 (2008).
- [143] V. Bernard, E. Epelbaum, H. Krebs, and U.-G. Meißner, *Subleading contributions to the chiral three-nucleon force II: Short-range terms and relativistic corrections*, Phys. Rev. C **84**, 054001 (2011).
- [144] E. Epelbaum, H. Krebs, and U.-G. Meißner, *Improved chiral nucleon-nucleon potential up to next-to-next-to-next-to-leading order*, Eur. Phys. J. A **51**, 53 (2015).
- [145] D. R. Entem and R. Machleidt, *Accurate charge-dependent nucleon-nucleon potential at fourth order of chiral perturbation theory*, Phys. Rev. C **68**, 041001(R) (2003).
- [146] R. Machleidt and D. R. Entem, *Chiral effective field theory and nuclear forces*, Phys. Rep. **503**, 1 (2011).
- [147] E. Epelbaum, W. Glöckle, and U.-G. Meißner, *Improving the convergence of the chiral expansion for nuclear forces II: Low phases and the deuteron*, Eur. Phys. J. A **19**, 401 (2004).
- [148] E. Epelbaum, W. Glöckle, and U.-G. Meißner, *The Two-nucleon system at next-to-next-to-next-to-leading order*, Nucl. Phys. A **747**, 362 (2005).
- [149] E. Epelbaum, W. Glöckle, and U.-G. Meißner, *Improving the convergence of the chiral expansion for nuclear forces – I: Peripheral phases*, Eur. Phys. J. A **19**, 125 (2004).
- [150] A. Gezerlis, I. Tews, E. Epelbaum, S. Gandolfi, K. Hebeler, A. Nogga, and A. Schwenk, *Quantum Monte Carlo Calculations with Chiral Effective Field Theory Interactions*, Phys. Rev. Lett. **111**, 032501 (2013).
- [151] A. Gezerlis, I. Tews, E. Epelbaum, M. Freunek, S. Gandolfi, K. Hebeler, A. Nogga, and A. Schwenk, *Local chiral effective field theory interactions and quantum Monte Carlo applications*, Phys. Rev. C **90**, 054323 (2014).
- [152] I. Tews, *Quantum Monte Carlo calculations with chiral effective field theory interactions*, Ph.D. thesis, Technische Universität Darmstadt (2015).

- [153] V. Baru, E. Epelbaum, C. Hanhart, M. Hoferichter, A. E. Kudryavtsev, and D. R. Phillips, *The Multiple-scattering series in pion-deuteron scattering and the nucleon-nucleon potential: perspectives from effective field theory*, Eur. Phys. J. A **48**, 69 (2012).
- [154] H. Krebs, A. Gasparyan, and E. Epelbaum, *Chiral three-nucleon force at N^4 LO. II. Intermediate-range contributions*, Phys. Rev. C **87**, 054007 (2013).
- [155] J. Carlson, S.-Y. Chang, V. R. Pandharipande, and K. E. Schmidt, *Superfluid Fermi Gases with Large Scattering Length*, Phys. Rev. Lett. **91**, 050401 (2003).
- [156] A. Schwenk and C. J. Pethick, *Resonant Fermi Gases with a Large Effective Range*, Phys. Rev. Lett. **95**, 160401 (2005).
- [157] J. Carlson, S. Gandolfi, and A. Gezerlis, *Quantum Monte Carlo approaches to nuclear and atomic physics*, Prog. Theor. Exp. Phys. **2012**, 01A209 (2012).
- [158] C. Drischler, V. Somà, and A. Schwenk, *Microscopic calculations and energy expansions for neutron-rich matter*, Phys. Rev. C **89**, 025806 (2014).
- [159] C. Drischler, A. Carbone, K. Hebeler, and A. Schwenk, *Neutron matter from chiral two- and three-nucleon calculations up to N^3 LO*, arXiv:1608.05615.
- [160] N. Kaiser, S. Fritsch, and W. Weise, *Chiral dynamics and nuclear matter*, Nucl. Phys. A **697**, 255 (2002).
- [161] W. Weise, *Nuclear chiral dynamics and phases of QCD*, Prog. Part. Nucl. Phys. **67**, 299 (2012).
- [162] S. K. Bogner, R. J. Furnstahl, and A. Schwenk, *From low-momentum interactions to nuclear structure*, Prog. Part. Nucl. Phys. **65**, 94 (2010).
- [163] R. J. Furnstahl and K. Hebeler, *New applications of renormalization group methods in nuclear physics*, Rep. Prog. Phys. **76**, 126301 (2013).
- [164] K. Hebeler, S. K. Bogner, R. J. Furnstahl, A. Nogga, and A. Schwenk, *Improved nuclear matter calculations from chiral low-momentum interactions*, Phys. Rev. C **83**, 031301(R) (2011).
- [165] K. Hebeler and R. J. Furnstahl, *Neutron matter based on consistently evolved chiral three-nucleon interactions*, Phys. Rev. C **87**, 031302 (2013).
- [166] K. Hebeler, *Momentum space evolution of chiral three-nucleon forces*, Phys. Rev. C **85**, 021002(R) (2012).
- [167] A. Carbone, A. Rios, and A. Polls, *Correlated density-dependent chiral forces for infinite matter calculations within the Green's function approach*, Phys. Rev. C **90**, 054322 (2014).
- [168] T. Krüger, I. Tews, K. Hebeler, and A. Schwenk, *Neutron matter from chiral effective field theory interactions*, Phys. Rev. C **88**, 025802 (2013).
- [169] I. Tews, T. Krüger, A. Gezerlis, K. Hebeler, and A. Schwenk, *Neutron matter with chiral EFT interactions: Perturbative and first QMC calculations*, Proceedings, International Conference on Nuclear Theory in the Supercomputing Era (NTSE-2013): Ames, Iowa, USA, May 13-17, 2013, p. 302 (2013).

- [170] T. Krüger, *Chiral four-nucleon forces in nucleonic matter*, Master's thesis, Technische Universität Darmstadt (2012).
- [171] S. K. Bogner, A. Schwenk, R. J. Furnstahl, and A. Nogga, *Is nuclear matter perturbative with low-momentum interactions?*, Nucl. Phys. A **763**, 59 (2005).
- [172] I. Tews, S. Gandolfi, A. Gezerlis, and A. Schwenk, *Quantum Monte Carlo calculations of neutron matter with chiral three-body forces*, Phys. Rev. C **93**, 024305 (2016).
- [173] A. Gezerlis and J. Carlson, *Low-density neutron matter*, Phys. Rev. C **81**, 025803 (2010).
- [174] A. Akmal, V. R. Pandharipande, and D. G. Ravenhall, *The Equation of state of nucleon matter and neutron star structure*, Phys. Rev. C **58**, 1804 (1998).
- [175] S. Gandolfi, J. Carlson, and S. Reddy, *The maximum mass and radius of neutron stars and the nuclear symmetry energy*, Phys. Rev. C **85**, 032801(R) (2012).
- [176] T. Krüger, I. Tews, B. Friman, K. Hebeler, and A. Schwenk, *The chiral condensate in neutron matter*, Phys. Lett. B **726**, 412 (2013).
- [177] A. Bazavov *et al.* (HotQCD Collaboration), *The chiral and deconfinement aspects of the QCD transition*, Phys. Rev. D **85**, 054503 (2012).
- [178] E. G. Drukarev and E. M. Levin, *The QCD sum rules and nuclear matter*, Nucl. Phys. A **511**, 679 (1990).
- [179] T. D. Cohen, R. J. Furnstahl, and D. K. Griegel, *Quark and gluon condensates in nuclear matter*, Phys. Rev. C **45**, 1881 (1992).
- [180] M. F. M. Lutz, B. Friman, and C. Appel, *Saturation from nuclear pion dynamics*, Phys. Lett. B **474**, 7 (2000).
- [181] N. Kaiser, P. de Homont, and W. Weise, *In-medium chiral condensate beyond linear density approximation*, Phys. Rev. C **77**, 025204 (2008).
- [182] J. Gasser, H. Leutwyler, and M. E. Sainio, *Sigma term update*, Phys. Lett. B **253**, 252 (1991).
- [183] M. Frink, U.-G. Meißner, and I. Scheller, *Baryon masses, chiral extrapolations, and all that*, Eur. Phys. J. A **24**, 395 (2005).
- [184] M. F. M. Lutz and A. Semke, *Chiral extrapolations and strangeness in the baryon ground states*, PoS **CD12**, 074 (2013).
- [185] J. M. Alarcon, J. Martin Camalich, and J. A. Oller, *The chiral representation of the πN scattering amplitude and the pion-nucleon sigma term*, Phys. Rev. D **85**, 051503 (2012).
- [186] J. Stahov, H. Clement, and G. J. Wagner, *Evaluation of the Pion-Nucleon Sigma Term from CHAOS data*, Phys. Lett. B **726**, 685 (2013).
- [187] M. Hoferichter, J. Ruiz de Elvira, B. Kubis, and U.-G. Meißner, *High-Precision Determination of the Pion-Nucleon σ Term from Roy-Steiner Equations*, Phys. Rev. Lett. **115**, 092301 (2015).

- [188] B. L. Friman, V. R. Pandharipande, and R. B. Wiringa, *Calculations of Pion Excess in Nuclei*, Phys. Rev. Lett. **51**, 763 (1983).
- [189] V. Bernard and U.-G. Meißner, *The Nucleon axial-vector coupling beyond one loop*, Phys. Lett. B **639**, 278 (2006).
- [190] J. C. Berengut, E. Epelbaum, V. V. Flambaum, C. Hanhart, U.-G. Meißner, J. Nebreda, and J. R. Peláez, *Varying the light quark mass: impact on the nuclear force and Big Bang nucleosynthesis*, Phys. Rev. D **87**, 085018 (2013).
- [191] N. Kaiser and W. Weise, *Chiral condensate in neutron matter*, Phys. Lett. B **671**, 25 (2009).
- [192] A. Lacour, J. A. Oller, and U.-G. Meißner, *The Chiral quark condensate and pion decay constant in nuclear matter at next-to-leading order*, J. Phys. G: Nucl. Part. Phys. **37**, 125002 (2010).
- [193] A. Lacour, J. A. Oller, and U.-G. Meißner, *Non-perturbative methods for a chiral effective field theory of finite density nuclear systems*, Annals Phys. **326**, 241 (2011).
- [194] T. Krüger, K. Hebeler, and A. Schwenk, *To which densities is spin-polarized neutron matter a weakly interacting Fermi gas?*, Phys. Lett. B **744**, 18 (2015).
- [195] T. Schäfer and A. Schwenk, *Stark gekoppelt und universell: Was lehren uns ultrakalte Gase über die Eigenschaften nuklearer Materie?*, Physik Journal **13**(1), 27 (2014).
- [196] I. Bloch, J. Dalibard, and W. Zwerger, *Many-body physics with ultracold gases*, Rev. Mod. Phys. **80**, 885 (2008).
- [197] A. Bulgac, M. M. Forbes, and P. Magierski, *The Unitary Fermi Gas: From Monte Carlo to Density Functionals*, Lect. Notes Phys. **836**, 305 (2012).
- [198] S. Goriely, N. Chamel, and J. M. Pearson, *Hartree-Fock-Bogoliubov nuclear mass model with 0.50 MeV accuracy based on standard forms of Skyrme and pairing functionals*, Phys. Rev. C **88**, 061302 (2013).
- [199] I. Vidana, A. Polls, and A. Ramos, *Spin polarized neutron matter and magnetic susceptibility within the Brueckner-Hartree-Fock approximation*, Phys. Rev. C **65**, 035804 (2002).
- [200] I. Bombaci, A. Polls, A. Ramos, A. Rios, and I. Vidana, *Microscopic calculations of spin polarized neutron matter at finite temperature*, Phys. Lett. B **632**, 638 (2006).
- [201] S. R. Beane, W. Detmold, K. Orginos, and M. J. Savage, *Nuclear Physics from Lattice QCD*, Prog. Part. Nucl. Phys. **66**, 1 (2011).
- [202] F. Sammarruca and P. G. Krastev, *Spin polarized neutron matter within the Dirac-Brueckner-Hartree-Fock approach*, Phys. Rev. C **75**, 034315 (2007).
- [203] G. H. Bordbar and M. Bigdeli, *Spin polarized asymmetric nuclear matter and neutron star matter within the lowest order constrained variational method*, Phys. Rev. C **77**, 015805 (2008).

- [204] M. C. M. Rentmeester, R. G. E. Timmermans, and J. J. de Swart, *Determination of the chiral coupling constants c_3 and c_4 in new pp and np partial-wave analyses*, Phys. Rev. C **67**, 044001 (2003).
- [205] H.-W. Hammer and R. J. Furnstahl, *Effective field theory for dilute Fermi systems*, Nucl. Phys. A **678**, 277 (2000).
- [206] M. Kutschera and W. Wójcik, *Polarized neutron matter with Skyrme forces*, Phys. Lett. B **325**, 271 (1994).
- [207] M. M. Forbes, A. Gezerlis, K. Hebeler, T. Lesinski, and A. Schwenk, *The neutron polaron as a constraint on nuclear density functionals*, Phys. Rev. C **89**, 041301 (2014).
- [208] M. Beiner, H. Flocard, N. van Giai, and P. Quentin, *Nuclear ground-state properties and self-consistent calculations with the Skyrme interaction: (I). Spherical description*, Nucl. Phys. A **238**, 29 (1975).
- [209] N. van Giai and H. Sagawa, *Spin-isospin and pairing properties of modified Skyrme interactions*, Phys. Lett. B **106**, 379 (1981).
- [210] J. Bartel, P. Quentin, M. Brack, C. Guet, and H.-B. Håkansson, *Towards a better parametrisation of Skyrme-like effective forces: A Critical study of the SkM force*, Nucl. Phys. A **386**, 79 (1982).
- [211] E. Chabanat, P. Bonche, P. Haensel, J. Meyer, and R. Schaeffer, *A Skyrme parametrization from subnuclear to neutron star densities. 2. Nuclei far from stabilities*, Nucl. Phys. A **635**, 231 (1998); *ibid.* **643**, 441 (E) (1998).
- [212] P. G. Reinhard, D. J. Dean, W. Nazarewicz, J. Dobaczewski, J. A. Maruhn, and M. R. Strayer, *Shape coexistence and the effective nucleon-nucleon interaction*, Phys. Rev. C **60**, 014316 (1999).
- [213] S. Goriely, M. Samyn, J. M. Pearson, and M. Onsi, *Further explorations of Skyrme–Hartree–Fock–Bogoliubov mass formulas. IV: Neutron-matter constraint*, Nucl. Phys. A **750**, 425 (2005).
- [214] D. Pines and M. A. Alpar, *Superfluidity in neutron stars*, Nature **316**, 27 (1985).
- [215] F. Sarazin *et al.*, *Halo neutrons and the β decay of ^{11}Li* , Phys. Rev. C **70**, 031302 (2004).
- [216] C. Drischler, T. Krüger, K. Hebeler, and A. Schwenk, *Pairing in neutron matter: New uncertainty estimates and three-body forces*, arXiv:1610.05213.
- [217] M. Baldo, U. Lombardo, and P. Schuck, *Deuteron formation in expanding nuclear matter from a strong coupling BCS approach*, Phys. Rev. C **52**, 975 (1995).
- [218] S. Ramanan, S. K. Bogner, and R. J. Furnstahl, *Weinberg eigenvalues and pairing with low-momentum potentials*, Nucl. Phys. A **797**, 81 (2007).
- [219] L. P. Gor'kov and T. K. Melik-Barkhudarov, *Contribution to the Theory of Superfluidity in an Imperfect Fermi Gas*, Sov. Phys. JETP **13**, 1018 (1961).

- [220] H. Heiselberg, C. J. Pethick, H. Smith, and L. Viverit, *Influence of Induced Interactions on the Superfluid Transition in Dilute Fermi Gases*, Phys. Rev. Lett. **85**, 2418 (2000).
- [221] D. Ding, A. Rios, H. Dussan, W. H. Dickhoff, S. J. Witte, A. Carbone, and A. Polls, *Pairing in high-density neutron matter including short- and long-range correlations*, Phys. Rev. C **94**, 025802 (2016).
- [222] J. W. Clark, V. A. Khodel, and M. V. Zverev, *Superfluid Phases of Triplet Pairing*, M. P. Das and F. Green (eds.), *Condensed Matter Theories*, vol. 17, chap. 2, p. 23 (Nova Science Publishers, New York, 2003), nucl-th/0203046.
- [223] T. Takatsuka, *Superfluid State in Neutron Star Matter. I*, Prog. Theor. Phys. **44**, 905 (1970).
- [224] V. V. Khodel, V. A. Khodel, and J. W. Clark, *Triplet pairing in neutron matter*, Nucl. Phys. A **679**, 827 (2001).
- [225] S. Maurizio, J. W. Holt, and P. Finelli, *Nuclear pairing from microscopic forces: Singlet channels and higher-partial waves*, Phys. Rev. C **90**, 044003 (2014).
- [226] S. Srinivas and S. Ramanan, *Triplet Pairing in pure neutron matter*, arXiv:1606.09053.
- [227] M. Baldo, Ø. Elgarøy, L. Engvik, M. Hjorth-Jensen, and H.-J. Schulze, $^3P_2 - ^3F_2$ pairing in neutron matter with modern nucleon-nucleon potentials, Phys. Rev. C **58**, 1921 (1998).
- [228] E. Krotscheck, *Superfluidity in neutron matter*, Z. Phys. **251**, 135 (1972).
- [229] S. Ramanan, S. Bogner, and R. J. Furnstahl, *Weinberg eigenvalues and pairing with low-momentum potentials*, Nucl. Phys. A **797**, 81 (2007).
- [230] J. Schrieffer, *Theory of Superconductivity* (Perseus Books, 1999).
- [231] D. D. Johnson, *Modified Broyden's method for accelerating convergence in self-consistent calculations*, Phys. Rev. B **38**, 12807 (1988).
- [232] V. A. Khodel, V. V. Khodel, and J. W. Clark, *Solution of the gap equation in neutron matter*, Nucl. Phys. A **598**, 390 (1996).
- [233] C. G. Broyden, *A Class of Methods for Solving Nonlinear Simultaneous Equations*, Math. Comp. **19**, 577 (1965).
- [234] A. Baran, A. Bulgac, M. M. Forbes, G. Hagen, W. Nazarewicz, N. Schunck, and M. V. Stoitsov, *Broyden's method in nuclear structure calculations*, Phys. Rev. C **78**, 014318 (2008).
- [235] K. Hebeler, A. Schwenk, and B. Friman, *Dependence of the BCS 1S_0 superfluid pairing gap on nuclear interactions*, Phys. Lett. B **648**, 176 (2007).
- [236] J. W. Holt, N. Kaiser, and W. Weise, *Density-dependent effective nucleon-nucleon interaction from chiral three-nucleon forces*, Phys. Rev. C **81**, 024002 (2010).
- [237] C. Wellenhofer, J. W. Holt, and N. Kaiser, *Divergence of the isospin-asymmetry expansion of the nuclear equation of state in many-body perturbation theory*, Phys. Rev. C **93**, 055802 (2016).

- [238] J. M. Dong, U. Lombardo, and W. Zuo, $^3\text{PF}_2$ pairing in high-density neutron matter, *Phys. Rev. C* **87**, 062801 (2013).
- [239] K. Hebeler, H. Krebs, E. Epelbaum, J. Gólk, and R. Skibinski, *Efficient calculation of chiral three-nucleon forces up to $N^3\text{LO}$ for ab initio studies*, *Phys. Rev. C* **91**, 044001 (2015).
- [240] S. Binder *et al.* (LENPIC Collaboration), *Few-nucleon systems with state-of-the-art chiral nucleon-nucleon forces*, *Phys. Rev. C* **93**, 044002 (2016).
- [241] S. Kurth, C. R. Proetto, and K. Capelle, *Dependence of Response Functions and Orbital Functionals on Occupation Numbers*, *J. Chem. Theory Comput.* **5**, 693 (2009).
- [242] S. Kümmel and L. Kronik, *Orbital-dependent density functionals: Theory and applications*, *Rev. Mod. Phys.* **80**, 3 (2008).
- [243] A. Görling and M. Levy, *Exact Kohn-Sham scheme based on perturbation theory*, *Phys. Rev. A* **50**, 196 (1994).
- [244] A. Görling, *New KS Method for Molecules Based on an Exchange Charge Density Generating the Exact Local KS Exchange Potential*, *Phys. Rev. Lett.* **83**, 5459 (1999).
- [245] E. Engel, A. Facco Bonetti, S. Keller, I. Andrejkovics, and R. M. Dreizler, *Relativistic optimized-potential method: Exact transverse exchange and Møller-Plesset-based correlation potential*, *Phys. Rev. A* **58**, 964 (1998).
- [246] S. Kümmel and J. P. Perdew, *Simple Iterative Construction of the Optimized Effective Potential for Orbital Functionals, Including Exact Exchange*, *Phys. Rev. Lett.* **90**, 043004 (2003).
- [247] S. Kümmel and J. P. Perdew, *Optimized effective potential made simple: Orbital functionals, orbital shifts, and the exact Kohn-Sham exchange potential*, *Phys. Rev. B* **68**, 035103 (2003).
- [248] M. R. Hestenes and E. Stiefel, *Methods of Conjugate Gradients for Solving Linear Systems*, *J. Res. Nat. Bur. Stand.* **49**, 409 (1952).
- [249] D. A. Varshalovich, A. N. Moskalev, and V. K. Khersonskii, *Quantum Theory Of Angular Momentum* (World Scientific, Singapore, 1988).
- [250] J. B. Krieger, Y. Li, and G. J. Iafrate, *Derivation and application of an accurate Kohn-Sham potential with integer discontinuity*, *Phys. Lett. A* **146**, 256 (1990).
- [251] J. B. Krieger, Y. Li, and G. J. Iafrate, *Systematic approximations to the optimized effective potential: Application to orbital-density-functional theory*, *Phys. Rev. A* **46**, 5453 (1992).
- [252] S. Kümmel and L. Kronik, *Orbital-dependent density functionals: Theory and applications*, *Rev. Mod. Phys.* **80**, 3 (2008).
- [253] B. A. Brown, *New Skyrme interaction for normal and exotic nuclei*, *Phys. Rev. C* **58**, 220 (1998).
- [254] S. Gandolfi, J. Carlson, and S. C. Pieper, *Cold Neutrons Trapped in External Fields*, *Phys. Rev. Lett.* **106**, 012501 (2011).

- [255] P. Maris, J. P. Vary, S. Gandolfi, J. Carlson, and S. C. Pieper, *Properties of trapped neutrons interacting with realistic nuclear Hamiltonians*, Phys. Rev. C **87**, 054318 (2013).
- [256] S. K. Bogner, R. J. Furnstahl, H. Hergert, M. Kortelainen, P. Maris, M. Stoitsov, and J. P. Vary, *Testing the density matrix expansion against ab initio calculations of trapped neutron drops*, Phys. Rev. C **84**, 044306 (2011).
- [257] T. Duguet and J. Sadoudi, *Breaking and restoring symmetries within the nuclear energy density functional method*, J. Phys. G: Nucl. Part. Phys. **37**, 064009 (2010).
- [258] D. R. Thompson, M. Lemere, and Y. C. Tang, *Systematic investigation of scattering problems with the resonating-group method*, Nucl. Phys. A **286**, 53 (1977).
- [259] G. P. Kamuntavičius, R. K. Kalinauskas, B. R. Barrett, S. Mickevičius, and D. Germanas, *The general harmonic-oscillator brackets: compact expression, symmetries, sums and Fortran code*, Nucl. Phys. A **695**, 191 (2001).
- [260] M. Galassi, J. Davies, J. Theiler, B. Gough, G. Jungman, P. Alken, M. Booth, and F. Rossi, *GNU Scientific Library Reference Manual - Third Edition* (Network Theory Ltd., United Kingdom, 2009).

Wissenschaftlicher Werdegang

ZUR PERSON

Name	Thomas Krüger
Geburtsdatum	18. Juni 1988
Geburtsort	Groß-Gerau
Nationalität	deutsch

AKADEMISCHE AUSBILDUNG

11/2012 – 10/2016	Doktorand (im Rahmen des DFG-Sonderforschungsbereichs 634), Institut für Kernphysik – Theoriezentrum, Technische Universität Darmstadt
10/2011 – 10/2012	Masterstudium in Physik, Technische Universität Darmstadt, Thesis: <i>Four-nucleon forces in nucleonic matter</i> , Betreuer: Professor Achim Schwenk, Ph.D., Master of Science in Physik
10/2009 – 06/2010	Auslandsstudium in Mathematik und Physik, University of Bath, Vereinigtes Königreich
10/2007 – 09/2011	Bachelorstudium in Physik und Mathematik, Technische Universität Darmstadt, Thesis: <i>Strongly interacting Fermions with unequal masses in harmonic traps</i> , Betreuer: Professor Achim Schwenk, Ph.D., Bachelor of Science in Physics

PREISE UND AUSZEICHNUNGEN

02/2015 – 10/2016	Promotionsstipendium der Studienstiftung des deutschen Volkes
01/2013	M.Sc.-Forschungspreis der Gerhard-Herzberg-Gesellschaft für die in der Masterarbeit gezeigten Leistungen
10/2007 – 10/2012	Stipendium der Studienstiftung des deutschen Volkes

Erklärung zur Dissertation

Hiermit versichere ich, die vorliegende Dissertation ohne Hilfe Dritter nur mit den angegebenen Quellen und Hilfsmitteln angefertigt zu haben. Alle Stellen, die aus Quellen entnommen wurden, sind als solche kenntlich gemacht. Diese Arbeit hat in gleicher oder ähnlicher Form noch keiner Prüfungsbehörde vorgelegen. Eine Promotion wurde bisher noch nicht versucht.

Darmstadt, den 19. September 2016

Thomas Krüger

